GOETHE UNIVERSITÄT FRANKFURT AM MAIN

Institut für **A**tmosphäre und **U**mwelt
Fachbereich Geowissenschaften/Geographie

Deriving stratospheric age of air spectra using chemically active trace gases from observations and models

Dissertation
zur Erlangung des Doktorgrades
der Naturwissenschaften

vorgelegt beim Fachbereich 11 Geowissenschaften/Geographie
der Johann Wolfgang Goethe-Universität
in Frankfurt am Main

von
Marius Hauck
aus Aschaffenburg

Frankfurt am Main 2020
(D 30)

Vom Fachbereich 11 Geowissenschaften/Geographie der Johann Wolfgang Goethe-Universität als Dissertation angenommen.

Dekan:
Prof. Dr. Georg Rümpker

Gutachter:
Apl. Prof. Dr. Andreas Engel (Goethe-Universität Frankfurt am Main)
Jun.-Prof. Dr. Felix Plöger (Forschungszentrum Jülich / Bergische Universität Wuppertal)
Prof. Dr. Joachim Curtius (Goethe-Universität Frankfurt am Main)

Datum der Disputation: 19.03.2021

Abstract

The analysis of the global stratospheric meridional circulation, known as the Brewer-Dobson circulation, is an essential part of both experimental and theoretical atmospheric sciences. This large-scale circulation has a crucial influence on the global burden of greenhouse gases and ozone depleting substances throughout the complete atmosphere. This makes it an important factor for the Earth's radiative budget, which is perceptible at the Earth's surface despite the remote location of the stratosphere. In the course of climate change it is generally expected that also the Brewer-Dobson circulation undergoes significant changes in structure and strength, although the exact repercussions are still uncertain and thus remain an open scientific question. A general problem for the observational investigation of the dynamical processes in the stratosphere is that residual mean transport cannot be measured directly and hence requires the use of sophisticated proxies. Many studies in the past consider the so-called mean age of air, which is a measure of the average time an air parcel has spent in the stratosphere since passing a certain reference point. While changes in the strength and structure can be detected and visualized using mean age of air, a more thorough distinction between the different involved transport mechanisms of the circulation (residual circulation, mixing) cannot be made. For that, consideration of a full distribution of all relevant transit times through the stratosphere, an age spectrum, is favorable and a powerful tool to analyze the spatial structure as well as possible future changes in detail. Mean age of air and age spectra can be readily derived in atmospheric modeling studies, but an observationally based retrieval is challenging. Mean age of air is usually approximated from measurements of very long-lived trace gas species that act as a dynamical tracer for the stratosphere. The retrieval of age spectra from observations, however, remains an open task for which different methods have been proposed in the past, that often require a combination of strong assumptions and model data explicitly. This is a major issue for a precise and independent investigation of stratospheric dynamics based on measurements.

The focus of this cumulative dissertation is on the development process and application of an inversion method to derive stratospheric age spectra from mixing ratios of chemically active substances that combines an applicable and precise ansatz with a minimized amount of necessary model data. Chemically active species have the important benefit that chemistry and transport in the stratosphere are strongly correlated so that the state of depletion of a trace gas can give some information on certain parts of the age spectrum. Considering a sufficient number of distinct trace gases simultaneously, a full approximation of the age spectrum should be possible. The main section of this thesis is split into three parts, which follow the main aspects and key results of the three publications involved (Hauck et al., 2019, 2020; Keber et al., 2020). The newly developed inverse method is based upon the previously established ansatz by Schoeberl et al. (2005), but constrains the shape of the age spectrum by a single parameter inverse Gaussian function. This keeps the balance between applicability and accuracy with a limited amount of measurement data. Additionally, the method introduces a seasonal scaling factor that imposes higher order maxima and minima onto the intrinsically monomodal spectrum based on the seasonal cycle of the tropical upward mass flux to incorporate phases of weaker and stronger transport. A proof of concept of the inverse method is provided using an idealized simulation of the ECHAM/MESSy Atmospheric Chemistry (EMAC) model, where the method is applied to a set of artificial radioactive trace gases with known chemical lifetime. The results imply that the method works properly and retrieves age spectra that match the EMAC reference spectra significantly well on the global and seasonal scale. Only in the lower stratosphere, the performance of the inverse method on the seasonal scale decreases as entrainment into the stratosphere is considered only across the tropical tropopause. Transport across the local extratropical tropopause, however, is a key feature for trace gases in the extratropical lowermost stratosphere so that this entrainment must be included explicitly.

In the second part, the discovered problems are approached to make the inverse method applicable to observations. The formulation of the method is extended to incorporate transport explicitly across the tropical (30° S – 30° N), northern extratropical (30° N – 90° N), and southern extratropical

tropopause (30° S – 90° S) each with a single age spectrum that can be inverted independently. Furthermore, a scaling factor is introduced for each of the tropopause sections that mirrors the seasonality of the relevant net upward mass flux through the tropopause and imposes corresponding maxima and minima onto the inverse age spectra. In an additional proof of concept with the Chemical Lagrangian Model of the Stratosphere (CLaMS) the extended method is tested using similar artificial radioactive substances as in the EMAC simulation. The results indicate that the extension of the method is valuable as the seasonality in transport is now correctly retrieved in the extratropical lowermost stratosphere. Corresponding extratropical inverse age spectra match the CLaMS reference spectra well so that the extended inverse method can be applied to real observational data.
This is done in the final part of the thesis. Mixing ratio data for 11 trace gas species from the two airborne measurement campaigns PGS (POLSTRACC / GW-LCYCLE / SALSA) and WISE (Wave-driven Isentropic Exchange) with the High Altitude and Long Range research aircraft (HALO) in the northern hemispheric lowermost stratosphere are considered for the application. Since the relevant chemical lifetimes of these substances are unknown, a Monte Carlo Cross-Validation (MCCV) is introduced where age spectra and chemical lifetimes are retrieved in stepwise fashion tainted by pseudo-random errors to estimate the uncertainty range of the results. The resulting mean age of air distributions and campaign-averaged age spectra are meaningful and implicate an enhanced entrainment of air prior to the WISE campaign (fall 2017) and the first PGS phase (winter 2015/2016) likely related to the weak northern hemispheric subtropical jet stream during summer. These findings coincide well with the findings of previous studies using mean age of air from observations and imply that the retrieval of age spectra with the inverse method works properly. The derived inverse age spectra from PGS and WISE give also implications for approximations applied in previous studies for the retrieval of mean age of air from trace gas measurements and thus might be re-assessed in the future.
In summary, the inverse method, which has been developed, extended, thoroughly tested, and finally applied to measurement data in the frame of this thesis, proves to retrieve age spectra reliably and consistent with previous work in the northern hemispheric lowermost stratosphere. The derived age spectra mirror the seasonality in stratospheric dynamics robustly and include important aspects of transport with minimized direct influence of model data. Although the results must be always seen in the light of the relatively large uncertainty range, the extended inverse method provides an additional tool for a quantitative analysis of stratospheric transport that could forward the assessment of possible changes of the Brewer-Dobson circulation in the future.

The German version of this abstract can be found below.

Kurzzusammenfassung

Das Verständnis der globalen meridionalen Zirkulation der Stratosphäre ist ein Kernaspekt der experimentellen und theoretischen Atmosphärenwissenschaften. Dieses großskalige Zirkulationssystem, welches nach ihren Entdeckern auch als Brewer-Dobson-Zirkulation benannt ist, hat einen essenziellen Einfluss auf die globalen atmosphärischen Budgets von Treibhausgasen und ozonzerstörenden Substanzen. Dies führt dazu, dass die Zirkulation einen wichtigen Prozess für den Strahlungshaushalt der Erde darstellt, dessen Auswirkungen trotz der Distanz auch am Erdboden direkt wahrnehmbar sind. Im Zuge des Klimawandels wird im Allgemeinen erwartet, dass sich auch die Struktur und Stärke der Zirkulation verändern wird. Die genauen Ausmaße und Richtungen dieser Änderungen sind aber bisher noch ungewiss und Gegenstand aktueller Forschung. Problematisch ist hierbei, dass die Zirkulation eine mittlere Residualzirkulation darstellt, wodurch der Transport nicht direkt messbar ist und aus geeigneten Messgrößen abgeleitet werden muss. Das gilt insbesondere für experimentelle Untersuchungen mit generell stark limitierter Datenmenge. In vielen Arbeiten wird hierzu das mittlere Alter der Luft herangezogen, welches ein Maß für Zeit darstellt, die im Mittel vergangen ist seit ein Luftpaket eine bestimmte Referenzfläche passiert hat. Mit dieser Größe können zwar Veränderungen in der Struktur und auch Stärke diagnostiziert und dargestellt werden, eine Unterscheidung zwischen den verschiedenen Transportmechanismen der Zirkulation (Mischung, Residualtransport) ist aber nicht möglich. Dazu muss die komplette Wahrscheinlichkeitsverteilung von Transitzeiten durch die Stratosphäre innerhalb eines Luftpakets betrachtet werden. Dieses Altersspektrum ist ein vielseitiges Werkzeug um die räumliche Struktur der Zirkulation und mögliche zeitliche Veränderungen detailliert zu analysieren. Während das mittlere Alter und auch Altersspektren im Modell leicht bestimmt werden können ist eine Ableitung aus Beobachtungen eine Herausforderung. Das mittlere Alter wird üblicherweise aus Messungen langlebiger Spurengase bestimmt, welche in der Stratosphäre gute dynamische Tracer sind. Altersspektren hingegen sind deutlich komplexer und eine große Zahl von verschiedenen Methoden existiert, die oftmals auf einer Kombination von starken Annahmen und Modelldaten beruhen. Dies stellt eine unabhängige und präzise Bestimmung von Altersspektren aus Beobachtungen vor besondere Probleme.

Das Ziel dieser kumulativen Dissertation ist die Entwicklung und Anwendung einer Inversionsmethode zur Ableitung stratosphärischer Altersspektren aus Mischungsverhältnissen chemisch aktiver Spurengase. Die Methode soll hierbei anwendbar gestaltet sein und zugleich die Anzahl notwendiger Modelldaten für die Ableitung minimieren, um möglichst unabhängige Analysen zu ermöglichen. Chemisch aktive Substanzen haben den großen Vorteil, dass stratosphärischer Transport und chemischer Abbau eng gekoppelt sind und somit der Grad des Abbaus Rückschlüsse auf Teile des Altersspektrums zulässt. Nutzt man eine ausreichende Anzahl verschiedener Spezies simultan für die Inversion sollte eine komplette Abschätzung des Altersspektrums möglich sein. Der Hauptteil dieser Dissertation ist dreigeteilt, wobei die einzelnen Abschnitte den Kernaspekten der drei involvierten Publikationen folgen (Hauck et al., 2019, 2020; Keber et al., 2020). Die neue inverse Methode basiert hierbei auf der Methode von Schoeberl et al. (2005), parametrisiert die Spektren aber durch eine inverse Gaußverteilung mit nur einem freien Parameter. Das ist ein guter Kompromiss für die Anwendbarkeit und Genauigkeit der Method bei gleichzeitig limitierter verfügbarer Datenmenge. Zusätzlich wird in der Methode ein saisonaler Skalierungsfaktor eingeführt, welcher höhere Maxima und Minima bei der Inversion auf die monomodalen Altersspektren aufprägt, um die saisonal variierende Stärke des stratosphärischen Transports zu approximieren. Der Skalierungsfaktor ist aus dem Aufwärtsmassenfluss in den Tropen abgeleitet. In einem Proof of Concept mit dem Klimachemiemodell EMAC (ECHAM/MESSy Atmospheric Chemistry) wird die Methode auf einen Datensatz künstlicher radioaktiver Substanzen mit bekannter Lebenszeit angewandt und getestet. Die Ergebnisse zeigen, dass die Inversion verlässlich funktioniert und die Altersspektren auf globaler und jahreszeitlicher Skala mit den Referenzspektren aus EMAC gut übereinstimmen. Nur in der unteren extratropischen Stratosphäre verschlechtert sich die Übereinstimmung, da der Eintrag von Luftmassen nur über die tropische Tropopause berücksichtigt wird. Lokaler Transport über die extratropische Tropopause

ist allerdings besonders relevant für die Zusammensetzung der Luft in der untersten Stratosphäre, sodass diese Prozesse berücksichtigt werden müssen und die Methode daher Modifikationen bedarf. Im zweiten Teil wird die Methode anhand der aufdeckten Probleme erweitert, um eine Anwendung auf echte Beobachtungsdaten zu ermöglichen. Der Formalismus der inversen Methode wird erweitert um Transport über die tropische (30° S – 30° N), nördliche extratropische (30° N – 90° N) und südliche extratropische Tropopause (30° S – 90° S) mit je einem eigenen Altersspektrum zu beschreiben, welches unabhängig invertiert werden kann. Für die beiden extratropischen Tropopausensegmente wird ebenfalls ein Skalierungsfaktor eingeführt, welcher die Saisonalität im jeweiligen netto aufwärts gerichteten Massenfluss auf die Spektren aufprägt. In einem zweiten Proof of Concept mit dem Chemietransportmodell CLaMS (Chemical Lagrangian Model of the Stratosphere) wird die erweiterte Methode an einem ähnlichen Datensatz künstlicher radioaktiver Substanzen wie in EMAC getestet. Die Resultate zeigen auch hier, dass die Erweiterung ein notwendiger und sinnvoller Schritt ist, da die invertierten Altersspektren nun die Saisonalität des Transports in der extratropischen unteren Stratosphäre richtig beschreiben. Die zugehörigen Altersspektren stimmen mit den Referenzspektren aus CLaMS gut überein und ermöglichen eine Anwendung der Methode auf Beobachtungen im letzten Schritt der Arbeit.
Zur Anwendung der Methode werden Daten von elf Spurengasspezies verwendet, welche während den zwei Flugzeugkampagnen PGS (POLSTRACC / GW-LCYCLE / SALSA) und WISE (Wave-driven Isentropic Exchange) mit dem Forschungsflugzeug HALO (High Altitude and Long Range research aircraft) in der nördlichen untersten Stratosphäre gemessen wurden. Da die relevanten chemischen Lebenszeiten der Substanzen unbekannt sind, wird eine Monte Carlo Kreuzvalidierung (MCCV – Monte Carlo Cross-Validation) implementiert, bei welcher die Lebenszeiten und Altersspektren schrittweise bestimmt und mit pseudozufälligen Fehlern verschränkt werden, um den Unsicherheitsbereich der Ergebnisse abzuschätzen. Die abgeleitete Verteilung des mittleren Alters sowie die kampagnengemittelten Altersspektren erscheinen sinnvoll und deuten einen verstärkten Eintrag frischer troposphärischer Luft in die Stratosphäre vor der WISE-Kampagne (Herbst 2017) sowie der ersten Phase von PGS (Winter 2015/2016) an. Das steht sehr wahrscheinlich mit dem schwachen Subtropenjetstream im nördlichen Sommer in Zusammenhang und ist in Einklang mit vorherigen Studien zu mittlerem Alter aus Beobachtungen in der nördlichen untersten Stratosphäre. Diese Ergebnisse implizieren, dass die Methode ordnungsgemäß funktioniert. Die invertierten Altersspektren zu PGS und WISE können weiterhin dazu genutzt werden, Näherungen zur Bestimmung des mittleren Alters aus Beobachtungen in früheren Arbeiten neu zu untersuchen und gegebenenfalls zu überarbeiten.
Zusammenfassend lässt sich festhalten, dass die inverse Methode, welche im Rahmen dieser Arbeit entwickelt, erweitert, ausgiebig getestet und schließlich angewandt wurde, verlässlich Altersspektren aus Messdaten chemisch aktiver Spurengase ableiten kann, welche in Einklang mit früheren Arbeiten zum Transport in der nördlichen untersten Stratosphäre stehen. Die Spektren spiegeln die Saisonalität und Struktur der stratosphärischen Dynamik korrekt wider und das bei minimiertem Einfluss von Modelldaten. Obwohl die Ergebnisse immer zusammen mit der vergleichsweise großen Schwankungsbreite betrachtet werden müssen, erweist sich die erweiterte inverse Methode als potentes zusätzliches Werkzeug zur quantitativen Analyse des Transports in der Stratosphäre aus Beobachtungen, welches das Verständnis von möglichen Änderungen der Zirkulation in der Zukunft voranbringen könnte.

Die englische Version dieser Kurzzusammenfassung ist weiter oben zu finden.

Table of Contents

List of Figures

List of Tables

List of Contributing Peer-Reviewed Articles

This cumulative dissertation summarizes concepts, methods, data, and key results that are published in detail in the following three articles, which can also be found in the attachment below:

- **Hauck, M.**, Fritsch, F., Garny, H., and Engel, A.: *Deriving stratospheric age of air spectra using an idealized set of chemically active trace gases*, Atmospheric Chemistry and Physics, 19, 5269-5291, DOI: https://doi.org/10.5194/acp-19-5269-2019, 2019
- **Hauck, M.**, Bönisch, H., Hoor, P., Keber, T., Ploeger, F., Schuck, T., and Engel, A.: *A convolution of observational and model data to estimate age of air spectra in the northern hemispheric lower stratosphere*, Atmospheric Chemistry and Physics, 20, 8763-8785, DOI: https://doi.org/10.5194/acp-20-8763-2020, 2020
- Keber, T., Bönisch, H., Hartick, C., **Hauck, M.**, Lefrancois, F., Obersteiner, F., Ringsdorf, A., Schohl, N., Schuck, T., Hossaini, R., Graf, P., Jöckel, P., and Engel, A.: *Bromine from short–lived source gases in the extratropical northern hemispheric upper troposphere and lower stratosphere (UTLS)*, Atmospheric Chemistry and Physics, 20, 4105-4132, DOI: https://doi.org/10.5194/acp-20-4105-2020, 2020

Deutsche Zusammenfassung

Die vielfältigen physikalischen und chemischen Prozesse in der Stratosphäre, der zweituntersten Schicht der Erdatmosphäre, sind trotz ihrer entfernten Lage von zentraler Bedeutung für das Leben am Erdboden. Das macht die Überwachung und das genaue Verständnis dieser Vorgänge in der Vergangenheit und Gegenwart zu einem Kernaspekt der Atmosphärenwissenschaften, sodass mögliche Veränderungen in der Zukunft durch elaborierte Modellsimulationen möglichst präzise prognostiziert und schließlich diagnostiziert werden können. Der Sinn dieser Maßnahmen hat sich besonders im letzten Viertel des 20. Jahrhunderts gezeigt, als die rasche Entdeckung und Erforschung des stratosphärischen Ozonzabbaus verursacht durch anthropogene Emissionen von Fluorchlorkohlenwasserstoffen zu einer Reglementierung der Quellsubstanzen geführt hat und sich so die Ozonschicht zum heutigen Zeitpunkt langsam wieder erholt. Im Rahmen des anthropogenen Klimawandels wird ebenfalls erwartet, dass auch die Stratosphäre durch Treibhausgasemissionen komplexe Veränderungen durchlaufen wird, welche sich schließlich durch die enge gegenseitige Wechselwirkung von Stratosphäre und Troposphäre auch auf das Wetter und Klima am Erdboden auswirken könnten (z.B. Gerber et al., 2012).
Das Problem, welches eine allumfassende Untersuchung der Stratosphäre erschwert, ist ihre große Entfernung zum Erdboden und gleichzeitige hohe vertikale Ausdehnung. Je nach geographischer Breite beginnt die Stratosphäre zwischen einer Höhe von 8 km im polaren Bereich und 18 km in äquatorialen Regionen der Erde. In diesem Bereich befindet sich auch die Tropopause, welche die Übergangsschicht zwischen Troposphäre und Stratosphäre darstellt. Am oberen Ende der Stratosphäre findet sich dann am Übergang zur Mesosphäre die Stratopause in einer Höhe von circa 50 km. Diesen großen Höhenbereich abzudecken stellt die experimentelle Erforschung der Stratosphäre seit Beginn der ersten Messungen vor große Probleme. Durch den technologischen Fortschritt kommen heute insbesondere Flugzeugmessungen in der unteren Stratosphäre zum Einsatz, wohingegen für die restlichen Bereiche Satelliten, Ballone und vereinzelt Raketen eingesetzt werden. Allerdings ist das Spektrum von gemessenen chemischen Substanzen und meteorologischen Parametern stark begrenzt und für die unterschiedlichen Messmethoden verschieden, sodass die allgemeine globale Datenbasis im Vergleich zur Troposphäre deutlich limitierter ist. Das führt auch dazu, dass die Analysen durch modernste Klimachemie- und Chemietransportmodelle ergänzt werden und zu einer im Allgemeinen engen Kooperation zwischen experimenteller und theoretischer Forschung führen. Obwohl Modellanalysen das Verständnis der stratosphärischen Chemie und Dynamik vorangebracht haben, so haben Vergleiche mit verfügbaren Messdaten auch gezeigt, dass es hinsichtlich der vom Modell prognostizierten und beobachteten Veränderungen des stratosphärischen Transports zum Teil große Diskrepanzen gibt (z.B. Waugh, 2009), welche eine genauere Analyse der Dynamik und möglicher Modifikationen zu einem relevanten Thema aktueller Forschung machen (z.B. Bönisch et al., 2011; Ploeger et al., 2015b; Stiller et al., 2017).
Der Transport in der Stratosphäre ist durch eine globale meridionale Zirkulation gekennzeichnet, welche Luft von den Tropen zu den Polen befördert und nach ihren beiden Entdeckern zumeist Brewer-Dobson-Zirkulation genannt wird. Die Luft tritt hierbei primär im Bereich der tropischen Tropopause in die Stratosphäre ein (Fueglistaler et al., 2009), obwohl insbesondere in der untersten Stratosphäre der Extratropen quasi-horizontale Mischungsprozesse durch die Tropopause einen starken Einfluss auf die chemische Zusammensetzung haben (z.B. Hoor et al., 2005; Bönisch et al., 2009). Transportprozesse in der Brewer-Dobson-Zirkulation lassen sich in eine Residualzirkulation mit einem Nettomassenfluss und bidirektionale Mischung ohne Nettomassenfluss unterteilen (z.B. Plumb, 2002; Butchart, 2014). Innerhalb der Residualzirkulation wird primär zwischen zwei Haupttransportpfaden unterschieden (Birner and Bönisch, 2011), auf denen die Luft von den Tropen durch verschiedene Bereiche der Stratosphäre transportiert wird und in den hohen Breiten wieder zurück in die Troposphäre absteigt. Der flache Ast der Zirkulation erstreckt sich knapp oberhalb der Tropopause von den Tropen direkt in die mittleren Breiten beider Hemisphären. Der tiefe Ast hingegen führt von den Tropen zunächst in die obere Stratosphäre und sogar Mesosphäre, bevor die

Luft auf beiden Hemisphären wieder in die unteren Bereiche absinkt, wobei dies verstärkt auf der jeweiligen Winterhalbkugel stattfindet. Die Transportzeiten entlang dieser Pfade unterscheiden sich stark und bewegen sich im Bereich von bis zu einem Jahr für den flachen Ast und mehreren Jahren für den tiefen Ast (Birner and Bönisch, 2011). Die bidirektionalen Mischungsprozesse treten hierbei verstärkt im Bereich der Tropopause und der sogenannten "Surf Zone" (McIntyre and Palmer, 1984) in den mittleren Breiten der Stratosphäre auf. Sowohl die Residualzirkulation als auch die Mischung werden durch verschiedene Arten planetarer und synoptischer Wellen angetrieben, die in der Troposphäre angeregt werden, in die Stratosphäre propagieren, dort schließlich brechen und einen Impulsfluss bewirken (McIntyre and Palmer, 1983). Ein großes Problem für die quantitative Analyse der stratosphärischen Zirkulation liegt in ihrem residualen Charakter, durch welchen sich nur im zeitlichen Mittel eine meridional gerichtete Zirkulation ergibt und diese somit nicht direkt mess- und damit quantifizierbar ist. In diversen Arbeiten in der Vergangenheit wurden daher verschiedene Näherungsgrößen entwickelt und herangezogen um die Stärke der Zirkulation zu quantifizieren und so ihre Struktur und mögliche zeitliche Veränderungen zu untersuchen. Das gilt insbesondere für beobachtungsbasierte Forschung, wo die limitierte Datenbasis die Möglichkeiten stark einschränkt. Eine häufig verwendete Größe ist das sogenannte mittlere Alter der Luft, welches für ein Luftpaket die im Mittel vergangene Zeit angibt seit das Paket eine bestimmte Referenzfläche passiert hat. Üblicherweise wird hierfür der Erdboden oder die tropische Tropopause verwendet. Zwar ist das mittlere Alter im Modell leicht realisierbar, in der Realität benötigt man hierfür allerdings dynamische Tracer, welche Rückschlüsse auf die abgelaufenen Transportprozesse geben. Dazu werden oft Messungen chemisch sehr stabiler Spurengase verwendet, unter anderem SF_6 oder CO_2 (z.B. Engel et al., 2002; Ray et al., 2014; Engel et al., 2017), die in guter Näherung durch ihre lange Lebenszeit als dynamische Tracer betrachtet werden können. Der Vergleich von mittlerem Alter zu zwei verschiedenen Zeitpunkten kann dann Aufschluss über Änderungen der Zirkulationsgeschwindigkeit am betrachteten Ort geben (Austin and Li, 2006).
Für tiefergehende Untersuchungen der Zirkulationsstruktur allerdings ist das mittlere Alter nicht ausreichend, da es als Mittelwert nur die generelle Stärke der Zirkulation widerspiegelt und keine Unterscheidung zwischen den einzelnen beteiligten Transportprozessen, also Residualtransport und Mischung, und deren Zeitskalen zulässt. Für eine solche Analyse ist die zugehörige Verteilung aller Transitzeiten durch die Stratosphäre innerhalb des Luftpakets, das sogenannte Altersspektrum (Kida, 1983), ein wichtiges Werkzeug zur Quantifizierung des Transports. Der Referenzpunkt für die Transitzeiten ist hier ebenfalls oftmals der Erdboden oder die tropische Tropopause. Da das Altersspektrum eine Wahrscheinlichkeitsdichtefunktion darstellt, ist das erste Moment dieser Verteilung das mittlere Alter. Durch eine Analyse der verschiedenen Bereiche des Altersspektrums zu verschiedenen Zeiten lassen sich die einzelnen Teile und Prozesse der Brewer-Dobson-Zirkulation analysieren. So beeinflusst zum Beispiel die Mischung von Luft aus den mittleren Breiten zurück in die Tropen, ein Prozess der auch als Alterung durch Mischung bekannt ist (Garny et al., 2014), primär den Schwanz der Verteilung. In Modellsimulationen lässt sich das Altersspektrum durch eine Serie von Pulsen idealisierter inerter Spurengase realisieren, wobei die Auflösung von der Gesamtanzahl der einzelnen Pulse bestimmt wird (z.B. Reithmeier et al., 2008; Li et al., 2012a; Ploeger and Birner, 2016). Die Bestimmung des Altersspektrums aus Beobachtungen ist dagegen eine große Herausforderung, da detaillierte Informationen über den vergangenen Zustand der Stratosphäre aus einzelnen Messgrößen in der Gegenwart abgeleitet werden müssen. Zur Lösung dieses Problems wurden diverse Methoden postuliert, welche aus den Mischungsverhältnissen verschiedener chemisch aktiver Spurengase Altersspektren bestimmen (z.B. Schoeberl et al., 2005; Ehhalt et al., 2007; Podglajen and Ploeger, 2019). Die generelle Idee dahinter nutzt den Fakt, dass stratosphärische Chemie und Transport eng miteinander verschränkt sind. Das bedeutet, dass der Abbauzustand eines Spurengases Informationen über Transportzeitskalen geben kann, die sich im Bereich der chemischen Lebenszeit des Gases bewegen. Nutzt man eine ausreichende Anzahl an Spurengasen mit unterschiedlichen Senkengeschwindigkeiten simultan, lässt sich das Altersspektrum als ganzes abschätzen (Schoeberl et al., 2005). Allerdings beruhen die in der Vergangenheit entwickelten Methoden oft auf starken

Annahmen über die Form des Spektrums, den Transport oder die Chemie oder beziehen explizit Modelldaten in die Ableitung mit ein. Das erschwert einen unabhängigen Vergleich mit Modellresultaten zur Identifizierung eventueller Inkonsistenzen und macht die Ableitung von Altersspektren aus Beobachtungsdaten zu einer offenen und sehr relevanten Fragestellung der Stratosphärenforschung. Darauf aufbauend fußt die Aufgabenstellung für diese kumulative Dissertation. Das Ziel ist die Entwicklung einer Methode zur Ableitung von stratosphärischen Altersspektren aus Mischungsverhältnissen verschiedener chemisch aktiver Spurengase, welche leicht anwendbar, präzise und so unabhängig von Modelldaten wie möglich arbeiten soll. Der Hauptteil der Dissertation ist in drei Teile gegliedert, welche den drei im Rahmen der Arbeit veröffentlichten Publikationen folgen und ihre wichtigen Aspekte sowie Schlüsselresultate aufzeigen und zusammenfassen. Im ersten Teil werden der grundlegende Entwicklungsprozess der Methode, die implementierten Modifikationen, ein erster Proof of Concept in einer idealisierten Modellsimulation sowie aufkommende Probleme behandelt. Dieser Abschnitt folgt den Aspekten von Hauck et al. (2019). Der zweite Teil beschäftigt sich mit einer grundlegenden Erweiterung der Methode zur Lösung der festgestellten Probleme und einem zweiten Proof of Concept mit der erweiterten Methode, was einen Teil der zweiten Publikation (Hauck et al., 2020) ausmacht. Im finalen Teil der Arbeit wird die Methode auf reale Messdaten elf verschiedener Spurengase angewandt, welche im Rahmen zweier Kampagnen mit dem HALO Forschungsflugzeug (High Altitude and Long Range research aircraft) durchgeführt wurden. Die Methodik und Ergebnisse dieser Anwendung sind in Hauck et al. (2020) publiziert, die Datengrundlage ist detailliert in Keber et al. (2020) angeführt, welche die dritte Publikation dieser Dissertation darstellt.

Als Ausgangsbasis für den Entwicklungsprozess im Rahmen dieser Dissertation dient die Methode von Schoeberl et al. (2005), da sie die besten Voraussetzungen für eine Methode mit den oben erwähnten Anforderungen birgt. Die Grundidee beruht auf einem mathematischen Inversionsproblem, weshalb die entwickelte Methode als inverse Methode bezeichnet wird. Schoeberl et al. (2005) parametrisieren das Altersspektrum als inverse Gaußfunktion mit drei freien Parametern, welche auf den grundlegenden Resultaten von Hall and Plumb (1994) beruht. Die Parametrisierung des Altersspektrums stellt eine starke Vereinfachung dar, welche nicht notwendigerweise für die komplette Stratosphäre valide ist. Verschiedene Modellstudien implizieren aber, dass eine inverse Gaußfunktion in vielen Fällen eine sehr gute Näherung für das Altersspektrum darstellt und den aus dem Modell bestimmten Verteilungen sehr nahe kommt, insbesondere im Jahresmittel (z.B. Li et al., 2012b; Ploeger and Birner, 2016). Zudem hat die Parametrisierung der Spektrumsform den enormen Vorteil, dass die benötigte Datenbasis deutlich geringer ausfällt als im unparametrisierten Fall und der komplette Informationsgehalt der Spurengasmischungsverhältnisse dazu genutzt wird die inverse Gaußverteilung so gut wie möglich anzupassen. Das Altersspektrum wird dann numerisch bestimmt, indem die Parameter der inversen Gaußverteilung solange iteriert werden bis der Fehler zwischen den aus dem Spektrum berechneten Mischungsverhältnissen und den gemessenen minimiert wurde. Zur Weiterentwicklung und Verbesserung der Methode werden drei hauptsächliche Änderungen vorgenommen. Zunächst wird die Parametrisierung der inversen Gaußverteilung so modifiziert, dass nur noch ein freier Parameter vorhanden ist. Das hat zur Folge, dass einerseits der numerische Aufwand reduziert wird und andererseits die Gefahr sinkt ein lokales statt des gewünschten globalen Minimums des Fehlers zu treffen. Zudem wird das Fehlermaß vereinfacht um das Minimierungsproblem in ein mathematisch simpleres Nullstellenproblem zu überführen für das numerisch sehr effektive Algorithmen existieren. Die dritte Änderung betrifft die Form der invertierten Spektren. Per Definition ist die inverse Gaußverteilung immer durch eine einzige ausgeprägte Mode gekennzeichnet. Allerdings haben Untersuchungen von Altersspektren im Modell gezeigt, dass auf der saisonalen Zeitskala mehrere ausgeprägte Maxima und Minima in den Spektren auftreten (z.B. Abb. 5 in Ploeger and Birner, 2016), welche durch die jahreszeitliche Schwankung des stratosphärischen Transports verursacht werden. Für Spektren, die an der tropischen Tropopause initialisiert werden ist hierfür primär die jahreszeitliche Schwankung des tropischen Aufwärtsmassenflusses verantwortlich, welcher maximal im nördlichen Winter und minimal im Sommer ist (Rosenlof, 1995). Dieser wichtige Aspekt des

stratosphärischen Transports ist somit bei Verwendung einer monomodalen inversen Gaußverteilung nicht intrinsisch in den invertierten Altersspektren enthalten. Das erschwert eine korrekte Beschreibung der Dynamik auf jahreszeitlicher Skala. Da die Moden höherer Ordnung nicht direkt aus den Mischungsverhältnissen abgeleitet werden können, dazu wäre eine detaillierte Zeitreihe über mehrere Jahre nötig, wird eine Parametrisierung implementiert, die die Maxima und Minima anhand der relativen Schwankung des tropischen Aufwärtsmassenflusses auf die Altersspektren aufprägt. Das lässt sich an einem Beispiel veranschaulichen. Der Massenfluss in den Tropen ist im Nordwinter etwa 60 % stärker als im Nordsommer (Rosenlof, 1995). Das bedeutet, dass das zugehörige Spektrum welches im Nordsommer invertiert wird an allen Transitzeiten, die auf einen Winter referenzieren, um 60 % nach oben skaliert werden muss. Diese Skalierung wird für jede mögliche Kombination an Jahreszeiten wiederholt. Die Parametrisierung ist als Cosinus-Funktion gestaltet um einen glatten Übergang zwischen den Jahreszeiten zu gewährleisten. Alle Altersspektren der inverse Methode sind somit auf eine saisonale Zeitskala beschränkt, was auch der Tatsache geschuldet ist, dass auf monatlicher oder sogar täglicher Skala die zunehmende atmosphärische Variabilität eine präzise Inversion erschwert.
Da die Methode durch diese Veränderungen von Grund auf verändert wird, ist ein Proof of Concept in einer kontrollierbaren Modellumgebung sinnvoll und notwendig. Dazu wird eine Simulation mit dem Klimachemiemodell EMAC (ECHAM/MESSy Atmospheric Chemistry; Jöckel et al. (2010)) durchgeführt, welche sowohl inerte Tracerpulse zur Bestimmung von Referenzspektren als auch 40 künstliche radioaktive Substanzen mit konstanter globaler Lebenszeit von 1 bis 118 Monaten beinhaltet. Dadurch kann die inverse Methode angewandt und mit den Modellreferenzspektren verglichen werden. Durch die konstante Lebenszeit der künstlichen radioaktiven Substanzen kann die Methode in einem idealisierten Set-up ohne Variabilität im chemischen Abbau getestet werden. Die Resultate zeigen, dass die invertierten Altersspektren im jahreszeitlichen und jährlichen Mittel sehr gut mit den Referenzspektren aus EMAC übereinstimmen. Die eingeführten Verbesserungen tragen zu einer schnellen, aber gleichzeitig präzisen Inversion bei. Die Parametrisierung der höheren Maxima und Minima anhand des tropischen Aufwärtsmassenflusses funktioniert verlässlich und erzeugt Moden an passenden Transitzeiten. Zudem implizieren die Ergebnisse, dass für eine stabile Inversion zehn unterschiedliche Substanzen ausreichend sind und circa 20 % Unsicherheit in der Lebenszeit der Substanzen toleriert werden können, was insbesondere für eine Anwendung auf limitierte Beobachtungsdaten von großer Relevanz ist. Allerdings sind die invertierten Altersspektren global systematisch zu breit, was sich ebenfalls anhand von überschätztem mittlerem Alter zeigt und höchstwahrscheinlich mit der Wahl der inversen Gaußverteilung zusammenhängt. In der unteren Stratosphäre, unterhalb von 1.5 Jahren mittlerem Alter, verschlechtert sich die Übereinstimmung mit den Referenzspektren aus EMAC deutlich und auch die saisonale Veränderung des mittleren Alters wird speziell auf der Nordhalbkugel im Frühjahr und Herbst falsch abgeleitet. Die wahrscheinliche Ursache liegt darin, dass die Altersspektren der inversen Methode den Transport auf die tropische Tropopause referenzieren und keinen Eintrag durch die Tropopause der Extratropen zulassen. Allerdings haben unter anderem Bönisch et al. (2009) auf der Nordhalbkugel gezeigt, dass gerade dieser Transportweg für die unterste Stratosphäre von großer Bedeutung ist und somit nicht vernachlässigt werden darf. Diese Aspekte sind in Hauck et al. (2019) publiziert.
Um die Methode auf Transport durch die extratropische Tropopause der nördlichen und südlichen Hemisphäre zu erweitern, wird die Tropopause in ein tropisches (30° S – 30° N), ein nördliches (30° N – 90° N) und ein südliches Segment (30° S – 90° S) aufgeteilt. Jede dieser Regionen wird mit einem eigenen Altersspektrum versehen, sodass die Superposition der einzelnen Subspektren an einem bestimmten Ort in der Stratosphäre den gesamten Transport durch die globale Tropopause zu diesem Punkt beschreibt. Das Spektrum für die tropische Tropopause entspricht weitestgehend dem oben beschriebenen in Hauck et al. (2019). Die Spektren für die beiden extratropischen Tropopausensegmente werden ebenfalls durch inverse Gaußverteilung parametrisiert, wobei mathematisch gezeigt werden kann, dass die einzelnen Subspektren unabhängig von einander invertiert werden können. Das erleichtert die spätere Anwendung auf Beobachtungsdaten deutlich. Mit dieser Erweiterung der

Methode wird erneut ein Proof of Concept durchgeführt, wobei diesmal das Chemietransportmodell CLaMS (Chemical Lagrangian Model of the Stratosphere; McKenna (2002a,b)) genutzt wird. Die Simulationen enthalten neben den gepulsten Tracern für die Referenzspektren auch zehn künstliche radioaktive Substanzen mit konstanten Lebenszeiten zwischen 1 und 107 Monaten zur Anwendung der Methode. Für eine präzise Beschreibung der Transportprozesse muss für das nördliche und südliche invertierte Altersspektrum ebenfalls eine Parametrisierung der höheren Maxima und Minima abgeleitet werden. Das gestaltet sich als schwierig, da der Transport in den Extratropen beider Hemisphären netto abwärts gerichtet ist (z.B. Olsen et al., 2004). Nur im Bereich des subtropischen Jetstreams ist auf beiden Hemisphären ein netto aufwärts gerichteter Transport durch die Tropopause erkennbar, welcher ein Maximum im Sommer und ein Minimum im Winter hat (Yang et al., 2016). Dies steht auch in Einklang mit den Ergebnissen von Bönisch et al. (2009), welche ebenfalls einen starken Eintrag troposphärischer Luft durch die nördliche extratropische Tropopause im Nordsommer und Nordherbst feststellen und dies auf den schwachen Subtropenjet in dieser Jahreszeit zurückführen. Da kein geeigneter Massenfluss aus früheren Studien herangezogen werden kann aus welchem ein Skalierungsfaktor für die einzelnen Jahreszeiten hergeleitet werden kann, werden diese Faktoren für die nördliche und südliche Tropopause aus integrierten CLaMS Referenzspektren bestimmt. Das verhindert zwar, dass die aufgeprägten Maxima und Minima direkt mit den Referenzspektren verglichen werden können, da allerdings integrierte globale Modelldaten verwendet werden um die Skalierung der Spektren durchzuführen wird keine direkte Information über die Altersspektren an die inverse Methode weitergegeben. Zusätzlich passt die abgeleitete Saisonalität sehr gut zu den Ergebnissen von Bönisch et al. (2009) und Yang et al. (2016), sodass dieser Weg den bestmöglichen Kompromiss darstellt.

Der Proof of Concept mit CLaMS zeigt, dass die Erweiterung der inverse Methode notwendig und sinnvoll ist, da die abgeleiteten Spektren gut mit den CLaMS Referenzspektren übereinstimmen. Auch die Skalierungsfaktoren scheinen korrekte höhere Maxima und Minima zu induzieren, obwohl ein Teil dieser Übereinstimmung erwartet ist, da die Parametrisierung aus CLaMS abgeleitet wurde. In der unteren Stratosphäre stimmen die Spektren und auch die Saisonalität des mittleren Alters nun mit CLaMS überein, sodass davon auszugehen ist, dass die inverse Methode nun den Transport vollumfänglich und präzise beschreiben kann. Allerdings lässt sich auch hier erneut feststellen, dass die Spektren systematisch zu breit sind und dadurch das mittlere Alter zu groß ausfällt. Dies hängt wahrscheinlich wieder mit der Wahl der Parametrisierung als inverse Gaußverteilung zusammen. Ein interessanter Fakt ist, dass interhemisphärischer Transport in der Stratosphäre in CLaMS kaum eine Rolle spielt, da sowohl Nordspektren auf der Südhalbkugel und Südspektren auf der Nordhalbkugel verschwindend gering sind. In der mittleren und oberen Stratosphäre dominiert der tropische Anteil, was unter anderem den Resultaten von Fueglistaler et al. (2009) folgt. Diese Aspekte sind in Hauck et al. (2020) publiziert.

Der finale Teil der Dissertation beschäftigt sich mit der Anwendung der erweiterten und intensiv getesten inversen Methode auf reale Beobachtungsdaten. Dazu werden Daten zu elf chemisch aktiven Spurengasen herangezogen (SF_6, N_2O, CFC-12, Halon 1211, Halon 1301, CH_3Br, $CHBr_3$, CH_2Br_2, $CHCl_2Br$, $CHClBr_2$ und CH_2ClBr), welche mit dem Forschungsflugzeug HALO während den beiden Messkampagnen PGS (POLSTRACC / GW-LCYCLE / SALSA; Oelhaf et al. (2019)) und WISE (Wave-driven Isentropic Exchange) gemessen wurden. Die Datenbasis für die halogenierten Kohlenwasserstoffe ist in Keber et al. (2020), die für N_2O in Krause et al. (2018) und Kunkel et al. (2019) einzusehen. Die PGS-Kampagne fand in zwei Phasen zwischen Winter 2015/2016 und Frühling 2016 mit Basis in Kiruna (Schweden) statt und war auf die Erforschung der polaren Stratosphäre sowie des Polarwirbels fokussiert. Die WISE-Kampagne fand im Herbst 2017 mit Basis in Shannon (Irland) statt. Ziel war die Erforschung von Austauschprozessen zwischen Troposphäre und Stratosphäre in den mittleren Breiten. Die Anwendung der Methode beschränkt sich hierbei auf die Ableitung der tropischen und nördlichen Altersspektren, da die Kampagnen auf der Nordhalbkugel stattfanden und der Einfluss interhemisphärischen Transports in CLaMS vernachlässigbar gering ist. Für die Anwendung der Methode auf diese Beobachtungsdaten sind zusätzlich Zeitreihen für jede

Substanz an der jeweiligen Referenzfläche erforderlich, welche von circa 1960 bis 2017 reichen müssen um eine ausreichende Länge der Altersspektren zu gewährleisten. Da keine konsistenten Messreihen für diesen Zeitraum existieren, schon gar nicht an der Tropopause, werden die Daten für SF_6, N_2O, CFC-12, Halon 1211, Halon 1301 und CH_3Br anhand von tropischen Bodenmessdaten des global Messnetzwerks ALE (Atmospheric Lifetime Experiment), GAGE (Global Atmospheric Gases Experiment) und AGAGE (Advanced Global Atmospheric Gases Experiment; Prinn et al. (2018, 2019)) approximiert und mit Daten der Representative Concentration Pathways (RCP; Meinshausen et al. (2011)) bis 1960 erweitert. Für die restlichen Substanzen wird ein konstantes Mischungsverhältnis an der Tropopause angenommen, welches direkt aus den PGS und WISE-Daten für die Nordtropopause beziehungsweise aus Engel and Rigby (2019) für die tropische Tropopause stammt. Das größte Hindernis für die Ableitung der Altersspektren stellt aber die relevante Lebenszeit der involvierten Spurengase dar, welche nicht bekannt ist. Um dieses Problem zu lösen und gleichzeitig die Unsicherheit der Inversion mit diesen Daten abzuschätzen, wird eine Monte Carlo Kreuzvalidierung eingeführt, welche auf der Studie von Holzer and Waugh (2015) aufbaut. Hierbei wird mit einem Subset von drei Spurengasen, welches immer aus SF_6 und zwei pseudozufällig ausgewählten Spezies besteht, zunächst ein erstes Altersspektrum mit Hilfe bekannter globaler und lokaler Lebenszeiten abgeschätzt. Dabei werden zusätzlich nach pseudozufälligem Prinzip Fehler in die Lebenszeit und Mischungsverhältnisse eingebaut um die Unsicherheit abzuschätzen. Mit Hilfe des ersten Altersspektrums wird dann für die übrigen Spezies die nicht in diesem Subset waren eine Lebenszeit invertiert. Diese Simulation wird 2000 mal wiederholt um eine solide Statistik zu gewährleisten. Schließlich wird für jede Substanz, mit Ausnahme von SF_6 welches in jedem Subset präsent ist, der Median der berechneten Lebenszeit gebildet und damit final das Altersspektrum invertiert. Dabei wird die Lebenszeit des 0.25- und 0.75-Quartils als untere beziehungsweise obere Fehlergrenze genutzt.
Die erhaltenen Altersspektren und Verteilungen für das mittlere Alter aus PGS und WISE erscheinen quantitativ und qualitativ sinnvoll. Das mittlere Alter aus PGS deckt sich mit den aus SF_6 abgeleiteten Werten von Krause et al. (2018). Sowohl die Altersspektren als auch das mittlere Alter implizieren, dass es kurz vor der WISE-Kampagne, aber auch abgeschwächt vor der ersten Phase von PGS, zu einem Eintrag von troposphärischer Luft durch die tropische und nördliche extratropische Tropopause gekommen sein muss. Dies ist in Übereinstimmung mit den Resultaten von Bönisch et al. (2009) und deutet ebenfalls an, dass der Eintrag durch den schwachen Subtropenjet im Sommer der Nordhalbkugel einen wichtigen Einflussfaktor für die Luft in der nördlichen extratropischen untersten Stratosphäre darstellt. Da diese Resultate sich sehr gut in den Stand der Forschung durch andere Studien eingliedern, erscheint die Ableitung von Altersspektren aus Messdaten chemisch aktiver Substanzen erfolgreich und physikalisch sinnvoll zu sein. Hierbei konnte der direkte Einfluss von Modelldaten auf die Anwendung der Methode minimiert werden, was eine unabhängige und robuste Analyse fördert. Diese Aspekte sind ebenfalls in Hauck et al. (2020) und die Datenbasis in Keber et al. (2020) publiziert.
Auch wenn die Entwicklung der inversen Methode und die schließliche Anwendung auf Beobachtungsdaten vielversprechende und sehr positive Resultate hervorgebracht haben, so müssen einige Aspekte kritisch beleuchtet werden. Alle Spektren werden zur Vereinfachung der Inversion idealisiert als inverse Gaußverteilung parametrisiert. Auch wenn die Ergebnisse der Proofs of Concept gezeigt haben, dass damit eine gute Übereinstimmung erzielt wird, so muss doch angeführt werden, dass diese Annahme nicht global zutreffend sein muss und daher zu Abweichungen führen kann. Zudem muss bei der Analyse der höheren Maxima und Minima der invertierten Altersspektren berücksichtigt werden, dass diese mit einem konstanten Skalierungsfaktor aufgeprägt werden. Zwar ist dieser direkt aus der Saisonalität des stratosphärischen Transports abgeleitet, beinhaltet aber keine Phasen ungewöhnlich starken oder schwachen Transports. Für die Skalierungsfaktoren der extratropischen Tropopause kommt noch erschwerend hinzu, dass diese nur für die in dieser Arbeit eingeführten Tropopausenregionen gültig sind und sich deutlich verändern könnten wenn die entsprechenden Regionen verändert werden. Schließlich bleibt die Unsicherheit der chemischen Lebenszeit als größte Quelle von Unsicherheiten für die Anwendung. Es wurde zwar mit der Monte Carlo Kreuzvalidierung eine Abschätzung

der Unsicherheit vorgenommen, da die tatsächlichen Lebenszeiten aber deutlich abweichen könnten, sollten die präsentierten Fehler eher als Minimum gesehen werden. Nichtsdestotrotz stellt die inverse Methode in ihrer in dieser Arbeit postulierten Form ein sehr vielversprechendes Werkzeug dar um den stratosphärischen Transport anhand von gemessenen chemisch aktiven Spurengasen zu analysieren und quantifizieren. Zusammen mit schon etablierten Methoden und Techniken kann die Methode in zukünftigen Studien dazu beitragen das Verständnis der Stratosphäre und ihrer Dynamik zu vertiefen und mögliche Veränderungen im Rahmen des Klimawandels zu erforschen.

1 Introduction and motivation

The observation of gaseous and particulate constituents is a cornerstone of atmospheric sciences to comprehend the ongoing physical and chemical processes within the Earth's atmosphere. A precise knowledge of the past and current states of the atmosphere confers the possibility to predict probable changes in the future using sophisticated techniques and computer models. Recent public discussions about means to contain the anthropogenic climate change focus heavily on the troposphere, the lowest layer of the atmosphere, as possible repercussions are directly perceptible. However, changes to the Earth's climate also strongly affect the remaining layers including the stratosphere, which is located right above the troposphere separated by the tropopause. Since the relationship of troposphere and stratosphere is characterized by strong mutual interaction and exchange mechanisms, changes throughout all layers of the atmosphere can modulate weather and climate at the surface (e.g., Gerber et al., 2012).

A vast number of studies in the past have addressed probable modifications of the stratosphere's chemical budget and physical mechanisms under the influence of climate change and the expectations are that global stratospheric temperatures decrease (e.g., Intergovernmental Panel on Climate Change, 2013) while the dynamical mechanisms are modified non-uniformly (e.g., Bönisch et al., 2011; Ploeger et al., 2015b; Stiller et al., 2017). Aside from climate change, abundant emissions of ozone depleting substances, especially chlorofluorocarbons (e.g., Engel and Rigby, 2019), in the late 20^{th} century have caused a significant reduction of stratospheric ozone that slowly recovers until this day due to quick political regulation of the species involved. Ozone absorbs incoming short-wave radiation from space and acts as an essential protective layer for life at the Earth's surface. A constant monitoring and investigation is therefore vital to give reliable reports about the current condition and future changes of the stratosphere.

While in situ studies of the troposphere can be realized readily and abundantly with modern technological possibilities, the direct investigation of the stratosphere is more difficult due to its remote location and large vertical extension up to circa 50 km altitude. This highly limits the observational capabilities and present investigations rely primarily on aircraft measurements for the lower parts close to the tropopause and on satellites, remote sensing instruments, balloons, or seldomly rockets to provide a data basis for a variety of trace gases in the stratosphere. For a comprehensive analysis, however, studies of state of the art chemistry climate and chemistry transport models are an obligatory part of stratospheric research. Albeit the undeniable benefit these models provide, past comparisons of models and observations have revealed strong inconsistencies in predicted changes of the stratospheric dynamics that require further research (e.g., Waugh, 2009).

This leads directly to the second challenge for the scientific exploration of the stratosphere. The chemical composition of the stratosphere can be observed with contemporary analytical and technological setups, whereas stratospheric dynamics are known to be immeasurable directly and thus demand indirect proxy quantities. Trace gases are a very suitable and frequently considered resource to do research on stratospheric dynamics and many studies have utilized chemically stable species as a proxy for transport speed in the stratosphere (e.g., Engel et al., 2009, 2017). The derived quantities are of average nature and therefore contain information primarily about the overall transport strength. To gain an insight into the structure of transport, these average measures are insufficient and a fully resolved probability density function of associated transit times is preferable. Although this is highly beneficial, the retrieval of these functions proves complicated as stratospheric transport is not directly observable and detailed information about past states of the transport would be required. Chemically reactive substances are a potent tool to gain insight into the structure of the stratospheric circulation since their state of depletion is coupled directly to the transport mechanisms. Using different species of trace gases with distinct depletion time scales the probability density function could be approximated. The problem is that albeit being abundantly measured during past research campaigns in the stratosphere, the methods to convey trace gas mixing ratios into probability density functions are sparse and often rely on model data that prevent an independent comparison.

The scientific goal of this cumulative dissertation is to develop an applicable and robust method to derive transit time distributions from observed mixing ratios of various chemically active trace gas species with distinct depletion time scales. The method shall be designed to include as many information about stratospheric transport and its seasonality as possible while the amount of necessary model data shall be minimized to ensure the independence for subsequent comparisons and assessments. The development process and a first application to in situ trace gas measurements, which I have been working on for the last three years in the working group of Andreas Engel at Goethe University Frankfurt am Main, are the subject of this thesis and explained in synoptic fashion in the chapters below. As stated, the thesis is cumulative and features the three publications in which the complete development process, limitations, modifications, data and results are extensively explained and discussed. The thesis starts with a concise introduction into the most relevant theory for the research within the project (section 2). In section 3, the three publications are interrelated and summarized to outline the guiding thread through the key results of my project.
The first publication is Hauck et al. (2019), where the basic concepts of the method are elucidated together with novel improvements and the numerical realization. The new method is then tested in a controllable idealized model setup to assess its general performance and applicability as well as upcoming problems. All these aspects are summarized in section 3.2. These discovered problems are then picked up by the second publication (Hauck et al., 2020), where necessary modifications are presented to improve the performance of the method in general. As these are major changes, a second proof of concept with a different model is conducted in a similar frame as for the first publication. These aspects are elaborated in section 3.3. The final topic of Hauck et al. (2020) is the application of the extensively tested method to real in situ measurements of trace gases gained during two aircraft research campaigns and the evaluation of results in the light of previous studies. The essential data basis for this final application is provided by Keber et al. (2020), the third publication of this thesis. The data of Keber et al. (2020), necessary techniques, and results from the application are summarized in section 3.4, followed by a general summary and an outlook in section 4. Each of the three publications can be found in the attachment of this thesis.

2 Theoretical principles

The following sections give a sound overview over the basic concepts that are the foundation to this thesis and begins with stratospheric dynamics (section 2.1.1), means of quantification of stratospheric transport (section 2.1.2), and the coupling of stratosphere and troposphere (section 2.1.3). As stratospheric transport processes and ongoing chemical mechanisms are closely linked, there is also a brief introduction into the mathematical description of the linkage (section 2.2.1) as well as relevant trace gas constituents for this work (section 2.2.2).

2.1 Stratospheric transport

2.1.1 Brewer-Dobson circulation

Dynamics in the stratosphere are characterized by a global-scale mean meridional circulation system, which conveys air primarily from the tropics to the poles. The discovery of this general circulation dates back to early measurements of unexpected amounts of water vapor and helium (Brewer, 1949) as well as ozone and water vapor (Dobson, 1929, 1956) in the lowermost stratosphere over England that could only be explained by a poleward drift of stratospheric air from the tropics into the extratropics. Today, the circulation is thus referred to as Brewer-Dobson circulation (BDC). The BDC constitutes a key feature of atmospheric transport and controls the mixing ratios of various gaseous species in the stratosphere both on temporal and spatial scale. Note that the term mixing ratio always refers to a volume mixing ratio in this thesis. As many trace gas constituents are potent greenhouse or ozone depleting gases, the radiative budget of the complete atmosphere as well as Earth's climate in general are significantly affected by the BDC (e.g., Shepherd, 2007; Solomon et al., 2010; Riese et al., 2012).

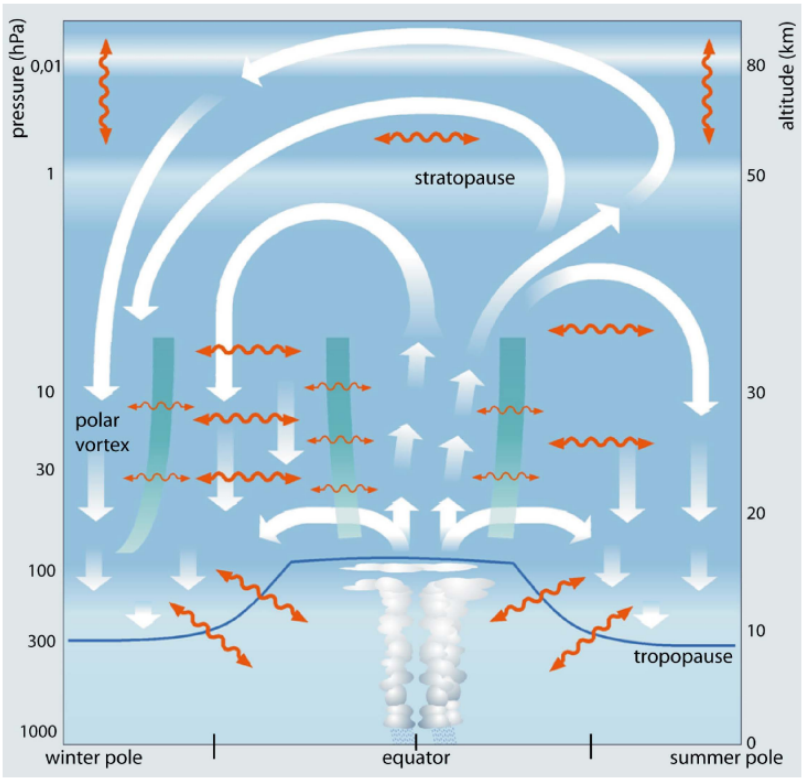

Figure 2.1: Schematic of the Brewer-Dobson circulation
This figure from Bönisch et al. (2011) illustrates the pattern of the Brewer-Dobson circulation in the stratosphere. White arrows denote residual transport, while orange wavy arrows represent bidirectional mixing. The green vertical bars are transport barriers in the subtropics of each hemisphere and at the edge of the polar vortex in the winter hemisphere that strongly inhibit a direct quasi-horizontal exchange between the tropics and extratropics.

Although the conclusion that a slow meridional circulation is present in the stratosphere proves to be correct, the real structure of transport comes out to be much more complex than proposed (see figure 5 in Brewer (1949)). The BDC, as shown in figure 2.1, superimposes a residual mean circulation (RC; white arrows) with net mass flux and quasi-horizontal bidirectional mixing processes (orange wavy arrows) where no net mass flux occurs (e.g., Plumb, 2002; Butchart, 2014). Fresh tropospheric air enters the stratosphere primarily across the tropical tropopause layer (TTL; e.g., Fueglistaler et al., 2009), albeit quasi-horizontal mixing occurs also across the extratropical tropopause and is especially relevant for the air composition in the lowermost stratosphere, i.e., the area below 100 hPa in figure 2.1 (e.g., Bönisch et al., 2009). Each of these exchange processes exhibits a distinct seasonal cycle and contributes significantly to the seasonally varying strength and structure of the BDC (see section 2.1.3 for details). In the tropics, the entrained air then slowly propagates upward and poleward, where it finally descends back down in mid- and high latitudes. The transport pathways and mechanisms are explained in detail in the following sections.

Residual mean mass circulation

When considering the residual mean circulation in figure 2.1 its structure seems to share similarities with large-scale circulation cells in the troposphere, such as the Hadley and Ferrel cell. However, as implied by its name, the RC does not show a direct meridional direction since strong zonal winds prevail in the stratosphere, but ensues on temporal and zonal mean due to a disturbance of the zonal background flow (see Shepherd (2007) for a concise overview). The main mechanical drivers of the circulation are tropospheric Rossby waves on both the planetary and synoptic scale, that propagate upward into the stratosphere to release their momentum when breaking in the midlatitudes of the middle and upper stratosphere (McIntyre and Palmer, 1983). The enhancement of wave breaking in this "surf zone" (McIntyre and Palmer, 1984) transfers the waves' momentum to the zonal background flow and induces a westward force. Charney and Drazin (1961) show that Rossby waves can primarily propagate in an eastward flow so that the released momentum eventually decelerates the zonal circulation, resulting in a diminished Coriolis force and thus in a poleward force. Due to mass conservation, air from the tropical lower stratosphere is pumped upward to balance the wave-induced drift to the poles and forms the depicted circulation pattern (Holton et al., 1995). The pronounced transport barriers in the subtropics below 40 km altitude (green vertical bars in figure 2.1) inhibit a direct horizontal motion and force tropical stratospheric air to rise within the enclosed area. Since mainly synoptic-scale waves break around the subtropical jet streams, some quasi-isentropic mixing still occurs across the barriers up to 25 km altitude (Butchart, 2014). The region between the subtropical transport barriers is therefore referred to as the tropical leaky pipe (Neu and Plumb, 1999). The mechanism that the stratospheric surf zone controls dynamical processes below is called the "downward control principle" (Haynes et al., 1991).
Transport within the RC can be separated into two major pathways, a shallow and a deep branch, which extend into different parts of the stratosphere and are characterized by distinct transport timescales (e.g., Plumb, 2002; Birner and Bönisch, 2011). The shallow branch is located in both hemispheres close to the tropopause and reaches from the tropics across the lower parts of the subtropical transport barriers down into the extratropical lowermost stratosphere. It is mainly driven by synoptic- and planetary-scale Rossby waves and shows a typical transport timescale of up to one year (Birner and Bönisch, 2011). For the upper and middle stratosphere, the deep branch of the RC is the predominant pathway and extends from the tropical leaky pipe up to to stratopause and back down into the mid- and high latitudes in both hemispheres. The associated transport timescales within these pathways can reach multiple years (Birner and Bönisch, 2011). In the summer hemisphere a further split of the deep branch is visible in figure 2.1 that leads up into the mesosphere and back down in the winter hemisphere. This branch is driven by inertia gravity waves and leads to even more prolonged transport times (Plumb, 2002).

Bidirectional mixing

Alongside the residual mean circulation, bidirectional mixing processes play an important role within the BDC for the exchange of air masses and their chemical composition in general. Mixing in the stratosphere is also mainly caused by breaking Rossby waves so that the surf zone can be characterized as major region for the mixing (e.g., Plumb, 2007; Butchart, 2014). An important aspect, which separates these processes clearly from the RC, is the absence of any net mass flux associated with mixing, although an exchange of gaseous components is present. It has already been mentioned above that stratospheric mixing occurs quasi-horizontally, but this is only an approximation. Physically precise, these processes emerge on surfaces of equal potential temperature θ, which is an important meteorological quantity that describes the temperature an air parcel would have if it was brought dry adiabatically to a predefined reference pressure level (usually 1000 hPa). This leads to

$$\theta = T \cdot \left(\frac{p_0}{p}\right)^{\frac{R}{c_p}}, \tag{1}$$

where T is the air temperature, p_0 the reference pressure level, p the air pressure, R the gas constant and c_p the specific heat capacity. Potential temperature and the thermodynamic measure of entropy for a dry air parcel differ only by a constant factor so that surfaces of constant potential temperature are identical with isentropic surfaces. This makes stratospheric mixing a bidirectional and irreversible isentropic process. A powerful and essential concept to comprehend and describe isentropic transport in the stratosphere has been developed by Rossby (1936) and Ertel (1942) and established as a tool in the analysis of stratospheric dynamics by Hoskins et al. (1985). The isentropic potential vorticity (IPV) of an air parcel provides a combined measure for angular momentum (vorticity) and stratification. IPV is usually given in potential vorticity units (PVU) which is equivalent to $1 \cdot 10^{-6} \frac{\mathrm{K \cdot m^2}}{\mathrm{kg \cdot s}}$. Under frictionless and adiabatic (i.e., isentropic) motions, such as in the stratosphere, the IPV is considered to be conserved within a time frame of several days. Therefore, constant IPV values can be utilized to track isentropic mixing on a preselected potential temperature layer, whereas sharp latitudinal gradients of IPV indicate strong transport barriers (e.g., Butchart, 2014). The momentum released by breaking waves causes mixing that leads to a reduction of latitudinal IPV as well as mixing ratio gradients for many trace gases along an isentropic surface. Especially in the surf zone, large areas of rather constant IPV can be detected and are accompanied by sharp gradients at the subtropical or polar transport barriers. This extends even to smaller-scale phenomena where IPV can be used to solidly identify transport barriers (e.g., Ploeger et al., 2015a).

Circulation changes

Climate change is expected to have a significant influence on the stratosphere and thus also on the strength and structure of the BDC. Studies of different climate models in the past indicate that rising greenhouse gas concentrations in the troposphere increase global tropospheric temperatures and eventually lead to an enhancement of wave propagation and thus to a general increase of the BDC speed (e.g., Garcia and Randel, 2008; Li et al., 2008; Shepherd and McLandress, 2011). However, balloon-borne observations of stratospheric transport derived from SF_6 and CO_2 measurements by Engel et al. (2009) in the midlatitude stratosphere between 24 km and 35 km altitude show an insignificant decrease of the transport strength (see figure 2.2). This trend is further corroborated using more recent measurement data (Engel et al., 2017) and a re-assessment with model and reanalysis data by Ray et al. (2014) even shows a significant deceleration. Analysis of stratospheric transport by Bönisch et al. (2011) with model simulations and observations of N_2O and O_3 suggest that transport might undergo non-uniform changes as they detected an enhancement of the northern shallow branch of the RC below 500 K potential temperature after the year 2000. This theory has since been affirmed by different satellite-based studies (e.g., Stiller et al., 2012; Hegglin et al., 2014; Haenel et al., 2015), which point to different structural changes of the BDC in the northern and southern hemisphere.

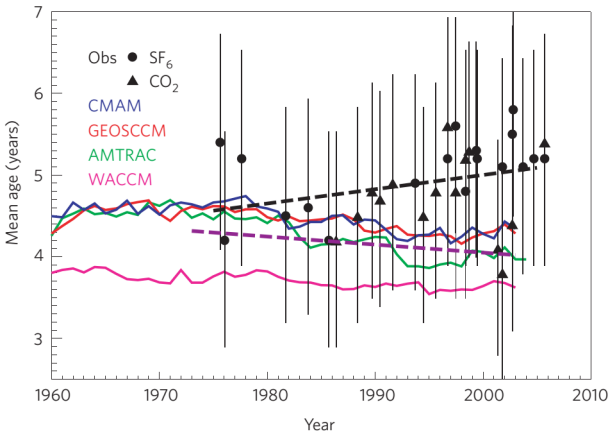

Figure 2.2: Circulation strength in the northern midlatitude lower stratosphere
Shown are values of mean age of air (see section 2.1.2 for details) derived from models (colored lines) and observations (black symbols and lines – Engel et al. (2009)) between 1960 and 2006. Mean age of air is an indicator for the time an air parcel spent in the stratosphere so that an increase is inversely proportional to a deceleration of the circulation and vice versa (Austin and Li, 2006). The figure is taken from Waugh (2009).

More recent modeling (e.g., Oberländer-Hayn et al., 2015) and reanalysis studies (e.g., Abalos et al., 2015) have disentangled some inconsistencies between models and observations, but the investigation of possible changes of the BDC remains a considerable task. Especially since Chabrillat et al. (2018) and Ploeger et al. (2019) could show that the applied reanalysis product can significantly modify the resulting dynamical variations. The problem of all studies of the BDC is that transport in a residual mean circulation cannot be measured directly (e.g., Butchart, 2014) and thus requires the use of proxy measures derived from available data. In the following, the most relevant quantities for this study are introduced and explained.

2.1.2 Quantification of transport

Mean age of air

A frequently applied tool for the analysis and quantification of stratospheric dynamics is the mean age of air (AoA; Hall and Plumb, 1994). It can be understood as the mean transit time an air parcel has traveled through the stratosphere starting at a specified reference surface. In most cases, this reference is set to be either the Earth's surface or the tropopause. The important characteristic of mean AoA is its inversely proportional link to the general circulation strength of the BDC (Austin and Li, 2006). That is, for example, if the transport speed accelerates over time, mean AoA will show a decrease and vice versa. Moreover, bidirectional mixing processes can also influence mean AoA when air parcels are recirculated from the extratropical back into the tropical stratosphere. This results in larger mean AoA and is hence referred to as aging by mixing (Garny et al., 2014).

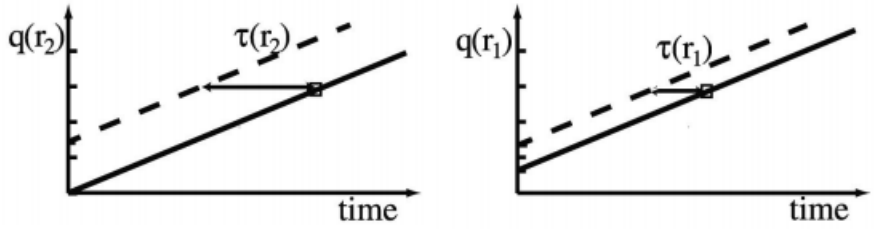

Figure 2.3: Time lag concept for mean age of air
Shown is mean AoA τ as time lag of a linearly increasing inert trace gas q between its time series at the reference surface (black dashed line) and at two points in the stratosphere (r_1 and r_2– black solid line). The figure is taken from Waugh and Hall (2002) and slightly modified.

Although providing a powerful means of quantification, there are two downsides to the use of mean AoA. Due to the average character of mean AoA it is quite complicated to separate the effects of the residual circulation and mixing so that it is mostly used as a general indicator for both processes combined. Besides, the derivation of mean AoA is not straightforward, especially in case of sparse observational data, and often relies on approximations or a combination with model data. In case of these atmospheric models, the simplest way of determination is the implementation of a fully inert trace gas with linear temporal trend at the reference surface (e.g., Ploeger and Birner, 2016). For this "clock tracer", mean AoA is given as the time lag between the mixing ratio at the reference point and the considered stratospheric location (Waugh and Hall, 2002). A schematic of this concept is shown in figure 2.3. In reality, perfectly linearly increasing trace gases with no chemical depletion are non-existent so that proper assumptions about the underlying probability density function (see down below) and replacements are needed. Commonly utilized trace gases for an observationally based derivation of mean AoA include SF_6 and (deseasonalized) CO_2 (e.g., Volk et al., 1997; Engel et al., 2002; Bönisch et al., 2009; Engel et al., 2009, 2017), where the respective temporal mixing ratio trend is approximated by a mathematical second degree polynomial fit. Both trace gases are considered to be very long-lived and therefore treated as quasi-inert. This technique proves to work properly with a robust and reliable performance. Recently, Fritsch et al. (2020) could show that the gained results strongly depend on the selected fits and assumptions.
Despite its undeniable benefit for studies of stratospheric dynamics, mean AoA holds another significant disadvantage. While changes in the strength of the circulation can be investigated properly by tracking variations of mean AoA, a structural analysis or separation between RC and mixing is not feasible. That is why the use of a full distribution of transit times, a so-called age spectrum, is favorable and can be directly linked to mean AoA.

Transit time distributions

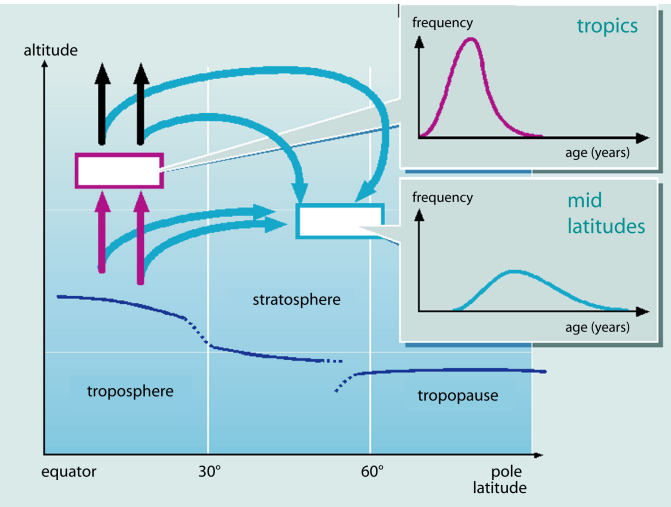

Figure 2.4: Concept of age spectra in the stratosphere
Illustrated are two exemplary age spectra at a location close to the tropical tropopause (purple) and at a larger distance in the midlatitudes (blue). Note that due to its proximity to the entry region, the peak of tropical age spectrum is centered around smaller age values than the spectrum in the midlatitudes. Also the width of the midlatitude peak appears much broader as the variety of possible transport pathways is larger at some distance from the entry region (blue arrows). The figure has been adapted from Schmidt et al. (2002).

The concept of considering full transit time distributions (age spectra) for analyses of transport dates back to Kida (1983). An age spectrum is characterized at any point in the stratosphere as probability density function (PDF) of transit times through the stratosphere from a reference surface to the given air parcel. The basic idea is illustrated in figure 2.4 for two arbitrary age spectra in the tropical (purple) and extratropical stratosphere (blue). In more modern work, especially with global

models, the age spectrum has become a powerful tool to forward the understanding of the strength and also structure of the stratospheric circulation, since RC and mixing can influence different sections of the spectrum (e.g., aging by mixing affects predominantly the tail of the distribution). The age spectrum can also be applied to calculate the mixing ratio of any inert trace gas at point $\vec{x}$ and time t without source reactions in the stratosphere by the following mathematical equation

$$\chi(\vec{x}, t) = \int_0^\infty \chi_0(t - t') \cdot G(\vec{x}, t, t') \cdot dt'. \tag{2}$$

Here, t' denotes the transit time, $\chi(\vec{x}, t)$ the mixing ratio, $\chi_0(t - t')$ the mixing ratio time series at the reference surface, and $G(\vec{x}, t, t')$ the age spectrum. An increase of transit time is always equivalent to going backward in real time. For being a correctly defined PDF and representing an air parcel to full extent, the age spectrum must fulfill the normalization condition

$$\int_0^\infty G(\vec{x}, t, t') \cdot dt' = 1. \tag{3}$$

This ensures that the moments of the PDF can be properly derived, including first $\Gamma(\vec{x}, t)$ and second central moment $\Delta^2(\vec{x}, t)$ (see Hall and Plumb (1994))

$$\Gamma(\vec{x}, t) = \int_0^\infty G(\vec{x}, t, t') \cdot t' \cdot dt', \tag{4}$$

$$\Delta^2(\vec{x}, t) = \frac{1}{2} \cdot \int_0^\infty G(\vec{x}, t, t') \cdot (t' - \Gamma(\vec{x}, t))^2 \cdot dt'. \tag{5}$$

The first moment represents the mean of the PDF and is therefore identical with mean AoA, while the second central moment is the variance and provides an estimate of the spread around the age spectrum's mean. In model studies, the age spectrum can be derived from a set of fully inert trace gases, which are pulsed periodically in a particularly defined boundary layer. If these tracer mixing ratios are then properly arranged, the outcome will be an age spectrum whose transit time resolution is defined by the number of different trace gas pulses (e.g., Reithmeier et al., 2008; Li et al., 2012a,b; Ploeger and Birner, 2016). Finding an analytical solution to equation (2) is not trivial, but in their fundamental theory on age spectra Hall and Plumb (1994) propose an inverse Gaussian PDF in a setup restricted to an one-dimensional flux gradient relation (Plumb and Ko, 1992) for quasi-inert trace gases. The age spectrum is then given as Green's function

$$G(z, t') = \frac{z}{2\sqrt{\pi K t'^3}} \cdot \exp\left(\frac{z}{2H} - \frac{Kt'}{4H^2} - \frac{z^2}{4Kt'}\right), \tag{6}$$

with K being a one-dimensional diffusion coefficient, z the altitude, and H the scale height of the air density ρ as in $\rho(z) = \rho_0 \cdot e^{-\frac{z}{H}}$. While this solution might appear to be only a rough approximation, studies of age spectra in different atmospheric models have shown that resulting distributions are quite similar to an inverse Gaussian PDF, especially on the annual mean scale (black line in figure 2.5 compared to the inverse Gaussian PDF in grey). On the seasonal scale (colored lines in figure 2.5), however, the inverse Gaussian function still is in agreement with the overall shape of the modeled seasonal spectra, but clearly lacks the multimodality. Nevertheless, the inverse Gaussian solution has been and still is to this day a well-established basis for studies on observational retrievals of age spectra (e.g., Andrews et al., 1999; Schoeberl et al., 2005; Ehhalt et al., 2007; Hauck et al., 2019).

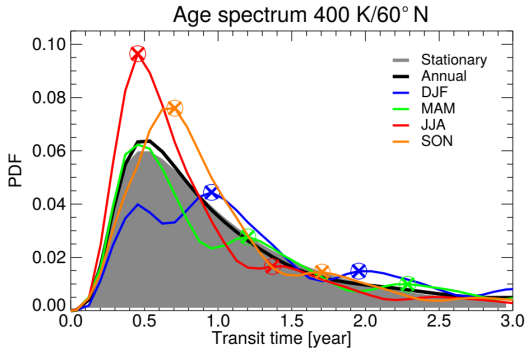

Figure 2.5: Modeled annual and seasonal age spectra
Depicted in this figure from Ploeger and Birner (2016) are annual and seasonal mean age spectra within a simulation of the chemistry transport model CLaMS at 60° N on 400 K potential temperature. For comparison, the inverse Gaussian PDF of equation (6) is shown as grey surface.

Despite the benefit the age spectrum provides for an analysis of the BDC, there are problems regarding its applicability. Analogous to mean AoA, age spectra cannot be observed directly and require even more detailed information about the past states of transport from measurable quantities. Since atmospheric chemistry and transport are intertwined, various chemically active trace gases with distinct depletion rates are a suitable tool to infer age spectra. Their state of depletion provides insight into transit time scales within the air parcel up to the respective atmospheric lifetime of the substance (see section 2.2.1). In the past, various methods have been proposed that rely on different techniques, data sources, models, assumptions, and constraints to succeed in this task (see section 3.1). However, as the amount of measurement data is highly limited in the stratosphere and a reduction of assumptions and model influence is always favorable, the deduction of age spectra from observations remains an open and highly relevant issue. This provides a perfect scientific basis for this thesis.

2.1.3 Stratosphere-troposphere coupling

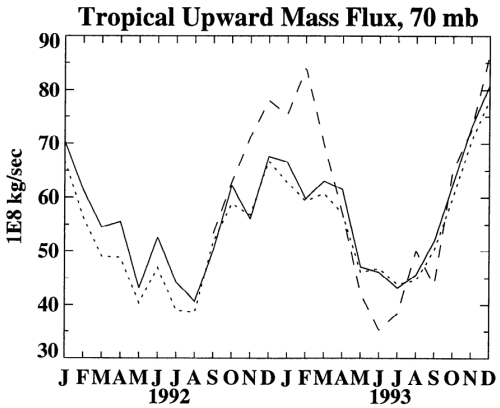

Figure 2.6: Tropical upward mass flux at 70 hPa
Shown in this figure from Rosenlof (1995) is the net upward mass flux in the tropical stratosphere derived from three different data sources (see Rosenlof, 1995) at 70 hPa for the years 1992 and 1993.

The seasonal regime of the BDC is not constant and features a significant seasonal variability that is directly related to the seasonality of wave breaking (e.g., Rosenlof, 1995). Hence, the seasonality of global exchange processes between the troposphere and stratosphere is strongly influenced by this wave forcing and has been in the focus of past studies (e.g., Appenzeller et al., 1996; Olsen et al., 2004; Škerlak et al., 2014). During winter time the excitation of Rossby waves strongly increases and

leads to an enhancement of wave drag in the surf zone. Especially in northern winter, the orographic structure of the northern hemisphere promotes the generation of large-scale waves. This is supported by the general eastward direction of the stratospheric background flow that attunes in the winter hemisphere.
During summer, the transfer of momentum from breaking waves then reaches its minimum as westward winds in the stratosphere inhibit Rossby wave propagation (Charney and Drazin, 1961). As a consequence of the downward control principle, this seasonal pattern in the midlatitude surf zone is transferred onto the upward and downward mass fluxes of the BDC in general. As shown by Rosenlof (1995), the tropical upward mass flux at 70 hPa (see figure 2.6) follows this seasonality consistently and exhibits accordingly a maximum during northern winter (December-January-February or DJF) and a minimum during northern summer (June-July-August or JJA). This implies that fresh tropospheric air enters the stratosphere across the tropical tropopause layer especially during northern winter. Northern spring (March-April-May or MAM) and fall (September-October-November or SON) constitute transition seasons.

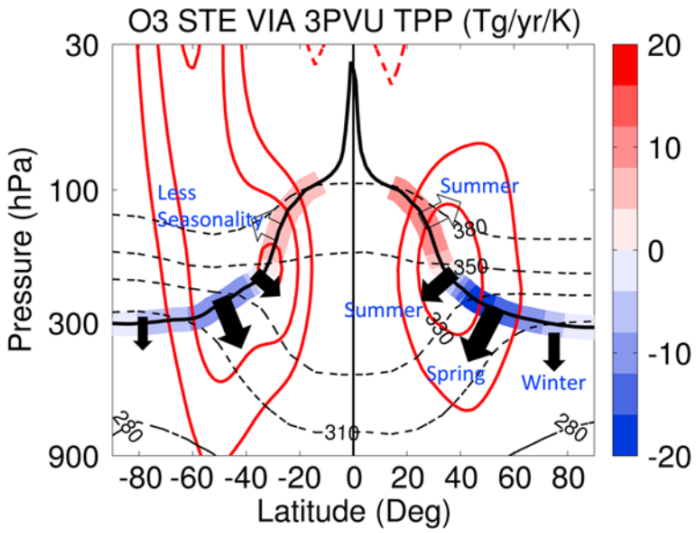

Figure 2.7: Exchange processes across the northern and southern hemispheric tropopause
Shown are different regions of net up- and downward transport across the 3 PVU tropopause (solid black line) together with the associated ozone flux. Filled arrows denote net downward transport, while unfilled arrows indicate a net upward motion. The season with maximum transport is given along the tropopause in the northern hemisphere. In the southern hemisphere, the maximum occurs in the same season, but with generally weaker strength. Isentropic surfaces are given as dashed lines together with the zonal mean zonal wind that indicates the subtropical jet stream (red lines). The figure is taken from Yang et al. (2016).

In the extratropical lowermost stratosphere (i.e., below 380 K), the cycle of the stratosphere-troposphere coupling is characterized by a superposition of different upward and downward motions. Due to the strong wave breaking in the midlatitudinal surf zone, air is forced downward through the lowermost stratosphere back into the troposphere. The net direction of the corresponding hemispherically integrated mass flux across the 380 K isentropic surface as well as the tropopause is downward with a pronounced maximum in spring in both hemsipheres (e.g., Appenzeller et al., 1996; Olsen et al., 2004; Škerlak et al., 2014). The upward component of this net downward mass flux attains its maximum in both hemispheres during (late) fall (e.g., Fig. 8 and 9 in Škerlak et al., 2014). However, Bönisch et al. (2009) identify the weak subtropical jet stream during northern summer as an important mechanism for cross-tropopause transport, since their results indicate that the northern hemispheric lowermost stratosphere is flushed during summer and fall with fresh tropospheric air. This is contrary to the seasonality in the hemispherically integrated upward mass flux across the northern hemispheric tropopause mentioned above. The inconsistencies can be disentangled considering the study by Yang et al. (2016), where different regions of net up- and downward motion

are identified using ozone fluxes at the tropopause (see figure 2.7 in this thesis for an overview). Their results reveal an area of strong year-round net upward directed transport within the region of the subtropical jet stream in both hemispheres with a maximum during summer. Poleward of the subtropics, the cross-tropopause transport changes its direction and shows a net downwelling with a maximum in summer, spring, and winter depending on the exact latitudinal range (see again figure 2.7). Thus, the seasonality of the local cross-tropopause transport around the subtropical jet stream in the northern hemisphere is in agreement with the findings of Bönisch et al. (2009) whereas the hemispherically integrated ozone flux in Yang et al. (2016, Fig. 5) is still consistent with Olsen et al. (2004, Fig. 2). This implies that although the net direction of cross-tropopause transport in the extra-tropics is downward, local regions of strong net upwelling, especially around the subtropical jet stream, are an important process for the air mass composition in the lowermost stratosphere. This analysis can also be found in Hauck et al. (2020).
The seasonally variable coupling of stratosphere and troposphere manifests also in stratospheric age spectra and causes, as shown exemplary in figure 2.5, their multimodal behavior (see also Reithmeier et al., 2008; Li et al., 2012a). Depending on the defined reference surface, these multimodal peaks can also represent a superposition of the mass flux seasonality in the tropics and extra-tropics. Therefore, the complex seasonality of transport must also be well-represented in age spectra derived from observations, but remains challenging especially for methods based on the intrinsically monomodal inverse Gaussian function (equation (6)). This leaves room for new techniques.

2.2 Atmospheric chemistry

As this thesis presents a novel method to derive age spectra from observations of chemically active substances in the stratosphere (see table 2.1), necessary concepts to understand the linkage between stratospheric chemistry and transport are introduced in section 2.2.1 and completed by an explanation of the relevant species for this study in section 2.2.2.

2.2.1 Nexus of stratospheric chemistry and transport

It has already been mentioned that stratospheric transport is strongly intertwined with the chemistry of certain trace gases along the pathways. As various substances exhibit highly diverse sink reactions and regions in the stratosphere, their state of depletion is considered as an indicator for the time the associated air parcel has been transported since entering the stratosphere (e.g., Schoeberl et al., 2000). This implies that substances with stratospheric sink mechanisms can be applied to extract information about relevant transit time scales, given that a precise description of the chemical processes is feasible. That is, age spectra can be retrieved from such species if a sufficient number of distinct species is available since each of these gases provides insight into certain parts of the spectrum. This is determined by the respective chemical lifetime of the trace gas (Schoeberl et al., 2005). A precise strategy to link chemical depletion with age spectra mathematically is the extension of equation (2) from inert substances to chemically active species by introduction of a path-dependent chemical lifetime for any substance at an arbitrary location in the stratosphere. However, the retrieval of these past pathways through the stratosphere is almost impossible so that a suitable and usually applied approximation involves transit-time-dependent chemical lifetimes $\tau(\vec{x}, t, t')$. Since transport pathways and transit times show a robust correlation the assumption appears reasonable (Engel et al., 2018). The inclusion of these lifetimes into equation (2) leads to

$$\chi(\vec{x}, t) = \int_0^\infty \chi_0(t - t') \cdot e^{-\frac{t'}{\tau(\vec{x}, t, t')}} \cdot G(\vec{x}, t, t') \cdot dt'. \tag{7}$$

Although this is a rather intelligible equation, there are problems regarding the determination of the age spectrum from it. The unique solution of $G(\vec{x}, t, t')$ requires a precise knowledge of the remaining involved parameters as well as numerical techniques. This is in no way a trivial problem, especially as the integral yields no information about the general shape of the age spectrum. A

possible conversion into a differential equation of the form $\frac{d\chi}{dt'}(\vec{x}, t)$ is not beneficial since then a single mixing ratio measurement would not suffice and demand an unrealizable transit time series of mixing ratios at one location. Additionally, transit-time-dependent lifetimes $\tau(\vec{x}, t, t')$ are a highly theoretical measure that cannot be quantified directly. These must be considered as concatenation of various local lifetimes along an average Lagrangian pathway through the stratosphere. While global steady-state lifetimes of many atmospheric constituents have been well-researched in recent years, local lifetimes are more complicated as they directly depend on the distribution of loss regions and the prevalent meteorological conditions in the stratosphere. Therefore, they exhibit a strong seasonal and spatial variability. Many studies in the past developed sophisticated constraints, mathematical approaches, approximations and model data to simplify the problem and derive age spectra from observations (e.g., Schoeberl et al., 2005; Holzer and Primeau, 2010; Holzer and Waugh, 2015). It has been stated above that the inverse Gaussian function by Hall and Plumb (1994) is a common approach to overcome the problem that the integral in equation (7) inhibits information about the exact shape of $G(\vec{x}, t, t')$. This eliminates one of the above mentioned problems and turns the focus of further development work onto the remaining parameters. Admittedly, this also heavily constrains the degrees of freedom for the spectrum and does not necessarily guarantee a well-matching spectrum a priori, but under consideration of the sparse number of available chemically active trace gases in the stratosphere and the demonstrable good performance in previous work using trace gases and models (see section 2.1.2) it appears justifiable. For the purpose of this thesis, which is the development and application of a reliable and precise method to derive age spectra from measurements of long- and short-lived trace gases in the stratosphere relying as little as possible on model data, the inverse Gaussian function and related studies provide the perfect scientific starting point for further development and problem solving (see section 3).

2.2.2 Relevant trace gas species

The trace gases that are used within the scope of this thesis are presented in table 2.1 below together with their ozone depletion potential (ODP) and global warming potential (GWP) that estimate how effective these species deplete ozone compared to the reference substance ($CFCl_3$) and how effective they contribute to the greenhouse effect relative to CO_2 on a timescale of 100 years. Values are taken from table A-1 in the appendix of World Meteorological Organization (2019).

Table 2.1: Trace gas species within the frame of this thesis

Chemical formula	Alternative name	ODP	GWP
SF_6	-	-	23500
N_2O	-	-	265
CF_2Cl_2	CFC-12	0.73 – 0.81	10300
CF_2ClBr	Halon 1211	6.9 – 7.7	1750
CF_3Br	Halon 1301	15.2 – 19.0	6670
CH_3Br	-	0.57	2
$CHBr_3$	-	1.0 – 5.0	<1
CH_2Br_2	-	3.0 – 4.0	1.4
$CHCl_2Br$	-	-	-
$CHClBr_2$	-	-	-
CH_2ClBr		-	4.7

Halogenated species

An important group of substances present in the atmosphere are halogenated trace gases. These species, which usually show mixing ratios of the order of parts per million (ppm; $1 \cdot 10^{-6}$) down to parts per trillion (ppt; $1 \cdot 10^{-12}$) and smaller, include a variety of different molecules and are

highly relevant for Earth's climate budget despite their low abundancies (see below). The majority of halogenated trace gases are of anthropogenic origin with only a few being also emitted by natural sources. A classification may be done as follows (e.g., Seinfeld and Pandis, 2006):

- Chlorofluorocarbons (CFCs): fully halogenated hydrocarbons where all hydrogen atoms are replaced by chlorine or fluorine atoms (e.g., CF_2Cl_2 known as CFC-12)
- Hydrochlorofluorocarbons (HCFCs): partly halogenated hydrocarbons where some, but not all hydrogen atoms are replaced by chlorine or fluorine atoms (e.g., CHF_2Cl known as HCFC-22)
- Hydrofluorocarbons (HFCs): partly halogenated hydrocarbons where some, but not all hydrogen atoms are replaced by fluorine atoms (e.g., $C_2H_2F_4$ known as HFC-134a)
- Halons: fully or partly halogenated hydrocarbons where hydrogen atoms are replaced by chlorine or fluorine atoms and at least one bromine atom (e.g., CF_2ClBr known as Halon 1211)
- Bromo-, chloro-, and iodocarbons: fully or partly halogenated hydrocarbons with only one type of halogen atom except fluorine (e.g., CH_2Br_2)
- Others: halogenated species where none of the above criteria apply (e.g., SF_6)

CFCs have been used abundantly in the past as refrigerants, propellants, blowing agents, and solvents (Seinfeld and Pandis, 2006) promoted by their physical properties (e.g., non-flammability). Due to their chemical stability, CFCs propagate readily into the stratosphere where halogen radicals are released during their photochemical dissociation. Chlorine and bromine radicals both induce a catalytical cycle that eventually leads to a rapid depletion of stratospheric ozone (Molina and Rowland, 1974; Rowland and Molina, 1975; Wofsy et al., 1975). Additionally, many CFCs are strong greenhouse gases. Both effects combined implicate long-term damage to the Earth's atmosphere and climate. The discovery of the catalytical ozone destruction paved the way for the ratification of the Montreal protocol in 1987. Thereby, CFCs were put into a phase-out state starting in 1989. HCFCs and HFCs have a generally shorter atmospheric lifetime than CFCs (e.g., Carpenter and Reimann, 2014) due to their reaction with the hydroxyl radical in the troposphere and therefore are much less effective regarding ozone destruction in the stratosphere. Besides, fluorine radicals rapidly recombine to form HF and show a much weaker ozone depletion potential than chlorine and bromine in general. However, as HCFCs and HFCs are strong greenhouse gases, their phase-out has been forced in different amendments to the Montreal protocol, the most recent being the Kigali amendment in 2016 (at the time of this thesis).
While halons are still used to this day in fire extinguishing systems aboard aircraft, their production is prohibited under the Montreal protocol which makes recycling of old halon stock an important process. The most common halons include halon 1211, halon 1301 (see table 2.1) and halon 2402 ($C_2F_4Br_2$), which all are highly potent ozone depleting substances and greenhouse gases. That is promoted by their large global chemical lifetime (see e.g., SPARC, 2013) that enables them to enter the stratosphere where the main sink constitutes photochemical depletion. SF_6 is not harmful to the ozone layer and therefore not regulated under the Montreal protocol. It has been, however, restricted by the Kyoto protocol in 1997, where emissions of greenhouse gases are regulated (e.g., World Meteorological Organization, 2019). It is primarily utilized in the high voltage, semiconductor or medical industry and one of the strongest known greenhouse gases (e.g., Ravishankara et al., 1993). In stratospheric science it is appreciated as a valuable tracer for transport processes with piecewise linear temporal trend and a very large global chemical lifetime of circa 850 years (580 years – 1400 years) (Ray et al., 2017) due to its main sink region in the mesosphere. For many applications, especially involving mean AoA, it can therefore be treated as quasi-inert trace gas.
The necessity to observe halogenated species in the stratosphere is also stressed by the fact that many more halogenated compounds are potent greenhouse gases. The rapid investigation and regimentation of CFCs/HCFCs/HFCs and halons inhibited further damage to the stratosphere and steady

monitoring reveals that the stratospheric ozone layer is slowly recovering (World Meteorological Organization, 2019). However, recent studies imply that the regeneration of ozone in the stratosphere weakens (Ball et al., 2018) and might be related to a combination of increasing emissions of the prohibited substance CFC-11 (Montzka et al., 2018) in eastern China (Rigby et al., 2019) and a long- and short-term variability of the underlying dynamics in general (Ball et al., 2019). This requires further persistent observations around the globe, both tropospheric and stratospheric, to ensure further compliance with the Montreal protocol and a thorough analysis of the variability in stratospheric transport in the future. All halogenated substances in table 2.1 undergo different depletion mechanisms with distinct lifetimes. This information can be used to deduce the time elapsed since entering the stratosphere as explained in section 3 above.

Nitrous oxide

Nitrous oxide N_2O is an important greenhouse gas in the atmosphere that is circa 265 times more effective than CO_2 (see the GWP in table 2.1), but its global tropospheric mixing ratio is almost three orders of magnitude lower. Its predominant sources are the natural emission by soils and ocean upwelling and anthropogenic production in agricultural landuse and industrial combustion processes (Seinfeld and Pandis, 2006). Due to its large chemical lifetime (see e.g., SPARC, 2013) it is well-mixed in the troposphere and propagates up into stratosphere where it is depleted mostly by photolysis. The forming oxygen atoms are involved in subsequent reactions that eventually lead to a production of NO radicals. These contribute to the catalytic ozone destruction cycle and gain even more importance in the future as halogenated trace gases strongly decline (Crutzen, 1970; Portmann et al., 2012). The stratospheric sink mechanisms of nitrous oxide provide valuable information about stratospheric transport so that it might be used in the frame of this thesis for age spectra derivation (see section 3).

3 Towards a new method to derive age of air spectra from chemically active trace gases

The focus of this cumulative dissertation is on the deduction of age of air spectra using mixing ratios of various short- and long-lived atmospheric trace gases. The idea is to develop a robust, efficient, precise, and applicable method, which comprises as much available measurement data as possbible and captures relevant features of stratospheric transport. At the same time, the direct use of model data shall be minimized to establish a mostly self-contained toolset, although it has to be stated clearly that a fully independent method is not feasible. To keep the balance between accuracy, variability, numerical effort, and data availability the developed method is restricted to the seasonal scale as a minimum. As the scientific foundation for the involved principles and concepts has been layed in the previous sections, the following sections outline the necessity for this research, the conducted development processes, idealized model tests, applications, and key findings within the involved publications. The thesis follows the substantial and logical structure of the publications and disregards their different chronological order.
In section 3.1 an overview of important established tools and techniques is presented together with upcoming problems and room for improvements that serve as starting point for this study. This is taken up in section 3.2, where the concept of the novel method, its modifications, and numerical implementation are delineated (section 3.2.1), followed by an introduction to the model simulation for the method's general proof of concept (section 3.2.2) and topped off with a presentation of major results and problems that came up during the evaluation (section 3.2.3). These sections summarize the prime aspects of Hauck et al. (2019).
The problems discovered during the first proof of concept are a major subject of section 3.3, where an extension of the method to multiple reference surfaces is introduced (section 3.3.1), tested in another proof of concept using a different model environment (section 3.3.2), and completed by an analysis of both performance and limitations of the extended method in section 3.3.3. This sums up the structure and findings of Hauck et al. (2020).
In section 3.4, the thoroughly tested method is applied to measurement data gained during two research campaigns. Relevant stratospheric aircraft and tropopause mixing ratio data are described in section 3.4.1 below. Atmospheric variability and measurement uncertainties play an important role for the derivation of age spectra so section 3.4.2 introduces a statistical inversion process to capture the impact on the spectra. Finally, key findings of the application are presented and evaluated in section 3.4.3. These sections summarize aspects of both Keber et al. (2020) and Hauck et al. (2020). All computations are done using the interactive data language (IDL, version 8.4).

3.1 Methodological overview

In the past, many different strategies have been proposed to derive the age spectrum from observations of long- and short-lived trace gases. One of the first studies is by Andrews et al. (1999), who use measurements of quasi-inert CO_2 in the lower tropical stratosphere in combination with equation (2). They parametrize the age spectrum by an inverse Gaussian solution similar to the one postulated by Hall and Plumb (1994) with two independent variables and treat the whole equation as a mathematical inverse problem. To iterate the pair of parameters in the age spectrum that best describe their observed profiles of CO_2, they introduce a Monte Carlo simulation and generate the initial guesses for their variables in pseudo-random fashion. This straightforward and robust approach lead to promising results that resemble age spectra within modern model studies, albeit being only monomodal. In a forward calculation the retrieved age spectra are found to reproduce vertical profiles of H_2O consistent with observations. However, although the performance of this approach is promising, precise age spectra need to be multimodal to capture seasonal variability to full extent and therefore describe transport on a long-term scale correctly. Moreover, their results significantly depend on the measurement accuracy and informative content of only one type of trace gas species with negligible depletion in the inversion. This is a strong bias and should be compensated by a

diversification of trace gas species with different chemical lifetimes to constrain various parts of the age spectrum. Schoeberl et al. (2000) propose a highly theoretical concept to include multiple trace gases with chemistry along average Lagrangian pathways through the stratosphere, where chemical lifetimes show a stronger dependency on transit time than on the explicit pathway. This leads to equation (7). They discretize the equation, turn it into a matrix inversion problem with N trace gases providing N pieces of information about the age spectrum, test the method in a 2D model simulation using N_2O and CFC-11, and conclude that chemical loss rates from a model simulation could be considered to derive age spectra from trace gases. Recently, the method has been further researched in a Lagrangian chemistry transport model by Podglajen and Ploeger (2019), who could even retrieve multimodal spectra from artificial sinusoidal trace gases. Although the method performs well, the authors stress that an application to observations requires a careful assessment of the chemical lifetime along the average pathway and the variability associated with it. A possible benefit could be provided by additional consideration of short-lived substances as these are especially suitable to gain information about rapid transport processes. The inversion approach by Schoeberl et al. (2000) is simplified by Schoeberl et al. (2005), where the transit-time-dependent lifetimes in equation (7) are turned into path averages and merged with an inverse Gaussian shape parametrization for the age spectrum. Their inversion problem can be formulated in the notation of this thesis as follows

$$\chi_i^*(y,z) = \int_0^\infty e^{-\lambda_i(y,z)\cdot t'} \cdot \underbrace{\frac{z}{2\sqrt{\pi K(t'-t_{off})^3}} \cdot \exp\left(\frac{z}{2H} - \frac{K(t'-t_{off})}{4H^2} - \frac{z^2}{4K(t'-t_{off})}\right)}_{=G(y,z,t')} \cdot dt'. \quad (8)$$

In this equation, χ_i^* is the mixing ratio of trace gase i at (y,z) in the stratosphere normalized to the mixing ratio at the reference surface, $\lambda_i(y,z)$ the path-averaged loss rate (inverse of the chemical lifetime) of the trace gas, and t_{off} an introduced transit time offset to regard that onedimensional diffusion and stratospheric transport do not show an instantaneous link. Knowing the real observed normalized mixing ratio χ_i at (y,z), the parameters K, z, and t_{off} are varied in a least squares fit to find the minimum of the following equation

$$F = \sum_i^N (\chi_i - \chi_i^*)^2, \quad (9)$$

which is equivalent to minimizing the squared deviation between observed χ_i and inverted mixing ratios χ_i^* for all trace gases simultaneously. Applying loss rates from a 2D model simulation and in situ observations of CFC-11, CFC-12, N_2O, and CH_4, they could retrieve reasonable monomodal age spectra and related mean AoA, although some inconsistencies with observationally derived mean AoA and the age spectra appear. The authors suggest that an extension of the range of substances could improve the results significantly. This is a promising outcome, but again involves only monomodal age spectra so that important seasonal key features are still missing. Additionally, the variation of three parameters (K, z, and t_{off}) must be reassessed. Especially, since the vertical coordinate z should be considered as constant to derive an age spectrum exactly at the given location in the stratosphere. Finally, the use of modeled depletion rates is a reasonable and solid choice, but for a sound assessment of stratospheric transport using primarily observations, a minimization of the direct influence of these data would be favorable to reduce the direct dependency on transport and chemical processes within the model. Schoeberl's method therefore provides an encouraging starting point for this thesis as its performance and applicability are already promising and further research can contribute to improve its potential and independence. Another promising method is introduced by Ehhalt et al. (2007) and refers to the method by Schoeberl et al. (2000) in an unidimensional diffusion approach. They propose the assumption of chemical lifetimes that are invariant in time and space. Together with a constant entry mixing ratio at the reference surface, in their case the tropical tropopause, this leads to a modified version of equation (7)

$$\chi(z,\tau) = \chi_0 \cdot \int_0^\infty e^{-\frac{t'}{\tau}} \cdot G(z,t') \cdot dt'. \tag{10}$$

Mathematically, this is equivalent to a Laplace transform of the age spectrum. In case of the inverse Gaussian (IG) parametrization for $G(z,t')$ (see Hall and Plumb, 1994), the Laplace transform results in

$$\chi(z,\tau) = \chi_0 \cdot \widetilde{G}(z,\tau) \overset{\text{IG}}{=} \chi_0 \cdot \exp\left(-\frac{z}{\zeta(\tau)}\right), \tag{11}$$

with

$$\zeta(\tau) = \frac{2H}{\sqrt{1+\frac{4H^2}{K\tau}}-1}. \tag{12}$$

The principle of Ehhalt's method is comprehensible and very elegant, as it offers an analytical solution to the problem. Following equation (11), the vertical mixing ratio profile of any trace gas within this assumption is characterized as exponential decay of the mixing ratio at the tropical tropopause prescribed by a trace gas scale height $\zeta(\tau)$. Measuring the vertical profile of suitable trace gases for which the rough assumption of a spatially and temporally constant chemical lifetime might be applicable, the trace gas scale height can be retrieved from an exponential fit of the vertical profile. The resulting value for $\zeta(\tau)$ is then applied to solve equation (12) for the diffusion coefficient K, which is assumed to be vertically constant, and finally results in an age spectrum retrieval. Ehhalt et al. (2007) use airborne measurements of CO, C_2H_6, C_3H_8, n-C_4H_{10}, and C_2H_2 in the frame of a model simulation for a test of their method in an altitude- and tracer-based (CFC-12) coordinate system to smoothen the variability of the trace gas measurements.
Their results reveal that the method produces reasonable monomodal age spectra from measurement data gathered between 30° N and 35° N in proximity to the tropopause, although results improve if the lifetimes are allowed to be height-dependent with numerically retrieved trace gas scale heights. Although the simplicity of this ansatz makes it a promising candidate, extensive tests in the frame of this thesis with airborne data of halogenated trace gases and idealized radiocative trace gases in a full 3D chemistry climate model (see section 3.2.2 and 3.4.1 for details on the data) have shown that Ehhalt's method works properly but is strongly restricted to a narrow band close to the tropopause and loses performance with increasing altitude even for the idealized model trace gases where the assumption of an uniform chemical lifetime is satisfied. Therefore, the best starting point for the research presented in this thesis constitutes the method by Schoeberl et al. (2005) which is selected for further refinements and applications.

3.2 Inverse method – general development

The following sections summarize concepts, methods, data, and key results that are published in detail in:
Hauck, M., Fritsch, F., Garny, H., and Engel, A.: *Deriving stratospheric age of air spectra using an idealized set of chemically active trace gases*, Atmospheric Chemistry and Physics, 19, 5269-5291, DOI: https://doi.org/10.5194/acp-19-5269-2019, 2019

3.2.1 Basic theory and implementation

Modifications and improvements

For the development of the inverse method, Schoeberl's approach holds the ideal prerequisites as it is a comprehensible concept with promising results. The selection of an inverse Gaussian shape

parametrization might be an approximation, but under consideration of the sparse amount of available observational data without explicit use of an atmospheric model, a constraint to the shape of the distribution sounds reasonable so that any available information about transport can be extracted to tune the spectrum as precisely as possbible. Additionally, as mentioned above, previous studies have shown that modeled age spectra bear many similarities with an inverse Gaussian PDF. Some major aspects, however, have to be discussed. First, the inclusion of the temporal offset t_{off} in equation (8) poses problems for transit times smaller than the offset. This is relevant in particular for age spectra at large altitudes in the stratosphere where the apex of the spectrum is shifted towards very large transit times. In such cases, negative values appear in the square root and lead to a partly complex-valued spectrum. Despite the fact that these transit times are most likely omitted in practice and the age spectrum being forced to zero in the respective transit time range, the general concept of the offset should be reassessed. For that, the standard inverse Gaussian formulation, as given by Chhikara and Folks (1989), is considered using transit time as independent variable.

$$f(t', \mu, \lambda) = \sqrt{\frac{\lambda}{2\pi t'^3}} \cdot \exp\left(\frac{\lambda}{\mu} - \frac{\lambda t'}{2\mu^2} - \frac{\lambda}{2t'}\right) \tag{13}$$

Here, μ is defined as the mean of the distribution (i.e., mean AoA) and λ as its scale parameter. Upon comparison with equation (6) it is apparent that $\mu = \frac{zH}{K}$ and $\lambda = \frac{z^2}{2K}$. In their introduction into the basic theory of the inverse Gaussian PDF, Chhikara and Folks (1989) demonstrate that variations of λ and μ can lead to a heavily shifted distribution without explicit inclusion of any offset that is subtracted from t' (see figures 2.1 and 2.2 in their study).

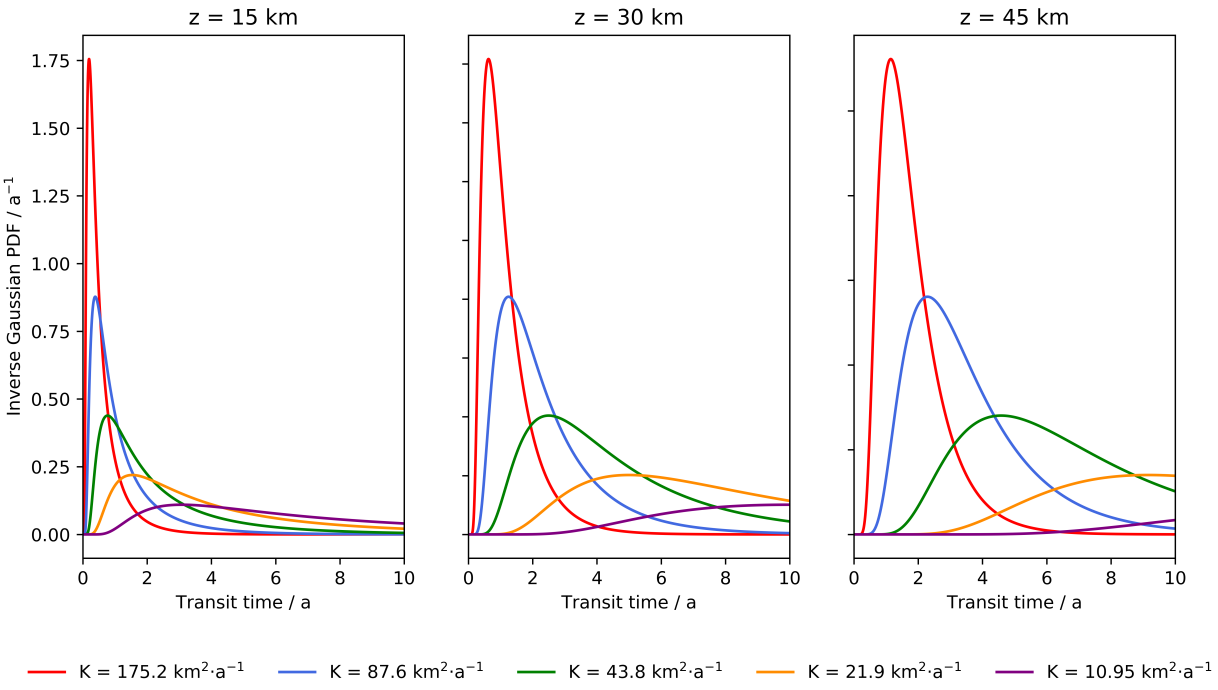

Figure 3.1: Inverse Gaussian distributions with different parameters at three altitude levels
Shown are five inverse Gaussian distributions using arbitrary values for K in equation (6) at 15 km (left), 30 km (mid) and 45 km (right) altitude. The scale height H has been preset to 7 km in all panels (e.g., Ehhalt et al., 2007).

In case of the used parametrization in this study, it is evident that the diffusion coefficient K affects both λ and μ at the same time. It should therefore be possible to retrieve a matching age spectrum only by variation of K at any selected altitude z without consideration of t_{off}. Figure 3.1 depicts tests with the inverse Gaussian PDF where five distinct values of K at three selected altitude levels have

been applied in equation (6). Generally, the smaller the diffusion coefficient gets, the smaller and broader the peak of the spectrum becomes. The altitude plays an important role for the shape of the spectrum, since any curve with a fixed value for K exhibits a height-dependent intrinsic transit time offset (compare e.g., the green curve at 15 km and 45 km). This is physically meaningful as it takes the air parcel a certain amount of time to reach 45 km and small transit times are thus negligible in the associated PDF. The presented distributions strongly imply that an exclusion of t_{off} will still lead to reasonable age spectra when performing the inversion. Additionally, the altitude z should be held constant during the inversion procedure as it critically influences the shape of the retrieved spectrum. This also guarantees that the spectrum represents transport exactly at the desired location in the stratosphere. The number of free parameters in equation (8) thus reduces from three to one, simplifying the numerical effort and error-proneness for the inversion considerably. A single parameter inversion also has the benefit that all information about ongoing dynamics is found in K, which is for the inverse method from now on treated as a general 3D transport parameter $K(\vec{x}, t)$ that provides non-directional information about three-dimensional stratospheric transport processes within a scalar quantity. The transport parameter shares similarities with mean AoA, but its interpretation regarding transport strength is not straightforward.

Transport seasonality

The most limiting factor for Schoeberl's and basically all of the above presented methods (except Podglajen and Ploeger, 2019) is the lack of multimodal age spectra. Since these modes represent alternating phases of a weaker and stronger BDC, they are an important feature that should be included into the inverted spectra. The problem with a mathematical inversion in the form presented in this thesis is that $K(\vec{x}, t)$ is independent of transit time and therefore not capable of considering the variable phases of transport directly. The retrieval of multiple modes is even more aggravated by the integral formulation of the inversion problem. The measured mixing ratio $\chi(\vec{x}, t)$ is the only quantity in the equation that could in theory provide information about seasonality since the related substance has experienced stratospheric transport. However, $\chi(\vec{x}, t)$ is also independent of transit time so a direct retrieval of the experienced seasonality is nearly impossible and requires the use of indirect strategies involving proxy measures of transport strength and variability. One possible approach is to introduce a predefined scaling factor that is used to impose the seasonality onto the age spectrum during the inversion process. In that way age spectra become multimodal although certainly it does not express the real occuring variability. However, since it is derived from an atmospheric proxy and affects every spectrum in equal fashion it can still be used to conduct a comparison between different age spectra and make a point about possible differences and underlying causing factors. This leads to a modified version of equation (7) where such scaling factor can be included as follows

$$\chi(\vec{x}, t) = \int_0^\infty \chi_0(t - t') \cdot e^{-\frac{t'}{\tau(\vec{x},t,t')}} \cdot G(\vec{x}, t, t') \cdot \omega(t') \cdot dt'. \tag{14}$$

$\omega(t')$ is the newly incorporated seasonal scaling factor and equation (14) the basic formula for the inverse method. Note that after the scaling procedure is finished, the resulting spectrum $G(\vec{x}, t, t') \cdot \omega(t')$ is manually re-normalized to satisfy equation (3) again. $G(\vec{x}, t, t')$ is here always parametrized by the inverse Gaussian function in equation (6) with the transport parameter $K(\vec{x}, t)$ instead of the original 1D diffusion coefficient (Hall and Plumb, 1994). This parameter is numerically optimized (see below) given that $\chi(\vec{x}, t)$, $\chi_0(t-t')$, and $\tau(\vec{x}, t, t')$ are known or approximated to some extent. Since the tropical tropopause is typically considered as the predominant source region for the stratosphere (Fueglistaler et al., 2009), all inverted age spectra $G(\vec{x}, t, t')$ use the tropical tropopause as reference surface. Air parcels that cross the tropical tropopause are likely influenced by the tropical net upward mass flux so that the seasonal variability of this flux is a suitable proxy to derive a proper seasonal scaling factor for the age spectrum. As mentioned above, the inverse method is herein always restricted to the seasonal scale. Considering the tropical upward mass flux at 70 hPa given by Rosenlof (1995) (see also figure 2.6 above) the transport strength in a specific season can be

compared relatively to the remaining three. For instance, taking the average of the first three columns in table 4 of Rosenlof (1995) for the mass flux in DJF leads to circa $7.02 \cdot 10^9$ kg/s, while for JJA the average is only approximately $4.25 \cdot 10^9$ kg/s. When both fluxes are divided, the result implies that the strength of the circulation during northern hemispheric summer (JJA) is only circa 60 % of the strength during winter (DJF). This can be transferred directly onto the age spectrum indicating that for a spectrum retrieved in DJF, the amplitude must be only 60 % of the intrinsic amplitude at transit times that correspond to JJA. As DJF and JJA are separated by half a year and increasing transit time is equivalent to going backward in real time, the age spectrum in DJF must be scaled down by 60 % at 0.5 years transit time and all previous northern hemispheric summers (1.5 years, 2.5 years, etc.). The scaling concept is then repeated for every remaining combination of seasons. Obviously, no scaling is implemented for transit times that equal the season the spectrum is retrieved in as the mass flux ratio always equals unity (DJF in the example above). To ensure a smooth transition between the seasons, the scaling factor is postulated as cosine function in the following form

$$\omega(t') = A + B \cdot \cos\left(\frac{2\pi}{365\,\text{days}} \cdot t' + C\right). \tag{15}$$

A, B, and C are scaling constants derived from the mass flux ratios and depend only on the specific season of the age spectrum. On the annual scale the minima and maxima of the cycle should cancel out and a monomodal spectrum emerges similar to the spectra in model simulations (see black line in figure 2.5). While the derived scaling constants from the tropical upward mass flux ratios are visible in table 1 in Hauck et al. (2019) appended to this thesis, the resulting scaling factors of all four seasons are shown in figure 3.2 for one year of transit time.

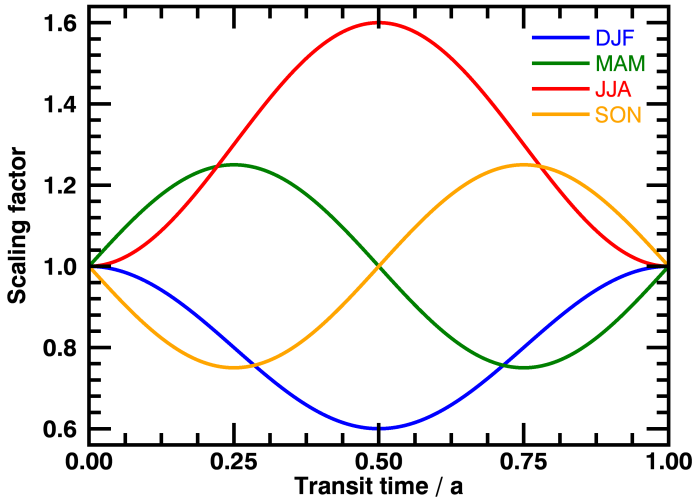

Figure 3.2: Seasonal scaling factors for the age spectrum in the inverse method
Presented are the seasonal scaling factors for the age spectra in the inversion procedure against one year transit time. The factors are derived from the tropical upward mass flux at 70 hPa ((Rosenlof, 1995) and designed in such way that no scaling occurs at 0 years and all integer multiples of 1 years. The figure is taken from Hauck et al. (2019).

Since this exemplifies one full period of the cosine function, all remaing transit time years are equivalent. Considering the blue curve (DJF) like in the above presented example, it is evident that the scaling process works as intended. Northern hemispheric winter (transit time 0 and 1 year) experiences no scaling, i.e., $\omega(t')= 1$, whereas northern hemispheric summer (transit time 0.5 years) undergoes the strongest downscaling with a diminished amplitude of 60 % compared to the intrinsic value. Northern spring and fall (transit times 0.25 and 0.75 years respectively) are shaped as transition seasons between minimum and maximum. Consistently, the northern summer curve (JJA – red) exhibits an inverted behavior where the maximum upward scaling occurs during northern winter

(DJF – transit time 0.5 years) showing an amplitude that is increased by 60 %. This implies that the scaling factor works properly and correctly transfers the information about seasonal variability from the tropical upward mass flux onto the age spectrum during the inversion process.

Numerical realization

The numerical implementation of the inverse method requires some further discussion. Decreasing the free parameters from three in Schoeberl's method to one in its presented form significantly reduced the numerical effort and also the risk to find a local minimum during the inversion rather than the desired global minimum. As the inverse method should process multiple mixing ratios simultaneously, a proper metric has to be defined to quantify the discrepancy between the inverted and the actual mixing ratios of the trace gases. In regressions and optimization problems these metrics are often referred to as loss functions. The variety of loss functions based on different mathematical approaches, prinicples, and equations is very large. These techniques have one specific problem in common that is especially known in the area of machine learning algorithms and predictive modeling: the bias-variance tradeoff. It describes the feature that in a set of given predicted samples the bias of these predictions from the true solution can only be decreased if at the same time the variance across the samples increases and vice versa. Optimization problems therefore have to keep the balance between bias and variance as both cannot be easily minimized at the same time. For the purpose of this study, stratospheric transport should affect all trace gas species within an air parcel equally. Therefore, the bias of the predicted trace gas mixing ratios should be more important than their variance, as it is very unlikely that for any given age spectrum in equation (14) some trace gas mixing ratios are highly overfitted while the remaining mixing ratios are strongly underestimated provided that the chemical lifetime is known precisely. The primary focus during the inversion should thus be on a reduction of the bias between the predicted and actual trace gas mixing ratios. For this study, a suitable loss function is the mean percentage error (MPE). It is also a very comprehensible measure that relies on percentage differences to estimate the deviation between predictions and actual values. MPE is defined as follows

$$\mathrm{MPE} = \frac{1}{N} \cdot \sum_{i}^{N} \frac{\chi_{i,ref} - \chi_i}{\chi_{i,ref}}. \tag{16}$$

$\chi_{i,ref}$ is the actual reference mixing ratio of trace gas species i (out of N in total) and χ_i the mixing ratio that is calculated from the age spectrum during the inversion of equation (14). The use of MPE as loss function has an important benefit compared to other common metrics such as root mean square error or mean absolute percentage error. Its quantitative range extends to negative values, which turns the optimization of equation (16) into a quite simple one parameter root finding problem with an optimal MPE of 0. A proper numerical method to determine roots in a numerically stable and rapid way has been proposed by Ridders (1979). Its main advantage is that if the desired root has been bracketed correctly, i.e., using two initial values for the transport parameter K_0 and K_1 where the according MPE_0 and MPE_1 have contrary signs, it is guaranteed that the algorithm will find the solution with reasonable convergence speed. The concept of the numerical implementation of the inverse method is shown in figure 3.3 below. With the initial values K_0 and K_1 the Ridders method computes two intermediate candiate values K_2 and K_3. All four K-values are plugged into the parametrization for the age spectrum so that four candidates of the spectrum G_0 to G_3 are derived. These spectra are fed back into equation (14) where for every age spectrum candidate a set of N mixing ratios and the associated MPE_0 to MPE_3 are determined. Using all retrieved MPEs, the algorithm decides whether brackets have to be replaced by new K-values closer to the solution. If the smallest absolute MPE is not below the defined tolerance, the algorithm returns the new brackets into Ridders' method and repeats the steps above until the stop criterion is satisfied. The K-value that led to the MPE closest to 0 is then finally turned into an age spectrum that is returned as output of the inverse method. In the rare occasion that the convergence of Ridders's method takes a certain

amount of repetitions, the algorithm of the inverse method switches to a coupled implementation of Newton's method that is known to be quite rapid but will only converge if the input value is close to the true solution already. If the root cannot be bracketed correctly upon initialization, the algorithm returns a NaN-value for the age spectrum and omits the datapoint for further calculations.

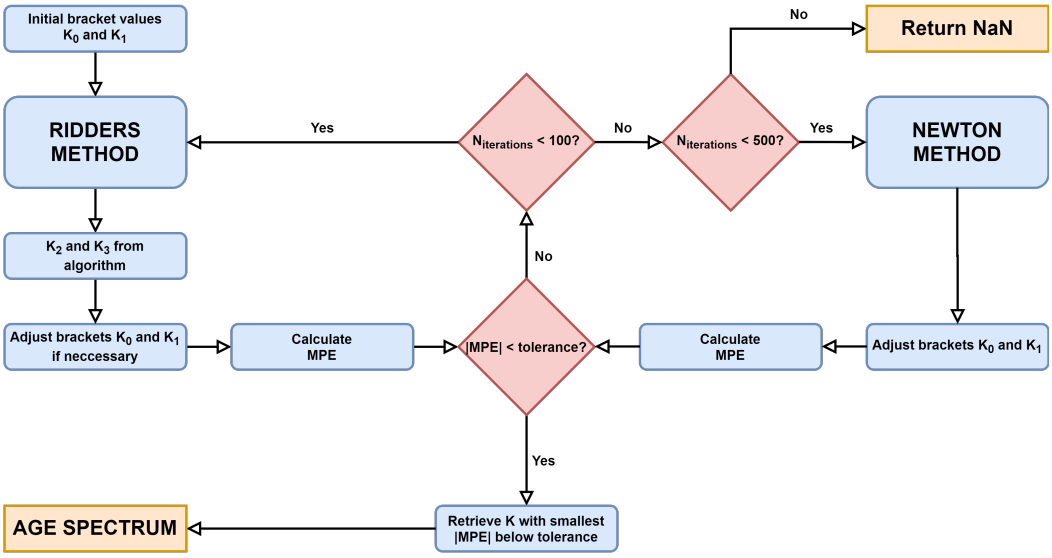

Figure 3.3: Diagram of the numerical inversion procedure
A block diagram of the numerical algorithm for the inverse method based on the Ridders (Ridders, 1979) and Newton method for root finding. The initial values K_0 and K_1 need to bracket the root correctly so that MPE_0 and MPE_1 have opposite signs. The stop criterion (bottom red diamond) is set to 5 % tolerance.

3.2.2 EMAC simulation setup

Now that the inverse method and its modifications have been postulated, a general proof of concept in an idealized model setup is necessary to test its performance and see if the method is able to retrieve spectra in a controllable environment. For that purpose, a simulation has been performed with the global chemistry climate model ECHAM/MESSy Atmospheric Chemistry (EMAC) that is frequently used to study atmospheric transport processes and its interactions with chemistry reliably (e.g., Jöckel et al., 2016). The EMAC model is a numerical chemistry and climate simulation system that includes sub-models describing tropospheric and middle atmosphere processes and their interaction with oceans, land and human influences (Jöckel et al., 2010). It uses the second version of the Modular Earth Submodel System (MESSy2) to link multi-institutional computer codes. The core atmospheric model is the 5th generation European Centre Hamburg general circulation model (ECHAM5, Roeckner et al., 2006). For the present study we applied EMAC (ECHAM5 version 5.3.02, MESSy version 2.53.0) in the T42L90MA-resolution, i.e. with a spherical truncation of T42 (corresponding to a quadratic Gaussian grid of approximately 2.8 by 2.8 degrees in latitude and longitude) with 90 vertical hybrid pressure levels up to 0.01 hPa (taken in an adapted version from www.messy-interface.org – last checked 23.03.2020).
The simulation is designed as a free-running (i.e., no nudging) time-slice simulation where greenhouse gas concentrations, sea surface temperatures, and sea ice concentrations are prescribed in the state of the year 2000. This ensures that the model output does not undergo any long-term temporal trends so that a constant test environment for the proof of concept can be established. However, interannual and seasonal variability is nevertheless included. Final output data are taken as zonal, monthly, and finally seasonal averages, as this has been introduced as timescale the inverse method is restricted to. The simulation covers a period of 20 years, which are numbered from 0 to 19 to stress that these are within a time-slice setup. The simulation features a perfectly linearly increasing inert trace gas released constantly globally at the surface. Mean AoA is derived from this clock tracer as timelag between the surface mixing ratio and the mixing ratio at any point. At the tropical

surface between 12.5° N and 12.5° S, 40 inert trace gases are consecutively released as pulses with a mixing ratio of 100 % every three months (January, April, July, and October) to cover a range of ten years. After every of these species has been pulsed once, they are gradually reset and repulsed. The temporal evolution of a winter (January – year 10) and a summer (July – year 10) pulse are shown in figure 3.4 as latitude pressure cross-sections.

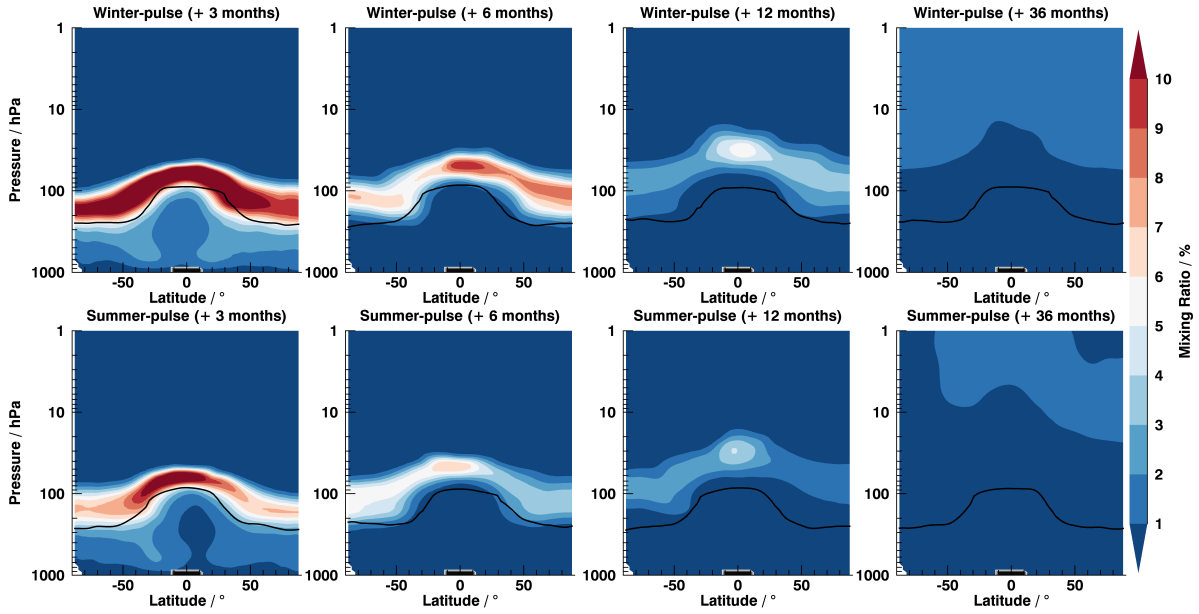

Figure 3.4: Temporal progression of an inert trace gas pulsed in summer/winter in EMAC
Shown is the temporal evolution of two distinct inert trace gase pulse within the EMAC model simulation initialized between 12.5° N and 12.5° S at the surface (black box). The pulse in the top row has been triggered during northern hemispheric winter, while the bottom row shows a pulse triggered during northern hemispheric summer. Each panel depicts a snapshot of the pulse mixing ratios after the given amount of time. The idea to this plot is taken from figure 2 in Ploeger and Birner (2016).

It is apparent that the pulses are transported rapidly from the tropical surface upward into the stratosphere so that already after three months the maximum mixing ratios can be found right above the tropopause in a broad latitudinal band. After 36 months, both winter and summer pulse are heavily diluted and can be found at almost any latitude and pressure surface. Note that due to stronger wave forcing during northern hemispheric winter (DJF), the winter pulse propagates faster and mixing ratios after three months are found to be larger than after the same amount of time for the summer pulse. After each of the 40 pulse tracers has been at least initialized once, their mixing ratios at any point can be converted into age spectra using the method of boundary impulse response (BIR, Haine et al., 2008). This concept has since been extended to transient simulations to form the boundary impulse evolving response (BIER, Ploeger and Birner, 2016). The principle is very elegant yet quite abstract. Consider, for instance, an arbitrary stratospheric location in January of model year 10. The most recent pulse at this time is tracer 1, which is initialized right in January year 10 and has thus been transported in the atmosphere for circa 0.5 months (considering monthly means). Hence, the mixing ratio of pulse tracer 1 is taken as value of the age spectrum at 0.5 months transit time. The second newest pulse is tracer 40 that has been triggered in October year 9, i.e., 3.5 months ago and its mixing ratio is transferred into the age spectrum at the matching transit time of 3.5 months. This procedure is repeated until all remaining pulses have been converted. For intermediate months between the pulsing, mixing ratios are interpolated. With this setup, the resulting pulse age spectra are limited to ten years transit time which is insufficient to describe transport to a full extent. The pulse age spectra are extended artificially to 300 years transit time by fitting the tail of the distributions with an exponential decay (see Ploeger and Birner, 2016).
With respect to the inverse method, the setup includes also 40 chemically active trace gases with

spatially and temporally constant lifetimes from 1 month to 118 months (9.8$\overline{3}$ years). These artificial radioactive trace gases are released globally at the Earth's surface with a constant mixing ratio of 100 % and thus provide a perfect test setup to apply the inverse method in a replicable and controllable setup. Using these trace gases some minor simplifications can be done to improve the numerical performance of the inverse method in this setup. First, mixing ratios at the tropical tropopause are approximately constant in time so that $\chi_0(t - t')$ in equation (14) is converted to an annual mean $\overline{\chi_0}$, independent of transit time. Secondly, the transit-time-dependent chemical lifetime is constant in time and space so that it also can be replaced by the constant lifetimes of the radioactive trace gases τ. This leads to

$$R(\vec{x}, t) := \frac{\chi(\vec{x}, t)}{\overline{\chi_0}} = \int_0^\infty e^{-\frac{t'}{\tau}} \cdot G(\vec{x}, t, t') \cdot \omega(t') \cdot dt'. \tag{17}$$

The ratio $R(\vec{x}, t)$ can be inserted equivalently into equation (16) to compute the MPE. Since it has been shown above (see section 2.1.1) that potential temperature is the best possible choice for a vertical coordinate regarding transport analysis in the stratosphere, the potential temperature difference to the local tropopause is from now on used as vertical coordinate in the inversion to reduce variability. The first 30 K above the tropopause are always omitted during the inversion, since this specific region is characterized as transition region with large extratropical tropospheric influence (e.g., Hoor et al., 2004), which the inverse method cannot treat correctly. A problem for the direct comparison between the inverse and pulse age spectra is their distinct reference surface. While all pulse spectra refer transport to the Earth's surface, the inverse spectra use the tropical tropopause. To overcome this problem as best as possible and to make the spectra more comparable, the annually average mean AoA from the clock tracer at the tropical tropopause is derived (~0.19 years) and subtracted from the transit time of the pulse spectra and also clock tracer mean AoA. Negative values are omitted. In this way, the reference surface is transformed, although some inconsistencies are nevertheless present and can cause problems for the direct comparison (in particular around the tropopause).

3.2.3 Proof of concept and upcoming problems

Key findings

In this section key results of the first proof of concept in EMAC are presented to point out the generally promising performance of the inverse method in this idealized test scenario to reveal problems where further work is necessary. For a full discussion of all results please see Hauck et al. (2019) in the appendix of this thesis. Figure 3.5 compares inverse age spectra with the newly proposed seasonal scaling factor (dashed lines) to the original monomodal inverse spectra (dash-dotted lines) and also to the model reference pulse age spectra (solid lines) exemplary at 55° N and 70 hPa. All spectra are on the annual (panel (a)) and seasonal scale (panel (b) to (e)). It is apparent that both annual inverse spectra with and without seasonal cycle are identical and match the general shape of the annual pulse age spectrum significantly well. This implies that the imposed seasonal cycle performs as intended and cancels out when all seasonal spectra are averaged. The tails of the inverse spectra are slightly enhanced while at the same time the peaks appear lower than the pulse spectrum reference. Interestingly, the annual inverse spectra seem to be slightly shifted to larger transit times, which might explain the visible minor deviations for tail and peak. This shift is also evident when comparing the transit time of the mode (i.e., modal age) for pulse and inverse age spectra, which is found to agree within 0.1 years. This could be also an effect of the coarse transit time resolution of the pulse age spectra that clips off information about the peak, for instance around 0.3 and 0.6 years transit time on the solid line in panel (a). An increased amount of pulses in future simulations would lead

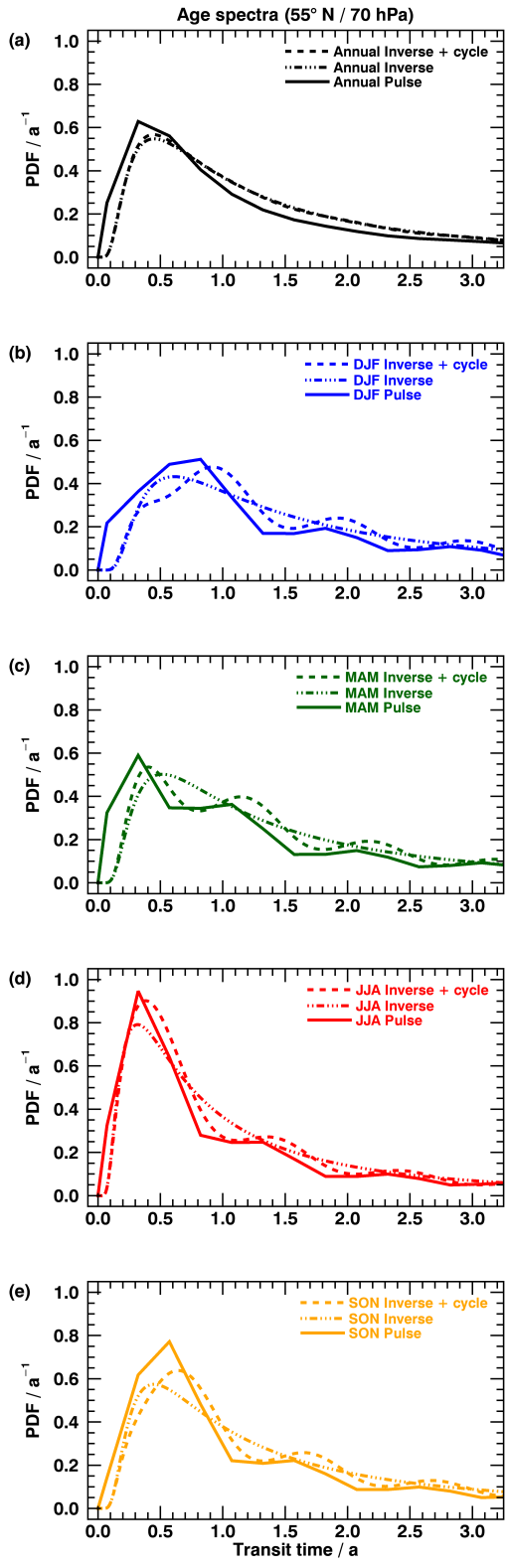

Figure 3.5: Age spectra at 55° N and 70 hPa of the proof of concept with the EMAC simulation
This figure from Hauck et al. (2019) shows exemplary results of the proof of concept with the EMAC model. Each panel consists of the retrieved inverse age spectra with (dashed) and without the developed seasonal cycle (dash-dotted). For comparison, the respective pulse age spectra from the EMAC simulation are depicted (solid line). Panel (a) shows the annual mean state, while panels (b) to (e) are the seasonal means from DJF (b) through SON (e).

to a finer transit time resolution that allows for an improved comparison between inverse and pulse age spectra. On the seasonal scale, the inverse method performs analogously well. Although the imposed seasonal cycle is based only on a proxy quantity of the variability in transport and not directly on EMAC data, it reproduces the maxima and minima of the pulse age spectra reliably with matching timing and amplitude. The modal ages of each seasonal inverse spectrum agree with the pulse spectra also within 0.1 years. The inclusion of the seasonal cycle constitutes a reasonable improvement to all inverse spectra as the intrinsic monomodal shapes lack important features of transport that the pulse age spectra reflect. Similar to the annual mean case, all seasonal inverse spectra exhibit an enhanced tail and in some cases a slightly decreased first mode (see e.g., DJF and SON). As this is also visible in inverse spectra at other pressure levels, Hauck et al. (2019) conclude that this might be either related to the assumed inverse Gaussian shape of the age spectra that is not perfectly matching or to the different original reference surface of pulse and inverse spectra that could not be compensated by the applied correction. Again, the coarse pulse spectra resolution seems to cut some parts of the peaks, which manifests in a right-tilted shape (e.g., MAM or SON). This good performance of both inverse method and seasonal cycle comes out quite similar at higher altitudes (55° N, 10 hPa) where also higher order maxima and minima are well-imposed. Here, the seasonality becomes even more important as more and more peaks emerge in the pulse spectra that cannot be described correctly by a monomodal shape. Only when approaching the extratropical tropopause (55° N, 140 hPa), the inverse method looses performance and retrieves spectra that deviate from the EMAC pulse spectra. This happens promotedly during northern spring and fall, while for summer and winter the agreement is again solid. Here, the coarse resolution of the pulse spectra again strongly inhibits a robust comparison as all peaks are only described by circa two tracer pulses. To corroborate the good performance of the inverse method also on the global scale, figure 3.6 shows mean AoA from the EMAC clock tracer, pulse age spectra and inverse age spectra as absolute annual mean values and relative seasonal differences to the annual mean state.

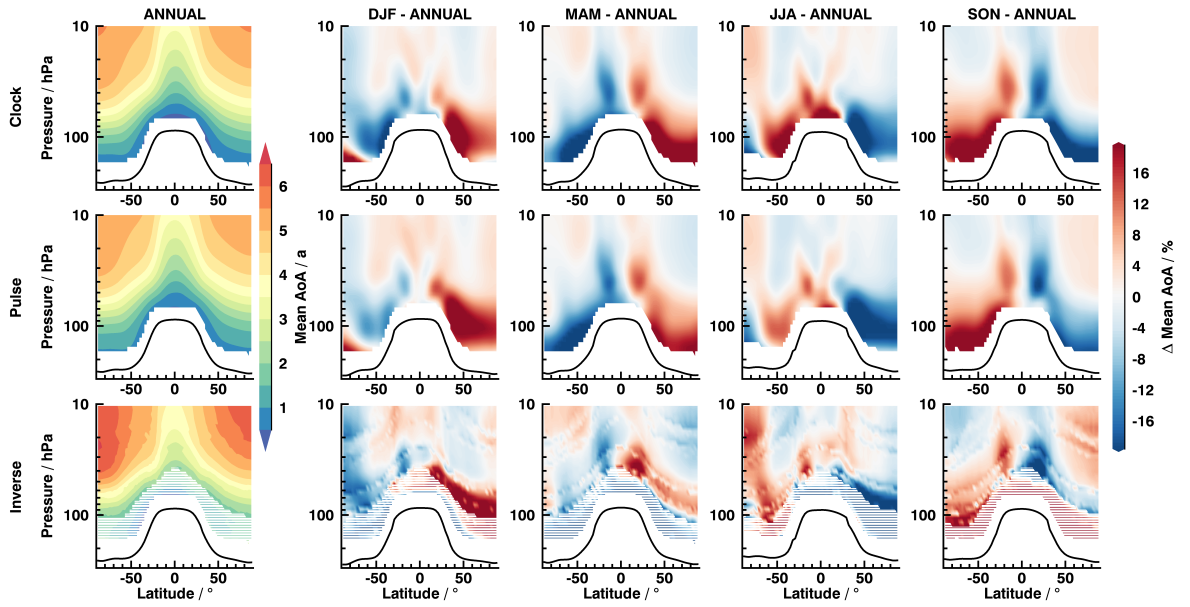

Figure 3.6: Cross-sections of mean AoA on annual and seasonal scale within the EMAC simulation
Mean AoA from the EMAC clock tracer (top row), integrated pulse spectra (mid row) and integrated inverse age spectra (bottom row) are shown as absolute annual mean (left column) and percentage seasonal differences (right four columns) relative to the respective annual mean state. The white-shaded contour marks areas where clock mean AoA is below 1.5 years (see text for details). The black line indicates the tropopause and negative latitudes refer to the southern hemisphere. The figure is taken from Hauck et al. (2019).

While annual mean clock and pulse mean AoA appear to be equivalent, which is due to the conducted tail extension of the pulse spectra (see section 3.2.2), inverse mean AoA is generally biased towards larger values. That is most probably linked to the enhanced tail and diminshed peak of the inverse spectra that are detected above. Seasonal variations of mean AoA come out to be consistent between pulse (mid row) and inverse spectra (bottom row) with correctly retrieved areas of positive and negative differences for most parts of the stratosphere. In a small band above the tropopause, the performance of the inverse method reduces and during MAM and SON in the northern hemisphere even an inverted seasonality is derived. Almost all of these discrepancies are found below a threshold of 1.5 years of clock mean AoA (white-striped area) and are mostly confined to the northern hemisphere. Above, only in some parts of the stratosphere the quantitative strength of the seasonality in inverse mean AoA exceeds that in pulse mean AoA (e.g., the red area above the south pole in JJA). That is also related to the deviation of tail and peak between inverse and pulse age spectra. The wavy structures of the inverse mean AoA that seem to follow isentropic surfaces are caused by the use of potential temperature difference on a pressure model grid in the inversion.
In terms of the age spectra width (i.e., the square root of equation (5) – not shown), the inverse method is found to perform similarly well above the introduced threshold of 1.5 years clock mean AoA even though the values are also biased towards larger values compared to the pulse spectra width. Both mean AoA and width of the inverse spectra are identical with and without the imposed seasonal cycle as the maxima and minima cancel out during the integration. Below the threshold, the performance of the inversion weakens again and implies that the inverse method has a systematic problem when approaching the extratropical tropopause especially in the northern hemisphere. This requires further modifications and tests (see below). With respect to the method's applicability to atmospheric measurement data, Hauck et al. (2019) show in the idealized model setup that an amount of five to ten distinct trace gases is sufficient to retrieve identical age spectra robustly and that during the inversion ± 20 % pseudo-random uncertainty in the applied chemical lifetime can be compensated with reasonably matching age spectra. That is an important aspect as in reality the number of different trace gas species observed in the stratosphere is highly limited and the knowledge about the chemical lifetime, especially the transit-time-dependent, is very uncertain.

Emerging problems

This first proof of concept shows that the newly established inverse method coupled with its novel imposed seasonal cycle derives multimodal age spectra that match the model reference pulse spectra very well in most parts of the stratosphere on the seasonal scale. However, the lower stratosphere below 1.5 years clock mean AoA, in particular close to the northern extratropical tropopause in MAM and SON, remains a problematic region where spectra and derived moments exhibit occasionally large deviations from the pulse spectra. The weaker performance during northern spring and fall should be directly related to the tropical tropopause as selected reference surface for the spectra. According to the results of Bönisch et al. (2009), the northern hemispheric lowermost stratosphere is flushed with fresh tropospheric air that enters across the extratropical tropopause during JJA and SON most probably due to the weak subtropical jet stream. This exchange through the extratropical tropopause is not included in the inverse method in its established form since the inverse spectra refer transport only to the tropical tropopause. In the pulse age spectra, however, these processes are included as the pulses are initialized at the Earth's surface in the tropics, although only limited due to the coarse pulse interval of three months. An increase of this resolution should lead to improvements as the rapid cross-tropopause transport is then robustly resolved. Tropical and extratropical mass fluxes also exhibit a quite different seasonal variability so that the imposed seasonal cycle might amplify the discrepancies between inverse and pulse age spectra. To reproduce the local transport mechanisms correctly, the inverse method has to be extended to refer transport to the extratropical tropopause sections. In the southern hemisphere, the strength of extratropical entrainment appears generally weaker which might explain why the inverse method performs better in that region (see section 2.1.3). The extension has to include also new seasonal cycles to account for the different seasonalities of the underlying mass fluxes. The extended concept is presented in the next section together with a second proof of concept of the new formalism.

3.3 Inverse method – extension

The following sections summarize concepts, methods, data, and key results that are published in detail in:
Hauck, M., Bönisch, H., Hoor, P., Keber, T., Ploeger, F., Schuck, T., and Engel, A.: *A convolution of observational and model data to estimate age of air spectra in the northern hemispheric lower stratosphere*, Atmospheric Chemistry and Physics, 20, 8763-8785, DOI: https://doi.org/10.5194/acp-20-8763-2020, 2020

3.3.1 Concept of multiple regions of entry

To include extratropical transport processes explicitly into the inversion concept, the global tropopause is split into a northern (90° N to 30° N; index N), a tropical (30° N to 30° S; index T) and a southern section (30° S to 90° S; index S) that each are used as reference surface for the age spectra. The concept is illustrated in figure 3.7 below. The regions are chosen so that each segment spreads an equal range of 60° latitude. Theoretically, this principle can be introduced with any amount of sections. This has the benefit that the relatively broad tropical tropopause section includes most of the seasonal shift of the intertropical convergence zone (ITCZ) which helps to define an latitudinal average mixing ratio for the section. With this extension one single age spectrum is now insufficient to fully quantify all occurring transport processes and each new tropopause segment i gets an age spectrum $g_i(\vec{x}, t, t')$ assigned to it. These subspectra then must add up to a composite age spectrum $G(\vec{x}, t, t')$ so that mass conservation holds. That is expressed as follows

$$G(\vec{x}, t, t') = g_N(\vec{x}, t, t') + g_T(\vec{x}, t, t') + g_S(\vec{x}, t, t'). \tag{18}$$

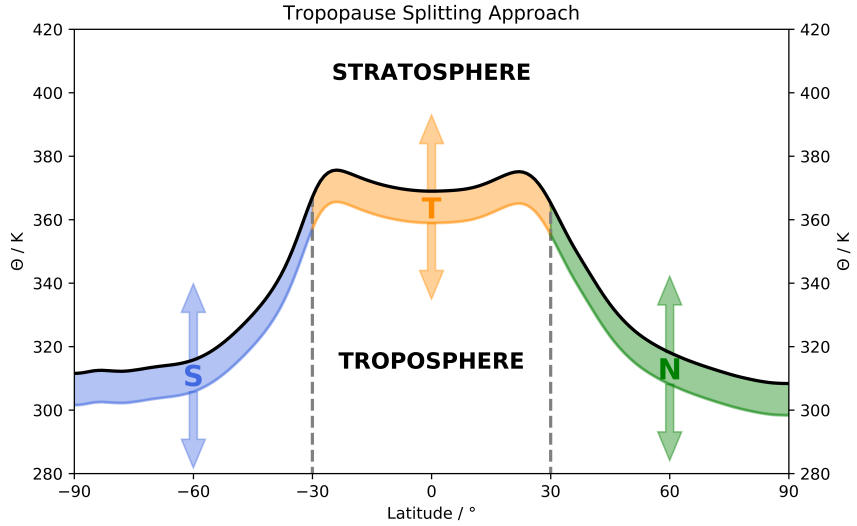

Figure 3.7: Concept of multiple entry regions to the stratosphere
This figure shows a sketch of the tropopause splitting approach that is conducted to extend the inverse method to the extratropical tropopause. The global tropopause is separated into a southern (90° S – 30° S; blue), a tropical (30° S – 30° N; orange), and a northern section (30° N – 90° N; green) that each span an equal latitude band of 60°. For each of the sections, a proper age spectrum and seasonal cycle is defined (see text for details).

Obviously, the subspectra $g_i(\vec{x}, t, t')$ do not satisfy the normalization criterion (equation (3)) as they describe only a certain fraction of transport within a given air parcel. These non-normalized spectra are always denoted with a lower-cased g, while for fully normalized age spectra an upper-cased G is used. Integration of equation (18) from 0 to ∞ years with respect to transit time leads to

$$1 = f_N(\vec{x}, t) + f_T(\vec{x}, t) + f_S(\vec{x}, t), \tag{19}$$

where $f_i(\vec{x}, t)$ is the norm of the underlying $g_i(\vec{x}, t, t')$. Vividly speaking, these norms provide a quantitative measure of the percentage of air at any point in the stratosphere that has tropopause section i as origin. The norms are thus hereafter referred to as origin fractions. Although each subspectrum remains non-normalized they can be utilized to compute for a specific substance with mixing ratio $\chi(\vec{x}, t)$ at $(\vec{x}, t)$ the fraction of that mixing ratio $\chi_i(\vec{x}, t)$ that is associated with the transport quantified by $g_i(\vec{x}, t, t')$. That mixing ratio fraction is equal to $f_i(\vec{x}, t) \cdot \chi(\vec{x}, t)$.

$$\chi_i(\vec{x}, t) = \int_0^\infty \chi_{0,i}(t - t') \cdot e^{-\frac{t'}{\tau_i(\vec{x},t,t')}} \cdot g_i(\vec{x}, t, t') \cdot \omega_i(t') \cdot n_i(\vec{x}, t) \cdot dt', \tag{20}$$

with $\chi_{0,i}(t - t')$ being the entry mixing ratio time series, $\tau_i(\vec{x}, t, t')$ the chemical lifetime of the substance, $\omega_i(t')$ the imposed seasonal cycle, and $n_i(\vec{x}, t)$ a newly introduced normalization factor that ensures that $g_i(\vec{x}, t, t')$ and $g_i(\vec{x}, t, t') \cdot \omega_i(t')$ both have the same norm upon integration (see Hauck et al. (2020) for the definition). All these quantities refer to the respective entry region i. Equation (20) holds some disadvantages that have to be overcome in order to be applicable within the inverse method. The parametrization of equation (6) always returns a normalized inverse Gaussian PDF, so that $g_i(\vec{x}, t, t')$ must be replaced by $f_i(\vec{x}, t) \cdot G_i(\vec{x}, t, t')$. Unfortunately, the origin fractions are a highly theoretical measure that cannot be easily determined from observations and require the use of some data from atmospheric models. As one goal of this thesis is to reduce the direct influence of model data as much as possible, the problem can be overcome in elegant fashion by division of the resulting equation through $f_i(\vec{x}, t)$.

$$\frac{\chi_i(\vec{x}, t)}{f_i(\vec{x}, t)} = \chi(\vec{x}, t) = \int_0^\infty \chi_{0,i}(t - t') \cdot e^{-\frac{t'}{\tau_i(\vec{x},t,t')}} \cdot G_i(\vec{x}, t, t') \cdot \omega_i(t') \cdot n_i(\vec{x}, t) \cdot dt' \tag{21}$$

This is a very important step and yields an equation that can be inverted using only the observed mixing ratio $\chi(\vec{x}, t)$ and without explicit knowledge of the origin fraction $f_i(\vec{x}, t)$ or mixing ratio fraction $\chi_i(\vec{x}, t)$, which are hard to obtain from sparse in situ measurements. $G_i(\vec{x}, t, t')$ is again parametrized for the inversion by the inverse Gaussian distribution given above using distinct transport parameters $K_i(\vec{x}, t)$. This independent inversion procedure is only successful if and only if neither $\chi_{0,i}(t - t')$ nor $\tau_i(\vec{x}, t, t')$ are identical for every given tropopause section. Only then the inverse method retrieves reasonable spectra that characterize entrainment across the extratropical tropopause correctly. As stated in section 2.1.3, the net direction of the hemispherically integrated mass flux across the northern and southern hemispheric tropopause is downward, which inhibits a straightforward derivation of the scaling factors as for the tropics. The use of a hemispherically integrated cross-tropopause mass flux is likely disadvantageous for the derivation of the scaling factors in the northern and southern extratropics, as it might underestimate the importance of local net upward motions. This is especially relevant for the subtropical jet stream, which has been shown to influence the air composition in the northern lowermost stratosphere (e.g., Bönisch et al., 2009). The results of Yang et al. (2016) corroborate this fact and show a rather narrow region of year-round net upwelling into the lowermost stratosphere in vicinity to the subtropical jet stream during summer in both hemispheres, while the net direction across the tropopause at higher latitudes turns downward rapidly. Since the specified northern and southern tropopause sections in this thesis might include some parts of the jet stream in the subtropics, it is likely that it has a relevant influence on the seasonality that shows in the modes of the age spectrum.

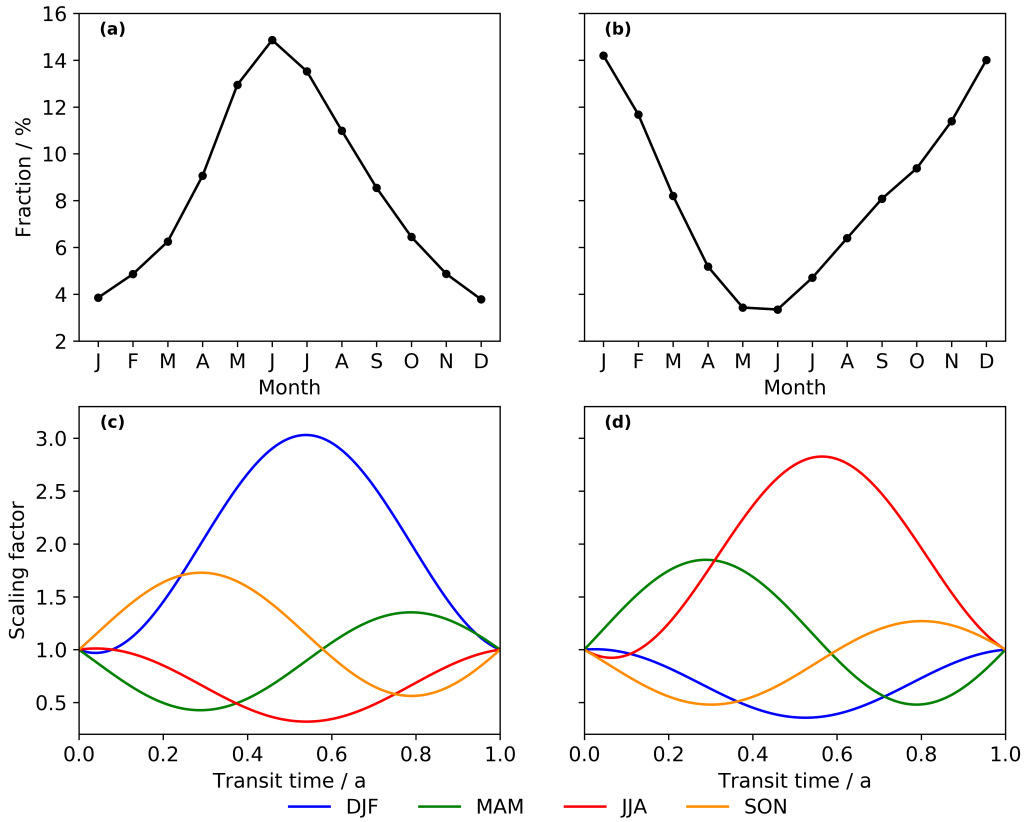

Figure 3.8: Tropopause entrainment fractions and seasonal scaling factors for the northern/southern tropopause section Shown in the top row are the fractions of air masses that enter the stratosphere per month through the northern (panel (a)) and southern (panel (b)) extratropical tropopause sections relative to all air that is entrained through the respective surface. The fractions are derived from CLaMS age spectra data with reference at the respective tropopause region (see text for details). In the bottom row, the derived scaling factors for the inverse age spectra with reference at the northern (panel (c)) and southern (panel (d)) are depicted. The figure is taken from Hauck et al. (2020).

However, the actual quantitative contribution of the subtropical jet stream to the net mass flux across the defined northern and southern tropopause segments remains unclear, since Yang et al. (2016) provide no explicit mass flux for the specific region. This requires the use of an alternative proxy for the scaling process. To estimate the seasonality as precisely as possible for the setup in this thesis, monthly mean CLaMS pulse age spectra from the simulation below are considered, which are initialized at the northern and southern hemispheric tropopause section (see section 3.3.2 for details on the data). This is advantageous as a bin-wise integration of an age spectrum provides the fraction of air enters the stratosphere across the given reference surface per transit time relative to all air that enters across that surface. When all global stratospheric age spectra with a given boundary region are cumulatively integrated and transit time bins are matched correctly against real time, this leads to a robust monthly average statistic of the predominant seasonality in entrainment across the considered tropopause section. This ansatz has been recently applied to tropical CLaMS pulse age spectra by Ploeger and Birner (2016, ; Figure 14b). The resulting fractions for the northern and southern hemispheric tropopause are shown in panel (a) and (b) of figure 3.8. Note that the fractions are normalized to equal 100 % when cumulated.
It is apparent that the maximum is located in both hemispheres in summer (July in the north and January in the south) with more than 14 % of all occurring entrainment across the respective tropopause section. The minimum is consequently found in winter (January in the north and July in the south) with values around 3 %. Spring and fall are transition seasons just as for the tropical tropopause above. Seasonally cumulated values imply that in the north, cross-tropopause upward transport during summer (JJA – circa 39 %) is approximately three times stronger than during winter (DJF – circa 13 %) and indicates that the corresponding inverse age spectrum in DJF should be scaled up by a factor of 3 for summer transit times (0.5 years, 1.5 years, etc.). Consistently, no scaling is implemented at winter transit times (0 years, 1.0 year, etc.).This procedure is done for all possible combinations of seasons in both the northern and southern hemisphere. The computed mass flux ratios are inserted into equation (15) to retrieve the scaling constants (A_N, B_N, C_N) and (A_S, B_S, C_S) for all four seasons. The final scaling factors are depicted in the bottom row of figure 3.8 and all applied constants are shown in table 1 of Hauck et al. (2020). All derived scaling factors exhibit the intended behavior with a pronounced upscaling at transit times that correspond to summer. Note that identical seasons have different colors in the northern and southern hemisphere, i.e., spring is green in panel (a) and orange in panel (b). With these scaling factors it is possible to derive matching age spectra that refer to the northern and southern extratropical tropopause (see also Hauck et al. (2020) for this discussion).
Although the use of CLaMS data provides a very robust and precise estimation of the seasonality in entrainment across the extratropical tropopause, it certainly inhibits an independent evaluation of CLaMS pulse and inverse age spectra. The higher order modes should now emerge at matching transit times in the inverse age spectra. Yet, no spatially dependent information about the shape of the pulse age spectra is transferred to the inverse age spectra during the inversion, as the fractions in figure 3.8 are a global average and integrated measure. Additionally, every inverse age spectrum in one specific season is convoluted with the identical scaling factor so that the intrinsic amplitude of the monomodal spectrum must be well-retrieved in the first place to derive matching higher order maxima and minima. As the season of maximum entrainment is consistent with the findings of Bönisch et al. (2009) and Yang et al. (2016), the retrieved scaling factors are considered the best achievable solution for this setup. This also connotes that the subtropical jet stream is very likely the driving mechanism for entrainment across the defined extratropical tropopause sections.

3.3.2 CLaMS simulation setup

For a test of the extended inverse method two simulations with the Chemical Lagrangian Model of the Stratosphere (CLaMS; McKenna, 2002a,b) have been conducted. CLaMS is a very suitable and frequently used model framework for dynamical studies of the stratosphere due to its Lagrangian transport formalism and sophisticated small-scale mixing scheme, that induces mixing in regions

where strong background flow deformations are present (Konopka, 2004). CLaMS models atmospheric transport and coupled chemical processes using a large amount of air parcels propagating along 3D forward trajectories with a hybrid vertical coordinate of orography-following layers in the lower and mid troposphere and potential temperature above.

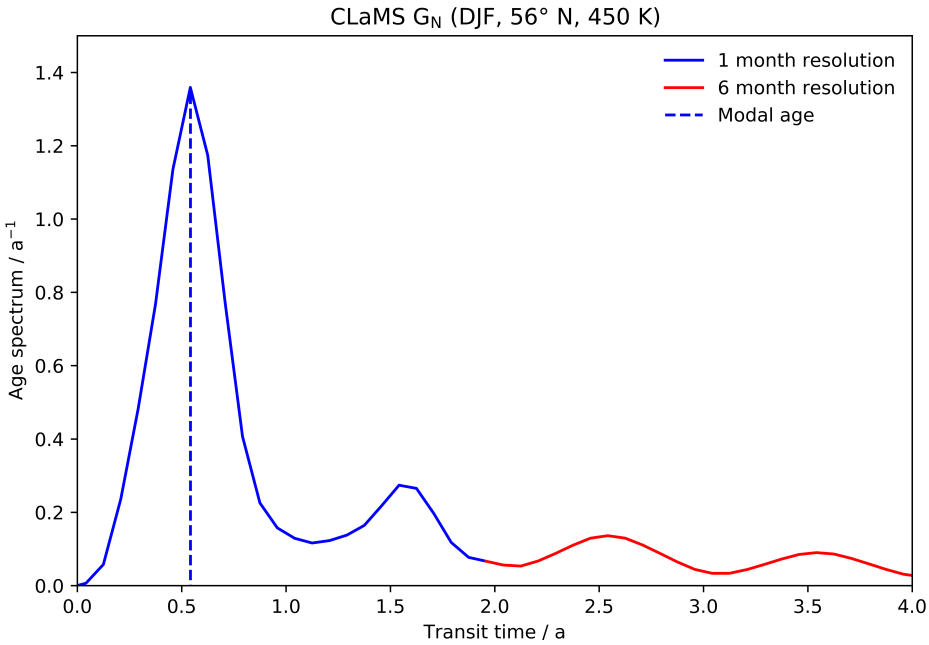

Figure 3.9: CLaMS age spectrum with variable transit time resolution
The figure shows an arbitrary normalized age spectrum with reference at the northern extratropical tropopause at 56° N and 450 K in DJF from CLaMS TpSim (see text for details). The blue part is simulated using a tracer set that consists of 24 pulses released every month, while the red section is retrieved using 20 pulse tracers triggered every six months in their source region. In postprocessing, each tracer set is turned into a separate age spectrum which are finally combined to form the PDF presented above. The red spectrum has been interpolated to a monthly resolution to shape a smoother curve. Modal age means transit time of the maximum.

The necessary meteorological input data for the simulations in this study, i.e, diabatic heating rates (Pommrich et al., 2014), come from the European Reanalysis Interim dataset (ERA Interim; Dee et al., 2011). The general framework of the two simulations in this thesis is similar to Ploeger and Birner (2016). Since raw output data of CLaMS are irregularly gridded due to its Lagrangian nature, the data are transformed in postprocessing onto a latitude-longitude-potential-temperature grid with a spatial resolution of $2^\circ \times 2^\circ$ and 37 θ-levels between 280 K and 3000 K. Both simulations run from January 1989 until December 2017. The data have a daily output frequency (12 UTC) and are finally evaluated as seasonal and zonal means for a period of 10 years (December 1999 – November 2009). Age spectra are implemented by inert trace gas pulses released consecutively at a certain predefined reference surface, just as for the EMAC simulation above (see section 3.2.2). Since it has been discovered in the first proof of concept of the inverse method that a pulse spectrum resolution of three months is insufficient for rapid transport processes around the tropopause, the CLaMS simulations pursue a different ansatz. Two separate sets of pulsed trace gases are included, which consist of 24 and 20 individual pulse tracers that are triggered monthly and semiannually respectively. After every pulse has been initialized once, they are gradually reset and re-initialized. The first set of pulse tracers thus provides very fine age spectra limited to two years transit time but with monthly resolution, while the second set offers a coarse resolution of six months but covers a period of ten years. The pulse tracer series are turned into proper age spectra with the BIER method (Ploeger and Birner, 2016) and combined afterwards so that a full age spectrum up to ten years transit time with variable resolution (monthly and semiannually) is established. An example of such spectrum is shown in figure 3.9 above for an arbitrary age spectrum referring to the northern hemispheric tropopause.

The coarse spectra are thereby interpolated for transit times where no pulse is present to smoothen their general appearance. Finally, all age spectra are extended to 50 years transit time (Ploeger and Birner, 2016), since Hauck et al. (2019) could show that this amount is sufficient to retrieve related moments correctly. All of these postprocessing steps for pulse age spectra are fully automated using the newly established Combined Age spectra Retrieval Procedure (CARP) in IDL.
The first simulation is called TpSim, where all inert pulse tracers are initialized within a small band between the WMO tropopause and 10 K below in the three defined sections (northern, tropical, and southern) visible in figure 3.7 above. These trace gases have a mixing ratio of 100 % upon release and are shaped as approximate Dirac delta distributions. Additionally, three inert species are released constantly with a mixing ratio of 100 % in each section and provide a tool to retrieve the origin fractions from the simulation directly provided that the simulation is given enough settling time. All these tracers will be forced to zero if entering one of the remaining source regions and forced to 100 % if re-entering their source region. In that way, mass conservation is satisfied. For the second simulation, the setup is almost identical, but the specified source regions of all trace gases are shifted to the Earth's surface conserving the separation between the northern, tropical, and southern section. This simulation is therefore named SurfSim. Finally, both simulation setups feature also ten trace gases with predefined spatially invariant chemical lifetimes. These radioactive tracers provide an identical idealized test environment as in the EMAC model setup and are constantly released globally either at the tropopause (TpSim) or the Earth's surface (SurfSim) with a mixing ratio of 100 %. The total number of these species has been significantly reduced compared to the first proof of concept because it has been shown that ten trace gases are sufficient for a proper inversion (Hauck et al., 2019). Lifetimes hereby range from 1 month to 118 months, but in steps of 12 months to still cover the full period of ten years transit time of the pulse age spectrum. The numerical principle of the inversion now uses only Ridders' method for this new proof of concept and is slightly improved, since for very small mixing ratios, which could occur when applied to real measurement data, the MPE is no suitable metric and shows extremely large values that distort the inversion outcome. Therefore, the new bias metric of the symmetric signed percentage bias (SSPB; Morley et al., 2018) is introduced, which uses a median statistic and the natural logarithm to smoothen the direct influence of mixing ratio outliers. Still, it is a percentage measure with positive and negative values and thus quite comprehensible. It is given as

$$SSPB = \operatorname{sgn}\left(\operatorname{Md}\left(\ln\left(\frac{\chi_{i,ref}}{\chi_i}\right)\right)\right) \cdot \left(\exp\left(\left|\operatorname{Md}\left(\ln\left(\frac{\chi_{i,ref}}{\chi_i}\right)\right)\right|\right) - 1\right), \tag{22}$$

where sgn() is the sign function and Md() the median. Application of the SSPB also implies that the ratio $R(\vec{x}, t)$ (equation (17)) is not used anymore and absolute mixing ratios $\chi_i(\vec{x}, t)$ are preferred. Additionally, Newton's method is excluded from the numerical implementation of the inverse method since Ridders' method proved sufficient during the first proof of concept. With this setup, a robust inversion of the three decoupled equations (21), one for every reference section, is conducted. Selected key results of the second proof of concept are presented in the next section.

3.3.3 Proof of concept and limitations

Key findings

This section presents a summary of results to stress the improved performance of the extended inverse method in proximity to the extratropical tropopause. For a comprehensive assessment of all results please see Hauck et al. (2020). In figure 3.10 age spectra from the CLaMS TpSim pulse tracers (solid) and extended inverse method (dashed) are presented at 56° N and 370 K. This location is very close to the tropopause and thus within the threshold of 1.5 years mean AoA where most problems were encountered in section 3.2.3. These spectra now refer to the northern hemispheric tropopause section, that has been defined above. Transit times below 1 month have been omitted

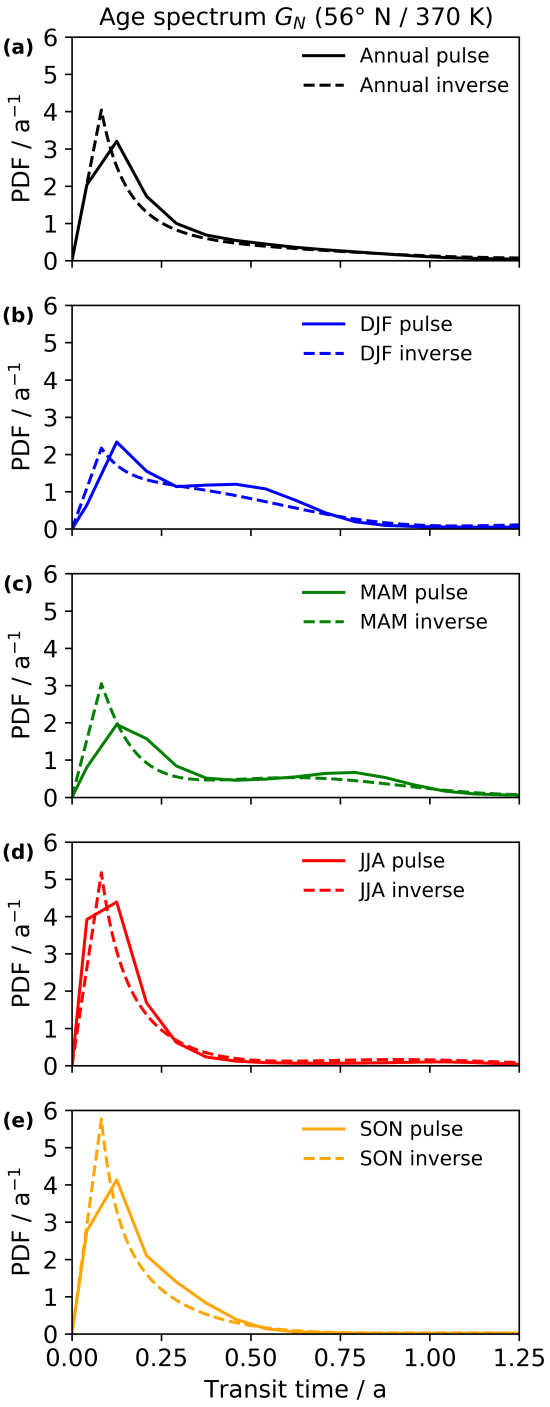

Figure 3.10: Age spectra at 56° N and 370 K of the proof of concept with the CLaMS TpSim simulation

Shown are age spectra with reference at the northern hemispheric tropopause section at 56° N and 370 K in CLaMS TpSim using pulse tracers (solid line) and the extended inverse method (dashed line). Panel (a) shows annual mean, while the remaining panels ((b) through (e)) are the four seasons of the year. The figure is taken from Hauck et al. (2020).

in all spectra as this is the lowest possible resolution the described model setup allows. It is evident that the inversion performs very well, since all seasonal and annual mean inverse spectra match the pulse spectra robustly. The annual mean inverse spectra (panel (a) in figure 3.10) exhibit only one prominent mode at transit times consistent with the pulse spectra, which is an indicator that the newly implemented seasonal cycle cancels out on average correctly. Nevertheless, the peak of the inverse spectrum is slightly higher and shifted to smaller transit times compared to the pulse spectra. The right-tilted shape of the pulse spectrum is an indicator that the apex is cut by the pulse resolution and therefore results in an artificially diminished amplitude of the spectrum. On the seasonal scale, the inverse method performs similarly well in all seasons. For the DJF and MAM spectrum, a primary and secondary mode are visible, while the spectra in JJA and SON appear mostly monomodal. The timing of all maxima and minima as well as their amplitude is consistent between inverse and pulse spectra. This is expected since the scaling factors are derived from CLaMS pulse age spectra and a quantitative comparison of the timing of the imposed maxima and minima is strongly aggravated. However, the scaling factors are approximated using integrated and globally cumulated CLaMS age spectra so that no information about the shape of the spectra is transferred to the inverse method. The qualitatively good agreement between the inverse and pulse age spectra implies that the underlying monomodal age spectrum is well-retrieved during the inversion or otherwise the scaling would nevertheless lead to deviating inverse age spectra. Since the seasonality of entrainment is in accordance with different studies in the past (e.g., Bönisch et al., 2009; Yang et al., 2016), the retrieved scaling factors are a robust estimator for higher maxima and minima in the inverse age spectra. The emerging discrepancies during MAM and SON are most likely caused by the transit time resolution of the pulse spectra that clips off parts of the apex loosing important information about the shape of the peak. An increase of the pulse resolution in future studies will further advance the resolution of the peak. On the right flank of the peaks, the

inverse age spectra appear systematically lower than the pulse spectra reference, which could again be related to the prescribed inverse Gaussian shape. Nevertheless, the decoupled inversion of age spectra for the northern hemispheric tropopause section performs very well and the imposed seasonal cycle can again contribute to an even better alignment, especially for seasons where obvious secondary maxima are present (e.g., here DJF and MAM). In the southern hemisphere (56° S and 370 K – not shown), the corresponding inverse spectra with reference at the southern tropopause section exhibit an equivalent performance and retrieve the model pulse spectra in similar fashion as in the north. The same applies to the southern seasonal scaling factor that improves the inversion significantly.
For a global scale comparison of the inverse method's performance, retrieved mean AoA is considered in a similar fashion as above and presented as absolute annual mean values and percentage seasonal differences in figure 3.11 for pulse and inverse spectra. Consistently, the first 30 K above the tropopause are omitted and treated as tropospheric transition region (Hoor et al., 2004) as specified for the EMAC simulation. Since for different parts of the stratosphere other age spectra with distinct references surfaces become important, an evaluation of composite mean AoA is useful so that the underlying age spectra are weighted by the respective origin fractions. However, the focus of the analysis should be on the seasonality in mean AoA, which implies that the seasonality of the origin fractions must be disregarded in some fashion without losing the weighting information. A simple yet efficient strategy is to use solely annual mean origin fractions for all age spectra, which translates into an approximate composite age spectrum as

$$G(\vec{x}, t, t') \approxeq \overline{f_N}(\vec{x}, t) \cdot G_N(\vec{x}, t, t') + \overline{f_T}(\vec{x}, t) \cdot G_T(\vec{x}, t, t') + \overline{f_S}(\vec{x}, t) \cdot G_S(\vec{x}, t, t'). \tag{23}$$

Here, $\overline{f_i}(\vec{x}, t)$ indicates the annual mean state. In that way, the age spectra are still weighted in a correct way and keep their uninfluenced seasonal features that the inverse method shall retrieve. The comparison reveals that inverse mean AoA and pulse mean AoA agree quite well qualitatively with respect to structure and strength, although the inverse mean AoA is found to be systematically larger (e.g., above the south pole).

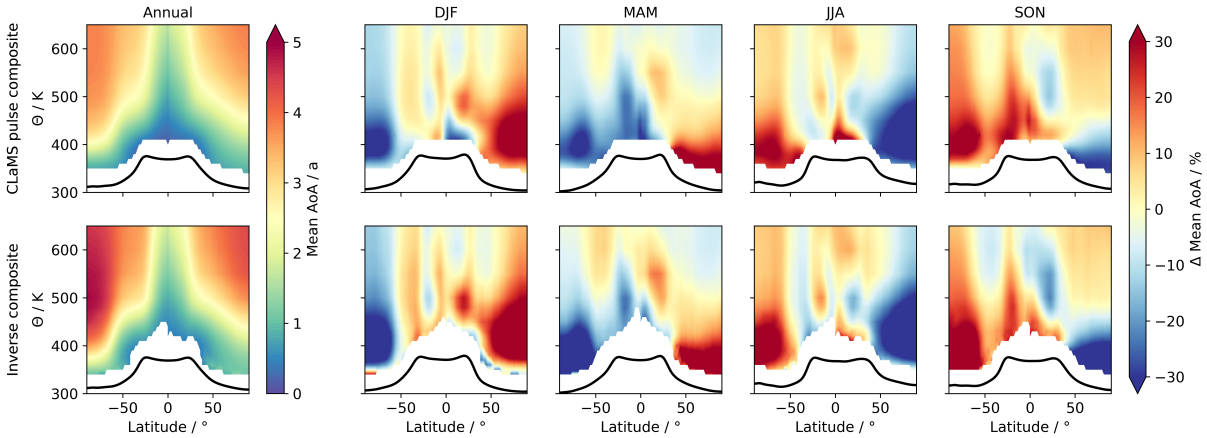

Figure 3.11: Cross-sections of composite mean AoA on annual and seasonal scale within the CLaMS TpSim simulation Shown is composite mean AoA (see text for details) computed using origin fractions with pulse age spectra (top row) and inverse age spectra (bottom row) as absolute annual mean values (left column) and relative percentage differences to the annual average (remaining four columns). The solid black line represents the WMO tropopause. To focus on the seasonality of mean AoA annual mean origin fractions are used for the computation of the composite mean AoA. The figure is taken from Hauck et al. (2020).

This behavior is consistent with the inverse mean AoA in EMAC, which is also biased towards larger values, and might also be caused by deviations in the inferred inverse age spectra tails and peaks. Quantitatively, the averaged bias of annual inverse mean AoA relative to pulse mean AoA is found to be +13.8 % below the threshold of 1.5 years mean AoA (see section 3.2.3) and +12.4 % above, while for the EMAC proof of concept this bias was +44.3 % below the threshold and +13.3 % above. This stresses the general benefit of the conducted extension despite the increased numerical effort

to retrieve three decoupled age spectra. Some of these improvements might also be related to the enhanced transit time resolution of the pulses.
On the seasonal scale it is apparent that the structure and sign of all seasonal variations in mean AoA are now well-emulated by the extended inverse method throughout the stratosphere. The strength of the variability is also derived robustly and only some scattered spots of overestimation are detected (e.g., DJF in the north above 400 K). This might be related to the inverse Gaussian shape that is certainly not a perfect estimate of the underlying age spectrum of transport at any stratospheric location. The strongest improvements are found in the northern lower stratosphere, the identified critical region for the age spectra with tropical origin. Additional consideration of age spectra with reference at the southern and northern tropopause proves to be a reasonable and well-functioning extension to describe transport correctly. Especially in MAM and SON, the seasonality is now accurately reproduced by the inverse method and no inverted patterns emerge anymore. Therefore, the inverse method in its extended form is capable of retrieving reliable age spectra throughout a spatially wide scale if all parameters for the inversion are known perfectly well. Interestingly, the investigation of CLaMS origin fractions (not shown) reveals that the relevance of cross-hemispheric age spectra, e.g., $G_N(\vec{x}, t, t')$ in the southern hemisphere and vice versa, is negligibly low. This reduces the numerical effort for the application of the inverse method, as certain spectra can be omitted depending on the considered location. For the final application of the method, some problems and limitations still have to be discussed in the following section as all input parameters (mixing ratios and chemical lifetimes) are only known to some limited extent and often prone to large uncertainties.

General limitations

Although the extension of the inverse method has proven to be valuable, there are certain problems and limitations that have to discussed and require further modifications or data when applying the method to observations. The prescribed inverse Gaussian shape might be a matching approximation in many stratospheric locations, but could lead to scattered deviations, in particular for the cross-hemispheric age spectra. However, as data are highly limited and prone to large uncertainties, the inverse Gaussian function is considered a proper assumption especially as the CLaMS simulation has shown that the influence of cross-hemispheric transport is vanishingly low. The introduced origin fractions are a handy toolset to study variability in stratospheric transport in a comprehensible way, but require a model simulation to be retrieved reliably. Although the inverse method offers a convenient one parameter inversion to derive age spectra with distinct reference regions reasonably well, these resulting spectra are always normalized and cannot be superimposed without the corresponding origin fractions to form the composite age spectrum. These normalized inverse age spectra already provide insight into stratospheric transport strength and structure, but for a thorough analysis including the relative influence of the origin regions, the origin fractions are inevitably required. This also implies that the direct influence of model data can be minimized, yet not excluded completely as some information from models has to be provided for the inverse method.
The largest factor of uncertainties is the chemical lifetime of the trace gases considered for the application. Since this quantity has been defined as transit-time-dependent $\tau_i(\vec{x}, t, t')$, it is not comparable to approximated global or local lifetimes for the species that have been in the focus of multiple past studies. There are two possible options to retrieve the chemical lifetime that might be applicable for the purpose of this thesis. The first one involves a third simulation with a global chemistry climate or chemistry transport model, where the desired chemically active trace gases are released as pulses equivalent to the inert trace gas pulses in the EMAC and CLaMS simulation above. If these pulse series are then transformed into age spectra, the transit-time-dependent lifetime will be directly computed using the pulse age spectrum from chemically active and inert substances. This method has been applied by Plumb et al. (1999) and recently by Fritsch et al. (2020). However, this implicates a strong model influence, since the derived observationally based age spectra are based on modeled age spectra and therefore strongly questions their independence. A promising alternative has been proposed by Holzer and Waugh (2015), where for very long-lived species a statistical

approach has been established to retrieve chemical lifetimes and age spectra in a successive way based on first guesses of the chemical lifetime. In theory, this should be transferable to short-lived trace gases considering proper first guess values and a Monte Carlo simulation to include as many uncertainties as possible into the inversion. This is a favorable approach that follows the aim of this thesis to reduce the amount of model data for the inversion as much as possible. It is explained together with the necessary modifications in section 3.4.2 below.

3.4 Inverse method – application

The following sections summarize concepts, methods, data, and key results that are published in detail in:
Keber, T., Bönisch, H., Hartick, C., Hauck, M., Lefrancois, F., Obersteiner, F., Ringsdorf, A., Schohl, N., Schuck, T., Hossaini, R., Graf, P., Jöckel, P., and Engel, A.: *Bromine from short–lived source gases in the extratropical northern hemispheric upper troposphere and lower stratosphere (UTLS)*, Atmospheric Chemistry and Physics, 20, 4105-4132, DOI: https://doi.org/10.5194/acp-20-4105-2020, 2020

and

Hauck, M., Bönisch, H., Hoor, P., Keber, T., Ploeger, F., Schuck, T., and Engel, A.: *A convolution of observational and model data to estimate age of air spectra in the northern hemispheric lower stratosphere*, Atmospheric Chemistry and Physics, 20, 8763-8785, DOI: https://doi.org/10.5194/acp-20-8763-2020, 2020

3.4.1 Data basis

Aircraft data

Figure 3.12: The high altitude and long range (HALO) research aircraft at Shannon Airport (Ireland) in September 2017

The essential data for the application of the inverse method are in situ observations of the trace gases in table 2.1 gained during two measurement campaigns with the high altitude and long range (HALO) research aircraft (see http://www.halo.dlr.de). HALO is based on a commercial Gulfstream G550 airplane that has been modified to offer space for a variety of scientific instruments. This modular payload makes HALO the perfect basis for the airborne investigation of atmospheric processes in the troposphere and even lower stratosphere, since it can reach altitudes of up to 15 km with a range of more than 10000 km at the same time (information taken from http://www.halo.dlr.de – last checked 01.04.2020). A picture of HALO is shown in figure 3.12 above.
The first campaign is a combination of the three projects Polar Stratosphere in a Changing Climate (POLSTRACC – see http://www.polstracc.kit.edu), Gravity Wave Life Cycle Experiment (GW-LCYCLE), and Seasonality of Air mass transport and origin in the Lowermost Stratosphere using HALO aircraft (SALSA), which are hereafter abbreviated as PGS. The PGS campaign took place in two phases from December 2015 until early February 2016 and again from late February 2016 until late March 2016. Its focus was on the observation of dynamical and chemical processes in the Arctic lowermost stratosphere and especially around the polar vortex and associated changes due to climate change. Mission base was set in Kiruna, northern Sweden. A detailed summary and overview of PGS is provided in Oelhaf et al. (2019). The second campaign was Wave-driven ISentropic Exchange (WISE – see https://www.wise2017.de) that took place from mid September 2017 until late October 2017 with focus on isentropic exchange processes between the upper troposphere and lower stratosphere and their influence on both dynamics and chemistry of the atmosphere in that specific region. Mission base for WISE was set in Shannon at the western coast of Ireland. All HALO flight trajectories during PGS and WISE are illustrated in figure 3.13.

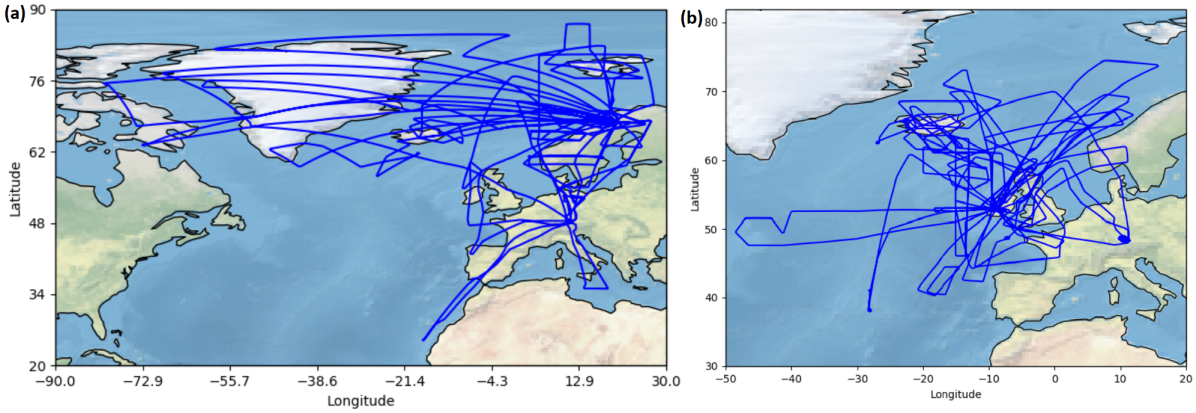

Figure 3.13: Flight tracks of HALO during the PGS and WISE campaigns
These graphics, which have been combined from Keber et al. (2020), illustrate all flight trajectories of the HALO aircraft during the PGS (panel (a)) and WISE campaign (panel (b)). Mission base for PGS was Kiruna, Sweden, while for WISE the base was situated in Shannon, Ireland. The accumulation of flight tracks in south-eastern Germany corresponds to HALO's home base at the German Aerospace Center's airfield in Oberpfaffenhofen.

Aboard HALO, the halogenated trace gas data for this thesis (see table 2.1) were retrieved during both PGS and WISE by the dual-channel Gas Chromatograph for Observational Studies using Tracers - Mass Spectrometer (GhOST-MS). It is a high-performance instrument and consists of an isothermal channel coupled with an Electron Capture Detector (ECD) for simultaneous measurements of SF_6 and CFC-12 every minute and a temperature-programmed channel with a quadrupole mass spectrometer (MS) to measure a variety of halogenated (mostly brominated) trace gases every four minutes. The setup of the ECD channel is similar to that for past research campaigns involving GhOST (e.g., Engel et al., 2006; Bönisch et al., 2009, for the SPURT campaign), while the set-up of the quadrupole channel is comparable to Sala et al. (2014). For a detailed description of the GhOST-MS set-up for PGS and WISE as well as related characteristics please see Keber et al. (2020) in the attachment of this thesis. GhOST-MS data are reported on the measurement scales SIO-05. The remaining species,

N_2O, was measured aboard HALO with two different instruments for PGS (TRIHOP; Schiller et al., 2008) and WISE (UMAQS; Müller et al., 2015). Both are infrared absorption quantum laser cascade spectrometers operated by the University of Mainz. The set-up of TRIHOP for the PGS campaign is explained in detail in Krause et al. (2018) and that of UMAQS for WISE is given in Kunkel et al. (2019). N_2O data are reported on the measurement scale WMO 2006a (Jens Krause and Armin Jordan, private communication, 2019).
All of the above described data are interpolated onto a spatial grid of potential temperature difference to the tropopause and equivalent latitude (Allen and Nakamura, 2003) with a bin size of 5 K and 5 ° respectively. Tropospheric data are hereby omitted completely. Equivalent latitude is an important quantity for an analysis for stratospheric dynamics. It is an equal-area projection where data are sorted in each hemisphere by their associated potential vorticity values decreasing from the pole to the equator. Each potential vorticity value gets a new equivalent latitude value assigned to it according to the area this datapoint encompasses. The transformation to equivalent latitude therefore reduces spatial variability. Each grid box must consist of at least five datapoints otherwise it will be omitted and treated as missing data. The binned data are considered to be phase or campaign averages for PGS phase 1 and phase 2 as well as WISE. The standard deviation values for these measurement data, which are important later on (see section 3.4.2), are derived during the binning process.

Entry mixing ratio data

Now that the underlying stratospheric measurement data basis has been established, the entry mixing ratio time series for the relevant tropopause segments need to be derived to conduct the inversion. Since the spatial focus of both PGS and WISE is explicitly on the northern hemispheric lowermost stratosphere for which the CLaMS simulation TpSim has shown that cross-hemispheric transport is circumstantial, entry mixing ratio time series for all relevant trace gases have to be constructed only for the tropical and northern extratropical tropopause regions. To ensure consistency between the CLaMS model simulations above and the observations, tropopause refers here also always to the WMO definition, although a PV-based tropopause can be a more suitable choice for dynamical studies. The time series should reach back from November 2017 to January 1960 as monthly means so that retrieved age spectra extend at least over a transit time range of 50 years like in the model proof of concepts. However, this is quite problematic since there are no consistent measurements available at the tropopause or at least at the Earth's surface that range from 1960 until late 2017. That affects mostly the six long-lived species in this study (SF_6, N_2O, CFC-12, halon 1211, halon 1301, and CH_3Br) as these exhibit a strong temporal trend over the last half a century. In particular the CFCs and halons have been used extensively in the past until their phase-out in the Montreal protocol. The five short-lived substances ($CHBr_3$, CH_2Br_2, $CHCl_2Br$, $CHClBr_2$, and CH_2ClBr) do not share this trend and it can be assumed that these have a rather constant mixing ratio in time. To overcome the limited data and approximate entry mixing ratios for all relevant trace gases, different datasets and assumptions are considered.
While for the Earth's surface time series can be partly established using the mixing ratio data for the long-lived species of the Advanced Global Atmospheric Gases Experiment (AGAGE – see http://agage.mit.edu) as well as its two predecessors Global Atmospheric Gases Experiment (GAGE) and Atmospheric Lifetime Experiment (ALE) (see Prinn et al., 2018, 2019), no such broad data archive is available at neither the tropical nor the extratropical tropopause. For the tropical tropopause, however, averaged ALE/GAGE/AGAGE surface data from the two tropical stations Ragged Point in Barbados (RPB – 13° N, 59° W) and Cape Matatula in American Samoa (SMO – 14° S, 171° W) can be transformed in a straightforward way into mixing ratios at the tropopause by lagging the complete data by two months with an uncertainty of 0.5 months. This ansatz has been applied by Andrews et al. (1999) for CO_2 data with promising outcome. Since all global tropospheric lifetimes of these six species are considerably larger than the lag time of two months (see SPARC (2013) for the lifetimes), chemical loss between the tropical surface and the tropopause is negligible. The

ALE/GAGE/AGAGE data does not cover the complete period form 1960 until 2017 so that missing parts are extended backward in time with data from the Representative Concentration Pathways (RCP; Meinshausen et al., 2011). These are aligned to the ALE/GAGE/AGAGE data so that they match the existing measurement data as close as possible. The ALE/GAGE/AGAGE halogenated species are reported on the SIO-05 scale and N_2O on both the SIO-98 and SIO-16 scale, which are treated as comparable to WMO 2006a in this thesis (World Meteorological Organization, 2018). The annual mean mixing ratios of the short-lived species at the tropical tropopause section are taken directly from table 1-4 in Engel and Rigby (2019) for the upper tropical tropopause layer (TTL), since the potential temperature interval best matches the range of the WMO tropopause in the tropics.

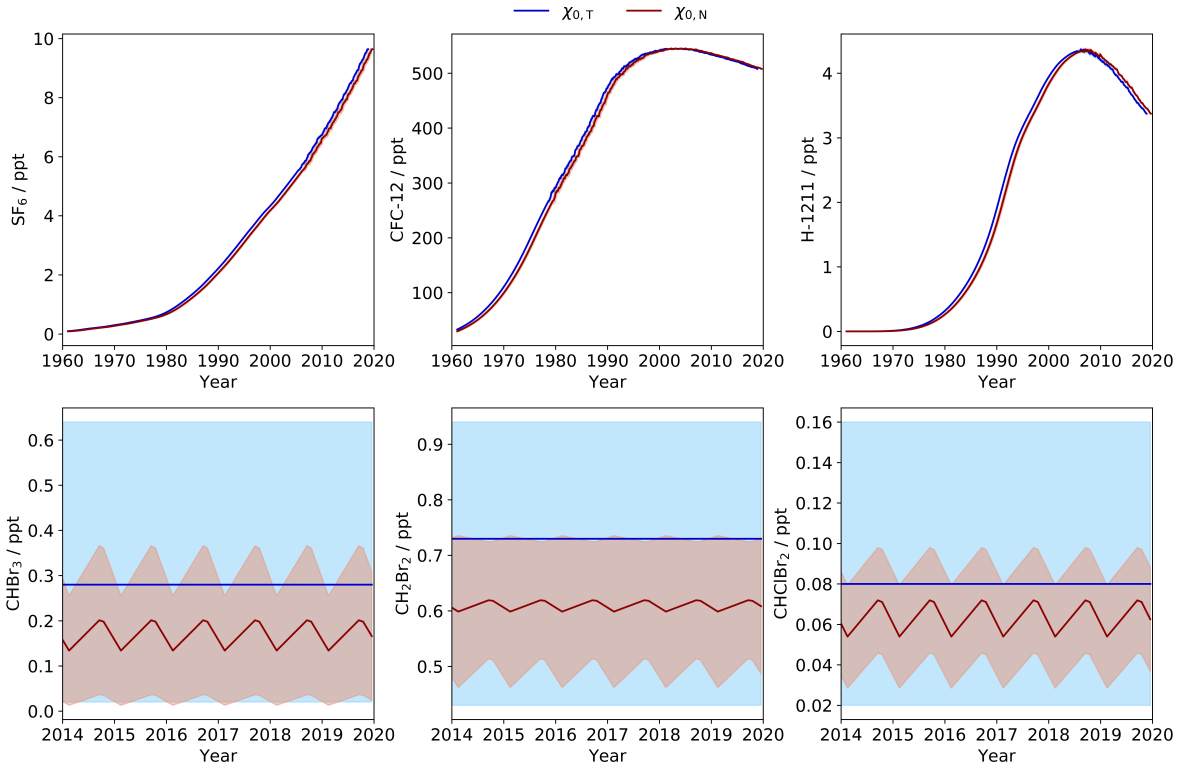

Figure 3.14: Entry mixing ratio time series at the northern and tropical tropopause sections for six selected species
This figure shows the derived entry mixing ratio time series at the tropical (blue) and northern extratropical tropopause section (red) for the selected species SF_6, CFC-12, halon 1211, $CHBr_3$, CH_2Br_2, and $CHClBr_2$ together with their uncertainty range (colored shading). In the upper three panels ALE/GAGE/AGAGE and RCP data are used, whereas in the lower three panels data from PGS and WISE (red) and from Engel and Rigby (2019) are applied (blue). For the bottom three species, only a snapshot is shown as it is assumed that no temporal trend is present.

The entry mixing ratios at the northern extratropical tropopause section are harder to retrieve. Air parcels in this layer are composed of an irreversible mixture of fresh tropospheric air and older stratospheric air where constituents have already been processed. Therefore, a straightforward lag approach is not as simple as for the tropical region, especially since air parcels at the extratropical tropopause likely show a variety of different origins. The annual mean origin fractions of the CLaMS SurfSim simulation give insight into the most important source region so that the available ALE/GAGE/AGAGE data in that region are utilized. An analysis reveals that the tropical surface constitutes the predominant source region with a corresponding origin fraction of 88 ± 4 % and a mean AoA of circa 1 ± 0.25 years on annual average. The entry mixing ratio can thus be approximated by lagging the tropical mixing ratio time series above by one year. While almost all long-lived species exhibit a global tropospheric lifetime larger than one year, for CH_3Br that lag approach is problematic due to its estimated lifetime of circa 1.6 years (table 5.6 in SPARC (2013)). However, the dominant sink reaction of CH_3Br is its combination with the hydroxyl radical where the reaction speed depends critically on the ambient temperature. With the rapidly decreasing air temperature in the mid and

upper troposphere, the actual local lifetime should be far larger so that chemical loss is again treated as negligible. The short-lived species are taken directly from PGS and WISE measurements averaged between 30° N and 90° N and in an interval of 30 K between the tropopause and above. This rather wide vertical range has been applied to account for the tropospheric character of that region (Hoor et al., 2004) and to include the strong seasonal variability of the WMO in the extra-tropics as well as its general deviation from the dynamical (i.e., PV-based) tropopause. During the inversion, these 30 K are always omitted just like in the proofs of concept. The retrieved entry mixing ratios from PGS and WISE are then elongated to form a full time series from 1960 until 2017. Six selected time series are shown in figure 3.14.
It is apparent that the extension of ALE/GAGE/AGAGE data with RCP data works properly and the resulting time series appear continuous with no obvious inconsistencies. In the next section, a statistical concept for the inversion is introduced which requires an estimate of the standard deviation of these mixing ratio time series. For the extended ALE/GAGE/AGAGE data this quantity combines the measurement error provided together with the data and the uncertainty when the standard deviation of the lag time is applied. Nevertheless, the estimated error of the time series is quite small (see figure 3.14). This is done for the northern and tropical tropopause section. In case of the short-lived species, the error range given by Engel and Rigby (2019) and the standard deviation of the averaged PGS and WISE data is used for the tropical and northern extratropical tropopause respectively. With these estimations, a proper statistical inversion should be realizable in the next section.

3.4.2 Statistical inversion concept

With the above introduced entry mixing ratio time series for all substances at the tropical and northern tropopause section, the chemical lifetime remains the only unknown parameter that has to be gauged in some way to apply the inverse method to the data from PGS and WISE. Unfortunately, this is no simple task as the explicit dependency on the transit time would require some prior information about the transport pathway, which could only be provided directly by a model simulation. As mentioned above, the goal of this thesis is to derive age spectra from observations relying on model data as little as possible. A probable solution is the concept by Holzer and Waugh (2015), where constant global tropospheric lifetimes for a small number of preselected long-lived trace gas species are applied to gain a prior estimate of the age spectrum. This initial guess is then tainted with statistical uncertainties to derive effective chemical lifetimes for the remaining substances, which are then convoluted with some of the preselected trace gas information to estimate the final age spectrum. This ansatz has the important benefit that a variety of statistical uncertainties can be considered using only trace gas information and some coarse approximation of the chemical lifetime. To use it with the implemented formulation of the inverse method in this thesis, equation (21) has to be modified, where the transit-time-dependent lifetime is replaced by a new quantity that characterizes chemical loss along all relevant transit times effectively. These scalar lifetimes are named effective lifetimes $\tau_{i,eff}(\vec{x}, t)$ from now on and can be implemented as follows

$$\chi(\vec{x}, t) = \int_0^\infty \chi_{0,i}(t - t') \cdot e^{-\frac{t'}{\tau_{i,eff}(\vec{x},t')}} \cdot G_i(\vec{x}, t, t') \cdot \omega_i(t') \cdot n_i(\vec{x}, t) \cdot dt'. \tag{24}$$

Effective lifetimes are rather abstract and always need to be given together with their underlying age spectrum. This also indicates that these values are not comparable to known global or local lifetimes. The inverse method's algorithm can now be applied to derive either the transport parameter $K_i(\vec{x}, t)$ if the effective lifetime $\tau_{i,eff}(\vec{x}, t)$ is known (K-inversion), or to invert the effective lifetime for every substance individually if the age spectrum is estimated to some extent (τ-inversion). The hereafter introduced modified version of the method by Holzer and Waugh (2015) is called Monte Carlo Cross-Validation (MCCV) and considers not only mixing ratios of long-lived, but also short-lived species to derive a robust approximation of the age spectrum. The principle of the MCCV is illustrated in figure 3.15. First, a subset of three species is sampled from the full trace gas set and always consists of the pseudo-inert SF_6 (orange in figure 3.15), one pseudo-randomly chosen species of the

long-lived constituents (blue group in figure 3.15), and one pseudo-randomly selected trace gas from the short-lived group (green in figure 3.15). With this subset and the initial guess for the effective lifetimes for the substances in the set, the prior guess of the age spectrum is derived. To account for the very uncertain nature of this method, systematic errors are included for the effective lifetimes ($\pm$50 %) and all (entry) mixing ratios ($\pm$1 standard deviation – see section 3.4.1) during the first inversion and get selected pseudo-randomly under a uniform distribution. This first estimate of the age spectrum is then applied in a τ-inversion, where for every remaining species the effective lifetime is derived with the same pseudo-random errors included. These two steps are then repeated 2000 times to form solid statistics. This number of repetitions is an empirical value for which the results of repeated MCCV simulations did not change anymore. After all repetitions have been successfully completed, the median effective lifetime for each species is computed and implemented in a final K-inversion where the desired age spectrum is derived. Since SF_6 is present in every initial subset, no effective lifetime is retrieved for it and thus it is excluded from this final K-inversion. This also ensures that its direct influence onto the inversion is restricted to the prior guess of the spectrum, which is then convoluted with additional information from the remaining trace gases involved. To gauge the uncertainty of these retrieved lifetimes, the 75th and 25th percentile values are chosen as upper and lower error margin respectively.

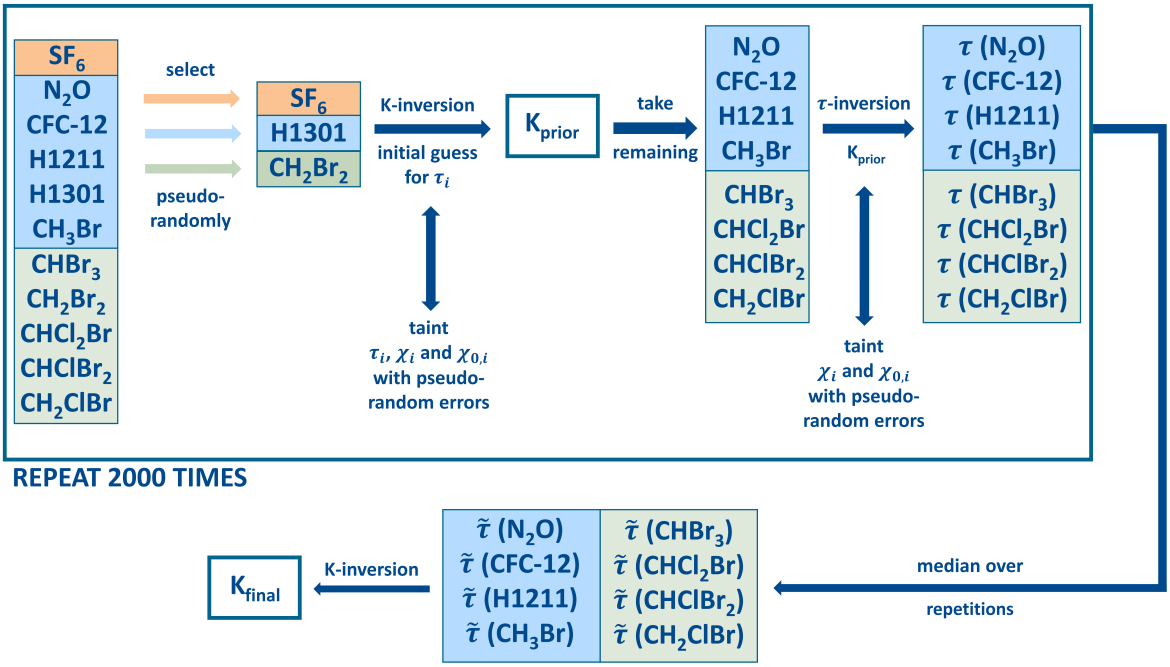

Figure 3.15: Schematic of the Monte Carlo Cross-Validation (MCCV)
The figure illustrates the basic idea behind the applied Monte Carlo Cross-Validation to derive age spectra and effective chemical lifetimes (see text) consecutively. The relevant trace gases are grouped according to their chemical lifetime into pseudo-inert (orange – SF_6 only), long-lived species (blue), and short-lived constituents (green). One gas from each group is chosen pseudo-randomly into a subset to invert a prior guess of the transport parameter $K_{prior}(\vec{x}, t)$ under consideration of pseudo-randomly selected errors for initial guess lifetimes and all mixing ratios. With the initial guess, the effective lifetimes for the remaining species that are not within the subset are retrieved numerically using Ridders' method. After 2000 repetitions, the median of the effective lifetimes is used in a final inversion to retrieve the transport parameter $K_{final}(\vec{x}, t)$ and the desired age spectrum $G_{final}(\vec{x}, t, t')$. SF_6 is only present in each initial subset and thus excluded from the final inversion.

Although this technique should lead to a robust approximation of the age spectrum considering only trace gas mixing ratios from observations, the performance hinges on a good first guess of the effective chemical lifetimes for each tropopause section. For SF_6 the choice is quite trivial as its main sink is situated in the mesosphere and thus mainly effective at very large transit times so that a global lifetime should be sufficient. Therefore, the refined value given by Ray et al. (2017) is applied globally. In case of the short-lived species, annual mean local lifetimes in the tropics and extra-tropics

are implemented as first guess and taken from table 1-4 in Carpenter and Reimann (2014). Finally, for the long-lived species a different strategy is pursued. Each initial lifetime for these trace gases is set to 10 % of the global stratospheric lifetime given in table 5.6 of SPARC (2013), to account for the fact that the stratosphere amounts to only 10 % of the total atmospheric mass burden (Volk et al., 1997). Each chosen initial guess is presented in table 2 of Hauck et al. (2020). Due to the rather larger statistical errors, it might occur that no median effective lifetime can be inferred so that in this seldom case the substance is excluded from all further processing steps.

3.4.3 Evaluation of campaign-averaged age spectra and moments

This final section illustrates prime aspects from the application of the inverse method to mixing ratio data of chemically active trace gases gained during PGS and WISE. The focus is hereby on campaign-averaged spectra and related moments. A full discussion of results can be found in Hauck et al. (2020), where also spatial distributions of mean AoA are analyzed.

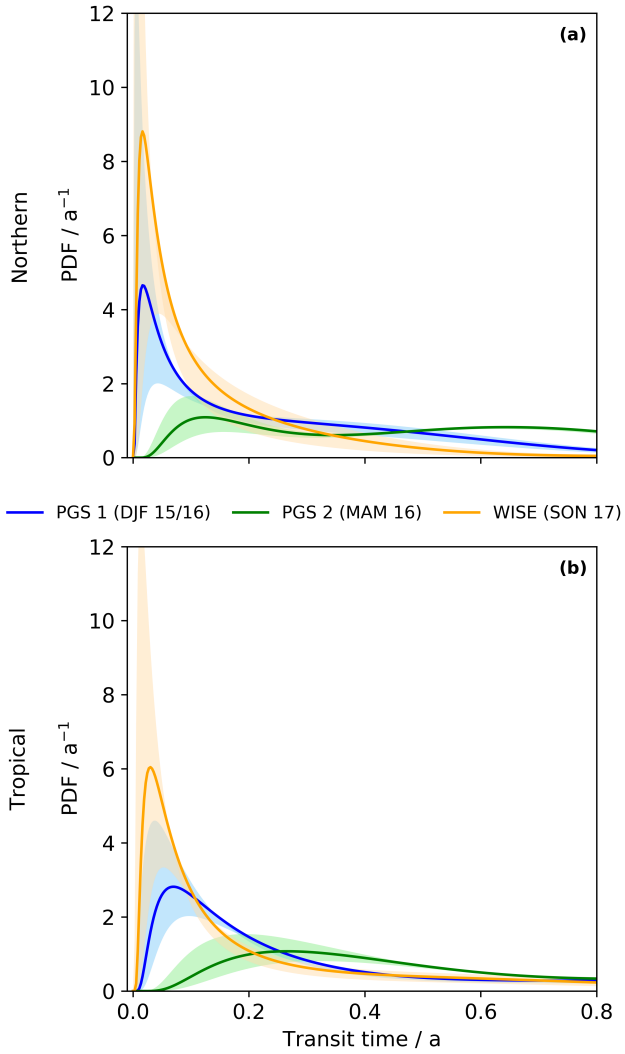

Figure 3.16: Campaign-averaged age spectra for the PGS and WISE campaign
Illustrated are campaign-averaged inverse age spectra for PGS phase 1 (blue), phase 2 (green) and WISE (orange) together with their retrieved uncertainty range from the Monte Carlo simulation (colored shadings – see section 3.4.2). Panel (a) gives age spectra with origin at the northern hemispheric tropopause section, while spectra in panel (b) refer to the tropical tropopause. The figure is taken from Hauck et al. (2020).

These mean AoA cross-sections for both tropical and northern extratropical reference surface come out to be quantitatively reasonable with lower values in the tropics and an increase with altitude and equivalent latitude. Minimal values are found during WISE, while the maximum mean AoA shows up during PGS phase 2, again for tropical and northern tropopause section. This implies that fresh tropospheric air has entered the midlatitude lowermost stratosphere through both tropopause sections predominantly in late summer and early fall (i.e., WISE), which is consistent with findings of previous studies (e.g., Bönisch et al., 2009) and most probably related to the weak subtropical jet stream during summer in the northern hemisphere that allows this entrainment of young air. This is also in accordance with the seasonality in Yang et al. (2016), where the subtropical jet stream is identified as important factor for entrainment across the extratropical tropopause in both hemispheres at lower latitudes. Although the cross-sections of mean AoA with tropical and northern extratropical origin appear very similar, this is not caused by the inverse method, as an comparison with TpSim data interpolated onto HALO flight tracks reveals (see the supplement to Hauck et al. (2020)).
In order to analyze derived inverse age spectra explicitly, the campaign-averaged spectra for PGS phase 1, phase 2 and WISE are shown in figure 3.16. The campaign average is constructed by using only datapoints that are finite in PGS phase 1, phase 2, and WISE data to enable quantitative comparability. It is evident that the inversion of spectra from observational data performs significantly well with meaningful outcome, although the retrieved age spectra exhibit sharp primary modes and are only partly multimodal (e.g., blue line in panel (a) or green line in panel (b)). Inverse age spectra of tropical origin are found wider than that of extratropical origin, coherent with larger mean AoA for the spectra referring to the tropical tropopause that is visible on the wider spatial scale (not shown). The uncertainty range is found to be largest for the sharpest spectra (WISE) and decreases with amplitude. The largest apex, and therefore the most recent entrainment of fresh tropospheric air, is found shortly prior to WISE (circa half a month) for spectra of both tropical and northern extratropical origin.

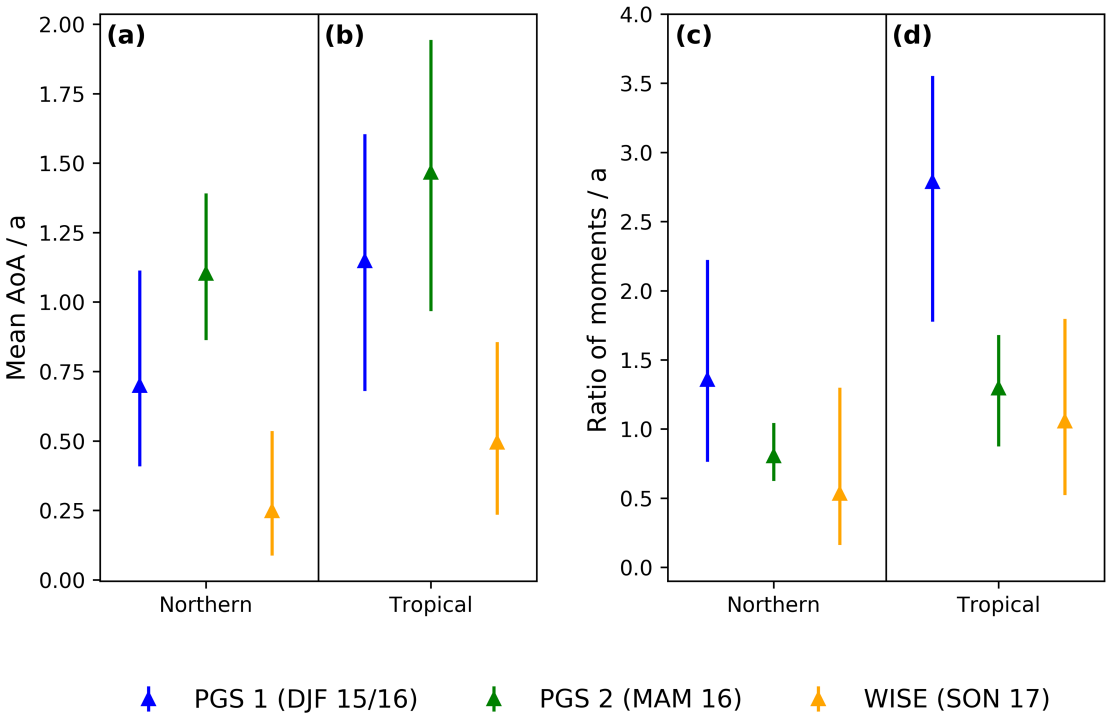

Figure 3.17: Mean AoA and ratio of moments for the campaign-averaged age spectra of PGS and WISE
Campaign-averaged mean AoA (panel (a) and (b)) and ratio of moments (panel (c) and (d)) values derived from the inverse age spectra with tropical and northern extratropical reference surface for PGS phase 1 (blue), phase 2 (green), and WISE (orange). The error bars denote the averaged uncertainty range from the Monte Carlo simulation (section 3.4.2). The figure is taken from Hauck et al. (2020).

Interestingly, the age spectrum for PGS phase 1 shows a similar behavior with a maximum of young air entering the stratosphere across both defined tropopause sections in late fall and early winter 2015/2016, albeit a bit weaker as indicated by the lower amplitude compared to the WISE spectra. The inverse age spectra for PGS phase 2 corroborate the detected intrusion of tropospheric air prior to PGS phase 1 and show a consistent maximum at transit times circa two months larger than for PGS phase 1. While for the WISE age spectra no clear secondary modes are present in each panel, especially the inverse spectra referring to the northern tropopause section exhibit a slight saddle point between approximately 0.2 and 0.75 years of transit time which are imposed by the newly introduced seasonal scaling factor. The pronounced peak of the WISE spectrum of tropical origin is quite unexpected since the maximum in the upward mass flux occurs during northern winter and should lead to a maximum at transit times that correspond to DJF. Yet, this behavior is already indicated by the related mean AoA distribution where a minimum was also detected during WISE and corroborates the theory that the weaker subtropical jet stream close to the tropical tropopause enables air entrainment that is then conveyed into the midlatitude lowermost stratosphere. As the resemblance between the spectra in panel (a) and (b) is again quite large, the interpolated CLaMS TpSim data have been considered and show that also CLaMS pulse spectra model this agreement so that a conceptual flaw of the inverse method is not the cause. This stresses the good performance of the novel inverse method even when considering observational data with large uncertainties. Again, see the supplement to Hauck et al. (2020) for this comparison.
For a thorough assessment of the age spectra, derived mean AoA and also the ratio of variance (i.e, second central moment) to mean AoA is analyzed and depicted in figure 3.17. Mean AoA with reference in the tropics comes out to be slightly larger in general than that with extratropical origin. Campaign differences for mean AoA are quantified in table 3.1 for inverse mean AoA (Inv), CLaMS pulse mean AoA from TpSim interpolated onto the flight trajectories (CLaMS) and for mean AoA based on SF_6 measurements during PGS from Krause et al. (2018). Despite the relatively large uncertainties of the inverse method, the shift of mean AoA of tropical (index T) and northern extratropical origin (index N) between PGS and WISE is consistent for all data with an increase of mean AoA from PGS phase 1 to phase 2 and a strong decrease from PGS phase 2 to WISE.

Table 3.1: Changes of campaign-averaged mean AoA between PGS phase 1 and 2 and between WISE and PGS phase 2 from different data sources

	PGS 2 - PGS 1	WISE - PGS 2
$\Delta\Gamma_N^{\text{Inv}}$	0.40 a	-0.85 a
$\Delta\Gamma_T^{\text{Inv}}$	0.32 a	-0.97 a
$\Delta\Gamma_N^{\text{CLaMS}}$	0.37 a	-0.80 a
$\Delta\Gamma_T^{\text{CLaMS}}$	0.28 a	-0.55 a
$\Delta\Gamma^{\text{SF}_6}$(Krause et al., 2018)	0.29 a	—

Data from Krause et al. (2018) indicates an aging process between the two PGS phases, which is correctly retrieved by the inverse method and also by CLaMS for both source regions. The minimum mean AoA with tropical and extratropical origin during WISE furthermore stresses the conclusion above that air entered promotedly through the tropical and northern tropopause in fall and is in accordance with the findings of Bönisch et al. (2009), who find minimum mean AoA based on SF_6 measurements for a different campaign (SPURT – see Hoor et al. (2004) for details on the campaign)

during fall. This agreement with previous findings corroborates the reliable performance of the inverse method and could make it a promising toolset that can be utilized for the analysis of stratospheric dynamics with chemically active trace gases in the future if retrieved uncertainties are taken into account.
The ratio of variance to mean AoA, which is also known as ratio of moments and shown additionally in figure 3.17, is an important parameter that has been and still is frequently applied to approximate the age spectrum with an inverse Gaussian PDF (e.g., Volk et al., 1997; Engel et al., 2002, 2009, 2017). Usually, approximations for this quantity follow the research by Hall and Plumb (1994), and use either 0.7 years (e.g., Engel et al., 2002, 2009, 2017) or 1.25 ± 0.5 years for observational studies in different latitudinal regions of the lower stratosphere below 30 km altitude. However, in Hauck et al. (2019) it has been shown that these values are probably underestimating the correct ratio of moments as the age spectra in the model study by Hall and Plumb (1994) are most probably restricted to a maximum transit time between 10 and 20 years (Timothy M. Hall, private communication, 2018). The analysis with a fully extended age spectrum reveals that the ratio of moments undergoes a seasonal cycle and that an annual average value of 2 years in the same geographical regions could be more appropriate according to the EMAC simulation above (Hauck et al., 2019). The derived inverse spectra from PGS and WISE therefore provide a good opportunity to reassess the assumptions using observations. It is evident that the applied 0.7 years and 1.25 ± 0.5 years are reasonable yet rough approximations for all campaign-averaged age spectra except during PGS phase 1 for the spectra of tropical origin where an even larger ratio of moments than 2 years is retrieved. The presented uncertainty ranges of the ratio of moments and also their seasonal variations are quite large so that a constant value might not be the perfect choice to estimate the age spectrum precisely. Additionally, the inverse method has shown in the proofs of concept that retrieved age spectra are generally wider than the pulse spectra reference, which feeds back squared into the ratio of moments so that the ratios in figure 3.17 could be systematically high-biased. For a precise estimation of age spectra, the direct derivation with newly introduced inverse method in this thesis is preferable over the approximation using the ratio of moments as it captures the direct transport signal from trace gas measurements and could be applied in future studies as an alternative.

4 Summary and outlook

Summary

This thesis outlined important steps and results in the development process of a novel inversion method to derive age of air spectra from measurements of multiple chemically active trace gas species. The focus of this process has been on an applicable and reliable technique that retrieves robust age spectra with comprehensive seasonal key features of stratospheric meridional transport while minimizing the required model data for the inversion and interpretation as much as possible. A large variety of different approaches to achieve this task have been postulated in the past, which have been discussed in detail and considered with regard to their advantages and limitations. Due to the close interconnection of atmospheric transport and chemical depletion, mixing ratios of chemically active trace gases can provide insight into the time an air parcel has spent in the stratosphere if the state of depletion of multiple gases is correctly inverted to decouple transport and chemistry. However, as in situ data of many of these species in the stratosphere are highly limited, the intended method must convert all information precisely into age spectra.
The most promising basis for the development provided the method postulated by Schoeberl et al. (2005), which parametrizes the shape of the spectrum as inverse Gaussian function (Hall and Plumb, 1994) and considers chemistry along average Lagrangian pathways. They use mathematical inversion techniques on three parameters of the distribution to optimize the desired age spectrum. However, while the principle of the method proves to work as intended in a model simulation, some important changes have to be made to improve the method's performance. Additionally, specific features of transport, such as the seasonal variation of strength in the stratospheric mass fluxes, have to be included into the spectrum to make it applicable to observational data. In a first step, the number of free parameters in the original Schoeberl's method was significantly reduced from three to one so that any available information is condensed into one single transport parameter. This also minimized the numerical effort as well as possible false solutions due to local minima of the applied metric. The numerical implementation was furthermore improved and turned into a root finding problem with a rapid and stable algorithm (Ridders, 1979). Many model studies have moreover shown that the seasonal cycle in stratospheric transport is coupled directly with age spectra in the form of multiple modes with a maximum during northern hemispheric winter (DJF) and a subsequent minimum in summer (JJA) (e.g., Ploeger and Birner, 2016). Most proposed methods to derive age spectra from observations do not include this multimodality explicitly and return monomodal PDFs.
An imposed seasonal cycle has been implemented where the monomodal age spectrum is scaled during the inversion process according to the seasonality of the tropical upward mass flux at 70 hPa (Rosenlof, 1995) to return proper maxima and minima. With these modifications the novel inverse method was applied in an idealized proof of concept with the EMAC model. The simulation featured model age spectra that serve as reference for the comparison as well as a set of 40 substances with constant chemical lifetimes that range from 1 month to almost 10 years, so that the basic principle of the new method could be extensively tested. Results showed that the concept works reliably if all parameters are known in the controllable test environment. The method retrieved age spectra and related moments very well globally on both the annual and seasonal scale, although the distributions appear slightly too wide systematically. This could be related to the prescribed inverse Gaussian shape. The imposed seasonal cycle works properly and imposes peaks and troughs that match the model reference at similar transit times. Using a Monte Carlo simulation, it was explained that five to ten different species are sufficient for a proper inversion that can even compensate a pseudo-random uncertainty of up to ± 20 % for the chemical lifetime robustly. However, in the lower stratosphere below 1.5 years of mean AoA, especially in the north, the inverse age spectra are deviating and mean AoA reveals even an inverted seasonal behavior compared to the model in spring (MAM) and fall (SON) in proximity to the tropopause. The reason for these major deviations is found in the reference surface, which is located at the tropical tropopause for all inverse method age spectra. Since local entry processes across the extratropical tropopause play an important role and show a

distinct seasonality, the method cannot capture these aspects correctly and requires modifications. All these aspects are published in Hauck et al. (2019).
The extension of the inverse method to the extratropical tropopause was achieved by splitting the reference surface, i.e, the tropopause, into three sections (northern, tropical, and southern) of 60° latitude each. Every of these defined entry sections has an age spectrum assigned to it, which is non-normalized and can be added to form a composite age spectrum that fully describes stratospheric transport. Upon integration, each spectrum provides an estimate of the percentage of air that entered the stratosphere across the associated tropopause segment. These newly established origin fractions provide a handy toolset to analyze the seasonality in air mass composition. Since the seasonal cycles of the spectra with northern and southern origin are different from that referring to the tropical tropopause, individual imposed seasonal cycles had to be included for the new reference sections. To estimate the seasonality in entrainment across the defined northern and southern tropopause sections precisely, monthly mean CLaMS pulse age spectra were integrated bin-wise and cumulated to derive an average statistic for the fraction of air that enters the stratosphere through the respective tropopause per month. These fractions were then applied to determine the scaling factors for the inverse age spectra of extratropical origin. The use of CLaMS data for the scaling factors inhibited a direct comparison of the peak timing between CLaMS pulse and inverse age spectra, but no information about the exact shape and amplitude of the spectra was transferred from the CLaMS spectra to the inverse method. Since the seasonality matched well with the results of previous studies (e.g., Bönisch et al., 2009; Yang et al., 2016), the retrieved scaling factors were a robust approximation of the seasonality within the setup specified in this thesis. This also lead to the conclusion that the subtropical jet stream likely plays an important role in the entrainment of air through the extratropical tropopause.
It was also shown that for the inversion method, the knowledge of neither the origin fractions nor the underlying composite spectrum is necessary to perform the inversion as the spectrum for each tropopause region can be retrieved independently, but only if the entry mixing ratios and chemical lifetimes differ. In two additional and refined proof of concept simulations with the CLaMS model, these modifications to the inverse method as well as the retrieved extratropical seasonal scaling factors were tested using ten of the idealized chemical species with constant lifetimes from the EMAC proof of concept. Results revealed that the inverse method performed well again and inverted age spectra with extratropical origin match the annual and seasonal mean model reference from CLaMS. Although especially cross-hemispheric age spectra cannot be well-approximated by inverse Gaussian functions and were therefore not retrieved well, this fact is negligible since the origin fractions of CLaMS showed that the influence of cross-hemispheric transport is vanishingly low. In the lowermost stratosphere, that has been identified as problematic zone in the first proof of concept, the seasonality of composite mean AoA improved significantly and was emulated correctly. This improved performance in the northern lowermost extratropical stratosphere is a key finding that made the method finally applicable. These results are published in Hauck et al. (2020).
In the final part of the thesis, the application of the novel inverse method has been conducted using in situ data for eleven distinct trace gas species from the two campaigns PGS and WISE with the HALO aircraft. The relevant halogenated species for the inversion (table 2.1) were measured during both campaigns by the gaschromatograph and mass spectrometer GhOST-MS (Sala et al., 2014), while N_2O has been detected by the two infrared quantum cascade laser spectrometers TRIHOP (Schiller et al., 2008) and UMAQS (Müller et al., 2015) that were all installed aboard HALO. All these data were transformed onto a grid of potential temperature difference to the tropopause and equivalent latitude, suitable for dynamical studies, and treated as phase or campaign average. The data basis is explained in detail in the third publication of this thesis (Keber et al., 2020), which constitutes an essential and substantial part of the development process of the inverse method. For a robust inversion, time series of mixing ratios at the northern and tropical tropopause for each of the substances had to be retrieved. The southern section is excluded since the CLaMS origin fractions showed that the influence of the southern hemisphere in the north is vanishingly low.

Unfortunately, no consistent time series from 2017 until 1960 was measured at the tropopause so that averaged surface measurements of the AGAGE (e.g., Prinn et al., 2019) stations in Barbados and American Samoa were considered. These data were lagged by two months (e.g., Andrews et al., 1999) for the tropical tropopause and one year for the northern extratropical sections (according to the CLaMS simulation in this thesis) for all substances with a strong long-term trend (mostly long-lived species). These observations were then extended back to 1960 with data from the RCP project (Meinshausen et al., 2011) to form a full required time series. The retrieved mixing ratios appeared consistent and continuous. For the short-lived species constant mixing ratios have been applied for the tropical (Engel and Rigby, 2019) and extratropical tropopause section (averaged PGS and WISE data). Since the chemical lifetimes along average Lagrangian pathways of all trace gases are unknown, a MCCV is introduced, based on Holzer and Waugh (2015), where lifetimes and age spectra are inverted in stepwise and statistical fashion using suitable constant initial guesses for the species and the measured mixing ratios. Within this MCCV, a number of pseudo-randomly chosen errors were included to provide an estimate of the influence of these uncertainties. The application to PGS and WISE data worked well, with mean AoA distributions and quantitative range that match estimates from past studies using suitable tracers. Derived campaign-averaged age spectra were meaningful and indicated that strong entrainment processes across both the tropical and extratropical tropopause regions occurred shortly prior to WISE (fall 2017) and also PGS phase 1 (winter 2015/2016), which matches the seasonality found for a different campaign in the past (Bönisch et al., 2009). This implies that the seasonally varying entrainment across the subtropical jet stream is likely a dominant transport mechanism for both the tropical and northern extratropical tropopause section. The results also indicate that parametrizations in previous studies (e.g., Volk et al., 1997; Engel et al., 2002) for the ratio of variance to mean AoA of the age spectra (ratio of moments) is valid, yet quite rough as the retrieved ratio of moments shows a strong seasonal variability which should be included into the assumption. The novel inverse method thus constitutes a promising technique with reliable performance that could be applied in future studies to analyze stratospheric transport and as an alternative for current age spectra approximations without significant direct influence of data from atmospheric models. These aspects are published also in Hauck et al. (2020).

Outlook

The inverse method, that has been developed, modified, extended, tested, and applied in the frame of this thesis, has proven to work reliably with in situ measurements and retrieved age spectra as well as moments that lead to conclusions consistent with previous investigations. These findings were all gained with special emphasis on the observational data and the minimized leverage of model data. However, there are some points that came up during the development process that require further discussion and could provide a starting point for studies in the future. The first aspect is the temporal scale for all spectra, which are confined to a seasonal perspective as a minimum. An extension to finer scales, such as monthly, would be preferable but requires finer approximations for all involved parameters and increases at the same time the variability of data. It is therefore not provided that a stable inversion would be possible with a similar promising performance. Additionally, the information about past seasonality in transport, i.e., the higher modes of the spectra, must be considered carefully. In this study, the seasonal variations are imposed onto the monomodal spectra and based on its intrinsic amplitude with scaling factors that constantly repeat for every year of transit time. Although this is a reliable technique that proved to work properly, the direct retrieval of this information is preferable and would include phases of stronger or weaker atmospheric transport directly. Yet, this is nearly impossible as it would need some feedback about transport for a period of 50 years transit time from a set of single mixing ratios. For the extratropical tropopause sections, integrated CLaMS data were used explicitly to approximate the seasonality in entrainment, which was in good agreement with past studies and indicated that the subtropical jet stream is a dominant factor for air entering the stratosphere across the extratropical tropopause. However, this is only valid for the specified tropopause sections in this thesis and the scaling factors might change significantly

when the borders of the regions are shifted. This aspect might be assessed in more detail in a future study.
Furthermore, the retrieved age spectra and their superposition for the composite spectrum are complicated. At the current stage of the inverse method, the retrieved spectra are always normalized and the computation of the composite PDF needs some information about the partitioning between the tropical and northern (or southern) entry region. So far, this information is only available in model simulations using suitable tracer simulations. As this is a major aspect of stratospheric transport that critically influences the results, future analyses could focus on an observationally based approach to derive the origin fractions from trace gas mixing ratios similar to the approach by Bönisch et al. (2009) for the distinction of a tropospheric and a stratospheric fraction. Another possible topic for further research are the introduced effective lifetimes for the substances that are quite abstract and could be analyzed more deeply to investigate their relationship with currently known global chemical lifetimes. Finally, the logical next step for the inverse method would be the application to more observational data to further establish it as a toolset for stratospheric dynamics that could even be applied on a regular basis to identify possible changes in the future. Available HALO research campaigns to this day are the TACTS (Transport and Composition in the Upper Troposphere/Lowermost Stratosphere - see Keber et al. (2020)) campaign in August and September 2012 over the northern midlatitudes, which would enable a perfect comparison with the WISE results. The recent SouthTrac campaign from September 2019 until November 2019 over Argentina could also provide the basis for a retrieval of inverse age spectra in the southern hemisphere, although this would require the derivation of entry mixing ratio time series for the southern tropopause section in similar fashion as for the north.
With the consideration of these limitations and ideas for further research, the inverse method constitutes an additional useful tool for analysis that can now be applied alongside other established methods and techniques to improve and enhance the understanding of the dynamics in the stratosphere and their changes in the future.

References

Abalos, M., Legras, B., Ploeger, F., and Randel, W. J.: Evaluating the advective Brewer-Dobson circulation in three reanalyses for the period 1979-2012, Journal of Geophysical Research: Atmospheres, 120, 7534–7554, DOI: 10.1002/2015JD023182, 2015.

Allen, D. R. and Nakamura, N.: Tracer Equivalent Latitude: A Diagnostic Tool for Isentropic Transport Studies, Journal of the Atmospheric Sciences, 60, 287–304, DOI: 10.1175/1520-0469(2003)060<0287:TELADT>2.0.CO;2, 2003.

Andrews, A. E., Boering, K. A., Daube, B. C., Wofsy, S. C., Hintsa, E. J., Weinstock, E. M., and Bui, T. P.: Empirical age spectra for the lower tropical stratosphere from in situ observations of CO_2: Implications for stratospheric transport, Journal of Geophysical Research: Atmospheres, 104, 26 581–26 595, DOI: 10.1029/1999JD900150, 1999.

Appenzeller, C., Holton, J. R., and Rosenlof, K. H.: Seasonal variation of mass transport across the tropopause, Journal of Geophysical Research: Atmospheres, 101, 15 071–15 078, DOI: 10.1029/96JD00821, 1996.

Austin, J. and Li, F.: On the relationship between the strength of the Brewer-Dobson circulation and the age of stratospheric air, Geophysical Research Letters, 33, DOI: 10.1029/2006GL026867, 2006.

Ball, W. T., Alsing, J., Mortlock, D. J., Staehelin, J., Haigh, J. D., Peter, T., Tummon, F., Stübi, R., Stenke, A., Anderson, J., Bourassa, A., Davis, S. M., Degenstein, D., Frith, S., Froidevaux, L., Roth, C., Sofieva, V., Wang, R., Wild, J., Yu, P., Ziemke, J. R., and Rozanov, E. V.: Evidence for a continuous decline in lower stratospheric ozone offsetting ozone layer recovery, Atmospheric Chemistry and Physics, 18, 1379–1394, DOI: 10.5194/acp-18-1379-2018, 2018.

Ball, W. T., Alsing, J., Staehelin, J., Davis, S. M., Froidevaux, L., and Peter, T.: Stratospheric ozone trends for 1985–2018: sensitivity to recent large variability, Atmospheric Chemistry and Physics, 19, 12 731–12 748, DOI: 10.5194/acp-19-12731-2019, 2019.

Birner, T. and Bönisch, H.: Residual circulation trajectories and transit times into the extratropical lowermost stratosphere, Atmospheric Chemistry and Physics, 11, 817–827, DOI: 10.5194/acp-11-817-2011, 2011.

Bönisch, H., Engel, A., Curtius, J., Birner, T., and Hoor, P.: Quantifying transport into the lowermost stratosphere using simultaneous in-situ measurements of SF_6 and CO_2, Atmospheric Chemistry and Physics, 9, 5905–5919, DOI: 10.5194/acp-9-5905-2009, 2009.

Bönisch, H., Engel, A., Birner, T., Hoor, P., Tarasick, D. W., and Ray, E. A.: On the structural changes in the Brewer-Dobson circulation after 2000, Atmospheric Chemistry and Physics, 11, 3937–3948, DOI: 10.5194/acp-11-3937-2011, 2011.

Brewer, A. W.: Evidence for a world circulation provided by the measurements of helium and water vapour distribution in the stratosphere, Quarterly Journal of the Royal Meteorological Society, 75, 351–363, DOI: 10.1002/qj.49707532603, 1949.

Butchart, N.: The Brewer-Dobson circulation, Reviews of Geophysics, 52, 157–184, DOI: 10.1002/2013RG000448, 2014.

Carpenter, L. J. and Reimann, S.: Chapter 1: Update on Ozone-Depleting Substances (ODSs) and Other Gases of Interest to the Montreal Protocol, in: Scientific Assessment of Ozone Depletion 2014, edited by Global Ozone Research and Monitoring Project, Global Ozone Research and Monitoring Project – Report No. 55, pp. 21–125, World Meteorological Organization, Geneva, Switzerland, 2014.

Chabrillat, S., Vigouroux, C., Christophe, Y., Engel, A., Errera, Q., Minganti, D., Monge-Sanz, B. M., Segers, A., and Mahieu, E.: Comparison of mean age of air in five reanalyses using the BASCOE transport model, Atmospheric Chemistry and Physics, 18, 14 715–14 735, DOI: 10.5194/acp-18-14715-2018, 2018.

Charney, J. G. and Drazin, P. G.: Propagation of planetary-scale disturbances from the lower into the upper atmosphere, Journal of Geophysical Research, 66, 83–109, DOI: 10.1029/JZ066i001p00083, 1961.

Chhikara, R. S. and Folks, J. L.: The inverse Gaussian distribution: Theory, methodology and applications, vol. 95 of *Statistics*, Dekker, New York, 1989.

Crutzen, P. J.: The influence of nitrogen oxides on the atmospheric ozone content, Quarterly Journal of the Royal Meteorological Society, 96, 320–325, DOI: 10.1002/qj.49709640815, 1970.

Dee, D. P., Uppala, S. M., Simmons, A. J., Berrisford, P., Poli, P., Kobayashi, S., Andrae, U., Balmaseda, M. A., Balsamo, G., Bauer, P., Bechtold, P., Beljaars, A. C. M., van de Berg, L., Bidlot, J., Bormann, N., Delsol, C., Dragani, R., Fuentes, M., Geer, A. J., Haimberger, L., Healy, S. B., Hersbach, H., Hólm, E. V., Isaksen, L., Kållberg, P., Köhler, M., Matricardi, M., McNally, A. P., Monge-Sanz, B. M., Morcrette, J.-J., Park, B.-K., Peubey, C., de Rosnay, P., Tavolato, C., Thépaut, J.-N., and Vitart, F.: The ERA-Interim reanalysis: configuration and performance of the data assimilation system, Quarterly Journal of the Royal Meteorological Society, 137, 553–597, DOI: 10.1002/qj.828, 2011.

Dobson, G. M. B.: Measurements of the amount of ozone in the Earth's atmosphere and its relation to other geophysical conditions.—Part III, Proceedings of the Royal Society of London. Series A, Containing Papers of a Mathematical and Physical Character, 122, 456–486, DOI: 10.1098/rspa.1929.0034, 1929.

Dobson, G. M. B.: Origin and Distribution of the Polyatomic Molecules in the Atmosphere, Proceedings of the Royal Society A: Mathematical, Physical and Engineering Sciences, 236, 187–193, DOI: 10.1098/rspa.1956.0127, 1956.

Ehhalt, D. H., Rohrer, F., Blake, D. R., Kinnison, D. E., and Konopka, P.: On the use of nonmethane hydrocarbons for the determination of age spectra in the lower stratosphere, Journal of Geophysical Research: Atmospheres, 112, 26 581, DOI: 10.1029/2006JD007686, 2007.

Engel, A. and Rigby, M.: Chapter 1: Update on Ozone-Depleting Substances (ODSs) and Other Gases of Interest to the Montreal Protocol, in: Scientific Assessment of Ozone Depletion 2018, edited by Global Ozone Research and Monitoring Project, vol. 58 of *Global Ozone Research and Monitoring Project – Report No. 58*, World Meteorological Organization, Geneva, Switzerland, 2019.

Engel, A., Strunk, M., Müller, M., Haase, H.-P., Poss, C., Levin, I., and Schmidt, U.: Temporal development of total chlorine in the high-latitude stratosphere based on reference distributions of mean age derived from CO_2 and SF_6, Journal of Geophysical Research, 107, 4483, DOI: 10.1029/2001JD000584, 2002.

Engel, A., Bönisch, H., Brunner, D., Fischer, H., Franke, H., Günther, G., Gurk, C., Hegglin, M., Hoor, P., Königstedt, R., Krebsbach, M., Maser, R., Parchatka, U., Peter, T., Schell, D., Schiller, C., Schmidt, U., Spelten, N., Szabo, T., Weers, U., Wernli, H., Wetter, T., and Wirth, V.: Highly resolved observations of trace gases in the lowermost stratosphere and upper troposphere from the Spurt project: an overview, Atmospheric Chemistry and Physics, 6, 283–301, DOI: 10.5194/acp-6-283-2006, 2006.

Engel, A., Möbius, T., Bönisch, H., Schmidt, U., Heinz, R., Levin, I., Atlas, E., Aoki, S., Nakazawa, T., Sugawara, S., Moore, F., Hurst, D., Elkins, J., Schauffler, S., Andrews, A., and Boering, K.: Age of stratospheric air unchanged within uncertainties over the past 30 years, Nature Geoscience, 2, 28–31, DOI: 10.1038/NGEO388, 2009.

Engel, A., Bönisch, H., Ullrich, M., Sitals, R., Membrive, O., Danis, F., and Crevoisier, C.: Mean age of stratospheric air derived from AirCore observations, Atmospheric Chemistry and Physics, 17, 6825–6838, DOI: 10.5194/acp-17-6825-2017, 2017.

Engel, A., Bönisch, H., Ostermöller, J., Chipperfield, M. P., Dhomse, S., and Jöckel, P.: A refined method for calculating equivalent effective stratospheric chlorine, Atmospheric Chemistry and Physics, 18, 601–619, DOI: 10.5194/acp-18-601-2018, 2018.

Ertel, H.: Ein neuer hydrodynamischer Erhaltungssatz, Die Naturwissenschaften, 30, 543–544, DOI: 10.1007/BF01475602, 1942.

Fritsch, F., Garny, H., Engel, A., Bönisch, H., and Eichinger, R.: Sensitivity of age of air trends to the derivation method for non-linear increasing inert SF_6, Atmospheric Chemistry and Physics, 20, 8709–8725, DOI: 10.5194/acp-20-8709-2020, 2020.

Fueglistaler, S., Dessler, A. E., Dunkerton, T. J., Folkins, I., Fu, Q., and Mote, P. W.: Tropical tropopause layer, Reviews of Geophysics, 47, DOI: 10.1029/2008RG000267, 2009.

Garcia, R. R. and Randel, W. J.: Acceleration of the Brewer–Dobson Circulation due to Increases in Greenhouse Gases, Journal of the Atmospheric Sciences, 65, 2731–2739, DOI: 10.1175/2008JAS2712.1, 2008.

Garny, H., Birner, T., Bönisch, H., and Bunzel, F.: The effects of mixing on age of air, Journal of Geophysical Research: Atmospheres, 119, 7015–7034, DOI: 10.1002/2013JD021417, 2014.

Gerber, E. P., Butler, A., Calvo, N., Charlton-Perez, A., Giorgetta, M., Manzini, E., Perlwitz, J., Polvani, L. M., Sassi, F., Scaife, A. A., Shaw, T. A., Son, S.-W., and Watanabe, S.: Assessing and Understanding the Impact of Stratospheric Dynamics and Variability on the Earth System, Bulletin of the American Meteorological Society, 93, 845–859, DOI: 10.1175/BAMS-D-11-00145.1, 2012.

Haenel, F. J., Stiller, G. P., von Clarmann, T., Funke, B., Eckert, E., Glatthor, N., Grabowski, U., Kellmann, S., Kiefer, M., Linden, A., and Reddmann, T.: Reassessment of MIPAS age of air trends and variability, Atmospheric Chemistry and Physics, 15, 13 161–13 176, DOI: 10.5194/acp-15-13161-2015, 2015.

Haine, T., Zhang, H., Waugh, D. W., and Holzer, M.: On transit-time distributions in unsteady circulation models, Ocean Modelling, 21, 35–45, DOI: 10.1016/j.ocemod.2007.11.004, 2008.

Hall, T. M. and Plumb, R. A.: Age as a diagnostic of stratospheric transport, Journal of Geophysical Research, 99, 1059, DOI: 10.1029/93JD03192, 1994.

Hauck, M., Fritsch, F., Garny, H., and Engel, A.: Deriving stratospheric age of air spectra using an idealized set of chemically active trace gases, Atmospheric Chemistry and Physics, 19, 5269–5291, DOI: 10.5194/acp-19-5269-2019, 2019.

Hauck, M., Bönisch, H., Hoor, P., Keber, T., Ploeger, F., Schuck, T. J., and Engel, A.: A convolution of observational and model data to estimate age of air spectra in the northern hemispheric lower stratosphere, Atmospheric Chemistry and Physics, 20, 8763–8785, DOI: 10.5194/acp-20-8763-2020, 2020.

Haynes, P. H., McIntyre, M. E., Shepherd, T. G., Marks, C. J., and Shine, K. P.: On the "Downward Control" of Extratropical Diabatic Circulations by Eddy-Induced Mean Zonal Forces, Journal of the Atmospheric Sciences, 48, 651–678, DOI: 10.1175/1520-0469(1991)048<0651:OTCOED>2.0.CO;2, 1991.

Hegglin, M. I., Plummer, D. A., Shepherd, T. G., Scinocca, J. F., Anderson, J., Froidevaux, L., Funke, B., Hurst, D., Rozanov, A., Urban, J., von Clarmann, T., Walker, K. A., Wang, H. J., Tegtmeier, S., and Weigel, K.: Vertical structure of stratospheric water vapour trends derived from merged satellite data, Nature Geoscience, 7, 768–776, DOI: 10.1038/ngeo2236, 2014.

Holton, J. R., Haynes, P. H., McIntyre, M. E., Douglass, A. R., Rood, R. B., and Pfister, L.: Stratosphere-troposphere exchange, Reviews of Geophysics, 33, 403, DOI: 10.1029/95RG02097, 1995.

Holzer, M. and Primeau, F. W.: Improved constraints on transit time distributions from argon 39: A maximum entropy approach, Journal of Geophysical Research: Atmospheres, 115, 473, DOI: 10.1029/2010JC006410, 2010.

Holzer, M. and Waugh, D. W.: Interhemispheric transit time distributions and path-dependent lifetimes constrained by measurements of SF_6 , CFCs, and CFC replacements, Geophysical Research Letters, 42, 4581–4589, DOI: 10.1002/2015GL064172, 2015.

Hoor, P., Gurk, C., Brunner, D., Hegglin, M. I., Wernli, H., and Fischer, H.: Seasonality and extent of extratropical TST derived from in-situ CO measurements during SPURT, Atmospheric Chemistry and Physics, 4, 1427–1442, DOI: 10.5194/acp-4-1427-2004, 2004.

Hoor, P., Fischer, H., and Lelieveld, J.: Tropical and extratropical tropospheric air in the lowermost stratosphere over Europe: A CO-based budget, Geophysical Research Letters, 32, DOI: 10.1029/2004GL022018, 2005.

Hoskins, B. J., McIntyre, M. E., and Robertson, A. W.: On the use and significance of isentropic potential vorticity maps, Quarterly Journal of the Royal Meteorological Society, 111, 877–946, DOI: 10.1002/qj.49711147002, 1985.

Intergovernmental Panel on Climate Change: Climate Change 2013 - The Physical Science Basis: Contribution of Working Group I to the fifth Assessment Report of the Intergovernmental Panel on Climate Change, Cambridge University Press, Cambridge, DOI: 10.1017/CBO9781107415324, 2013.

Jöckel, P., Kerkweg, A., Pozzer, A., Sander, R., Tost, H., Riede, H., Baumgaertner, A., Gromov, S., and Kern, B.: Development cycle 2 of the Modular Earth Submodel System (MESSy2), Geoscientific Model Development, 3, 717–752, DOI: 10.5194/gmd-3-717-2010, 2010.

Jöckel, P., Tost, H., Pozzer, A., Kunze, M., Kirner, O., Brenninkmeijer, Carl A. M., Brinkop, S., Cai, D. S., Dyroff, C., Eckstein, J., Frank, F., Garny, H., Gottschaldt, K.-D., Graf, P., Grewe, V., Kerkweg, A., Kern, B., Matthes, S., Mertens, M., Meul, S., Neumaier, M., Nützel, M., Oberländer-Hayn, S., Ruhnke, R., Runde, T., Sander, R., Scharffe, D., and Zahn, A.: Earth System Chemistry integrated Modelling (ESCiMo) with the Modular Earth Submodel System (MESSy) version 2.51, Geoscientific Model Development, 9, 1153–1200, DOI: 10.5194/gmd-9-1153-2016, 2016.

Keber, T., Bönisch, H., Hartick, C., Hauck, M., Lefrancois, F., Obersteiner, F., Ringsdorf, A., Schohl, N., Schuck, T., Hossaini, R., Graf, P., Jöckel, P., and Engel, A.: Bromine from short-lived source gases in the extratropical northern hemispheric upper troposphere and lower stratosphere (UTLS), Atmospheric Chemistry and Physics, 20, 4105–4132, DOI: 10.5194/acp-20-4105-2020, 2020.

Kida, H.: General Circulation of Air Parcels and Transport Characteristics Derived from a Hemispheric GCM, Journal of the Meteorological Society of Japan, 61, 510–523, DOI: 10.2151/jmsj1965.61.4_510, 1983.

Konopka, P.: Mixing and ozone loss in the 1999–2000 Arctic vortex: Simulations with the three-dimensional Chemical Lagrangian Model of the Stratosphere (CLaMS), Journal of Geophysical Research, 109, 23,487, DOI: 10.1029/2003JD003792, 2004.

Krause, J., Hoor, P., Engel, A., Plöger, F., Grooß, J.-U., Bönisch, H., Keber, T., Sinnhuber, B.-M., Woiwode, W., and Oelhaf, H.: Mixing and ageing in the polar lower stratosphere in winter 2015–2016, Atmospheric Chemistry and Physics, 18, 6057–6073, DOI: 10.5194/acp-18-6057-2018, 2018.

Kunkel, D., Hoor, P., Kaluza, T., Ungermann, J., Kluschat, B., Giez, A., Lachnitt, H.-C., Kaufmann, M., and Riese, M.: Evidence of small-scale quasi-isentropic mixing in ridges of extratropical baroclinic waves, Atmospheric Chemistry and Physics, 19, 12 607–12 630, DOI: 10.5194/acp-19-12607-2019, 2019.

Li, F., Austin, J., and Wilson, J.: The Strength of the Brewer–Dobson Circulation in a Changing Climate: Coupled Chemistry–Climate Model Simulations, Journal of Climate, 21, 40–57, DOI: 10.1175/2007JCLI1663.1, 2008.

Li, F., Waugh, D. W., Douglass, A. R., Newman, P. A., Pawson, S., Stolarski, R. S., Strahan, S. E., and Nielsen, J. E.: Seasonal variations of stratospheric age spectra in the Goddard Earth Observing System Chemistry Climate Model (GEOSCCM), Journal of Geophysical Research: Atmospheres, 117, DOI: 10.1029/2011JD016877, 2012a.

Li, F., Waugh, D. W., Douglass, A. R., Newman, P. A., Strahan, S. E., Ma, J., Nielsen, J. E., and Liang, Q.: Long-term changes in stratospheric age spectra in the 21st century in the Goddard Earth Observing System Chemistry-Climate Model (GEOSCCM), Journal of Geophysical Research: Atmospheres, 117, 32,295, DOI: 10.1029/2012JD017905, 2012b.

McIntyre, M. and Palmer, T.: The 'surf zone' in the stratosphere, Journal of Atmospheric and Terrestrial Physics, 46, 825–849, DOI: 10.1016/0021-9169(84)90063-1, 1984.

McIntyre, M. E. and Palmer, T. N.: Breaking planetary waves in the stratosphere, Nature, 305, 593–600, DOI: 10.1038/305593a0, 1983.

McKenna, D. S.: A new Chemical Lagrangian Model of the Stratosphere (CLaMS) 1. Formulation of advection and mixing, Journal of Geophysical Research, 107, 1435, DOI: 10.1029/2000JD000114, 2002a.

McKenna, D. S.: A new Chemical Lagrangian Model of the Stratosphere (CLaMS) 2. Formulation of chemistry scheme and initialization, Journal of Geophysical Research: Atmospheres, 107, 361, DOI: 10.1029/2000JD000113, 2002b.

Meinshausen, M., Smith, S. J., Calvin, K., Daniel, J. S., Kainuma, M. L. T., Lamarque, J.-F., Matsumoto, K., Montzka, S. A., Raper, S. C. B., Riahi, K., Thomson, A., Velders, G. J. M., and van Vuuren, D. P.: The RCP greenhouse gas concentrations and their extensions from 1765 to 2300, Climatic Change, 109, 213–241, DOI: 10.1007/s10584-011-0156-z, 2011.

Molina, M. J. and Rowland, F. S.: Stratospheric sink for chlorofluoromethanes: chlorine atomc-atalysed destruction of ozone, Nature, 249, 810–812, DOI: 10.1038/249810a0, 1974.

Montzka, S. A., Dutton, G. S., Yu, P., Ray, E., Portmann, R. W., Daniel, J. S., Kuijpers, L., Hall, B. D., Mondeel, D., Siso, C., Nance, J. D., Rigby, M., Manning, A. J., Hu, L., Moore, F.,

Miller, B. R., and Elkins, J. W.: An unexpected and persistent increase in global emissions of ozone-depleting CFC-11, Nature, 557, 413–417, DOI: 10.1038/s41586-018-0106-2, 2018.

Morley, S. K., Brito, T. V., and Welling, D. T.: Measures of Model Performance Based On the Log Accuracy Ratio, Space Weather, 16, 69–88, DOI: 10.1002/2017SW001669, 2018.

Müller, S., Hoor, P., Berkes, F., Bozem, H., Klingebiel, M., Reutter, P., Smit, H. G. J., Wendisch, M., Spichtinger, P., and Borrmann, S.: In situ detection of stratosphere-troposphere exchange of cirrus particles in the midlatitudes, Geophysical Research Letters, 42, 949–955, DOI: 10.1002/2014GL062556, 2015.

Neu, J. L. and Plumb, R. A.: Age of air in a "leaky pipe" model of stratospheric transport, Journal of Geophysical Research: Atmospheres, 104, 19 243–19 255, DOI: 10.1029/1999JD900251, 1999.

Oberländer-Hayn, S., Meul, S., Langematz, U., Abalichin, J., and Haenel, F.: A chemistry-climate model study of past changes in the Brewer-Dobson circulation, Journal of Geophysical Research: Atmospheres, 120, 6742–6757, DOI: 10.1002/2014JD022843, 2015.

Oelhaf, H., Sinnhuber, B.-M., Woiwode, W., Bönisch, H., Bozem, H., Engel, A., Fix, A., Friedl-Vallon, F., Grooß, J.-U., Hoor, P., Johansson, S., Jurkat-Witschas, T., Kaufmann, S., Krämer, M., Krause, J., Kretschmer, E., Lörks, D., Marsing, A., Orphal, J., Pfeilsticker, K., Pitts, M., Poole, L., Preusse, P., Rapp, M., Riese, M., Rolf, C., Ungermann, J., Voigt, C., Volk, C. M., Wirth, M., Zahn, A., and Ziereis, H.: POLSTRACC: Airborne Experiment for Studying the Polar Stratosphere in a Changing Climate with the High Altitude and Long Range Research Aircraft (HALO), Bulletin of the American Meteorological Society, 100, 2634–2664, DOI: 10.1175/BAMS-D-18-0181.1, 2019.

Olsen, M. A., Schoeberl, M. R., and Douglass, A. R.: Stratosphere-troposphere exchange of mass and ozone, Journal of Geophysical Research: Atmospheres, 109, 15,071, DOI: 10.1029/2004JD005186, 2004.

Ploeger, F. and Birner, T.: Seasonal and inter-annual variability of lower stratospheric age of air spectra, Atmospheric Chemistry and Physics, 16, 10 195–10 213, DOI: 10.5194/acp-16-10195-2016, 2016.

Ploeger, F., Gottschling, C., Griessbach, S., Grooß, J.-U., Guenther, G., Konopka, P., Müller, R., Riese, M., Stroh, F., Tao, M., Ungermann, J., Vogel, B., and von Hobe, M.: A potential vorticity-based determination of the transport barrier in the Asian summer monsoon anticyclone, Atmospheric Chemistry and Physics, 15, 13 145–13 159, DOI: 10.5194/acp-15-13145-2015, 2015a.

Ploeger, F., Riese, M., Haenel, F., Konopka, P., Müller, R., and Stiller, G.: Variability of stratospheric mean age of air and of the local effects of residual circulation and eddy mixing, Journal of Geophysical Research: Atmospheres, 120, 716–733, DOI: 10.1002/2014JD022468, 2015b.

Ploeger, F., Legras, B., Charlesworth, E., Yan, X., Diallo, M., Konopka, P., Birner, T., Tao, M., Engel, A., and Riese, M.: How robust are stratospheric age of air trends from different reanalyses?, Atmospheric Chemistry and Physics, 19, 6085–6105, DOI: 10.5194/acp-19-6085-2019, 2019.

Plumb, I. C., Vohralik, P. F., and Ryan, K. R.: Normalization of correlations for atmospheric species with chemical loss, Journal of Geophysical Research: Atmospheres, 104, 11 723–11 732, DOI: 10.1029/1999JD900014, 1999.

Plumb, R. A.: Stratospheric Transport, Journal of the Meteorological Society of Japan, 80, 793–809, DOI: 10.2151/jmsj.80.793, 2002.

Plumb, R. A.: Tracer interrelationships in the stratosphere, Reviews of Geophysics, 45, DOI: 10.1029/2005RG000179, 2007.

Plumb, R. A. and Ko, M. K. W.: Interrelationships between mixing ratios of long-lived stratospheric constituents, Journal of Geophysical Research, 97, 10 145–10 156, DOI: 10.1029/92JD00450, 1992.

Podglajen, A. and Ploeger, F.: Retrieving the age of air spectrum from tracers: Principle and method, Atmospheric Chemistry and Physics, 19, 1767–1783, DOI: 10.5194/acp-19-1767-2019, 2019.

Pommrich, R., Müller, R., Grooß, J.-U., Konopka, P., Ploeger, F., Vogel, B., Tao, M., Hoppe, C. M., Günther, G., Spelten, N., Hoffmann, L., Pumphrey, H.-C., Viciani, S., D'Amato, F., Volk, C. M., Hoor, P., Schlager, H., and Riese, M.: Tropical troposphere to stratosphere transport of carbon monoxide and long-lived trace species in the Chemical Lagrangian Model of the Stratosphere (CLaMS), Geoscientific Model Development, 7, 2895–2916, DOI: 10.5194/gmd-7-2895-2014, 2014.

Portmann, R. W., Daniel, J. S., and Ravishankara, A. R.: Stratospheric ozone depletion due to nitrous oxide: influences of other gases, Philosophical transactions of the Royal Society of London. Series B, Biological sciences, 367, 1256–1264, DOI: 10.1098/rstb.2011.0377, 2012.

Prinn, R. G., Weiss, R. F., Arduini, J., Arnold, T., DeWitt, H. L., Fraser, P. J., Ganesan, A. L., Gasore, J., Harth, C. M., Hermansen, O., Kim, J., Krummel, P. B., Li, S., Loh, Z. M., Lunder, C. R., Maione, M., Manning, A. J., Miller, B. R., Mitrevski, B., Mühle, J., O'Doherty, S., Park, S., Reimann, S., Rigby, M., Saito, T., Salameh, P. K., Schmidt, R., Simmonds, P. G., Steele, L. P., Vollmer, M. K., Wang, R. H., Yao, B., Yokouchi, Y., Young, D., and Zhou, L.: History of chemically and radiatively important atmospheric gases from the Advanced Global Atmospheric Gases Experiment (AGAGE), Earth System Science Data, 10, 985–1018, DOI: 10.5194/essd-10-985-2018, 2018.

Prinn, R. G., Weiss, R. F., Arduini, J., Arnold, T., Fraser, P. J., Ganesan, A. L., Gasore, J., Harth, C. M., Hermansen, O., Kim, J., Krummel, P. B., Li, S., Loh, Z. M., Lunder, C. R., Maione, M., Manning, A. J., Miller, B. R., Mitrevski, B., Mühle, J., O'Doherty, S., Park, S., Reimann, S., Rigby, M., Salameh, P. K., Schmidt, R., Simmonds, P. G., Steele, L. P., Vollmer, M. K., Wang, R. H., and Young, D.: The ALE / GAGE / AGAGE Network (DB1001), DOI: 10.3334/CDIAC/atg.db1001, 2019.

Ravishankara, A. R., Solomon, S., Turnipseed, A. A., and Warren, R. F.: Atmospheric lifetimes of long-lived halogenated species, Science, 259, 194–199, DOI: 10.1126/science.259.5092.194, 1993.

Ray, E. A., Moore, F. L., Rosenlof, K. H., Davis, S. M., Sweeney, C., Tans, P., Wang, T., Elkins, J. W., Bönisch, H., Engel, A., Sugawara, S., Nakazawa, T., and Aoki, S.: Improving stratospheric transport trend analysis based on SF6 and CO2 measurements, Journal of Geophysical Research: Atmospheres, 119, 14,110–14,128, DOI: 10.1002/2014JD021802, 2014.

Ray, E. A., Moore, F. L., Elkins, J. W., Rosenlof, K. H., Laube, J. C., Röckmann, T., Marsh, D. R., and Andrews, A. E.: Quantification of the SF_6 lifetime based on mesospheric loss measured in the stratospheric polar vortex, Journal of Geophysical Research: Atmospheres, 122, 4626–4638, DOI: 10.1002/2016JD026198, 2017.

Reithmeier, C., Sausen, R., and Grewe, V.: Investigating lower stratospheric model transport: Lagrangian calculations of mean age and age spectra in the GCM ECHAM4, Climate Dynamics, 30, 225–238, DOI: 10.1007/s00382-007-0294-1, 2008.

Ridders, C.: A new algorithm for computing a single root of a real continuous function, IEEE Transactions on Circuits and Systems, 26, 979–980, DOI: 10.1109/TCS.1979.1084580, 1979.

Riese, M., Ploeger, F., Rap, A., Vogel, B., Konopka, P., Dameris, M., and Forster, P.: Impact of uncertainties in atmospheric mixing on simulated UTLS composition and related radiative effects, Journal of Geophysical Research, 117, DOI: 10.1029/2012JD017751, 2012.

Rigby, M., Park, S., Saito, T., Western, L. M., Redington, A. L., Fang, X., Henne, S., Manning, A. J., Prinn, R. G., Dutton, G. S., Fraser, P. J., Ganesan, A. L., Hall, B. D., Harth, C. M., Kim, J., Kim, K.-R., Krummel, P. B., Lee, T., Li, S., Liang, Q., Lunt, M. F., Montzka, S. A., Mühle, J., O'Doherty, S., Park, M.-K., Reimann, S., Salameh, P. K., Simmonds, P., Tunnicliffe, R. L., Weiss, R. F., Yokouchi, Y., and Young, D.: Increase in CFC-11 emissions from eastern China based on atmospheric observations, Nature, 569, 546–550, DOI: 10.1038/s41586-019-1193-4, 2019.

Roeckner, E., Brokopf, R., Esch, M., Giorgetta, M., Hagemann, S., Kornblueh, L., Manzini, E., Schlese, U., and Schulzweida, U.: Sensitivity of Simulated Climate to Horizontal and Vertical Resolution in the ECHAM5 Atmosphere Model, Journal of Climate, 19, 3771–3791, DOI: 10.1175/JCLI3824.1, 2006.

Rosenlof, K. H.: Seasonal cycle of the residual mean meridional circulation in the stratosphere, Journal of Geophysical Research: Atmospheres, 100, 5173, DOI: 10.1029/94JD03122, 1995.

Rossby, C.-G.: Dynamics of steady ocean currents in the light of experimental fluid mechanics, Massachusetts Institute of Technology and Woods Hole Oceanographic Institution, Cambridge, MA, DOI: 10.1575/1912/1088, 1936.

Rowland, F. S. and Molina, M. J.: Chlorofluoromethanes in the environment, Reviews of Geophysics, 13, 1–35, DOI: 10.1029/RG013i001p00001, 1975.

Sala, S., Bönisch, H., Keber, T., Oram, D. E., Mills, G., and Engel, A.: Deriving an atmospheric budget of total organic bromine using airborne in situ measurements from the western Pacific area during SHIVA, Atmospheric Chemistry and Physics, 14, 6903–6923, DOI: 10.5194/acp-14-6903-2014, 2014.

Schiller, C. L., Bozem, H., Gurk, C., Parchatka, U., Königstedt, R., Harris, G. W., Lelieveld, J., and Fischer, H.: Applications of quantum cascade lasers for sensitive trace gas measurements of CO, CH4, N2O and HCHO, Applied Physics B, 92, 419–430, DOI: 10.1007/s00340-008-3125-0, 2008.

Schmidt, U., Engel, A., and Volk, M.: Ist der globale Ozonabbau gestoppt? Spurengasmessungen in der Stratosphäre geben Aufschluss, in: Geowissenschaften in Frankfurt, edited by Junge, A., Kleine Senckenberg-Reihe, pp. 1–12, Schweizerbart, Stuttgart, 2002.

Schoeberl, M. R., Sparling, L. C., Jackman, C. H., and Fleming, E. L.: A Lagrangian view of stratospheric trace gas distributions, Journal of Geophysical Research: Atmospheres, 105, 1537–1552, DOI: 10.1029/1999JD900787, 2000.

Schoeberl, M. R., Douglass, A. R., Polansky, B., Boone, C., Walker, K. A., and Bernath, P.: Estimation of stratospheric age spectrum from chemical tracers, Journal of Geophysical Research: Atmospheres, 110, 32 295, DOI: 10.1029/2005JD006125, 2005.

Seinfeld, J. H. and Pandis, S. N.: Atmospheric chemistry and physics: From air pollution to climate change, J. Wiley, Hoboken, N.J., 2. edn., 2006.

Shepherd, T. G.: Transport in the Middle Atmosphere, Journal of the Meteorological Society of Japan, 85B, 165–191, DOI: 10.2151/jmsj.85B.165, 2007.

Shepherd, T. G. and McLandress, C.: A Robust Mechanism for Strengthening of the Brewer–Dobson Circulation in Response to Climate Change: Critical-Layer Control of Subtropical Wave Breaking, Journal of the Atmospheric Sciences, 68, 784–797, DOI: 10.1175/2010JAS3608.1, 2011.

Škerlak, B., Sprenger, M., and Wernli, H.: A global climatology of stratosphere–troposphere exchange using the ERA-Interim data set from 1979 to 2011, Atmospheric Chemistry and Physics, 14, 913–937, DOI: 10.5194/acp-14-913-2014, 2014.

Solomon, S., Rosenlof, K. H., Portmann, R. W., Daniel, J. S., Davis, S. M., Sanford, T. J., and Plattner, G.-K.: Contributions of stratospheric water vapor to decadal changes in the rate of global warming, Science, 327, 1219–1223, DOI: 10.1126/science.1182488, 2010.

SPARC: Lifetimes of Stratospheric Ozone-Depleting Substances, Their Replacements, and Related Species, SPARC Report No. 6, URL www.sparc-climate.org/publications/sparc-reports/, 2013.

Stiller, G. P., von Clarmann, T., Haenel, F., Funke, B., Glatthor, N., Grabowski, U., Kellmann, S., Kiefer, M., Linden, A., Lossow, S., and López-Puertas, M.: Observed temporal evolution of global mean age of stratospheric air for the 2002 to 2010 period, Atmospheric Chemistry and Physics, 12, 3311–3331, DOI: 10.5194/acp-12-3311-2012, 2012.

Stiller, G. P., Fierli, F., Ploeger, F., Cagnazzo, C., Funke, B., Haenel, F. J., Reddmann, T., Riese, M., and von Clarmann, T.: Shift of subtropical transport barriers explains observed hemispheric asymmetry of decadal trends of age of air, Atmospheric Chemistry and Physics, 17, 11 177–11 192, DOI: 10.5194/acp-17-11177-2017, 2017.

Volk, C. M., Elkins, J. W., Fahey, D. W., Dutton, G. S., Gilligan, J. M., Loewenstein, M., Podolske, J. R., Chan, K. R., and Gunson, M. R.: Evaluation of source gas lifetimes from stratospheric observations, Journal of Geophysical Research: Atmospheres, 102, 25 543–25 564, DOI: 10.1029/97JD02215, 1997.

Waugh, D.: Atmospheric dynamics: The age of stratospheric air, Nature Geoscience, 2, 14–16, DOI: 10.1038/ngeo397, 2009.

Waugh, D. and Hall, T. M.: Age of stratospheric air: Theory, observations, and models, Reviews of Geophysics, 40, 4483, DOI: 10.1029/2000RG000101, 2002.

Wofsy, S. C., McElroy, M. B., and Yung, Y. L.: The chemistry of atmospheric bromine, Geophysical Research Letters, 2, 215–218, DOI: 10.1029/GL002i006p00215, 1975.

World Meteorological Organization: WMO WDCGG Data Summary: World Data Centre For Greenhouse Gases No. 42 - Global Atmospheric Watch Data: Volume IV - Greenhouse Gases and Other Atmospheric Gases, Japan Meteorological Agency, 2018.

World Meteorological Organization: Scientific Assessment of Ozone Depletion 2018, Global Ozone Research and Monitoring Project – Report No. 58, World Meteorological Organization, Geneva, Switzerland, 2019.

Yang, H., Chen, G., Tang, Q., and Hess, P.: Quantifying isentropic stratosphere-troposphere exchange of ozone, Journal of Geophysical Research: Atmospheres, 121, 3372–3387, DOI: 10.1002/2015JD024180, 2016.

Paper I: Deriving stratospheric age of air spectra using an idealized set of chemically active trace gases

Published as:

Hauck, M., Fritsch, F., Garny, H., and Engel, A.: *Deriving stratospheric age of air spectra using an idealized set of chemically active trace gases*, Atmospheric Chemistry and Physics, 19, 5269-5291, DOI: https://doi.org/10.5194/acp-19-5269-2019, 2019

Author Contributions:

Marius Hauck wrote the manuscript and prepared the answers to the referees during the revision process. Novel concepts presented in the paper were developed by Marius Hauck in collaboration with Andreas Engel. The manuscript and the answers to the referees were proofread by the co-authors.

Marius Hauck developed all numerical code of the inverse method, the seasonal cycle and the Monte Carlo simulation. Marius Hauck evaluated the model data and prepared the results and figures for the publication.

Frauke Fritsch and Hella Garny planned and performed the EMAC model simulation and tested a method by Schoeberl et al. (2000) mentioned in section 2.1 of paper I. Reanalysis data were provided by Hella Garny.

All co-authors contributed to the preparation of the paper in many useful discussions.

Frankfurt am Main

_____

Marius Hauck

Atmos. Chem. Phys., 19, 5269–5291, 2019
https://doi.org/10.5194/acp-19-5269-2019

Atmospheric Chemistry and Physics
Open Access
EGU

Deriving stratospheric age of air spectra using an idealized set of chemically active trace gases

Marius Hauck[1], **Frauke Fritsch**[2,3], **Hella Garny**[2,3], **and Andreas Engel**[1]

[1]Institute for Atmospheric and Environmental Sciences, Goethe University Frankfurt, Frankfurt am Main, Germany
[2]Deutsches Zentrum für Luft- und Raumfahrt (DLR), Institut für Physik der Atmosphäre, Oberpfaffenhofen, Germany
[3]Meteorological Institute Munich, Ludwig Maximilian University of Munich, Munich, Germany

Correspondence: Marius Hauck (hauck@iau.uni-frankfurt.de)

Received: 18 September 2018 – Discussion started: 9 October 2018
Revised: 8 March 2019 – Accepted: 18 March 2019 – Published: 17 April 2019

Abstract. Analysis of stratospheric transport from an observational point of view is frequently realized by evaluation of the mean age of air values from long-lived trace gases. However, this provides more insight into general transport strength and less into its mechanism. Deriving complete transit time distributions (age spectra) is desirable, but their deduction from direct measurements is difficult. It is so far primarily based on model work. This paper introduces a modified version of an inverse method to infer age spectra from mixing ratios of short-lived trace gases and investigates its basic principle in an idealized model simulation. For a full description of transport seasonality the method includes an imposed seasonal cycle to gain multimodal spectra. An ECHAM/MESSy Atmospheric Chemistry (EMAC) model simulation is utilized for a general proof of concept of the method and features an idealized dataset of 40 radioactive trace gases with different chemical lifetimes as well as 40 chemically inert pulsed trace gases to calculate pulse age spectra. It is assessed whether the modified inverse method in combination with the seasonal cycle can provide matching age spectra when chemistry is well-known. Annual and seasonal mean inverse spectra are compared to pulse spectra including first and second moments as well as the ratio between them to assess the performance on these timescales. Results indicate that the modified inverse age spectra match the annual and seasonal pulse age spectra well on global scale beyond 1.5 years of mean age of air. The imposed seasonal cycle emerges as a reliable tool to include transport seasonality in the age spectra. Below 1.5 years of mean age of air, tropospheric influence intensifies and breaks the assumption of single entry through the tropical tropopause, leading to inaccurate spectra, in particular in the Northern Hemisphere. The imposed seasonal cycle wrongly prescribes seasonal entry in this lower region and does not lead to a better agreement between inverse and pulse age spectra without further improvement. Tests with a focus on future application to observational data imply that subsets of trace gases with 5 to 10 species are sufficient for deriving well-matching age spectra. These subsets can also compensate for an average uncertainty of up to $\pm 20\,\%$ in the knowledge of chemical lifetime if a deviation of circa $\pm 10\,\%$ in modal age and amplitude of the resulting spectra is tolerated.

1 Introduction

Stratospheric meridional circulation, referred to as Brewer–Dobson circulation (BDC), is a key process for the comprehension of air mass transport throughout the atmosphere. The spatial distributions and atmospheric lifetimes of various greenhouse gases and ozone-depleting substances, such as halocarbons, are strongly influenced by this large-scale motion (Butchart and Scaife, 2001; Solomon et al., 2010). Therefore, the BDC affects not only the chemical composition of the stratosphere but also the radiative budget of the complete atmosphere. The BDC is a combination of a residual mean circulation with net mass flux and eddy-induced isentropic bidirectional mixing (Plumb, 2002; Shepherd, 2007; Butchart, 2014). Air is transported mainly through the tropical tropopause and then advected to higher latitudes, where it eventually descends. Primary drivers are tropospheric planetary- and synoptic-scale Rossby waves that

propagate upward and transfer their momentum by breaking in the extratropical middle stratosphere (Haynes et al., 1991; Holton et al., 1995). At the same time, this wave drag induces stirring processes that are especially enhanced in this "surf zone" (McIntyre and Palmer, 1984). It has been shown that the tropical upward mass flux has a distinct seasonal cycle with a maximum during northern hemispheric (NH) wintertime, when wave excitation is largest (Rosenlof and Holton, 1993; Rosenlof, 1995).

A problem that arises especially regarding observational investigation of the stratospheric circulation is the impossibility of direct measurements of the underlying dynamics, i.e., slow overturning circulation. However, a suited tool for quantification, which can be derived from observations of chemically very long-lived trace gases and directly compared to model results, is the concept of mean age of air (AoA; Hall and Plumb, 1994; Waugh and Hall, 2002). Mean AoA can be understood as the average period of time that elapsed for an air parcel at any arbitrary location since passing a certain reference point. Usually, the reference is either earth's surface or the tropical tropopause layer. Mean AoA provides not only insight into the current overall strength of the BDC but also allows for an investigation of temporal changes. If the circulation intensity varies over time, the value of mean AoA will also show this trend but will be inversely proportional (Austin and Li, 2006). Different models predict an enhanced stratospheric circulation indicated by a negative trend of mean AoA (Garcia and Randel, 2008; Li et al., 2008; Oman et al., 2009; Shepherd and McLandress, 2011) in response to strengthened wave drag by rising greenhouse gas concentrations. On the other hand, sparse observationally derived mean AoA from balloon-borne SF_6 and CO_2 data by Engel et al. (2009) show an insignificant positive change between 1975 and 2005 in northern midlatitude stratosphere above 24 km altitude. Recently, this trend is further affirmed by Engel et al. (2017), where existing data are extended and still show an insignificant trend for the same spatial region. Ray et al. (2014) reexamined these data of SF_6 and CO_2 using a simplified tropical leaky pipe model and even found a statistically significant positive trend in mean AoA at similar ranges of altitude and latitude as Engel et al. (2009). The analyses of satellite data by Stiller et al. (2012) and Haenel et al. (2015) additionally indicate that the temporal changes in mean AoA exhibit hemispheric asymmetries. Analysis of in situ trace gas measurements of N_2O, O_3 and model trajectories by Bönisch et al. (2011) suggest an increased tropical upwelling combined with an enhanced transport from the tropical into the extratropical lower stratosphere. These results suggest that the strength of the BDC is not changing uniformly. Similar findings are presented by Hegglin et al. (2014) using merged satellite H_2O data. In fact, Birner and Bönisch (2011) propose a separation of the residual mean circulation into two distinct branches conveying air from the tropics into the extratropics. The shallow branch is mainly effective in the lower stratosphere, while air in the middle and upper stratosphere is primarily affected by the deep branch. Since more recent studies of models (Okamoto et al., 2011; Oberländer-Hayn et al., 2015), reanalyses (Monge-Sanz et al., 2013; Abalos et al., 2015) and observations (Ray et al., 2014; Haenel et al., 2015; Engel et al., 2017) still exhibit some inconsistencies about possible future changes in the strength of the circulation pathways, further analyses are necessary. Recent studies of model and satellite observations also suggest that a southward (Stiller et al., 2017) and upward (Oberländer-Hayn et al., 2016) shift of the BDC might be key factors for these inconsistencies.

For an even more thorough analysis of stratospheric transport, the usage of a full transit time distribution is of advantage. The interaction of mean residual transport and bidirectional mixing as well as the influence of shallow and deep branch is expressed in this distribution, which is also referred to as age spectrum (Hall and Plumb, 1994; Waugh and Hall, 2002). At any given point in the stratosphere, the age spectrum denotes the fraction of fluid elements in an air parcel that had a certain transit time from the reference point to the chosen location. It can be considered a probability density function (PDF), with the mean AoA being the first moment of this distribution. An important advantage is that changes in the different ranges of transit times of the BDC can be visualized with a comparison of age spectra at different points in time. Variations of the shallow branch influence the age spectrum mostly at short transit times (ca. 1 to 2 years – Birner and Bönisch, 2011), whereas changes in the deep branch influence mostly at long transit times (ca. 4 to 5 years – Birner and Bönisch, 2011). Additionally, the effect of aging by mixing (Garny et al., 2014) on the tail of the spectrum may also be assessed during such an analysis. In model experiments, the age spectrum can be gained via periodically occurring pulses of a chemically inert trace gas. For mean AoA, either a linearly increasing chemically inert trace gas or the mean of the age spectrum can be applied. In reality, only few very long-lived trace gases exhibit a linear trend in the first approximation and can be utilized to gain mean AoA (Andrews et al., 2001a). When deriving mean AoA from observations of very long-lived trace gases with non-linear increase, however, assumptions about the shape of the age spectrum are required, where mostly the pioneering work of Hall and Plumb (1994) is considered. The underlying age spectrum for this calculation is only an approximation, which might not be representative in all cases and could bias the inferred mean AoA. A directly inferred complete age spectrum may constitute an improvement and could give further insight into transport processes. This information might be extracted from mixing ratios of long- and short-lived trace gases in an air parcel, as for such species, residual transport, mixing and chemical depletion are inevitably associated with each other. The state of depletion of these gases provides an estimate of the elapsed transit time since passing the reference point. In addition, trace gases with varying chemical depletion are only sensitive to certain transport pathways and thus contribute

mainly to the age spectrum for transit time ranges up to their respective chemical lifetime (Schoeberl et al., 2000, 2005). The complete age spectrum may then theoretically be derived as a combination of those pieces of information, provided that a sufficient number of distinct mixing ratios are known. Since the amount of air parcels with transit times larger than 10 years is likely to be low even in the uppermost part of the stratosphere, trace gases with lifetimes of up to 10 years should be sufficient for retrieving a meaningful age spectrum. That makes short-lived trace gases a suitable tool, as a variety of species with diverse lifetimes were frequently measured during past airborne research campaigns. Unfortunately, to the best of our knowledge, there are only few publications about possible techniques to finally convert the information of the mixing ratios of short-lived trace gases into stratospheric age spectra (Schoeberl et al., 2005; Ehhalt et al., 2007) and none that include seasonality in transport. When analyzing seasonal variation in stratospheric dynamics by inferring age spectra from observations, though, a proper consideration of the seasonal cycle is also required to achieve reliable results.

This paper presents an application and evaluation of a modified version of the method by Schoeberl et al. (2005; Schoeberl's method) with a reduced set of fit parameters and an imposed seasonal cycle to account for seasonality in stratospheric transport. The modified technique is applied as a proof of concept to an idealized simulation of the ECHAM/MESSy Atmospheric Chemistry (EMAC) model (Jöckel et al., 2006, 2010). Section 2 provides insight into the method and the model simulation. In Sect. 3, resulting age spectra and related quantities are analyzed and assessed with respect to future application to observational data. Finally, there is a summary, conclusion and outlook in Sect. 4.

2 Methodology

2.1 Age spectra derivation

A frequent basis for the estimation of age spectra, which is also utilized in Schoeberl et al. (2005) and Ehhalt et al. (2007), is the mathematical description of a mixing ratio $\chi(\boldsymbol{x},t)$ for any substance with a stratospheric sink at an arbitrary location $\boldsymbol{x}$ at any time t in the stratosphere, given by the following equation:

$$\chi(\boldsymbol{x},t) = \int_0^\infty \chi\left(\boldsymbol{x}_0, t-t'\right) \cdot e^{-\frac{t'}{\tau(t')}} \cdot G\left(\boldsymbol{x},t,t'\right) \cdot \mathrm{d}t'. \quad (1)$$

Here, t' is the transit time through the stratosphere, $\chi\left(\boldsymbol{x}_0, t-t'\right)$ the mixing ratio time series at the tropical tropopause (entry mixing ratio), $\tau\left(t'\right)$ the chemical lifetime and $G\left(\boldsymbol{x},t,t'\right)$ the age spectrum. Usually, a PDF is integrated from $-\infty$ to ∞, but since negative transit times are physically undefined for our analysis, zero is taken instead. To simplify the derivation, a constant annual mean entry mixing ratio $\overline{\chi_0} = \overline{\chi(\boldsymbol{x}_0, t-t')}$ is assumed. This keeps the balance between a physically accurate description and practicability for observational studies, since time series of short-lived species at the tropical tropopause are hard to attain. Equation (1) then becomes

$$\chi(\boldsymbol{x},t) = \overline{\chi_0} \cdot \int_0^\infty e^{-\frac{t'}{\tau(t')}} \cdot G\left(\boldsymbol{x},t,t'\right) \cdot \mathrm{d}t'. \quad (2)$$

One of the first approaches to obtain the age spectrum from such an equation in an unidimensional case without chemical loss was made by Hall and Plumb (1994). In their study, the vertical diffusion equation with a constant diffusion coefficient was used to calculate the distribution as Green's function in response to a Dirac delta distribution at the tropical tropopause. The result is an inverse Gaussian PDF that describes transport reasonably well. Their results show moreover that the ratio of the second and first moment of the age spectrum is rather constant in certain stratospheric regions, a relationship that is still used for the observational estimation of mean AoA from SF_6 or CO_2. Mathematically, the age spectrum in Hall and Plumb (1994) is described as follows:

$$G\left(z,t'\right) = \frac{z}{2\sqrt{\pi K t'^3}} \cdot e^{\left(\frac{z}{2H} - \frac{Kt'}{4H^2} - \frac{z^2}{4Kt'}\right)}, \quad (3)$$

with K as the constant diffusion coefficient, z as the vertical coordinate and H as the scale height of the air density ϱ. The latter can either be gained from an density-altitude fit ($\varrho = \varrho_0 \cdot e^{-\frac{z}{H}}$) or approximated by a constant value. The first moment Γ (i.e., mean) and the central second moment Δ^2 (i.e., variance) are then defined as (Hall and Plumb, 1994)

$$\Gamma(z) = \int_0^\infty G\left(z,t'\right) \cdot t' \cdot \mathrm{d}t', \quad (4)$$

$$\Delta^2(z) = \frac{1}{2} \cdot \int_0^\infty G\left(z,t'\right) \cdot (t' - \Gamma(z))^2 \cdot \mathrm{d}t'. \quad (5)$$

Transfer of Eq. (3) to complex stratospheric transport is quite difficult, as Hall and Plumb (1994) state that their inverse Gaussian solution for one-dimensional diffusion is restricted to long-lived trace gases (Holton, 1986; Plumb and Ko, 1992) in a setup with only annual mean transport. In such cases, the diffusion coefficient K has to be considered to be a measure of net vertical advection and mixing rather than simply small-scale diffusion. Their age spectra therefore do not incorporate any seasonal or inter-annual variability in transport. Model studies of annual and seasonal age spectra (Reithmeier et al., 2008; Li et al., 2012a, b; Ploeger and Birner, 2016) have shown that age spectra exhibit multiple modes representing seasonal fluctuations of stratospheric transport (see Sect. 2.2). However, even though the inverse Gaussian

solution of Hall and Plumb (1994) does not include multiple peaks intrinsically and might not provide a perfect solution at any point in the stratosphere, it can certainly provide a robust approximation of the general (smoothed) shape of these multimodal spectra in models (e.g., Fig. 3 in Li et al., 2012a, Fig. 7 in Li et al., 2012b, or Fig. 5 in Ploeger and Birner, 2016). A prescribed age spectrum shape, even if only a fit, is indeed valuable for observational studies with very limited data. If the general shape is well constrained a priori, all information from trace gases measurements will solely be used to tune the spectrum until it is as close as possible to real transport. Approaches of this kind require fewer data than cases with a fully unconstrained shape, where more information about transport processes is needed. Together with the relatively low amount of free parameters of the inverse Gaussian distribution in Hall and Plumb (1994), these are important factors of why Eq. (3) has been the basis of many studies focusing on the retrieval of age spectra from observational data.

Ehhalt et al. (2007) used the formalism of Hall and Plumb (1994) to derive a method where mixing ratios of short-lived trace gases are correlated against those of very long-lived ones. This correlation is identical to a vertical profile in a trace-gas-based coordinate system. Technically, the method can also be applied using other vertical coordinates such as altitude, pressure or potential temperature as long as there is an exponential decay in the vertical space. In order for this to work, a height-independent chemical lifetime has to be assumed, as Eq. (2) only then turns into a Laplace transform of the age spectrum and makes for a constant vertical diffusion coefficient. This is quite an elegant approach, since it allows for an analytical solution of the equation. The study concluded that the resulting age spectra from data between 30 and 35° N in the lowermost stratosphere are most probably valid for transit times of up to 1 year. Application of Ehhalt's method is restricted to this very narrow region around the subtropical and midlatitude tropopause. Complete global stratospheric transport, though, cannot be described by a height-independent diffusion coefficient and constant chemical depletion. Schoeberl et al. (2000) had already proposed a generalized solution to this problem by discretizing Eq. (2) for long-lived trace gases with chemistry along an average Lagrangian path and solving the corresponding system of linear equations. This strategy does not require a prescribed age spectrum, but our tests with the method show that the matrix that has to be inverted is close to singular and does not lead to numerically stable solutions even considering appropriate solvers. In a very recent study by Podglajen and Ploeger (2019), this method is modified leading to a stable matrix inversion and promising results. Schoeberl et al. (2005) took a different approach by allowing both transit-time-dependent lifetimes and a vertically varying diffusion coefficient in the age spectrum of Hall and Plumb (1994). They insert Eq. (3) into Eq. (2), replace t' by $(t' - t_{\mathrm{off}})$, and perform a multiparameter least-squares fit on z, K and t_{off} to find a matching age spectrum by minimizing the sum of squared deviations between the observed and inverted trace gas mixing ratio in their model. The temporal offset t_{off} is introduced to incorporate the effect that diffusion does not show an instantaneous response to advected trace gases. In comparison to Ehhalt's method, Schoeberl's method provides major advantages, as it is still straightforward to use but with a less restrictive approximation of ongoing physical mechanisms. It holds a much larger area of applicability in the stratosphere. A similar approach for long-lived trace gases (deseasonalized CO_2) has been applied by Andrews et al. (1999) with reasonable results.

There are, however, two points concerning the method's formulation that are worthy of discussion. First, the vertical coordinate z should be considered to be a measure of position in the atmosphere to ensure that the result represents the age spectrum exactly at the given location. We propose excluding it from the fit so that all information about transport is inverted into the time- and space-dependent diffusion coefficient $K(\boldsymbol{x}, t)$. Technically, calling $K(\boldsymbol{x}, t)$ a diffusion coefficient is imprecise, since it includes information about all occurring transport processes and does not depend on a specific substance. It provides an undirected measure of transport strength and will therefore be generally referred to as a transport parameter. Second, the formulation of the age spectrum by Schoeberl et al. (2005) results in a complex age spectrum for $t' < t_{\mathrm{off}}$, as negative values appear in the square root. Chhikara and Folks (1989) demonstrate in their Fig. 2.1 and 2.2 that an inverse Gaussian distribution in its most general form can include an offset when varying only shape parameter and mean. Reasonable age spectra might still be derived when neglecting an explicit temporal offset in the formulation. With this reflection, the necessary fit parameters reduce to only the diffusion coefficient, simplifying the numerical implementation of the method considerably. This also requires that the tail of the spectrum is considered on a reasonably long timescale to regard the mathematical necessity of integrating from 0 to infinity (see Appendix A for numerical details). Additionally, a single parameter fit is by definition less prone to run in a local instead of a global minimum when optimizing its parameter. Applying those simplifications to Eqs. (2) and (3) leads to

$$\frac{\chi(\boldsymbol{x}, t)}{\overline{\chi_0}} := R = \int_0^\infty e^{-\frac{t'}{\tau(t')}} \cdot \frac{z}{2\sqrt{\pi K(\boldsymbol{x}, t) t'^3}} \cdot e^{\left(\frac{z}{2H} - \frac{K(\boldsymbol{x}, t) t'}{4H^2} - \frac{z^2}{4K(\boldsymbol{x}, t) t'}\right)} \cdot \mathrm{d}t'. \quad (6)$$

The ratio of measured mixing ratio and entry mixing ratio will from now on be called R. This is the main equation for the modified inverse method. The transport parameter $K(\boldsymbol{x}, t)$ is then optimized numerically until the inverted ratio R equals the modeled or measured ratio with 5 % accuracy. The procedure is described in detail in Appendix A. In order

to obtain a mathematically correct PDF, it is always enforced that $G(\boldsymbol{x}, t', t)$ satisfies the following equation:

$$\int_0^\infty G(\boldsymbol{x}, t', t) \cdot \mathrm{d}t' = 1. \tag{7}$$

The inverse method yields the important benefit that the procedure can be applied to punctual data rather than complete vertical profiles of mixing ratios (Ehhalt's method). This is particularly relevant for observational data, since complete vertical profiles at a fixed latitude are hard to retrieve from airborne measurements. By using the inverse method, every data point can be evaluated separately and provides information without depending on values above or below it. The modified inverse method allows for a sophisticated analysis of stratospheric transport by providing a possibility to estimate age spectra from short-lived trace gases with reduced numerical effort. We tested the applicability of Ehhalt's method within the model setup of this paper and found results that are in accordance with Ehhalt et al. (2007). As the method proves to be indeed restricted to the lowest part of the stratosphere, we decided not to consider it further on. All methods discussed here are limited to a transit-time-independent transport parameter $K(\boldsymbol{x}, t)$ and express transport without consideration of an explicit temporal trend in the analyzed range of transit time. At the same time, resulting age spectra of both methods have the important drawback that they only show one clear peak and do not intrinsically reproduce seasonal variation in the net upward mass flux.

2.2 Imposed seasonal cycle

When studying seasonal variability in transport processes, it was already mentioned that the tropical upward mass flux has a distinct seasonal cycle, with a clear maximum during NH wintertime and a minimum in NH summer (Rosenlof, 1995). This cycle is also visible in age spectra, as recent transport model studies have shown (e.g., Reithmeier et al., 2008; Li et al., 2012a; Ploeger and Birner, 2016). The annual mean shape of the pulse spectra is well approximated by an inverse Gaussian distribution with one obvious mode. But age spectra for single seasons show several modes representing the variable flux of mass into stratosphere during the different seasons. This is an important feature, especially for species with a seasonal cycle (e.g., CO_2). The inverse method does not reproduce those multiple peaks intrinsically when inferring seasonal mean spectra, since Eq. (3) is the formulation of a monomodal inverse Gaussian PDF. The amplitude of the age spectra is likely to differ in all four seasons as a feedback to seasonal variability in trace gas mixing ratios but yet is only monomodal.

A possible approach to derive a multimodal spectrum for a specific season is to scale the age spectrum in Eq. (6) appropriately. Rosenlof (1995) found that the strength of the tropical mass flux into the stratosphere across the tropical tropopause at 70 hPa has its maximum in NH winter and its minimum in NH summer. The strength of this upward mass transport is reflected in the maxima and minima of the age spectrum. Knowing how the upward mass flux varies within a year might be used to adjust the age spectrum of a specific season. On the basis of the first three columns of Table 4 in Rosenlof (1995), the average ratio of the mass flux in each season relative to the remaining three is derived, which is, for instance, winter relative to summer etcetera. The intrinsic monomodal spectrum of each season will then be adjusted using these flux ratios at every point in transit time. When considering, for example, an arbitrary monomodal summer spectrum, its amplitude has to be modulated by approximately +25 % for transit times that correspond to spring and fall and by circa +60 % for transit times that represent winter according to the flux ratio. For every transit time in between a proper intermediate ratio has to be applied. Finally, no scaling takes place at transit times that correspond to the respective season of the spectrum (summer in the example – see down below for further detail). All this can be realized mathematically by a cosine, which is phase shifted to fit for a specific season. That results in the definition of a transit-time-dependent scaling factor S for each season:

$$S\left(t'\right) = \left(A + B \cdot \cos\left(\frac{2\pi}{365\ \mathrm{days}} \cdot t' + C\right)\right). \tag{8}$$

Herein, A, B and C denote constant factors that are only depending on the considered season. Due to the fact that increasing transit time is equivalent to going back in time, NH winter (December–January–February or DJF) is followed by NH fall (September–October–November or SON), then NH summer (June–July–August or JJA) and finally NH spring (March–April–May or MAM). In order to estimate the uncertainty of the tropical upward mass flux in Rosenlof (1995), the dataset is compared to data of the ERA-Interim reanalysis (Dee et al., 2011), the MERRA-2 reanalysis (Gelaro et al., 2017), the JRA-55 reanalysis (Kobayashi et al., 2015), the NCEP CFSR reanalysis (Saha et al., 2010) and also the EMAC simulation. The resulting tropical upward mass fluxes at 70 hPa are shown in Fig. 1a. The relative seasonal cycle is quite similar throughout all datasets although the absolute values differ, with EMAC having the strongest mass flux and Rosenlof (1995) the weakest. EMAC is also the only case where the maximum is situated in SON rather than DJF, but only with a small difference. Since it is only of interest for Eq. (8) how the seasons scale relative to each other, all data show that this behavior appears to be quite similar. The scaling components A and B are derived in such a way that they provide a robust approximation of the seasonal cycle in Rosenlof (1995). The resulting constants are depicted together with the phase shift C in Table 1. When approximating the combined data of all reanalyses and EMAC similarly, the resulting scaling factors agree within 15 % with the scaling factor of the Rosenlof (1995) data. The scaled age spectrum

$G_{\text{seas}}(\boldsymbol{x}, t', t)$ is then given by

$$G_{\text{seas}}(\boldsymbol{x}, t', t) = \frac{z}{2\sqrt{\pi K(\boldsymbol{x}, t) t'^3}} \cdot e^{\left(\frac{z}{2H} - \frac{K(\boldsymbol{x},t)t'}{4H^2} - \frac{z^2}{4K(\boldsymbol{x},t)t'}\right)} \cdot \left(A + B \cdot \cos\left(\frac{2\pi}{365\text{ days}} \cdot t' + C\right)\right) = G(\boldsymbol{x}, t', t) \cdot S(t'). \quad (9)$$

As above, it is always ensured that the integral of the consequent spectrum $G_{\text{seas}}(\boldsymbol{x}, t', t)$ satisfies Eq. (7). The age spectrum $G_{\text{seas}}(\boldsymbol{x}, t', t)$ is manually normalized ($G^N_{\text{seas}}(\boldsymbol{x}, t', t)$) after the scaling process by

$$G^N_{\text{seas}}(\boldsymbol{x}, t', t) = \frac{G_{\text{seas}}(\boldsymbol{x}, t', t)}{\int_0^\infty G_{\text{seas}}(\boldsymbol{x}, t', t) \cdot \mathrm{d}t'}. \quad (10)$$

It is mandatory that t' must be given in days in Eqs. (8) and (9) for a correct result. A year is approximated only by 365 days. Fig. 1b illustrates the evolution of the complete scaling factor S with transit time during 1 year. All scaling factors equal 1 for transit times 0 years and all integer multiples of 1 year (i.e., 2, 3 years, etc.). In that way, the spectrum of the considered season remains unmodified within its season of origin during the scaling process and is then only altered when re-normalizing the whole spectrum uniformly. As intended, JJA has the weakest upward mass transport of the year, with all other seasons being scaled up relatively, while DJF exhibits the strongest flux with downscaling during every other season. The intermediate periods MAM and SON display a similar scaling only with the phase shift that was striven for by introducing parameter C. Besides this, the scaling factor correctly shows its desired maximum on any curve at transit times that represent DJF, whereas the corresponding minimum always appears at summer transit times. When inserting this new formulation into the basic equation of the inverse method (Eq. 6), the modified version becomes

$$R_{\text{seas}} = \int_0^\infty e^{-\frac{t'}{\tau(t')}} \cdot G^N_{\text{seas}}(\boldsymbol{x}, t', t) \cdot \mathrm{d}t'. \quad (11)$$

The numerical procedure to find a matching age spectrum is described in Appendix A. Implementing both Eqs. (11) and (6), it can be estimated whether the seasonal cycle distorts the result or contributes to a better approximation of the pulse age spectra with respect to seasonality. In theory, the annual mean spectrum should be equivalent in both versions of the inverse method if the imposed seasonal cycle works correctly. The lowermost stratosphere is hereby likely to be a critical region where tropospheric air also enters through the extratropical tropopause. This mechanism violates the assumption of a single entry through the tropical tropopause, which is the basis of the inverse method. Transport through the extratropical tropopause also exhibits a distinct seasonal cycle, especially in the Northern Hemisphere (Appenzeller et al., 1996), possibly leading to wrongly scaled spectra when using the scaling factor presented above. The inverse method is thus likely to produce distorted age spectra when applied in this critical region. The seasonal cycle is not included in the fitting procedure as a free parameter but imposed based on mean values of the tropical upward transport. The inverse method is also not able to incorporate any temporal variabilities in the seasonality of the flux.

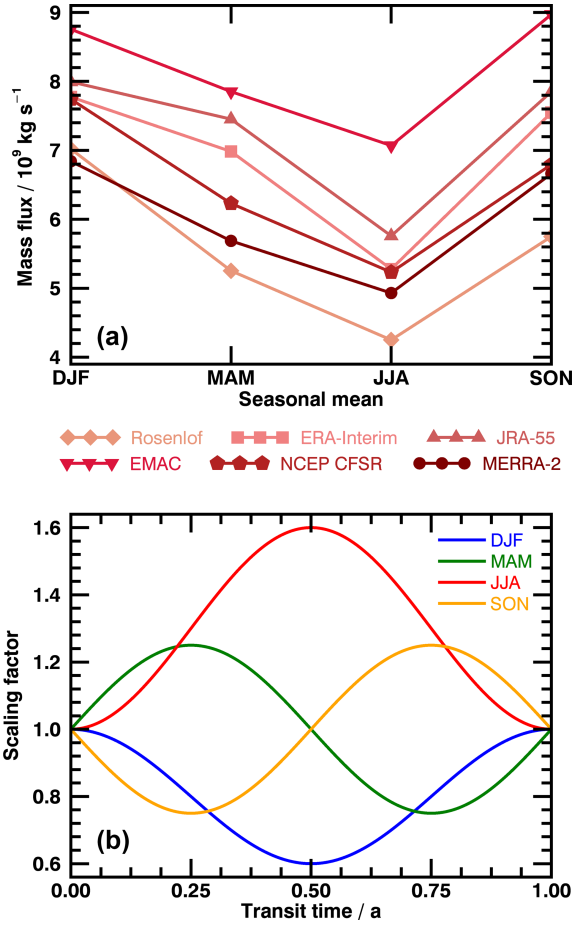

Figure 1. **(a)** shows the tropical upward mass flux at 70 hPa. Data are from four reanalyses as well as the evaluated EMAC simulation and Rosenlof (1995). **(b)** illustrates derived scaling factors of age spectra in 1 year as a function of transit time. The four seasons are color coded. Increasing transit time means backward in time. The starting point of each curve is equivalent to the season it depicts.

Table 1. Scaling constants and phase shift for each season.

	A	B	C
DJF	0.8	0.2	$0.0 \cdot \pi$
MAM	1.0	0.25	$1.5 \cdot \pi$
JJA	1.3	0.3	$1.0 \cdot \pi$
SON	1.0	0.25	$0.5 \cdot \pi$

The use of model data for a general proof of concept of the method's capabilities is very suitable, since the idealized setup yields the advantage of lifetimes being independent of transit time and transport pathways. Scientific focus in this study is on the method's potential to capture stratospheric transport with its underlying assumptions in a solely dynamical model setup. The model of choice is EMAC, being a potent and very well-performing chemistry climate model which has been used in many studies regarding stratospheric transport and chemistry.

2.3 EMAC model simulations and data preparation

The ECHAM/MESSy Atmospheric Chemistry (EMAC) model is a numerical chemistry and climate simulation system that includes sub-models describing tropospheric and middle atmosphere processes and their interaction with oceans, land and human influences (Jöckel et al., 2010). It uses the second version of the Modular Earth Submodel System (MESSy2) to link multi-institutional computer codes. The core atmospheric model is the fifth-generation European Centre Hamburg general circulation model (Roeckner et al., 2006). For the present study we applied EMAC (ECHAM5 version 5.3.02, MESSy version 2.53.0) in the T42L90MA resolution, i.e., with a spherical truncation of T42 (corresponding to a quadratic Gaussian grid of approximately 2.8° by 2.8° in latitude and longitude) with 90 vertical hybrid pressure levels up to 0.01 hPa. The free-running time-slice simulation covers a period of 20 model years and is performed without chemistry and ocean models, i.e., sea surface temperatures and radiatively active trace gases are prescribed. This is a valid approach, since the study focuses on transport of passive trace gases as well as conceptual tests of the inverse method. As a lower boundary, observations of sea surface temperatures and sea ice concentrations from the Hadley Centre Sea Ice and Sea Surface Temperature dataset (HADISST) are fixed at monthly mean values averaged from 1995 to 2004. Additionally, greenhouse gases are prescribed at the constant value of year 2000. The climatology is therefore set to the state of the year 2000 and has no temporal trend over the whole model period. Still, seasonal and interannual variability is present. Here, monthly and zonal average data are used and analyzed from December of year 9 to November of year 19. All data in this range are then finally averaged with respect to seasons, on the one hand, and annually, on the other hand, over the complete period of 10 years to gain solid statistics.

In order to retrieve age spectra from the model itself, 40 chemically completely inert trace gases are included that are released as a pulse every 3 months at the tropical surface between 12.5° N and 12.5° S, starting in January of year 1. After 10 years, every pulse tracer has been pulsed once, the cycle starts again with resetting the first tracer back to 0 in October of year 9, it is pulsed again in January of year 10, etc. From this period on, complete age spectra that range over the full period of 10 years can be inferred by creating a map of the boundary impulse response (BIR) for every point on the model grid. This concept is first described by Haine et al. (2008) and refined for transient simulations by Ploeger and Birner (2016). An illustration of such a map from our EMAC simulation is shown in Fig. 2, where a horizontal cut (backward in source time) through the complete map gives the age spectrum at a specific field time. This provides an age spectrum with a temporal resolution of 3 months. Finer resolutions would require further pulse tracers (120 for a resolution of 1 month) and are numerically expensive. Li et al. (2012a) presented a sophisticated simulation with 12 pulse tracers released in every month of 1 model year simulated over 20 years field time, which is then cyclically repeated to cover a period of 20 years source time. This computationally efficient procedure provides seasonal age spectra with a high temporal resolution of 1 month by neglecting inter-annual variability in the spectra. The simulation presented in this paper, however, features inter-annual variability. To keep the balance between numerical costs and scientific value, a resolution of 3 months in source time is selected as being the absolute minimum for an investigation of seasonality, where each season is represented by one point per year of transit time. Together with the pulse tracers, a linearly increasing completely inert trace gas (clock tracer) is implemented to derive the mean AoA as a lag time that the surface mixing ratio needs to reach an arbitrary location in the stratosphere. In general, the clock tracer mean AoA will be larger than the first moments of the intrinsic pulse tracer age spectra. This is a direct consequence of the transit time being limited to 10 years. The tail of the age spectrum is underestimated and an extension is required. The formulation by Ploeger and Birner (2016),

$$G\left(\boldsymbol{x},t',t\right)=\begin{cases} G\left(\boldsymbol{x},t',t\right) & \text{for} \quad t'<10 \text{ years} \\ G\left(\boldsymbol{x},t'_{\omega},t\right)\cdot e^{-\frac{(t'-t'_{\omega})}{\omega}} & \text{for} \quad t'>10 \text{ years} \end{cases}, \tag{12}$$

is applied to all seasonal pulse spectra to correct them for transit times up to 300 years (see Appendix A). ω is a scale time derived from an exponential fit of the age spectrum between t'_{ω} and 10 years transit time. t'_{ω} is set to 5 years as threshold for the fit, in accordance with Ploeger and Birner (2016). The extended age spectra are then normalized to be mathematically correct.

For the application of the inverse method, a further set of 40 trace gases is included with prescribed constant lifetimes ranging from 1 month up to 118 months by steps of 3 months. This simplification allows for an investigation of the method's basic principle by eliminating the variability in chemical depletion. These trace gases are constantly released in the same source region as the pulse tracers with a mixing ratio of 100 %. Figure 3 visualizes annual mean vertical profiles of five of these radioactive tracers at 85, 55 and 10° N relative to the tropopause. The dashed line marks the

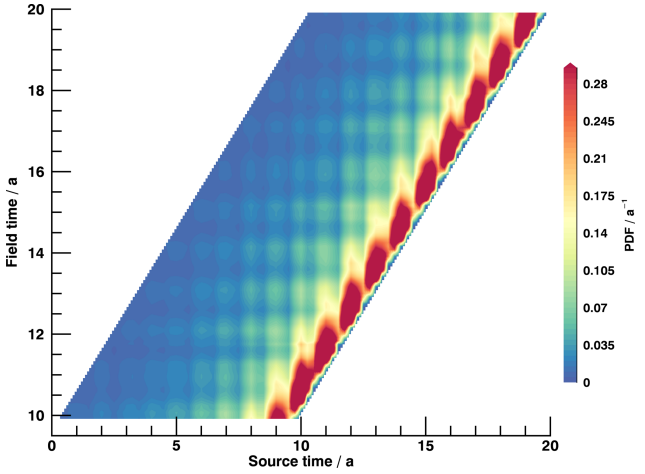

Figure 2. Exemplary BIR map for the analyzed time span of the EMAC simulation at 55° N and 70 hPa. Source time represents the date when a specific pulse tracer is initialized, while field time is the progressive time of the model simulation. The amount fraction of the PDF is color coded.

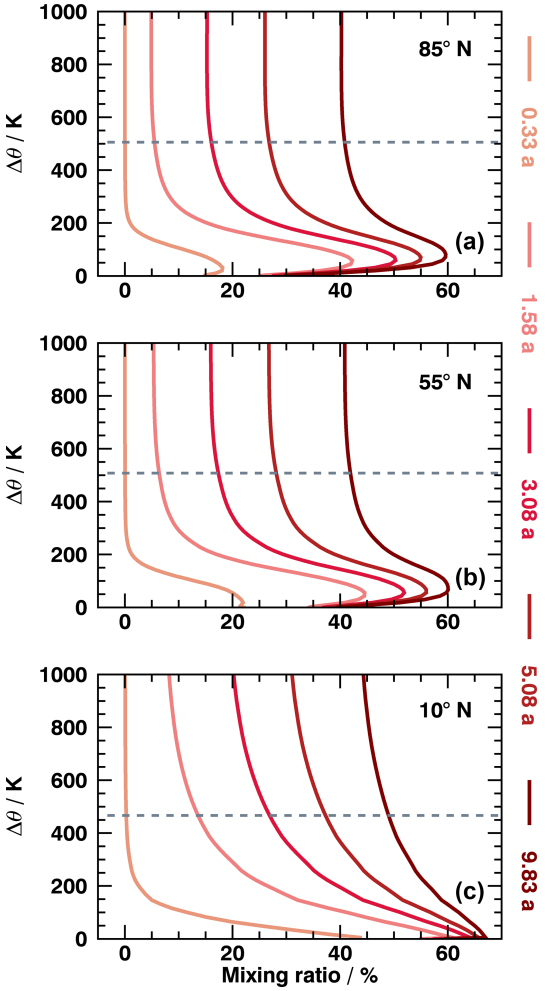

Figure 3. Vertical profiles of five radioactive trace gases at 85° N **(a)**, 55° N **(b)** and 10° N **(c)** as a function of potential temperature above tropopause. Lifetimes of species are colored. Dashed horizontal line marks the 10 hPa level.

level of 10 hPa, where multiple short-lived trace gases have a mixing ratio of less than 10 %. As this is critically close to the accuracy of the inversion, no reliable information will be gained by the respective tracers. 10 hPa marks the upper boundary for the analysis in this paper. The maxima are located above the tropopause at extratropical latitudes, which is not intuitive, since one would expect them to be within the tropopause layer. This might be caused by an inhomogeneous distribution of these trace gases in the troposphere due to their sole initialization in the tropical boundary layer in combination with cross-tropopause transport. Since their mixing ratio is lower in the extratropical troposphere than in the tropics (source region), mixing of this air mass into the corresponding region of the stratosphere could be the cause of the reduced burden in the extratropical tropopause layer. Profiles in the Southern Hemisphere exhibit a qualitatively identical behavior (not shown).

A problem for the comparison of the spectra is that all pulse spectra are referred to earth's surface, whereas the inverse method uses the tropical tropopause as a reference layer. When trying to refer inverse spectra to the surface, results broaden significantly and do not match the pulse spectra. This is likely a consequence of the solution given by Hall and Plumb (1994) that uses one-dimensional diffusion to approximate transport above the tropopause and might not be sufficient for application in the tropical troposphere. Still, to make the spectra comparable, the annually averaged mean AoA from the clock tracer at the tropical tropopause is derived for the evaluated field time period. It is considered to be the mean transit time from surface to the tropopause within the model. This quantity (~ 0.19 years) is then subtracted from all clock tracer mean AoA as well as transit times of the pulse age spectra, ensuring that the first transit time value is still 0 years. Resulting negative values are omitted. The tropopause is directly extracted from EMAC for the complete analysis, with the exact definition being described in Jöckel et al. (2006). To reduce errors in spectra, mean AoA and variance when approaching the tropopause, data are omitted up to 30 K above the tropopause, as this is described as a transition layer with major tropospheric influence (Hoor et al., 2004; Bönisch et al., 2009). Possible inadequacies of the inverse method and of the artificial seasonal cycle in the lowermost stratosphere (see Sect. 2.2) are incorporated by introducing a threshold of 1.5 years of clock mean AoA for the evaluation of the inverse method. The clock tracer provides the most accurate intrinsic value of mean AoA available in the model. Above the threshold, the tropopause is reasonably far off and seasonality should, in theory, mostly be steered by the tropical upward mass flux. In the model data, the tropical region is defined as average between 12.5° N and 12.5° S to

be consistent with the source region of the pulse and radioactive tracers. The entry mixing ratios for the inverse method are derived within this area as annual mean values.

Atmospheric pressure is in general not a suitable choice when investigating transport processes and especially mixing. In the stratosphere, bidirectional stirring occurs mainly parallel to isentropic surfaces, which makes potential temperature the best choice for such a study. To include an adequate description of all transport mechanisms, the local potential temperature difference to the tropopause is calculated for every stratospheric model grid point and used as vertical coordinate z for the inverse method. The scale height H is then fitted properly along this introduced coordinate.

3 Results

The following section provides the results of the model study to evaluate the performance of the inverse method. Annual and seasonal spectra are presented for three different pressure levels (70, 10 and 140 hPa) in the midlatitudes at 55° N for pulse and inverse spectra, the latter being presented with and without the seasonal cycle. This is a major region of interest, where both branches of the BDC are present and mixing is especially enhanced due to wave breaking. Many observational campaigns focus specifically on the northern midlatitudes with abundant trace gas measurements. Age spectra are derived in this specific region in order to deeply understand ongoing transport processes. In the second part, the first and second moments of the distributions are shown to compare resulting spectra on a larger scale, both annual and seasonal. The moments are derived using Eqs. (4) and (5) and constitute a suitable analytical tool, since an inverse Gaussian PDF can be well approximated by its mean and width. The width of a spectrum around its first moment is computed as the square root of the spectrum's variance. There is also a brief analysis of the ratio of the second to first moment ($\frac{\Delta^2}{\Gamma}$ or ratio of moments), which is used to infer mean AoA from measurements of very long-lived trace gases. The pulse and inverse spectra's performance is assessed and evaluated with respect to the results of Hall and Plumb (1994). Finally, tests of applicability to observational data are presented, which include the number of trace gases necessary for the inversion as well as an estimation of how uncertainties in the knowledge of chemical lifetimes influence resulting age spectra and might be compensated.

3.1 Stratospheric age of air spectra

3.1.1 70 hPa

Figure 4 shows age spectra at 70 hPa and 55° N. Since 70 hPa is the origin of the tropical upward mass flux, the seasonal cycle should in theory work best on this pressure surface. The annual mean inverse spectrum without a seasonal cy-

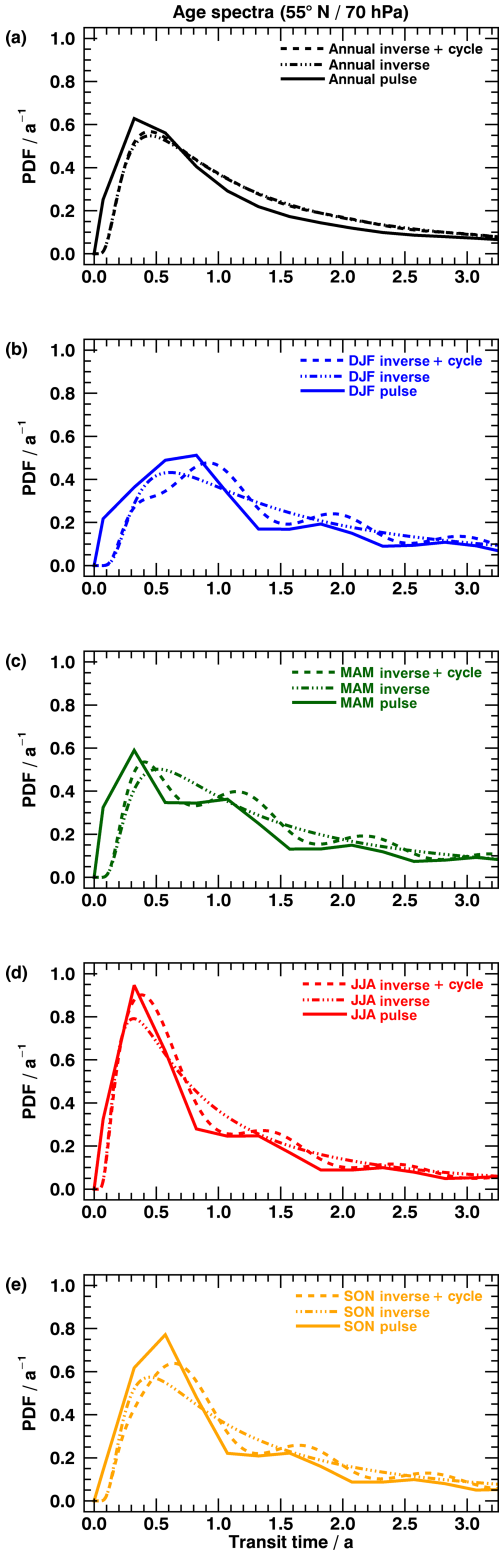

Figure 4. Age spectra at 55° N and 70 hPa. **(a)** shows annual mean age spectra; **(b–e)** shows related seasonal spectra. Solid lines represent pulse spectra, dashed lines inverse spectra with seasonal cycle and dashed–dotted lines inverse spectra without seasonal cycle.

cle (dashed–dotted line in panel a) complies well with the annual pulse spectrum (black solid line), with slightly reduced amplitude and overestimated tail. The modal age (transit time at maximum) of the inverse spectrum agrees qualitatively with the modal age of the pulse spectrum. Including the seasonal cycle into the spectrum (dashed line in panel a) does not noticeably alter the annual mean curve, as it exhibits nearly identical modal age and amplitude. This is an indicator that the formalism of the seasonal cycle modifies the seasons but cancels out the annual average. The seasonal pulse spectra (solid curves in panels b to e) indicate that the seasonal cycle of tropical upward transport is important at this pressure level as multiple distinct maxima and minima are evolving with deviating modal ages. The inverse spectra without a seasonal cycle (dashed–dotted – panels b to e) also show diminished amplitudes for all seasons but still approximate the pulse spectra quite reliably. Yet the inverse spectra without a seasonal cycle do not reflect transport seasonality due to their prescribed monomodal shape, and a comparison of modal ages with the multimodal seasonal pulse spectra is not useful. When including the seasonal cycle, however, the results (dashed – panels b to e) coincide remarkably with the pulse spectra, exhibiting equivalent minima and maxima at according transit times, but still with slightly enhanced tails and underestimated amplitudes (especially SON). The timing of modal ages for the different seasons agrees with the pulse spectra within 0.1 years, and the resemblance of the amplitudes has also increased. The transit time of the secondary and ternary peaks are then prescribed with 1 year of distance and match the pulse spectra qualitatively well. It seems that the prescribed seasonal cycle constitutes a reasonable choice for describing seasonality in transport at this altitude. Also, it is evident that exclusion of t_{off} in the formalism of the inverse method still leads to matching spectra, all with a similar offset. Clock mean AoA values range between 2.51 years (maximum – DJF) and 1.92 years (minimum – JJA) and are located above the threshold of 1.5 years (see Sect. 2.3).

3.1.2 10 hPa

Age spectra around the previously defined upper boundary (10 hPa) of the inverse method at 55° N are depicted in Fig. 5. At this pressure level, the tail of the spectrum is important to fully describe transport. Annual mean inverse spectra with and without a seasonal cycle (panel a) show a similar performance, both with underestimated amplitude and enhanced tail with respect to the pulse spectra, but no significant differences between them. Also, the imposed cycle leads to similar modal ages for the annual mean spectra. Qualitative agreement of the annual inverse spectra with the annual mean pulse spectrum is nevertheless fairly good, although the modal age does not agree with the pulse peaks. Again, the inverse spectra derived here show an offset without explicit inclusion of t_{off}, similar to that found in the pulse spectra. The inverse spectra without a seasonal cycle (dashed–dotted

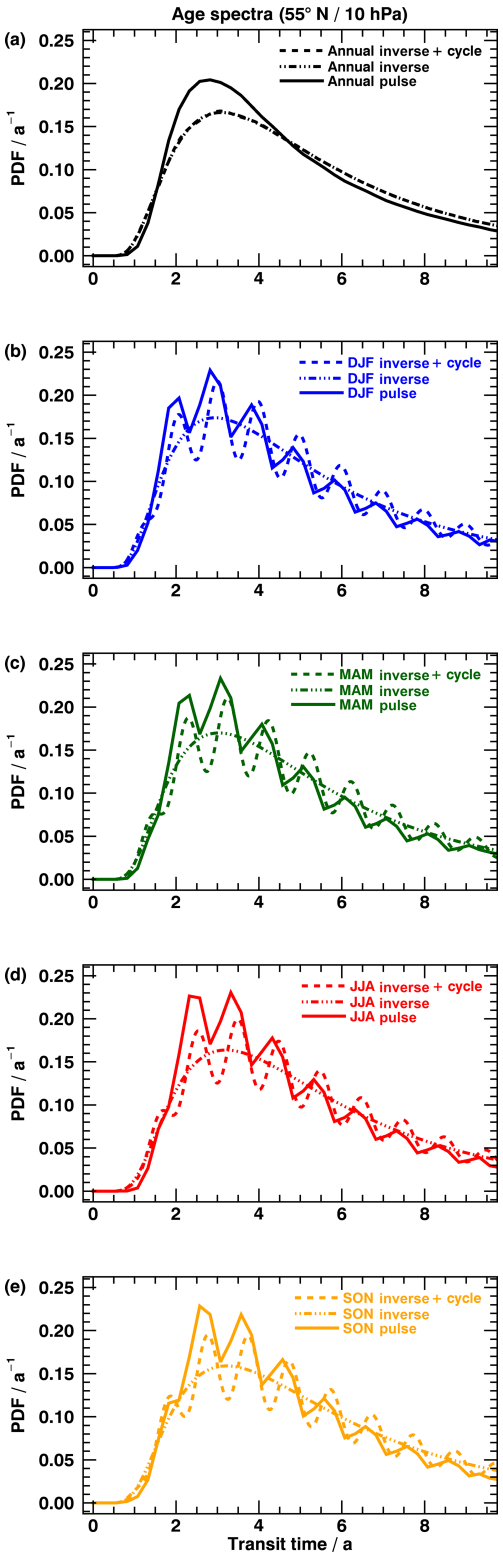

Figure 5. Same as Fig. 4, but at 55° N and 10 hPa.

– panels b to e) exhibit only small differences between their seasonal amplitudes. Since the annual mean of inverse and pulse spectra are very similar, it is likely that the seasonal pulse spectra would show a similar behavior if smoothed. The inverse spectra without a seasonal cycle show, just as in Fig. 4 for the 70 hPa level, underestimated amplitudes and slight overly pronounced tails. Again, a comparison of modal ages between the monomodal inverse and multimodal pulse spectra is not useful. Including the seasonal cycle (dashed – panels b to e), the resulting spectra prove to be similar to the pulse spectra only with slightly enhanced peaks for transit times greater than 4 years, which is probably a consequence of the coarse resolution of the spectra or of the scaling factor overestimating the actual influence of the tropical upward mass flux. The modal ages of the inverse spectra's maxima agree with the pulse spectra within up to 0.15 years. Some minor peaks appear between 1 and 2 years of transit time in the inverse spectra, which are not found in the pulse spectra. On the one hand, this may be caused by the coarse temporal resolution of the pulse spectra. On the other hand, the minor peaks could be an artefact in the inverse spectra due to the prescribed cycle. Again, the seasonal cycle provides an improvement such that the inverse spectra concur reasonably with the pulse spectra in this region of the stratosphere in contrast to monomodal spectra. The corresponding clock mean AoA values range from 5.42 years (maximum – SON) to 5.16 years (minimum – DJF) and are clearly above the threshold of 1.5 years (see Sect. 2.3).

3.1.3 140 hPa

Finally, age spectra for the lower stratosphere on the 140 hPa level are shown in Fig. 6. The temporal resolution of 3 months in the pulse spectra is quite critical for an evaluation in the lower stratosphere. The annual mean inverse spectrum without the seasonal cycle (dashed–dotted – panel a) fits the annual mean pulse spectrum (solid line) very well, exhibiting qualitatively similar amplitude and modal age. An exact comparison of the modal age is not useful due to very small transit times and comparatively large uncertainties. As above, the tail of the inverse spectrum seems to be slightly overestimated compared to the pulse spectrum. It is evident that now all seasonal pulse age spectra (solid – panels b to e) display a very similar modal age, with one clearly pronounced peak and only minor secondary maxima. This implies that seasonality is dominated in this area by a local seasonal cycle in the extratropical cross-tropopause transport and not by the tropical upward mass flux. Inverse spectra without a seasonal cycle (dashed–dotted – panels b to e) reproduce that shift between the seasons qualitatively, but yielding a much larger difference among the seasonal amplitudes, with an underestimated SON (slightly DJF) and overly pronounced MAM and JJA. The annual curve (dashed–dotted – panel a) compares well with the pulse spectrum nevertheless, indicating that over- and underestimation cancel out coincidentally. Since

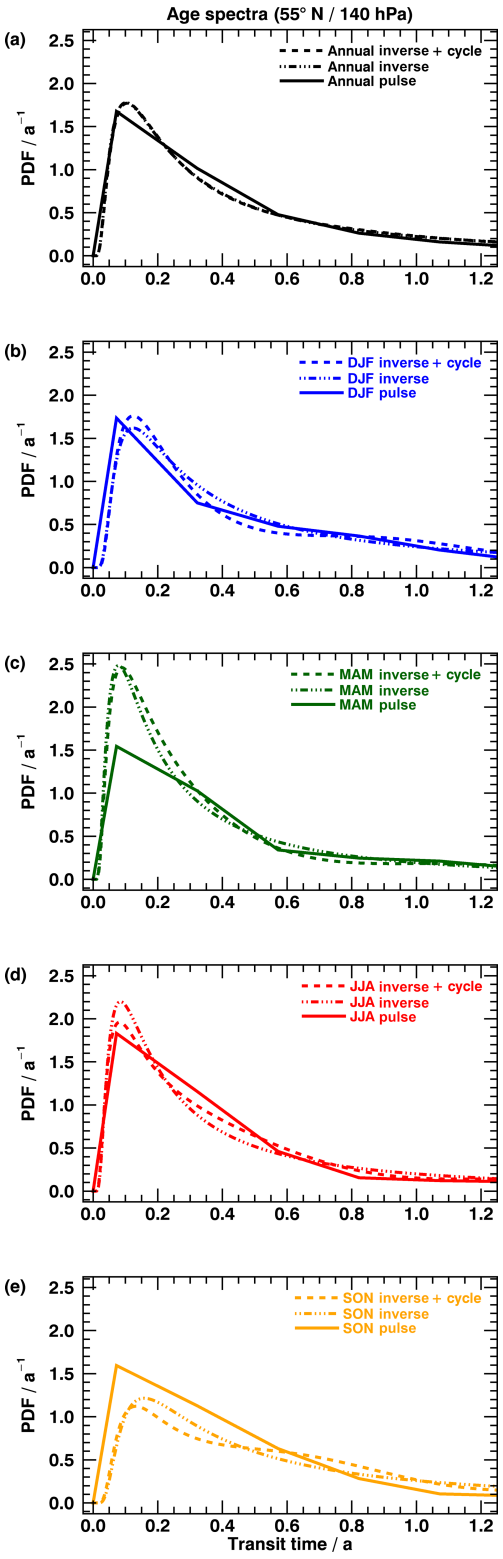

Figure 6. Same as Fig. 4, but at 55° N and 140 hPa.

seasonality seems to be controlled by local entrainment into the stratosphere in this region in the midlatitudes, a comparison of spectra including the artificial seasonal cycle (dashed – panels b to e) with the pulse spectra reveals seasonal differences that are inordinately distinct and very similar to the inverse spectra without a seasonal cycle. Also, all inverse spectra again exhibit a slightly overestimated tail. The extratropical cross-tropopause transport violates the assumption of single entry in the inverse method, which does not reproduce the pulse spectra correctly. The imposed cycle prescribes seasonality wrongly, as it cannot include variability in local transport trough the tropopause. The cycle of this extratropical transport across the tropopause is visible in Fig. 6 of Appenzeller et al. (1996) and differs significantly from the variability in the tropical upward mass flux. Hence, a modification of the imposed seasonal cycle would be necessary to include this effect. All these findings coincide well with our defined threshold, since 140 hPa at 55° N corresponds to a clock mean AoA between 1.04 years (maximum – MAM) and 0.52 years (minimum – SON) and falls below the introduced threshold of 1.5 years (see Sect. 2.3).

3.2 Analysis of moments

Since the seasonal cycle leads to an improvement of the inverse spectra except for the lower stratosphere and no significant changes in the annual mean state, all of the following results of the inverse method will include the imposed cycle.

3.2.1 Mean AoA

The percentage differences of the annual pulse and inverse mean AoA to the clock tracer are given in Fig. 7. The pulse mean AoA (panel a) matches the clock mean AoA very well except for the lower stratosphere. This is expected for sharp peaks of the age spectrum, such as in Fig. 6, where the temporal resolution of 3 months might not be sufficient and leads to inaccurate mean AoA. The tail correction of the spectra as well as their sole initialization in the tropics might also contribute to these deviations. For lower pressures, however, the approximation of the tail correction seems to be adequate with matching mean AoA values. The main differences between pulse and clock mean AoA also appear to follow the shaded area (panel b) of the 1.5-year threshold (see Sect. 2.3). If globally averaged for the pulse spectra, this results in deviations of -0.61 % above the threshold and $+14.5$ % below it. These findings imply that the tail correction works mostly as intended and only needs to be applied with caution around the tropopause region. The inverse mean AoA (Fig. 7b) is biased towards larger values, with the largest positive differences at polar and tropical latitudes. Negative differences are only found in the southern midlatitude lowermost stratosphere, which fall below the threshold of 1.5 years of mean clock AoA (dashed) for the most part. This is most probably linked to inaccurate seasonal spectra, which do not cancel out on annual average. Below the threshold, a global difference of $+44.3$ % is derived, whereas above the threshold this deviation reduces to $+13.3$ %. The bias may be attributed to the prescribed inverse Gaussian shape of the inverse spectra and is already indicated in the enhanced tails of all inverse spectra (Figs. 4 to 6). Since the annual mean is distorted towards larger mean AoA, it is likely that the seasonal fields show a similar behavior. To compare their structure and the reproduction of pulse spectra and clock tracer qualitatively, percentage changes relative to the annual mean state are evaluated.

Figure 8 shows mean AoA of the clock tracer and the pulse and inverse spectra as a latitude–pressure cross section. The left column gives the absolute annual average, and the remaining four columns give the percentage deviations of all seasons from each annual mean. The seasonal patterns of pulse spectra and clock tracer are matching very well with a few differences in the lowermost stratosphere (especially DJF and JJA). This coincides with the results of Fig. 7. The structures of mean AoA for the inverse method match the pulse spectra and clock tracer in each season very well qualitatively above the dashed area. Only the amplitude of the seasonal changes seems to be enhanced in direct comparison. This indicates that the seasonality that could already be detected in Figs. 4 and 5 extends mostly to the global scale. A clear boundary of those seasonal patterns is visible in the lower stratosphere around the threshold of 1.5 years of clock mean AoA (see, in particular, MAM or SON in the north). Below, the contours do not agree with the pulse spectra and clock tracer in multiple seasons and spatial regions and display an opposite sign to the pulse or clock tracer, especially in MAM and SON in the north. These differences generally emerge particularly in the Northern Hemisphere and are only visible to a small extent in the Southern Hemisphere (e.g., DJF – polar below 100 hPa). This is again consistent with the results of Appenzeller et al. (1996). They state that the net mass flux across the northern extratropical tropopause is largest downward in late MAM and largest upward in SON, whereas the upward mass flux across the tropical tropopause has its maximum in DJF and minimum in JJA. This local entry cannot be described by an annual mean entry mixing ratio at the tropical tropopause and is not well represented in the inverse method. The seasonal cycles of transport at the tropical and the extratropical tropopause differ distinctly so that the imposed seasonal cycle is not appropriate and leads to distorted inverse spectra (see Fig. 6). A combination of both effects is most probably the reason for the differences of the inverse method from clock tracer and pulse spectra in the northern midlatitude lower stratosphere in MAM and SON. In DJF and JJA, however, the strength of the extratropical cross-tropopause transport is vanishingly low (Appenzeller et al., 1996) so that an assumption of single entry through the tropical tropopause should be appropriate, leading to changes in inverse mean AoA that match clock tracer and pulse spectra. This seasonal cycle in extratropical cross-

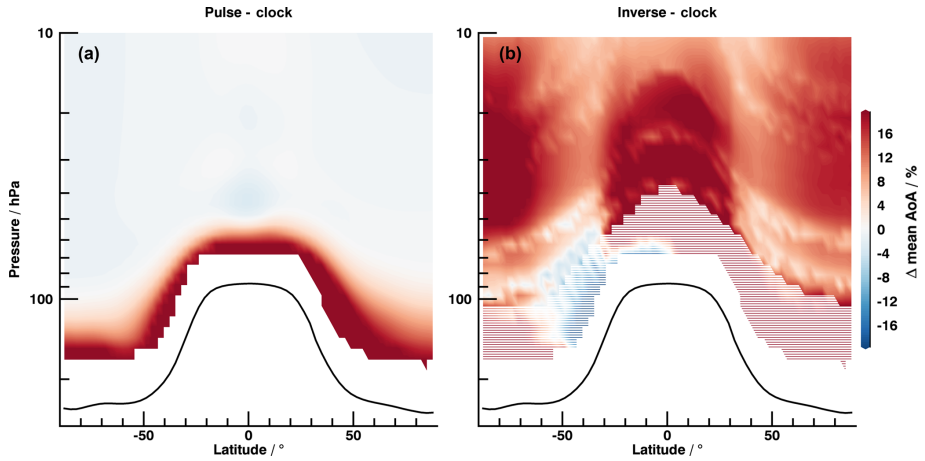

Figure 7. Annually averaged deviation of pulse **(a)** and inverse **(b)** mean AoA from clock mean AoA. White shaded area indicates threshold of 1.5 years of clock mean AoA. Tropopause is given as solid black line. Negative x values always denote southern hemispheric latitudes.

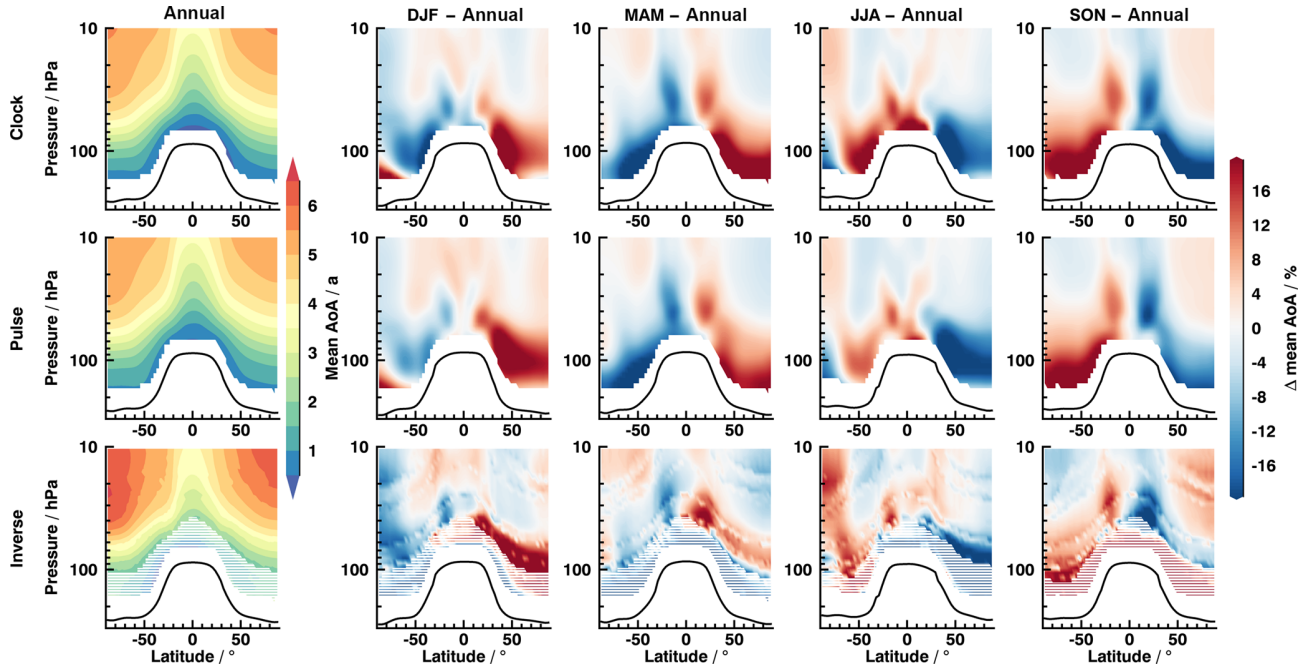

Figure 8. Mean AoA as global cross section. Left column shows absolute annual mean values, and remaining four columns denote percentage seasonal difference to annual average. Data are from clock tracer (Clock), from pulse spectra (Pulse) and from inverse spectra including the imposed seasonal cycle (Inverse). The tropopause is indicated by the solid black line. White dashed area marks pressure levels below clock mean AoA of 1.5 years. The wavy structure is visible in all seasonal plots of the inverse method, which follow hypothetical isentropic surfaces. Since potential temperature relative to the tropopause is used as vertical coordinate for the inverse method, these structures are artefacts of the implementation and do not influence the validity of results.

tropopause transport is much less pronounced in the Southern Hemisphere, being a plausible reason for a better performance of the inverse method there. The lower stratosphere proves to be a critical region for the inverse method on the global scale also, where further improvements are necessary. The deviations of inverse mean AoA from the pulse mean AoA and clock tracer at the tropical tropopause, however, are more likely only a result of the choice of an annual mean entry mixing ratio for the inverse method. The first moment of a distribution is an integrated measure of the complete spectrum and, as expected, the cross sections of mean AoA for the inverse method without a seasonal cycle (not shown) are identical in structure and strength to the ones presented in Fig. 8. The seasonal cycle only modulates seasons of weak

and strong transport properly, while keeping the average over the complete transit time period unchanged, similar to the annual mean spectrum.

3.2.2 Width

The following analysis focuses on three fixed latitudes, since the results presented in Fig. 8 have already shown a good performance of the inverse method beyond 1.5 years of clock mean AoA in both hemispheres. 85, 55 and 10° N are selected because the Northern Hemisphere appears to be more challenging to the method and is better covered by in situ measurement campaigns. The analysis on fixed latitudes is also advantageous, as the second moment of a PDF is strongly dependent on its first moment. An interpolation of mean AoA as vertical coordinate would be required for a global cross section, which might lead to inaccuracies and errors. Figure 9 depicts the width of spectra as function of their mean AoA for pulse (panels a, b and c) and inverse (panels d, e and f) spectra. Mean AoA serves as vertical coordinate. Filled diamonds represent data of vertical levels above the threshold of 1.5 years. For a better comparison, the pulse width is also given as grey shading in the bottom-row graphics. Seasonal differences of the pulse spectra widths appear to be marginal below mean AoA of 3 years at all latitudes. The width of a spectrum at a given mean AoA is similar and independent of the chosen latitude. With increasing mean AoA, curves begin to fan out for the different seasons, especially at 85° N. The curves at 55 and 85° N seem to be skewed towards smaller widths for larger mean AoA, indicating that the spectra become slightly tighter around their means at the upper boundary of the analyzed area. The inverse method again captures these effects quite well with similar curvatures, although the resulting spectra are systematically wider, just as presented in Figs. 4 to 6. A steady width ensues at larger mean AoA than for the pulse spectra. When the necessary threshold of 1.5 years is applied, primarily the obvious outliers and only few possibly matching data points are omitted (unfilled diamonds) at 85 and 55° N. That improves the overall agreement of the inverse and pulse width. Seasonal fluctuations in the tropics are comparatively high over the complete data range. Since the entry mixing ratio is significantly important for transport in that region, the annual mean entry mixing ratio is most probably the cause of this variability. At 55 and 85° N, however, the seasonality is of minor influence below 4 years of mean AoA, just as for the pulse spectra. Beyond that level, the curves start to fan out similarly, but with a stronger signal in particular at polar regions above 5 years. Coherently, the difference between pulse and inverse spectra regarding the initial point of curves fanning out is approximately the mean AoA bias of +13.3 % detected in Fig. 7. It might be concluded that the inverse method also reproduces the pulse width in a qualitative manner but is biased towards larger values, equivalent to the results for mean AoA and midlatitude spectra. The lowermost stratosphere likewise arises as a critical region with false width below the threshold. Since width is also an integrated value, exclusion of the imposed seasonal cycle gives an identical outcome.

3.2.3 Ratio of moments

The ratio of second to first moment $\frac{\Delta^2}{\Gamma}$ is crucial for some observational studies of mean AoA with mixing ratios of SF_6. Volk et al. (1997) propose a second-order fit to describe the temporal trend of this trace gas. They derive a relation to calculate mean AoA in the stratosphere up to 20 km altitude between 60° N and 70° S as a function of the fit parameters and the variance of the underlying age spectrum. A ratio of moments of 1.25 years with an uncertainty of 0.5 years is then chosen, according to Hall and Plumb (1994) and Waugh et al. (1997), to prescribe the dependence on the variance. This technique has since been refined and applied in further research (Engel et al., 2002, 2009, 2017; Bönisch et al., 2009) and is still used to this day albeit with different parameterizations. However, due to developments in climate modeling during the past 24 years, the EMAC model might include more processes on a finer grid than the models of Hall and Plumb (1994) and Waugh et al. (1997). This study offers the possibility to reassess the ratio of moments in a modern climate model also with focus on possible seasonal variability. Figure 10 depicts the absolute pulse and inverse ratio of moments for all four seasons and annual mean. The pulse results (top row) differ in terms of numbers from the results presented in Fig. 9 of Hall and Plumb (1994) as well as from the 1.25 years applied by Volk et al. (1997) below 20 km. The spatial distribution of the ratio of moments is nevertheless quite similar to Hall and Plumb (1994), with similar large areas of constant values in the lower stratosphere in both hemispheres in all seasons, but with increased vertical gradients at the same time. The seasonal cycle of transport affects the distribution of the ratio of moments slightly, with a maximum in DJF and a minimum in JJA on both hemispheres. Values in the Southern Hemisphere appear to be slightly larger in the lowermost stratosphere compared to the north. On the basis of Fig. 10, an annual mean ratio of moments of approximately 2.0 years for the same spatial region as in Volk et al. (1997) is detected. The inverse method (bottom row) does not reproduce the ratio from the pulse spectra in any season with globally divergent structures and numbers. This is likely caused by the biased mean AoA and width presented in the previous sections. Since the shape of the annual mean ratio of moments of the pulse spectra compares well with absolute annual clock, pulse and also inverse mean AoA (Fig. 8), it seems plausible that the inverse spectra variance is more likely the driving factor of arising deviations. The mathematical fact that variations in mean AoA always contribute squared to the second moment (Eq. 5) stresses this assumption. Again, removing the imposed seasonal cycle from the inverse method yields identical results.

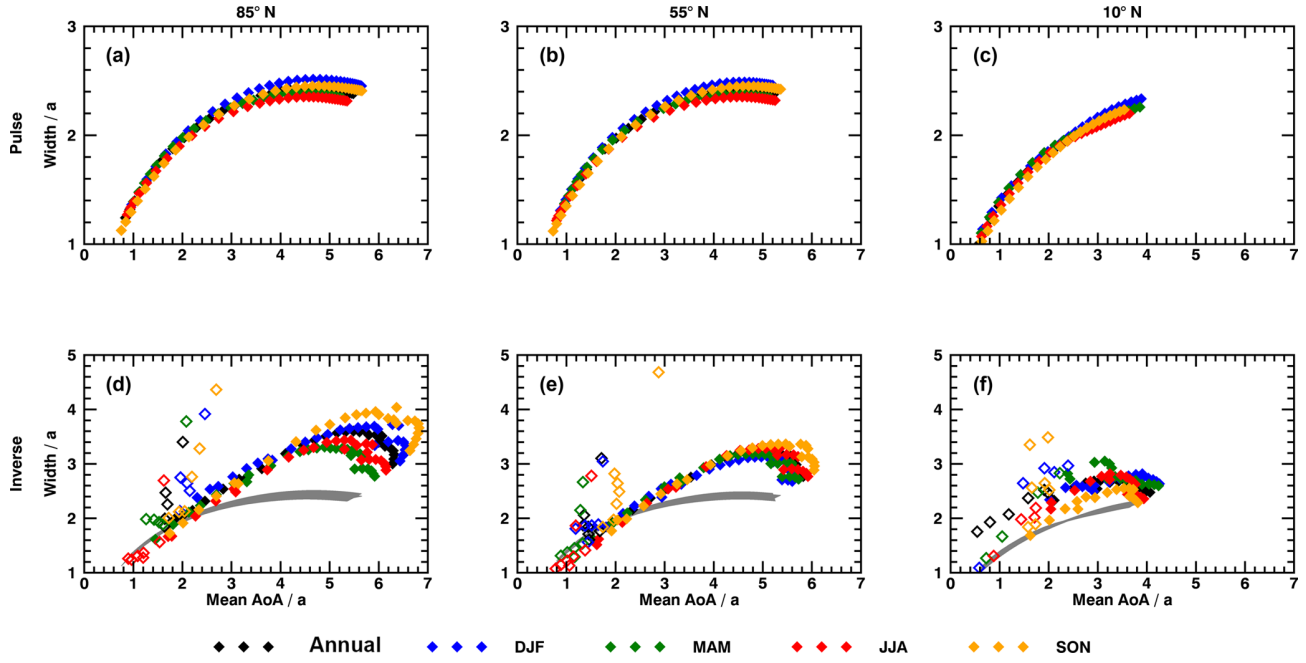

Figure 9. Vertical profiles of age spectra width as a function of their mean AoA at 85° N **(a, d)**, 55° N **(b, e)** and 10° N **(c, f)**. **(a–c)** show pulse spectra (Pulse) and **(d–f)** inverse method (Inverse). Seasons are given in colors. The unfilled diamonds denote data points that are found below the threshold of 1.5 years of clock mean AoA. Data of pulse spectra are also given as grey shading in **(d–f)** for better comparison.

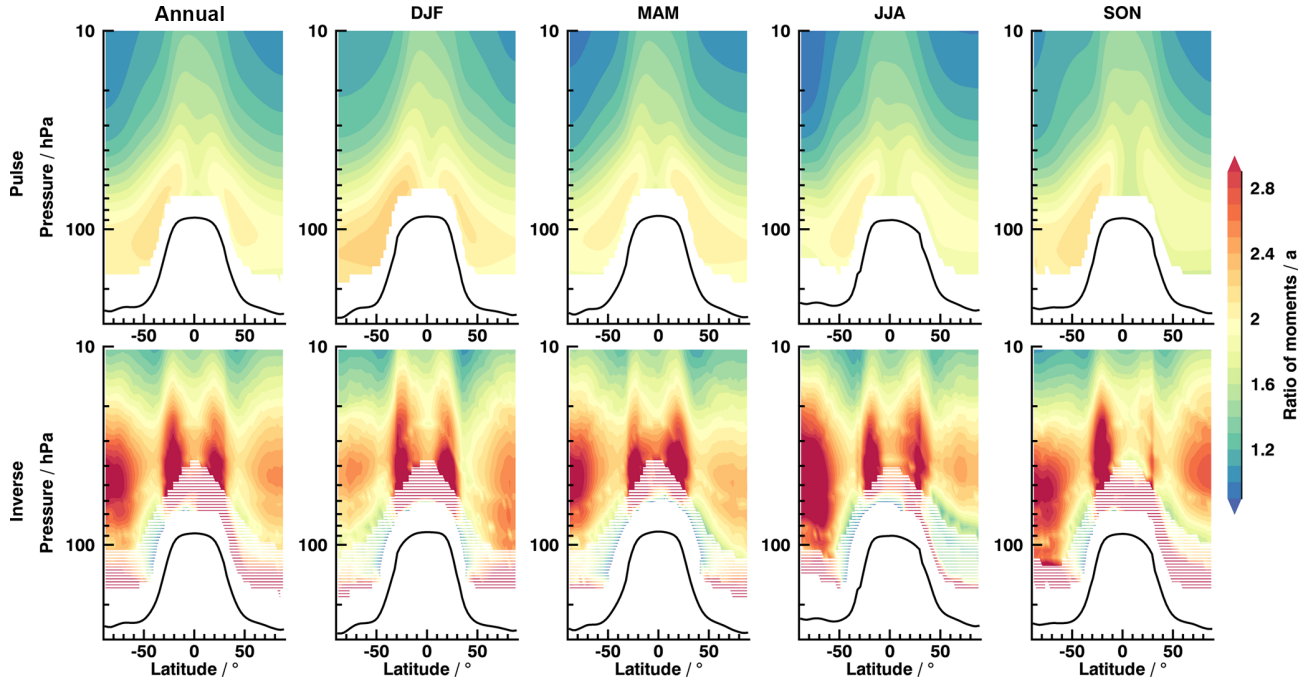

Figure 10. Absolute annual and seasonal ratio of moments as global cross section for pulse (top row) and inverse spectra (bottom row). Again, the white dashed area represents data below clock mean AoA of 1.5 years.

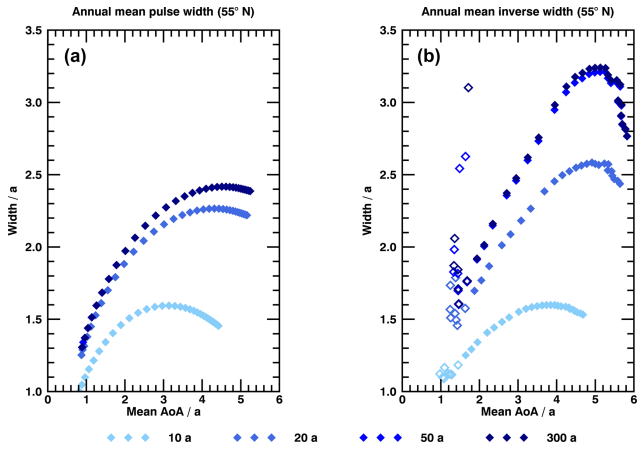

Figure 11. Influence of spectra's tail length on width and mean AoA for pulse **(a)** and inverse spectra **(b)** at 55° N as annual mean. Different tail lengths are colored. Filled diamonds denote data above 1.5 years of clock mean AoA.

The reason for the deviation from Hall and Plumb (1994) and Volk et al. (1997) may not only be coarser resolution and lesser complexity of the models compared to EMAC. The tail of the age spectrum is vital for a mathematically and physically correct description of transport. The width of annual mean pulse and inverse spectra with tail lengths of 10, 20, 50 and 300 years is shown as a function of mean AoA at 55° N in Fig. 11. Unfilled diamonds denote data below 1.5 years of clock mean AoA. The tail of the spectrum needs to be properly specified with an appropriate length. There seems to be no distinct difference for the pulse spectra between a tail length of 50 and 300 years, whereas in case of the inverse method there still appears to be some small shift towards larger mean AoA and increased width. This is expected, since the maximum transit time is selected in accordance with the integral over the spectrum (see Appendix A). When using the intrinsic tail length of 10 years, the ratio of moments of pulse and inverse spectra have similar orders of magnitude as presented by Hall and Plumb (1994). A maximum transit time between 10 and 20 years was also used in Hall and Plumb (1994; Timothy M. Hall, private communication, 2018). The spatial distribution of the inverse ratio of moments agrees very well with the pulse results if using a tail length of 10 years for both. Thus, on the one hand, a fully included tail is needed for physically precise results. On the other hand, the width in Fig. 11 exhibits a much stronger dependence on the tail length than mean AoA, making variations in variance even more likely to be the primary factor for the discrepancies between inverse method and pulse spectra in Fig. 10.

3.3 Applicability to observational data

Results of the proof of concept presented above have shown that the inverse method in combination with the imposed seasonal cycle is in principle capable of deriving seasonal age spectra correctly, except for the region below 1.5 years of mean AoA. However, when it comes to real atmospheric data, application of the method becomes even more challenging. One of the most critical factors is the chemical lifetime of the gases used in the inversion which is strongly dependent on time and space, tainted with seasonal and inter-annual variability and only known with limited accuracy. The inverse method in its form postulated above (Eq. 11) can include variability in lifetimes, since the lifetime τ is designed to be transit-time dependent, although a constant lifetime is used for all tracers implemented in this study. Transit-time dependence is a more approximate choice compared to real space dependence, since two distinct spatial pathways could in theory exhibit an equal transit time but different lifetimes along them. However, as discussed in Engel et al. (2018), a good average correlation between chemical loss and time spent in the stratosphere is expected. Extension of the method to variable chemistry could involve the ansatz of Schoeberl et al. (2000, 2005), who reduced the depletion of trace gas species to chemistry along average Lagrangian paths starting at the reference point to any location in the stratosphere (see Sect. 4).

Table 2. Radioactive trace gas subsets.

Number of radioactive tracers	Selected lifetimes in months
10	1, 13, 25, 37, 49, 61, 73, 85, 97 and 109
5	1, 25, 49, 73 and 97
3	1, 49 and 97

A further limitation of the method when applying it to observational data is the number of trace gases necessary for the inversion to work properly. In reality, it is impossible to find 40 trace gases with lifetimes ranging from 1 to 118 months evenly spaced in steps of 3 months. Considering data and measured species of modern airborne research campaigns, it is more likely to find a set of 10 trace gases at most, which span a range of 10 years in chemical lifetime. On this basis, three subsets of tracers with 10, 5 and 3 trace gas species are selected and shown in Table 2 together with their corresponding lifetimes to investigate the effects of reducing the number of trace gases and introducing uncertainty in the knowledge of the lifetime. Three trace gases are considered to be the minimum in order to constrain different parts of the age spectrum (e.g., left flank of the peak, right flank and tail). A reduction of trace gases removes, on the one hand, redundant information about transport and strongly diminishes the amount of data but, on the other hand, also increases the risk of errors during the inversion leading to wrong age spectra. This is especially precarious if chemical depletion is spatially varying and inaccurately estimated.

To test the influence of uncertainties in assumed lifetimes, a Monte Carlo approach has been used in which chemical lifetimes are varied pseudo-randomly. In this simulation the mean lower error margin is evaluated by giving a pseudo-randomly selected number of lifetimes in a trace gas subset a certain preset uncertainty ϵ_{lower} (e.g., $-20\,\%$). In a second similar run, the opposite error ϵ_{upper} (e.g., $+20\,\%$) is then applied to retrieve the mean upper margin. All simulations are repeated 5000 times for each of the three trace gas subsets (Table 2) while pseudo-randomly varying the lifetimes of some of the species used in the inversion. This setup will provide a mean deviation of the spectra for all cases where the exact amount of error-prone lifetimes is unknown. Since the pseudo-random numbers are distributed uniformly, the simulation mean is equivalent to a case where the lifetimes of approximately half of the species in a subset exhibit an error but are pseudo-randomly chosen with equal probability. Each simulation is designed as a single sensitivity experiment, where lifetimes are varied constantly in transit time either upwards or downwards, which provides an estimation of the maximum and minimum error of an age spectrum for a preset uncertainty. Note that an underestimation of the lifetime causes the peak of the age spectrum to shift upward and to smaller transit times, as depletion becomes faster. Errors of $\pm 10\,\%$, $\pm 20\,\%$ and $\pm 50\,\%$ have been selected for this study. Results are shown in Fig. 12 at 55° N and 70 hPa as annual mean, but analog results are found at 10 hPa (not shown). As the main differences for the trace gas subsets occur within the first year of transit time, only this small slice is presented to make lines distinguishable. The age spectra of the subsets with 10 (panel a) and also 5 (panel b) trace gases without error (solid blue line) are in good agreement with the spectrum of the full tracer set (black line). Modal age increases by 2.5 % (10 tracers) and by 3.1 % (5 tracers) compared to the full set, whereas the amplitude changes by $-0.03\,\%$ (10 tracers) and $-2.5\,\%$ (5 tracers). The inversion results are robust even if using only a fourth and an eighth of all trace gases. In the case of only three trace gases (panel c), the solid blue line exhibits a growing shift of amplitude ($-9\,\%$) and also greater modal age (10 %). Overall agreement is still reasonable but not as good as for the other two subsets. The shift towards larger modal age and smaller amplitudes when decreasing the size of the subset is unexpected and not intuitive. Errors in the knowledge of chemical lifetime of the trace gases affect all subsets equally, as all non-solid lines in all three panels show an equivalent behavior relative to the reference spectrum of each subset (solid blue lines). All averaged percentage uncertainties of amplitudes and modal ages are depicted in Table 3. An overestimation of chemical lifetime generally leads to smaller deviations of modal age and amplitude than an underestimation.

These results imply that a reduced set of trace gases with either 10 (optimum) or 5 (sufficient) species should be recommended in order to retrieve age spectra from observations. Values in Table 3 and also the general shape of the

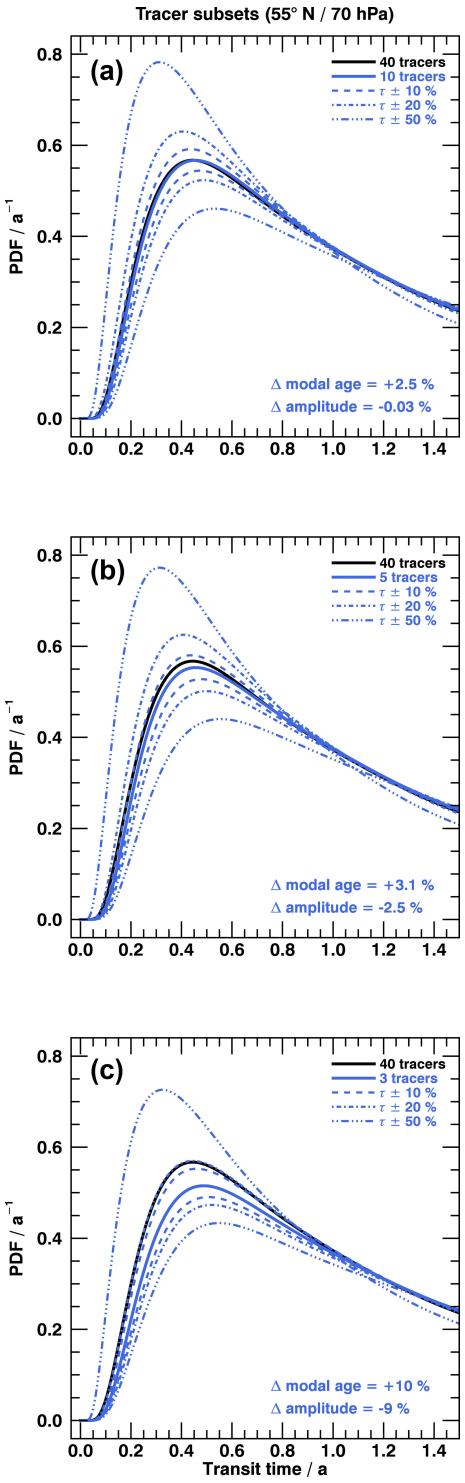

Figure 12. Annual mean age spectra from radioactive tracer subsets compared to full set at 55° N and 70 hPa. The black solid line corresponds to the full set (40 tracers), while the solid blue line denotes spectra of a subset with 10 tracers **(a)**, 5 tracers **(b)** and 3 tracers **(c)**. The changes in modal age and amplitude for the solid blue lines relative to the black lines are given in each panel in the bottom right corner. The three dashed and dashed–dotted spectra in each panel include an error in the knowledge of the local chemical lifetimes of $\pm 10\,\%$, $\pm 20\,\%$ and $\pm 50\,\%$ (see text for details).

Table 3. Percentage deviations of spectra amplitudes and modal ages averaged over all three subsets presented in Fig. 12. The calculated values are relative to the spectra of each subset without errors in the knowledge of chemical lifetime.

	Amplitude	Modal age
+10 % or −10 %	−4.5 % or +5.5 %	+3.9 % or −4.9 %
+20 % or −20 %	−8.4 % or +11.6 %	+7.7 % or −10.2 %
+50 % or −50 %	−12.6 % or +19.4 %	+11.4 % or −16.7 %

error spectra indicate that on average both of these subsets can also compensate a chemical lifetime uncertainty of up to ±20 % of a random number of species if small deviations of modal age (−10 % or +8 %) and amplitude (−8 % or +12 %) are tolerated. Given the assumptions that the inverse method is based on, the accuracy level of 5 % during the inversion and atmospheric variability when applied to in situ data, this threshold might be considered a reasonable choice. If the number of trace gases with lifetime error is decreased and kept constant, the deviation from the reference spectrum will become smaller due to more compensation by the remaining species. Opposite effects will apply if the number is increased.

4 Summary and conclusion

This paper presents a modified version of the inverse method by Schoeberl et al. (2005) to derive stratospheric age of air spectra from radioactive trace gases with fewer free parameters. It introduces a formulation of an imposed seasonal cycle in the spectra to approximate seasonality in stratospheric transport. The development process always focuses on achieving the best possible compromise between accuracy and practicability for observational studies with very limited data. The resulting spectra are evaluated in comparison to EMAC pulse spectra. The inverse method is applied on a simplified set of 40 short-lived trace gases with globally constant prescribed lifetimes as proof of concept. Resulting spectra are assessed as well as their first and second moments and the ratio between them. This comparison is conducted for annual mean state and for respective seasonal variation. Data within the transition layer, the first 30 K beyond the tropopause, are always omitted in our study, as the strong tropospheric influence distorts the concept of age of air referred to the tropical tropopause. A threshold of 1.5 years of clock mean AoA is introduced as a region where entry through the local tropopause is not negligible. 10 hPa is selected as upper boundary, since the mixing ratios of trace gases with lifetimes smaller than 2 years are critically close to the accuracy level of the inverse algorithm.

The modified inverse spectra match the pulse spectra well both on an annual and seasonal timescale with its new set of reduced fit parameters for most parts of the stratosphere. The imposed seasonal cycle improves the already well-described intrinsic seasonality and reproduces seasonal variation in the spectra correctly. Multiple peaks of the inverse age spectra at 55° N coincide with the pulse spectra in time of appearance and amplitude during all seasons in 70 and 10 hPa. The artificial seasonal cycle moreover does not change the moments of the distributions, as they are integrated measures. This extends to the annual mean spectra, which are also almost unchanged when applying the seasonal cycle. Additionally, a need for an explicit temporal offset in the formulation of the inverse method is not detected. In the lower stratosphere at 55° N and 140 hPa, which is below the threshold of 1.5 years of mean AoA, the inverse spectra differ from the pulse spectra on the seasonal scale, whereas the annual mean matches coincidentally. The imposed seasonal cycle does not contribute to a better agreement of the seasonal spectra. In the northern extratropics at 140 hPa, entrainment of air through the local tropopause is important. This process is not considered in the assumption of single entry through the tropical tropopause and not included in the inverse method presented here. The seasonality of the local entry of air through the extratropical tropopause (Appenzeller et al., 1996) differs strongly from the seasonality in tropical upward mass flux (Fig. 1). The imposed seasonal cycle leads to mismatching spectra, as it does not take this seasonal cycle in local entrainment into account. Global mean AoA as well as spectra's width at 85, 55 and 10° N reveal that the inverse method also performs well on the global scale, reproducing the annual state as well as seasonality for air masses with more than 1.5 years of mean AoA. Below the threshold, similar problems in the seasonality of the inverse method as at 55° N arise globally in large areas around the extratropical tropopause. These mechanisms are enhanced in the Northern Hemisphere and only occur to some small extent in the south, which is again in accordance with Appenzeller et al. (1996). Due to its assumptions, the inverse method and the imposed seasonal cycle are likely not applicable in the lowermost stratosphere below 1.5 years of mean AoA without further improvements. The chosen annual mean entry mixing ratio influences results only in close vicinity to the tropical tropopause. All inverse age spectra exhibit systematically enhanced tails, leading to larger global mean AoA compared to pulse spectra and clock tracer and larger width compared to the pulse spectra, most probably caused by the prescribed inverse Gaussian shape.

The ratio of moments of the pulse and inverse spectra is compared to the results of Hall and Plumb (1994). The ratio of moments of the pulse spectra exceeds their values by a factor of 3 but show a similar spatial structure. Since the results show that the ratio of moments undergoes seasonal variability, an annual average value of 2.0 years for the lower stratosphere in both hemispheres is promoted. This is larger than the values implemented by Volk et al. (1997; 1.25±0.5 years) and Engel et al. (2002; 0.7 years). The large deviation between EMAC and Hall and Plumb (1994) is most probably a result of an underestimated spectrum tail in Hall and Plumb

(1994). A properly considered tail is required to fully describe stratospheric transport using age spectra, since the tail affects both mean AoA and width. As the ratio of moments is usually implemented for the derivation of mean AoA from observations (Volk et al., 1997; Engel et al., 2002), these findings might contribute to improved results. The inverse method is not capable of reproducing the pulse spectra's ratio of moments, likely because of the systematic errors in mean AoA and width not scaling accordingly.

With respect to observational data, a set of 40 trace gases with lifetimes ranging evenly spaced from 1 month to 10 years cannot be found in reality. Tests with reduced numbers of trace gases show that subsets consisting of 5 (sufficient) to 10 (optimal) chemically active trace gases should be used in order to invert consistent and matching age spectra in the northern midlatitudes. It is recommended that the species in these subsets are selected so that their average local lifetimes along the transport pathway cover a period of 10 years uniformly. The analysis shows moreover that errors in the assumed chemical lifetime, which affect a random number of trace gases in these subsets, can be compensated during the inversion to some degree. On average an uncertainty in the knowledge of lifetimes up to $\pm 20\,\%$ still leads to reasonable agreement of age spectra if an amplitude and modal age deviation of approximately $\pm 10\,\%$ is accepted. The more lifetimes are known correctly, the smaller these deviations will become due to better compensation by the correctly prescribed species. While the method's presented formalism allows for varying lifetime in the form of transit-time dependence, actual application to observations requires further development and analyses. Possible approaches might include chemistry along average Lagrangian paths (e.g., Schoeberl et al., 2000, 2005) in combination with chemistry transport models. In addition, for the lower stratosphere with mean AoA below 1.5 years, a fractional approach as proposed by Andrews et al. (2001b) and Bönisch et al. (2009) for chemically inert trace gases could be applied, which splits the stratosphere into an upper and lower section and derives an age spectrum as superposition of the sub-spectra of each section. If chemical depletion is then approximated by lifetimes representative of each compartment, this separation of the stratosphere possibly leads to more reasonable results than in the complete stratospheric case. In such a case, different entry mixing ratios of short-lived trace gases at the tropical and extratropical tropopause could also be prescribed to better represent temporal and spatial variability. A limiting factor for long-term analyses is the fact that real stratospheric transport is not stationary and afflicted with a long-term temporal trend coupled with seasonal and inter-annual variation. This trend can neither be included in the transport parameter K, as it is independent of transit time, nor in the prescribed seasonal cycle. Despite these additional difficulties when applying the method to observational data, the basic principle of both modified inverse method and imposed seasonal cycle proved to work. Further work is required to make the method finally applicable to measurement data and possibly contribute to a deepened understanding of stratospheric transport. In particular, the method's application on more realistic trace gases should be included in future studies regarding observationally derived age spectra.

Data availability. All data can be made accessible on request to the authors.

Appendix A: Numerical implementation

Deriving the reference ratio R_{ref} from observational or modeled data, K will be numerically optimized until R_{seas} or R is equivalent to R_{ref} within a range of 5 % accuracy. This is possible for a single trace gas as well as for a set of given species simultaneously. The more distinct substances with varying lifetimes are included, the more information about the underlying transport processes of the BDC is condensed into K. To estimate the deviation of R from the reference ratio R_{ref} for every trace gas, the mean percentage error (MPE) between them is minimized and given as follows:

$$\frac{1}{n} \cdot \sum_{i}^{n} \frac{R^i_{\mathrm{ref}} - R^i}{R^i_{\mathrm{ref}}} \stackrel{!}{=} 0. \tag{A1}$$

The index i denotes a single trace gas within a set of n species. To achieve the optimization numerically, a combination of an algorithm postulated by Ridders (1979) and Newton's method is applied. This also justifies the choice of MPE as an measure of error, besides the fact that it is a robust deviation estimate. Ridders' method is known to be convergent in any case, if and only if the root (MPE $= 0$) is correctly bracketed. This implies that there must be always one value of K where MPE is less than 0 and one K where MPE is greater than 0. Only then is convergence for large deviations of K from the solution ensured and rapid. When approaching the solution of K, Newton's method is significantly faster for converging and yet very stable, which is an advantage to keep the computational effort as small and efficient as possible. If the satisfaction criterion is reached, the corresponding age spectrum of the matching K is returned. A problem arises when reaching upper or lower boundary regions. Both algorithms will become unstable in such regions. If the ratio is larger than 1, which is possible in close proximity to the tropopause where entrainment of tropospheric air occurs, or nearly equal to 0, no suitable K will be optimized. In this case, the respective points will be omitted and treated as missing data. Other than in the original method of Schoeberl et al. (2005), there are no trace gases with a constant mixing ratio of 1 at the tropical tropopause in the model, since in reality there will be uncertainties, seasonalities and temporal trends affecting this quantity. To include this effect and test if it influences the performance of the method critically, the annual mean mixing ratios are calculated at the tropical tropopause and utilized in respect of future observational approaches. The scale height H is derived from the air density ϱ at each latitude. This can also be done with observed data, as the density is frequently measured along with trace gases. A critical aspect for the calculation of age spectra as an inverse Gaussian PDF is the numerical choice of a value large enough to be equivalent to infinity. That is especially relevant for the tail of the age spectrum and hence for its variance, since only at infinity are all possible values considered. Multiple tests with the spectra have shown that a maximum transit time of 300 years with a resolution of 30 days is sufficient. With this selection, Eq. (7) settles at 0.999 and does not significantly change anymore if the maximum is further increased. All spectra are therefore be integrated from 0 to 300 years.

Author contributions. MH wrote the paper, evaluated the model data and developed the ideas presented in this study in close collaboration with AE. FF and HG planned and performed the EMAC model simulation and implemented and tested the method of Schoeberl et al. (2000) mentioned in Sect. 2.1. FF, HG and AE contributed to the preparation of the paper in many discussions.

Competing interests. The authors declare that they have no conflict of interest.

Acknowledgements. This work is supported by the German Research Foundation (DFG) priority program 1294 (HALO) under the project number 316588118. The model simulations were performed on the HPC system Mistral of the German Climate Computation Center (DKRZ) supported by the German Federal Ministry of Education and Research (BMBF). The authors cordially thank Felix Plöger from Forschungszentrum Jülich and Harald Bönisch from the Karlsruhe Institute of Technology (KIT) for their help and the useful discussions regarding the research presented in this paper.

Review statement. This paper was edited by Rolf Müller and reviewed by three anonymous referees.

References

Abalos, M., Legras, B., Ploeger, F., and Randel, W. J.: Evaluating the advective Brewer-Dobson circulation in three reanalyses for the period 1979–2012, J. Geophys. Res., 120, 7534–7554, https://doi.org/10.1002/2015JD023182, 2015.

Andrews, A. E., Boering, K. A., Daube, B. C., Wofsy, S. C., Hintsa, E. J., Weinstock, E. M., and Bui, T. P.: Empirical age spectra for the lower tropical stratosphere from in situ observations of CO_2: Implications for stratospheric transport, J. Geophys. Res., 104, 26581–26595, https://doi.org/10.1029/1999JD900150, 1999.

Andrews, A. E., Boering, K. A., Daube, B. C., Wofsy, S. C., Loewenstein, M., Jost, H., Podolske, J. R., Webster, C. R., Herman, R. L., Scott, D. C., Flesch, G. J., Moyer, E. J., Elkins, J. W., Dutton, G. S., Hurst, D. F., Moore, F. L., Ray, E. A., Romashkin, P. A., and Strahan, S. E.: Mean ages of stratospheric air derived from in situ observations of CO_2, CH_4, and N_2O, J. Geophys. Res., 106, 32295–32314, https://doi.org/10.1029/2001JD000465, 2001a.

Andrews, A. E., Boering, K. A., Wofsy, S. C., Daube, B. C., Jones, D. B., Alex, S., Loewenstein, M., Podolske, J. R., and Strahan, S. E.: Empirical age spectra for the midlatitude lower stratosphere from in situ observations of CO_2: Quantitative evidence for a subtropical "barrier" to horizontal transport, J. Geophys. Res., 106, 10257–10274, https://doi.org/10.1029/2000JD900703, 2001b.

Appenzeller, C., Holton, J. R., and Rosenlof, K. H.: Seasonal variation of mass transport across the tropopause, J. Geophys. Res., 101, 15071–15078, https://doi.org/10.1029/96JD00821, 1996.

Austin, J. and Li, F.: On the relationship between the strength of the Brewer-Dobson circulation and the age of stratospheric air, Geophys. Res. Lett., 33, L17807, https://doi.org/10.1029/2006GL026867, 2006.

Birner, T. and Bönisch, H.: Residual circulation trajectories and transit times into the extratropical lowermost stratosphere, Atmos. Chem. Phys., 11, 817–827, https://doi.org/10.5194/acp-11-817-2011, 2011.

Bönisch, H., Engel, A., Curtius, J., Birner, Th., and Hoor, P.: Quantifying transport into the lowermost stratosphere using simultaneous in-situ measurements of SF_6 and CO_2, Atmos. Chem. Phys., 9, 5905–5919, https://doi.org/10.5194/acp-9-5905-2009, 2009.

Bönisch, H., Engel, A., Birner, Th., Hoor, P., Tarasick, D. W., and Ray, E. A.: On the structural changes in the Brewer–Dobson circulation after 2000, Atmos. Chem. Phys., 11, 3937–3948, https://doi.org/10.5194/acp-11-3937-2011, 2011.

Butchart, N.: The Brewer–Dobson circulation, Rev. Geophys., 52, 157–184, https://doi.org/10.1002/2013RG000448, 2014.

Butchart, N. and Scaife, A. A.: Removal of chlorofluorocarbons by increased mass exchange between the stratosphere and troposphere in a changing climate, Nature, 410, 799–802, https://doi.org/10.1038/35071047, 2001.

Chhikara, R. S. and Folks, J. L.: The inverse Gaussian distribution: Theory, methodology and applications, Statistics, 95, Dekker, New York, 1989.

Dee, D. P., Uppala, S. M., Simmons, A. J., Berrisford, P., Poli, P., Kobayashi, S., Andrae, U., Balmaseda, M. A., Balsamo, G., Bauer, P., Bechtold, P., Beljaars, A. C. M., van de Berg, L., Bidlot, J., Bormann, N., Delsol, C., Dragani, R., Fuentes, M., Geer, A. J., Haimberger, L., Healy, S. B., Hersbach, H., Hólm, E. V., Isaksen, L., Kållberg, P., Köhler, M., Matricardi, M., McNally, A. P., Monge-Sanz, B. M., Morcrette, J.-J., Park, B.-K., Peubey, C., de Rosnay, P., Tavolato, C., Thépaut, J.-N., and Vitart, F.: The ERA-Interim reanalysis: configuration and performance of the data assimilation system, Q. J. Roy. Meteor. Soc., 137, 553–597, https://doi.org/10.1002/qj.828, 2011.

Ehhalt, D. H., Rohrer, F., Blake, D. R., Kinnison, D. E., and Konopka, P.: On the use of nonmethane hydrocarbons for the determination of age spectra in the lower stratosphere, J. Geophys. Res., 112, 26581, https://doi.org/10.1029/2006JD007686, 2007.

Engel, A., Strunk, M., Müller, M., Haase, H.-P., Poss, C., Levin, I., and Schmidt, U.: Temporal development of total chlorine in the high-latitude stratosphere based on reference distributions of mean age derived from CO_2 and SF_6, J. Geophys. Res., 107, 4483, https://doi.org/10.1029/2001JD000584, 2002.

Engel, A., Möbius, T., Bönisch, H., Schmidt, U., Heinz, R., Levin, I., Atlas, E., Aoki, S., Nakazawa, T., Sugawara, S., Moore, F., Hurst, D., Elkins, J., Schauffler, S., Andrews, A., and Boering, K.: Age of stratospheric air unchanged within uncertainties over the past 30 years, Nat. Geosci., 2, 28–31, https://doi.org/10.1038/NGEO388, 2009.

Engel, A., Bönisch, H., Ullrich, M., Sitals, R., Membrive, O., Danis, F., and Crevoisier, C.: Mean age of stratospheric air derived from AirCore observations, Atmos. Chem. Phys., 17, 6825–6838, https://doi.org/10.5194/acp-17-6825-2017, 2017.

Engel, A., Bönisch, H., Ostermöller, J., Chipperfield, M. P., Dhomse, S., and Jöckel, P.: A refined method for calculating equivalent effective stratospheric chlorine, Atmos. Chem. Phys., 18, 601–619, https://doi.org/10.5194/acp-18-601-2018, 2018.

Garcia, R. R. and Randel, W. J.: Acceleration of the Brewer–Dobson Circulation due to Increases in Greenhouse Gases, J. Atmos. Sci., 65, 2731–2739, https://doi.org/10.1175/2008JAS2712.1, 2008.

Garny, H., Birner, T., Bönisch, H., and Bunzel, F.: The effects of mixing on age of air, J. Geophys. Res., 119, 7015–7034, https://doi.org/10.1002/2013JD021417, 2014.

Gelaro, R., McCarty, W., Suárez, M. J., Todling, R., Molod, A., Takacs, L., Randles, C. A., Darmenov, A., Bosilovich, M. G., Reichle, R., Wargan, K., Coy, L., Cullather, R., Draper, C., Akella, S., Buchard, V., Conaty, A., da Silva, A. M., Gu, W., Kim, G.-K., Koster, R., Lucchesi, R., Merkova, D., Nielsen, J. E., Partyka, G., Pawson, S., Putman, W., Rienecker, M., Schubert, S. D., Sienkiewicz, M., and Zhao, B.: The Modern-Era Retrospective Analysis for Research and Applications, Version 2 (MERRA-2), J. Climate, 30, 5419–5454, https://doi.org/10.1175/JCLI-D-16-0758.1, 2017.

Haenel, F. J., Stiller, G. P., von Clarmann, T., Funke, B., Eckert, E., Glatthor, N., Grabowski, U., Kellmann, S., Kiefer, M., Linden, A., and Reddmann, T.: Reassessment of MIPAS age of air trends and variability, Atmos. Chem. Phys., 15, 13161–13176, https://doi.org/10.5194/acp-15-13161-2015, 2015.

Haine, T. W. N., Zhang, H., Waugh, D. W., and Holzer, M.: On transit-time distributions in unsteady circulation models, Ocean Model., 21, 35–45, https://doi.org/10.1016/j.ocemod.2007.11.004, 2008.

Hall, T. M. and Plumb, R. A.: Age as a diagnostic of stratospheric transport, J. Geophys. Res., 99, 1059, https://doi.org/10.1029/93JD03192, 1994.

Haynes, P. H., McIntyre, M. E., Shepherd, T. G., Marks, C. J., and Shine, K. P.: On the "Downward Control" of Extratropical Diabatic Circulations by Eddy-Induced Mean Zonal Forces, J. Atmos. Sci., 48, 651–678, https://doi.org/10.1175/1520-0469(1991)048<0651:OTCOED>2.0.CO;2, 1991.

Hegglin, M. I., Plummer, D. A., Shepherd, T. G., Scinocca, J. F., Anderson, J., Froidevaux, L., Funke, B., Hurst, D., Rozanov, A., Urban, J., Clarmann, T. von, Walker, K. A., Wang, H. J., Tegtmeier, S., and Weigel, K.: Vertical structure of stratospheric water vapour trends derived from merged satellite data, Nat. Geosci., 7, 768–776, https://doi.org/10.1038/ngeo2236, 2014.

Holton, J. R.: Meridional Distribution of Stratospheric Trace Constituents, J. Atmos. Sci., 43, 1238–1242, https://doi.org/10.1175/1520-0469(1986)043<1238:MDOSTC>2.0.CO;2, 1986.

Holton, J. R., Haynes, P. H., McIntyre, M. E., Douglass, A. R., Rood, R. B., and Pfister, L.: Stratosphere-troposphere exchange, Rev. Geophys., 33, 403, https://doi.org/10.1029/95RG02097, 1995.

Hoor, P., Gurk, C., Brunner, D., Hegglin, M. I., Wernli, H., and Fischer, H.: Seasonality and extent of extratropical TST derived from in-situ CO measurements during SPURT, Atmos. Chem. Phys., 4, 1427–1442, https://doi.org/10.5194/acp-4-1427-2004, 2004.

Jöckel, P., Tost, H., Pozzer, A., Brühl, C., Buchholz, J., Ganzeveld, L., Hoor, P., Kerkweg, A., Lawrence, M. G., Sander, R., Steil, B., Stiller, G., Tanarhte, M., Taraborrelli, D., van Aardenne, J., and Lelieveld, J.: The atmospheric chemistry general circulation model ECHAM5/MESSy1: consistent simulation of ozone from the surface to the mesosphere, Atmos. Chem. Phys., 6, 5067–5104, https://doi.org/10.5194/acp-6-5067-2006, 2006.

Jöckel, P., Kerkweg, A., Pozzer, A., Sander, R., Tost, H., Riede, H., Baumgaertner, A., Gromov, S., and Kern, B.: Development cycle 2 of the Modular Earth Submodel System (MESSy2), Geosci. Model Dev., 3, 717–752, https://doi.org/10.5194/gmd-3-717-2010, 2010.

Kobayashi, S., Ota, Y., Harada, Y., Ebita, A., Moriya, M., Onoda, H., Onogi, K., Kamahori, H., Kobayashi, C., Endo, H., Miyaoka, K., and Takahashi, K.: The JRA-55 Reanalysis: General Specifications and Basic Characteristics, J. Meteorol. Soc. Jpn., 93, 5–48, https://doi.org/10.2151/jmsj.2015-001, 2015.

Li, F., Austin, J., and Wilson, J.: The Strength of the Brewer–Dobson Circulation in a Changing Climate: Coupled Chemistry–Climate Model Simulations, J. Climate, 21, 40–57, https://doi.org/10.1175/2007JCLI1663.1, 2008.

Li, F., Waugh, D. W., Douglass, A. R., Newman, P. A., Pawson, S., Stolarski, R. S., Strahan, S. E., and Nielsen, J. E.: Seasonal variations of stratospheric age spectra in the Goddard Earth Observing System Chemistry Climate Model (GEOSCCM), J. Geophys. Res., 117, D05134, https://doi.org/10.1029/2011JD016877, 2012a.

Li, F., Waugh, D. W., Douglass, A. R., Newman, P. A., Strahan, S. E., Ma, J., Nielsen, J. E., and Liang, Q.: Long-term changes in stratospheric age spectra in the 21st century in the Goddard Earth Observing System Chemistry-Climate Model (GEOSCCM), J. Geophys. Res., 117, 32295, https://doi.org/10.1029/2012JD017905, 2012b.

McIntyre, M. E. and Palmer, T. N.: The 'surf zone' in the stratosphere, J. Atmos. Terr. Phys., 46, 825–849, https://doi.org/10.1016/0021-9169(84)90063-1, 1984.

Monge-Sanz, B. M., Chipperfield, M. P., Dee, D. P., Simmons, A. J., and Uppala, S. M.: Improvements in the stratospheric transport achieved by a chemistry transport model with ECMWF (re)analyses: Identifying effects and remaining challenges, Q. J. Roy. Meteor. Soc., 139, 654–673, https://doi.org/10.1002/qj.1996, 2013.

Oberländer-Hayn, S., Meul, S., Langematz, U., Abalichin, J., and Haenel, F.: A chemistry-climate model study of past changes in the Brewer-Dobson circulation, J. Geophys. Res., 120, 6742–6757, https://doi.org/10.1002/2014JD022843, 2015.

Oberländer-Hayn, S., Gerber, E. P., Abalichin, J., Akiyoshi, H., Kerschbaumer, A., Kubin, A., Kunze, M., Langematz, U., Meul, S., Michou, M., Morgenstern, O., and Oman, L. D.: Is the Brewer-Dobson circulation increasing or moving upward?, Geophys. Res. Lett., 43, 1772–1779, https://doi.org/10.1002/2015GL067545, 2016.

Okamoto, K., Sato, K., and Akiyoshi, H.: A study on the formation and trend of the Brewer-Dobson circulation, J. Geophys. Res., 116, D03103, https://doi.org/10.1029/2010JD014953, 2011.

Oman, L., Waugh, D. W., Pawson, S., Stolarski, R. S., and Newman, P. A.: On the influence of anthropogenic forcings on changes in the stratospheric mean age, J. Geophys. Res., 114, L17807, https://doi.org/10.1029/2008JD010378, 2009.

Ploeger, F. and Birner, T.: Seasonal and inter-annual variability of lower stratospheric age of air spectra, Atmos. Chem. Phys., 16, 10195–10213, https://doi.org/10.5194/acp-16-10195-2016, 2016.

Plumb, R. A.: Stratospheric Transport, J. Meteorol. Soc. Jpn., 80, 793–809, https://doi.org/10.2151/jmsj.80.793, 2002.

Plumb, R. A. and Ko, M. K. W.: Interrelationships between mixing ratios of long-lived stratospheric constituents, J. Geophys. Res., 97, 10145–10156, https://doi.org/10.1029/92JD00450, 1992.

Podglajen, A. and Ploeger, F.: Retrieving the age of air spectrum from tracers: principle and method, Atmos. Chem. Phys., 19, 1767–1783, https://doi.org/10.5194/acp-19-1767-2019, 2019.

Ray, E. A., Moore, F. L., Rosenlof, K. H., Davis, S. M., Sweeney, C., Tans, P., Wang, T., Elkins, J. W., Bönisch, H., Engel, A., Sugawara, S., Nakazawa, T., and Aoki, S.: Improving stratospheric transport trend analysis based on SF_6 and CO_2 measurements, J. Geophys. Res., 119, 14110–14128, https://doi.org/10.1002/2014JD021802, 2014.

Reithmeier, C., Sausen, R., and Grewe, V.: Investigating lower stratospheric model transport: Lagrangian calculations of mean age and age spectra in the GCM ECHAM4, Clim. Dynam., 30, 225–238, https://doi.org/10.1007/s00382-007-0294-1, 2008.

Ridders, C.: A new algorithm for computing a single root of a real continuous function, IEEE Trans. Circuits Syst., 26, 979–980, https://doi.org/10.1109/TCS.1979.1084580, 1979.

Roeckner, E., Brokopf, R., Esch, M., Giorgetta, M., Hagemann, S., Kornblueh, L., Manzini, E., Schlese, U., and Schulzweida, U.: Sensitivity of Simulated Climate to Horizontal and Vertical Resolution in the ECHAM5 Atmosphere Model, J. Climate, 19, 3771–3791, https://doi.org/10.1175/JCLI3824.1, 2006.

Rosenlof, K. H.: Seasonal cycle of the residual mean meridional circulation in the stratosphere, J. Geophys. Res., 100, 5173, https://doi.org/10.1029/94JD03122, 1995.

Rosenlof, K. H. and Holton, J. R.: Estimates of the stratospheric residual circulation using the downward control principle, J. Geophys. Res., 98, 10465, https://doi.org/10.1029/93JD00392, 1993.

Saha, S., Moorthi, S., Pan, H.-L., Wu, X., Wang, J., Nadiga, S., Tripp, P., Kistler, R., Woollen, J., Behringer, D., Liu, H., Stokes, D., Grumbine, R., Gayno, G., Wang, J., Hou, Y.-T., Chuang, H.-y., Juang, H.-M. H., Sela, J., Iredell, M., Treadon, R., Kleist, D., van Delst, P., Keyser, D., Derber, J., Ek, M., Meng, J., Wei, H., Yang, R., Lord, S., van den Dool, H., Kumar, A., Wang, W., Long, C., Chelliah, M., Xue, Y., Huang, B., Schemm, J.-K., Ebisuzaki, W., Lin, R., Xie, P., Chen, M., Zhou, S., Higgins, W., Zou, C.-Z., Liu, Q., Chen, Y., Han, Y., Cucurull, L., Reynolds, R. W., Rutledge, G., and Goldberg, M.: The NCEP Climate Forecast System Reanalysis, B. Am. Meteorol. Soc., 91, 1015–1058, https://doi.org/10.1175/2010BAMS3001.1, 2010.

Schoeberl, M. R., Sparling, L. C., Jackman, C. H., and Fleming, E. L.: A Lagrangian view of stratospheric trace gas distributions, J. Geophys. Res., 105, 1537–1552, https://doi.org/10.1029/1999JD900787, 2000.

Schoeberl, M. R., Douglass, A. R., Polansky, B., Boone, C., Walker, K. A., and Bernath, P.: Estimation of stratospheric age spectrum from chemical tracers, J. Geophys. Res., 110, 32295, https://doi.org/10.1029/2005JD006125, 2005.

Shepherd, T. G.: Transport in the Middle Atmosphere, J. Meteorol. Soc. Jpn., 85B, 165–191, https://doi.org/10.2151/jmsj.85B.165, 2007.

Shepherd, T. G. and McLandress, C.: A Robust Mechanism for Strengthening of the Brewer–Dobson Circulation in Response to Climate Change: Critical-Layer Control of Subtropical Wave Breaking, J. Atmos. Sci., 68, 784–797, https://doi.org/10.1175/2010JAS3608.1, 2011.

Solomon, S., Rosenlof, K. H., Portmann, R. W., Daniel, J. S., Davis, S. M., Sanford, T. J., and Plattner, G.-K.: Contributions of stratospheric water vapor to decadal changes in the rate of global warming, Science, 327, 1219–1223, https://doi.org/10.1126/science.1182488, 2010.

Stiller, G. P., von Clarmann, T., Haenel, F., Funke, B., Glatthor, N., Grabowski, U., Kellmann, S., Kiefer, M., Linden, A., Lossow, S., and López-Puertas, M.: Observed temporal evolution of global mean age of stratospheric air for the 2002 to 2010 period, Atmos. Chem. Phys., 12, 3311–3331, https://doi.org/10.5194/acp-12-3311-2012, 2012.

Stiller, G. P., Fierli, F., Ploeger, F., Cagnazzo, C., Funke, B., Haenel, F. J., Reddmann, T., Riese, M., and von Clarmann, T.: Shift of subtropical transport barriers explains observed hemispheric asymmetry of decadal trends of age of air, Atmos. Chem. Phys., 17, 11177–11192, https://doi.org/10.5194/acp-17-11177-2017, 2017.

Volk, C. M., Elkins, J. W., Fahey, D. W., Dutton, G. S., Gilligan, J. M., Loewenstein, M., Podolske, J. R., Chan, K. R., and Gunson, M. R.: Evaluation of source gas lifetimes from stratospheric observations, J. Geophys. Res., 102, 25543–25564, https://doi.org/10.1029/97JD02215, 1997.

Waugh, D. and Hall, T. M.: Age of stratospheric air: Theory, observations, and models, Rev. Geophys., 40, 4483, https://doi.org/10.1029/2000RG000101, 2002.

Waugh, D. W., Hall, T. M., Randel, W. J., Rasch, P. J., Boville, B. A., Boering, K. A., Wofsy, S. C., Daube, B. C., Elkins, J. W., Fahey, D. W., Dutton, G. S., Volk, C. M., and Vohralik, P. F.: Three-dimensional simulations of long-lived tracers using winds from MACCM2, J. Geophys. Res., 102, 21493–21513, https://doi.org/10.1029/97JD00793, 1997.

Paper II: A convolution of observational and model data to estimate age of air spectra in the northern hemispheric lower stratosphere

Published as:

Hauck, M., Bönisch, H., Hoor, P., Keber, T., Ploeger, F., Schuck, T., and Engel, A.: *A convolution of observational and model data to estimate age of air spectra in the northern hemispheric lower stratosphere*, Atmospheric Chemistry and Physics, 20, 8763-8785, DOI: https://doi.org/10.5194/acp-20-8763-2020, 2020

Author Contributions:

Marius Hauck wrote the manuscript, created the figures for the publication and prepared the answers to the referees during the review process. Presented concepts were developed by Marius Hauck in collaboration with Andreas Engel. All versions of the manuscript were proofread by the co-authors.

Marius Hauck wrote the code for the extended inverse method and the Monte Carlo simulations. The CLaMS simulations were planned and conducted by Felix Plöger and Marius Hauck, who both postprocessed retrieved data.

Marius Hauck processed both AGAGE and HALO data, applied the inverse method to the data and evaluated the results.

Harald Bönisch, Timo Keber and Andreas Engel were strongly involved in the development of the GhOST instrument, in its operation during the PGS and WISE research campaign and in the evaluation and interpretation of the data.

Marius Hauck and Tanja Schuck operated the GhOST instrument during WISE, evaluated and interpreted the data.

Peter Hoor was an active part during both PGS and WISE with the TRIHOP and UMAQS instruments.

All co-authors contributed to the preparation of the manuscript in many useful discussions.

Frankfurt am Main

_____

Marius Hauck

Atmos. Chem. Phys., 20, 8763–8785, 2020
https://doi.org/10.5194/acp-20-8763-2020

Atmospheric Chemistry and Physics
Open Access
EGU

A convolution of observational and model data to estimate age of air spectra in the northern hemispheric lower stratosphere

Marius Hauck[1], **Harald Bönisch**[5], **Peter Hoor**[4], **Timo Keber**[1], **Felix Ploeger**[2,3], **Tanja J. Schuck**[1], **and Andreas Engel**[1]

[1]Institute for Atmospheric and Environmental Sciences, Goethe University Frankfurt am Main, Frankfurt am Main, Germany
[2]Institute for Energy and Climate Research: Stratosphere (IEK-7), Forschungszentrum Jülich, Jülich, Germany
[3]Institute for Atmospheric and Environmental Research, University of Wuppertal, Wuppertal, Germany
[4]Institute for Atmospheric Physics, Johannes Gutenberg University Mainz, Mainz, Germany
[5]Karlsruhe Institute of Technology, Institute of Meteorology and Climate Research – Atmospheric Trace Gases and Remote Sensing, Eggenstein-Leopoldshafen, Germany

Correspondence: Marius Hauck (hauck@iau.uni-frankfurt.de)

Received: 20 February 2020 – Discussion started: 30 March 2020
Revised: 8 June 2020 – Accepted: 29 June 2020 – Published: 24 July 2020

Abstract. Derivation of mean age of air (AoA) and age spectra from atmospheric measurements remains a challenge and often requires output from atmospheric models. This study tries to minimize the direct influence of model output and presents an extension and application of a previously established inversion method to derive age spectra from mixing ratios of long- and short-lived trace gases. For a precise description of cross-tropopause transport processes, the inverse method is extended to incorporate air entrainment into the stratosphere across the tropical and extratropical tropopause. We first use simulations with the Chemical Lagrangian Model of the Stratosphere (CLaMS) to provide a general proof of concept of the extended principle in a controllable and consistent environment, where the method is applied to an idealized set of 10 trace gases with predefined constant lifetimes and compared to reference model age spectra. In the second part of the study we apply the extended inverse method to atmospheric measurements of multiple long- and short-lived trace gases measured aboard the High Altitude and Long Range (HALO) research aircraft during the two research campaigns POLSTRACC–GW-LCYCLE–SALSA (PGS) and Wave-driven Isentropic Exchange (WISE). As some of the observed species undergo significant loss processes in the stratosphere, a Monte Carlo simulation is introduced to retrieve age spectra and chemical lifetimes in stepwise fashion and to account for the large uncertainties. Results show that in the idealized model scenario the inverse method retrieves age spectra robustly on annual and seasonal scales. The extension to multiple entry regions proves reasonable as our CLaMS simulations reveal that in the model between 50 % and 70 % of air in the lowermost stratosphere has entered through the extratropical tropopause (30–90° N and S) on annual average. When applied to observational data of PGS and WISE, the method derives age spectra and mean AoA with meaningful spatial distributions and quantitative range, yet large uncertainties. Results indicate that entrainment of fresh tropospheric air across both the extratropical and tropical tropopause peaked prior to both campaigns, but with lower mean AoA for WISE than PGS data. The ratio of moments for all retrieved age spectra for PGS and WISE is found to range between 0.52 and 2.81 years. We conclude that the method derives reasonable and consistent age spectra using observations of chemically active trace gases. Our findings might contribute to an improved assessment of transport with age spectra in future studies.

1 Introduction

Spatial distributions of many greenhouse gases and ozone-depleting trace gases throughout the stratosphere are determined by the global mean meridional circulation, known as the Brewer–Dobson circulation (BDC), making it a crucial factor for the Earth's radiative budget and climate (Shepherd, 2007; Solomon et al., 2010). The BDC is usually characterized as a superposition of a mean residual circulation with

net mass transport and two-way eddy mixing with tracer exchange but no net mass flux (Plumb, 2002; Butchart, 2014). Birner and Bönisch (2011) recognized two distinct pathways for the BDC, a shallow and a deep branch, with different transport timescales along them. The shallow branch reaches from the tropics into the extratropics close to the tropopause, while the deep branch extends up into the middle and upper stratosphere (Birner and Bönisch, 2011). Mechanical drivers of the BDC are planetary- and synoptic-scale atmospheric waves that get excited in the troposphere and propagate upward into the extratropical middle stratosphere where they finally break and transfer their momentum to induce a poleward motion (Haynes et al., 1991; Holton et al., 1995). The wave drag causes air to rise slowly in the tropics mainly through the tropical tropopause layer (TTL) to compensate for the poleward drift (Fueglistaler et al., 2009). Eventually, air descends at higher latitudes back into the troposphere. The upward mass flux in the tropics presents a distinct seasonality with maximum upward transport during northern hemispheric winter, due to a maximum of tropospheric waves (Rosenlof and Holton, 1993; Rosenlof, 1995). Although the TTL is identified as the main entry point to the stratosphere, transport mechanisms across the extratropical tropopause play an important role in air composition in the lowermost stratosphere (LMS) below 380 K potential temperature (Olsen et al., 2004; Boothe and Homeyer, 2017). Those exchange processes exhibit their own distinct seasonality (Appenzeller et al., 1996; Schoeberl, 2004) and geographical distribution (Škerlak et al., 2014; Yang et al., 2016).

As global greenhouse gas concentrations and sea surface temperatures keep rising, model studies expect that the BDC will strengthen due to enhanced wave drag (Garcia and Randel, 2008; Li et al., 2008; Shepherd and McLandress, 2011). Studies of suitable dynamical tracers (e.g., SF_6, CO_2 or N_2O) from different observational sources, however, show a much more complex and contradictory state, indicating that the strength of the BDC might undergo nonuniform structural changes with hemispheric asymmetries (Engel et al., 2009; Bönisch et al., 2011; Ray et al., 2014; Stiller et al., 2017; Laube et al., 2020). Although more recent analyses of global models (Oberländer-Hayn et al., 2015, 2016) and also reanalyses (Diallo et al., 2012; Abalos et al., 2015) were able to disentangle some inconsistencies, possible trends of the BDC remain an open issue, especially in the case of reanalyses, as recent studies show that different reanalysis products can alter the outcome significantly (Chabrillat et al., 2018; Ploeger et al., 2019).

A major problem that studies of the BDC share is the difficulty to measure transport directly (Butchart, 2014). While model simulations provide possibilities to derive quantities that describe the strength and structure of the BDC and potential trends, observational analysis is challenging, especially in remote parts of the stratosphere where only sparse measurements exist. A well-established diagnostic tool used in many studies of both models and observations is mean age of air (AoA) (Hall and Plumb, 1994). Mean AoA is defined as the average transit time an air parcel needs to reach the considered location starting at a specified reference surface, usually the Earth's surface or the tropical tropopause. It is inversely proportional to the general circulation strength (Austin and Li, 2006). Mean AoA is also influenced by mixing processes (Waugh and Hall, 2002; Garny et al., 2014), and separation between residual transport and mixing is complicated due to the average nature of mean AoA. For such analysis, a full transit time distribution should be considered, since stratospheric air consists of an irreversible mixture of air parcels with different transit times from the source region. The age spectrum of any arbitrary air parcel represents a probability density function (PDF) of the transit timescales within the parcel (Kida, 1983).

In many model simulations, the age spectrum is constructed by an implementation of chemically inert trace gases that are periodically pulsed in a specified boundary region (Haine et al., 2008; Li et al., 2012; Ploeger and Birner, 2016). Mean AoA is then defined as the first moment of the age spectrum. In the case of observations, the derivation of both mean AoA and age spectra is more complex and follows different approaches. The basis of many past studies has been measurements of (very) long-lived trace gases together with the fundamental theory on age spectra by Hall and Plumb (1994) to constrain the shape of the spectra and the ratio of variance to mean AoA beforehand (Volk et al., 1997; Engel et al., 2002, 2009). Recent results by Fritsch et al. (2019) show that the parameter choice in such constraint methods strongly influences resulting mean AoA trends. Other methods rely on a more general shape of the spectrum but require more data than in the constrained case (Holzer and Primeau, 2010; Holzer and Waugh, 2015). However, the number of suitable stratospheric trace gases with a (very) large chemical lifetime is limited. One possible solution is to additionally consider substances with rapid chemical depletion, since stratospheric chemistry and transport are strongly intertwined. Such approaches also exist in different constrained (Schoeberl et al., 2005; Ehhalt et al., 2007) and unconstrained versions (Schoeberl et al., 2000; Podglajen and Ploeger, 2019). An improved parametric approach has been introduced in Hauck et al. (2019), which relies only on a constrained age spectrum shape to achieve applicability together with well-matched results in a model test scenario. Unfortunately, the method shows quite large discrepancies in the lowermost stratosphere where most stratospheric aircraft measurements are taken.

This paper constitutes a direct follow-up to Hauck et al. (2019). We extend the inverse method described therein to the lowermost stratosphere with a new formulation and provide a short proof of concept using a simulation of the Chemical Lagrangian Model of the Stratosphere (CLaMS) (McKenna, 2002a, b; Pommrich et al., 2014) with idealized radioactive tracers. We then apply the extended method

to in situ measurement data gained during the campaigns POLSTRACC–GW-LCYCLE–SALSA (PGS) and Wave-driven Isentropic Exchange (WISE) of the High Altitude and Long Range (HALO) research aircraft and analyze the resulting age spectra and their moments. Section 2 gives insight into the extended formulation of the method and the statistical procedure to estimate age spectra and chemical lifetimes from observations. Section 3 describes the data basis for this study. Finally, results are presented in Sect. 4 and completed by an outlook and a critical discussion in Sect. 5.

2 Methodology

2.1 Inverse method – general approach and problems

The theory of the inverse method is provided in detail by Hauck et al. (2019). It is a modified version of the method presented by Schoeberl et al. (2005) and utilizes mixing ratios of a set of different chemically active compounds to derive an age spectrum using a numerical optimization scheme. The age spectrum shape is constrained by the inverse Gaussian distribution proposed by Hall and Plumb (1994). At the same time, seasonality in stratospheric transport, which is visible in modeled age spectra in the form of multiple modes (Reithmeier et al., 2008; Li et al., 2012; Ploeger and Birner, 2016), has to be imposed by a seasonal scaling factor as the inverse Gaussian function is intrinsically a monomodal PDF. Mathematically, the inverse method is based on the following equation.

$$\chi(\boldsymbol{x},t) = \int_0^\infty \chi_0\left(t-t'\right)\cdot e^{-\frac{t'}{\tau(\boldsymbol{x},t,t')}}\cdot G\left(\boldsymbol{x},t,t'\right)\cdot\omega\left(t'\right) \cdot n(\boldsymbol{x},t)\cdot \mathrm{d}t' \quad (1)$$

$\chi(\boldsymbol{x},t)$ denotes the mixing ratio of any arbitrary trace gas at $(\boldsymbol{x},t)$ in the stratosphere with chemical depletion, but no stratospheric sources. t' is the transit time through the stratosphere, $\chi_0\left(t-t'\right)$ the mixing ratio time series of the substance at the reference surface, $\tau(\boldsymbol{x},t,t')$ the transit-time-dependent chemical lifetime, $G\left(\boldsymbol{x},t,t'\right)$ the age spectrum, and $\omega\left(t'\right)$ the seasonal scaling factor to gain multimodal PDFs (see below). $n(\boldsymbol{x},t)$ is a normalization factor for the age spectrum, which ensures that $G\left(\boldsymbol{x},t,t'\right)$ and $G\left(\boldsymbol{x},t,t'\right)\cdot\omega\left(t'\right)$ have identical norms. It is defined as

$$n(\boldsymbol{x},t) = \frac{\int_0^\infty G\left(\boldsymbol{x},t,t'\right)\cdot\mathrm{d}t'}{\int_0^\infty G(\boldsymbol{x},t,t')\cdot\omega(t')\cdot\mathrm{d}t'}. \quad (2)$$

The definition of $n(\boldsymbol{x},t)$ above preserves the norm of the age spectrum $G\left(\boldsymbol{x},t,t'\right)$ during the scaling process. Although age spectra must usually be normalized, there are cases in this study where a non-normalized spectrum is physically meaningful (see Sect. 2.2.1). Full consideration of a transit-time-dependent entry mixing ratio has been introduced for applicability purposes, since many atmospheric trace gases exhibit a strong long-term temporal trend that should be considered properly. An approximation of the stratospheric age spectrum in Eq. (1) is provided by Hall and Plumb (1994):

$$G\left(\boldsymbol{x},t,t'\right) = \frac{z}{2\sqrt{\pi\,K(\boldsymbol{x},t)t'^3}}\cdot e^{\left(\frac{z}{2H}-\frac{K(\boldsymbol{x},t)t'}{4H^2}-\frac{z^2}{4K(\boldsymbol{x},t)t'}\right)}, \quad (3)$$

but with a three-dimensional transport parameter $K(\boldsymbol{x},t)$ instead of an originally one-dimensional diffusion coefficient. z is the potential temperature difference to the local tropopause and H the scale height of the air density. The first moment $\Gamma(\boldsymbol{x},t)$ (i.e., mean AoA) and centered second moment $\Delta^2(\boldsymbol{x},t)$ (i.e., variance) of the spectrum are given as (Hall and Plumb, 1994)

$$\Gamma(\boldsymbol{x},t) = \int_0^\infty G\left(\boldsymbol{x},t,t'\right)\cdot t'\cdot\mathrm{d}t', \quad (4)$$

$$\Delta^2(\boldsymbol{x},t) = \frac{1}{2}\cdot\int_0^\infty G\left(\boldsymbol{x},t,t'\right)\cdot\left(t'-\Gamma(\boldsymbol{x},t)\right)^2\cdot\mathrm{d}t'. \quad (5)$$

For the inversion process, mixing ratios of a given set of distinct trace gases are considered, and $K(\boldsymbol{x},t)$ is optimized numerically for all species simultaneously. Hauck et al. (2019) provide a general proof of concept of this method in a controllable model environment featuring a set of several artificial radioactive trace gases with constant chemical lifetimes. Despite the robust performance of the inverse method compared to the model reference in general, the lower stratosphere proves challenging, especially during northern hemispheric spring and fall. That is most probably linked to a conceptual flaw in the design of the inverse method. In its presented form, all derived inverse age spectra assume the tropical tropopause to be a single source region into the stratosphere. Although this appears valid for the upper and middle stratosphere (Fueglistaler et al., 2009), studies have shown that for the lowermost extratropical stratosphere, quasi-isentropic transport across the local tropopause has critical influence and strongly affects trace gas burdens in that region (Hoor et al., 2005; Bönisch et al., 2009). Therefore, the assumption of single entry through the tropical tropopause layer is insufficient to estimate a precise age spectrum and must be modified to include air entrainment through the complete tropopause together with related seasonality.

2.2 Inverse method with multiple entry sections

2.2.1 Concept

To fully incorporate transport processes in the extratropical lowermost stratosphere, an extension of the methodology to multiple entry regions is required. A rather intuitive way to divide the tropopause is the partitioning into a northern (index N), a tropical (index T) and a southern (index S) section, each with a separate age spectrum assigned to them. All entry regions must then add up geographically to span the global

tropopause. A mathematically strict derivation of age spectra for several different source regions is given by Holzer and Hall (2000). The ansatz is similar to Bönisch et al. (2009), but with a split of the reference surface rather than a separation into a tropospheric and a stratospheric fraction. Due to mass conservation, this concept translates into a composite age spectrum by

$$G\left(\boldsymbol{x},t,t'\right)=g_{\mathrm{N}}\left(\boldsymbol{x},t,t'\right)+g_{\mathrm{T}}\left(\boldsymbol{x},t,t'\right)+g_{\mathrm{S}}\left(\boldsymbol{x},t,t'\right), \tag{6}$$

with $g_i\left(\boldsymbol{x},t,t'\right)$ being the age spectrum referring to transport through the tropopause section i. Since the normalization of $G\left(\boldsymbol{x},t,t'\right)$ must also hold in the extended case, the integration of $G\left(\boldsymbol{x},t,t'\right)$ now yields

$$\begin{aligned}\int_0^\infty G\left(\boldsymbol{x},t,t'\right)\cdot \mathrm{d}t' &= \int_0^\infty g_{\mathrm{N}}\left(\boldsymbol{x},t,t'\right)\cdot \mathrm{d}t' \\ &+ \int_0^\infty g_{\mathrm{T}}\left(\boldsymbol{x},t,t'\right)\cdot \mathrm{d}t' + \int_0^\infty g_{\mathrm{S}}\left(\boldsymbol{x},t,t'\right)\cdot \mathrm{d}t' \\ &:= f_{\mathrm{N}}\left(\boldsymbol{x},t\right)+f_{\mathrm{T}}\left(\boldsymbol{x},t\right)+f_{\mathrm{S}}\left(\boldsymbol{x},t\right)=1.\end{aligned} \tag{7}$$

The lowercased $g_i\left(\boldsymbol{x},t,t'\right)$ indicates a non-normalized age spectrum and $f_i\left(\boldsymbol{x},t\right)$ its respective norm. In terms of transport, the norm $f_i\left(\boldsymbol{x},t\right)$ provides an estimate of the fraction of air at $(\boldsymbol{x},t)$ which has entered the stratosphere through tropopause region i. The norms are referred to as origin fractions and provide an important toolset for an analysis of seasonality in air entrainment (see Sect. 4.1). Any non-normalized age spectrum can be converted into a proper PDF by division through its origin fraction.

$$G_i\left(\boldsymbol{x},t,t'\right)=\frac{g_i\left(\boldsymbol{x},t,t'\right)}{f_i\left(\boldsymbol{x},t\right)} \tag{8}$$

Since each $g_i\left(\boldsymbol{x},t,t'\right)$ constitutes a description of transport for the percentage of air at $(\boldsymbol{x},t)$ that entered the stratosphere through tropopause region i, it can therefore also be utilized to calculate the mixing ratio fraction $\chi_i\left(\boldsymbol{x},t\right)$ associated with that respective entrainment. Multiplication of Eq. (7) with $\chi\left(\boldsymbol{x},t\right)$ includes those mixing ratio fractions in the new concept

$$\begin{aligned}\chi\left(\boldsymbol{x},t\right) = {} & f_{\mathrm{N}}\left(\boldsymbol{x},t\right)\cdot\chi\left(\boldsymbol{x},t\right)+f_{\mathrm{T}}\left(\boldsymbol{x},t\right)\cdot\chi\left(\boldsymbol{x},t\right) \\ & + f_{\mathrm{S}}\left(\boldsymbol{x},t\right)\cdot\chi\left(\boldsymbol{x},t\right) := \chi_{\mathrm{N}}\left(\boldsymbol{x},t\right) \\ & + \chi_{\mathrm{T}}\left(\boldsymbol{x},t\right)+\chi_{\mathrm{S}}\left(\boldsymbol{x},t\right),\end{aligned} \tag{9}$$

where each individual $\chi_i\left(\boldsymbol{x},t\right)$ can be derived from $g_i\left(\boldsymbol{x},t,t'\right)$ and Eq. (1) as

$$\begin{aligned}\chi_i\left(\boldsymbol{x},t\right) = {} & \int_0^\infty \chi_{0,i}\left(t-t'\right)\cdot e^{-\frac{t'}{\tau_i\left(\boldsymbol{x},t,t'\right)}}\cdot g_i\left(\boldsymbol{x},t,t'\right) \\ & \cdot\omega_i\left(t'\right)\cdot n_i\left(\boldsymbol{x},t\right)\cdot \mathrm{d}t'.\end{aligned} \tag{10}$$

The parameterization provided by Eq. (3) returns an invariably normalized inverse Gaussian function so that Eq. (10) must be modified with Eq. (8) to correctly yield

$$\begin{aligned}\chi_i\left(\boldsymbol{x},t\right) = {} & f_i\left(\boldsymbol{x},t\right)\cdot\int_0^\infty \chi_{0,i}\left(t-t'\right)\cdot e^{-\frac{t'}{\tau_i\left(\boldsymbol{x},t,t'\right)}} \\ & \cdot G_i\left(\boldsymbol{x},t,t'\right)\cdot\omega_i\left(t'\right)\cdot n_i\left(\boldsymbol{x},t\right)\cdot \mathrm{d}t'.\end{aligned} \tag{11}$$

Each entry region is now treated with a single entry mixing ratio time series $\chi_{0,i}\left(t-t'\right)$, a transit-time-dependent lifetime $\tau_i(t')$, a normalized age spectrum $G_i\left(\boldsymbol{x},t,t'\right)$, and an imposed seasonal cycle $\omega_i\left(t'\right)$ with its respective normalization factor $n_i\left(\boldsymbol{x},t\right)$. The introduced formulation is valid for any partitioning of the tropopause into three subregions. For this study, the tropical tropopause is chosen to range from 30° S up to 30° N to incorporate the seasonal shift of the intertropical convergence zone (ITCZ). The northern and southern parts extend from 30 to 90° N and 30 to 90° S, respectively. With that choice, all entry regions span an identical range of 60° latitude, although the actual enclosed area is larger for the tropical section. Transport is now characterized by three separate parameters $K_i(\boldsymbol{x},t)$. Since the mixing ratio fraction $\chi_i\left(\boldsymbol{x},t\right)$ is usually unknown for any stratospheric location, Eq. (11) is divided by $f_i\left(\boldsymbol{x},t\right)$ knowing that $\chi_i\left(\boldsymbol{x},t\right)$ has been introduced as $\chi\left(\boldsymbol{x},t\right)\cdot f_i\left(\boldsymbol{x},t\right)$. This important step yields a set of three decoupled equations, which can be treated separately:

$$\begin{aligned}\chi\left(\boldsymbol{x},t\right) = {} & \int_0^\infty \chi_{0,i}\left(t-t'\right)\cdot e^{-\frac{t'}{\tau_i\left(\boldsymbol{x},t,t'\right)}}\cdot G_i\left(\boldsymbol{x},t,t'\right) \\ & \cdot\omega_i\left(t'\right)\cdot n_i\left(\boldsymbol{x},t\right)\cdot \mathrm{d}t'.\end{aligned} \tag{12}$$

The inversion process of Eq. (12) is independent of $f_i\left(\boldsymbol{x},t\right)$ but only works correctly if $\chi_{0,i}\left(t-t'\right)$ or $\tau_i\left(t'\right)$ are unequal for all tropopause regions. Otherwise, each inversion leads to the identical age spectrum. Due to refinements of the optimization algorithm, these equations are optimized for all considered species at once now with 0.1 % tolerance (5 % in Hauck et al., 2019) and the new metric of the symmetric signed percentage bias (SSPB) (Morley et al., 2018). The SSPB is suitable if the overall quantitative range of mixing ratios is large and utilizes the median and logarithm to smooth the strong percentage influence of very small mixing ratios. That inversion process is now called K-inversion. Note that the decision to optimize bias rather than variance, e.g., root-mean-square error, has been made to return an average age spectrum that captures even fine effects of the underlying mixing ratio data robustly. In return, this comes at the cost of higher variance around the true solution due to the bias–variance tradeoff.

2.2.2 Extratropical seasonal cycles

Exchange processes across the northern hemispheric (NH) and southern hemispheric (SH) extratropical tropopause each display a different seasonality than the transport through the tropical tropopause layer. These seasonal cycles are rele-

vant for stratospheric age spectra as they cause the multimodal shape of modeled spectra. The inverse method rests upon the monomodal inverse Gaussian function by Hall and Plumb (1994) so that multiple peaks are not included intrinsically but are imposed by the fixed scaling factor $\omega_i\left(t'\right)$ during the inversion process. In Hauck et al. (2019) it has been shown that the ratio of the tropical net upward mass flux at 70 hPa between different seasons can be used to scale the age spectrum at matching transit times. The scaling factor by Hauck et al. (2019) is given as

$$\omega_i\left(t'\right) = A_i + B_i \cdot \cos\left(\frac{2\pi}{365\,\mathrm{d}} \cdot t' + C_i\right). \tag{13}$$

A_i, B_i, and C_i are constants that now depend on the entry region and the considered season. Seasons are hereafter abbreviated as DJF (NH winter), MAM (NH spring), JJA (NH summer), and SON (NH fall). Note that an increase in transit time is always equivalent to going backward in real time so that DJF is followed by SON (0.25 years transit time), JJA (0.5 years), and MAM (0.75 years). The values for the tropical tropopause section are taken from Hauck et al. (2019) and given in the first three columns of Table 1.

The extratropical cycles are more challenging as distinct transport processes superimpose in the extratropical lowermost stratosphere. For a proper scaling factor in these regions, a net upward-directed mass flux should be considered that reflects the ongoing dynamical processes as precisely as possible. Previous observationally based studies of SF_6, CO_2, and mean AoA find a flushing of the NH lowermost stratosphere with fresh tropospheric air during summer (JJA) and autumn (SON) that is most likely linked to the weaker subtropical jet stream and a dominance of the shallow branch of the BDC during that time (Bönisch et al., 2009). In contrast to these results, different mass budget analyses of the lowermost stratosphere in both hemispheres show that the net direction of the hemispherically integrated mass flux across the tropopause is downward with a maximum during spring in each hemisphere and a generally weaker seasonality in the SH. The upward component of this net mass flux is shown to reach its maximum during fall and its minimum conversely in spring in each hemisphere (Olsen et al., 2004; Schoeberl, 2004). The contradicting seasonality patterns imply that a hemispherically integrated mass flux might not be a suitable proxy for upward transport across the defined extratropical tropopause sections in this study, especially since the net direction of this flux is downward. It is more likely that a geographically narrow section of the NH and SH tropopause with year-round net upwelling causes the modes of the age spectra. Yang et al. (2016) investigate the ozone flux across the tropopause with a different framework where regions of net up- and downwelling are distinguishable. Their results indicate that in a small region in the subtropics of each hemisphere (around the equatorward flank of the subtropical jet stream), net upward transport across the tropopause with a maximum in summer is present, while at higher latitudes the net direction of the flux turns downward with a maximum in spring or winter depending on the latitudinal range (see their Fig. 12). In the SH, the seasonality is found to be generally weaker. This matches the observational results for the NH mentioned above. As the subtropical jet region is partly included in the defined tropopause sections for this study (30–90° N and S), it is likely that the enhanced entrainment across the subtropical jet stream during summer is a key feature of transport visible in derived age spectra. Unfortunately, Yang et al. (2016) provide only an ozone flux in their study (see their Fig. 7a and b) and no mass flux for the desired region so that a different proxy must be found.

To estimate the seasonality and the strength of the dominant entrainment processes specifically across the introduced extratropical tropopause sections, the modeled age spectra from the CLaMS simulation below are considered, which are initialized in the specified NH and SH tropopause section (see Sect. 3.1 for details on the simulation). We follow the ansatz of Fig. 14b in Ploeger and Birner (2016) and integrate all monthly stratospheric age spectra of one source region bin-wise to compute the fraction of air that entered the stratosphere across this given source region per transit time bin. The fractions of all age spectra are cumulated and transit times are matched correctly against real time so that an average statistic for air mass entrainment across the NH and SH tropopause section per month is retrieved. Results of this ansatz are shown in Fig. 1a, b for the NH (panel a) and SH (panel b) tropopause section. It is evident that in the model for both regions the strongest entrainment occurs during July (NH) and January (SH), where more than 14 % of all air masses that cross the respective tropopause section are found to enter the stratosphere. This seasonality follows the observations of Bönisch et al. (2009) and also the ozone flux of Yang et al. (2016) very well and makes the subtropical jet region the most likely source mechanism for the tropopause sections defined above. The minimum of entrainment is found consistently in December (NH) and June (SH) with a fraction of less than 3 %. The cumulated values for each season are used to derive a scaling factor for the age spectra referring to the NH and SH tropopause sections. For instance, the fraction during JJA in the NH (ca. 39 %) is approximately 3 times larger than during DJF (ca. 13 %) so that corresponding age spectra in DJF must be tripled at transit times that correspond to JJA (0.5 years, 1.5 years, etc.). This principle is repeated for all remaining combinations of seasons in the NH and SH to estimate the coefficients in Eq. (13). No scaling is applied at transit times that represent the season the age spectrum is derived in, e.g., DJF in the example above. Resulting coefficients are shown in Table 1 and the final scaling factors are exemplified for the first year of transit time in Fig. 1c, d. The scaling works consistently as the maximum of each curve is found at summer transit times while the minimum is located consistently during winter.

The scaling factors are approximated from integrated CLaMS age spectra, which aggravates a comparison of

Table 1. Scaling constants of Eq. (13) for the northern, tropical, and southern tropopause sections (N, T, S) in all four seasons. The tropical values are taken from Hauck et al. (2019).

	A_T	B_T	C_T	A_N	B_N	C_N	A_S	B_S	C_S
DJF	0.8	0.2	$0.0 \cdot \pi$	2.00	−1.031	$-0.078 \cdot \pi$	0.68	0.324	$-0.05 \cdot \pi$
MAM	1.0	0.25	$1.5 \cdot \pi$	0.89	0.463	$0.424 \cdot \pi$	1.17	−0.685	$0.423 \cdot \pi$
JJA	1.3	0.3	$1.0 \cdot \pi$	0.67	0.346	$-0.08 \cdot \pi$	1.88	−0.952	$-0.129 \cdot \pi$
SON	1.0	0.25	$0.5 \cdot \pi$	1.15	−0.583	$0.42 \cdot \pi$	0.88	0.395	$0.398 \cdot \pi$

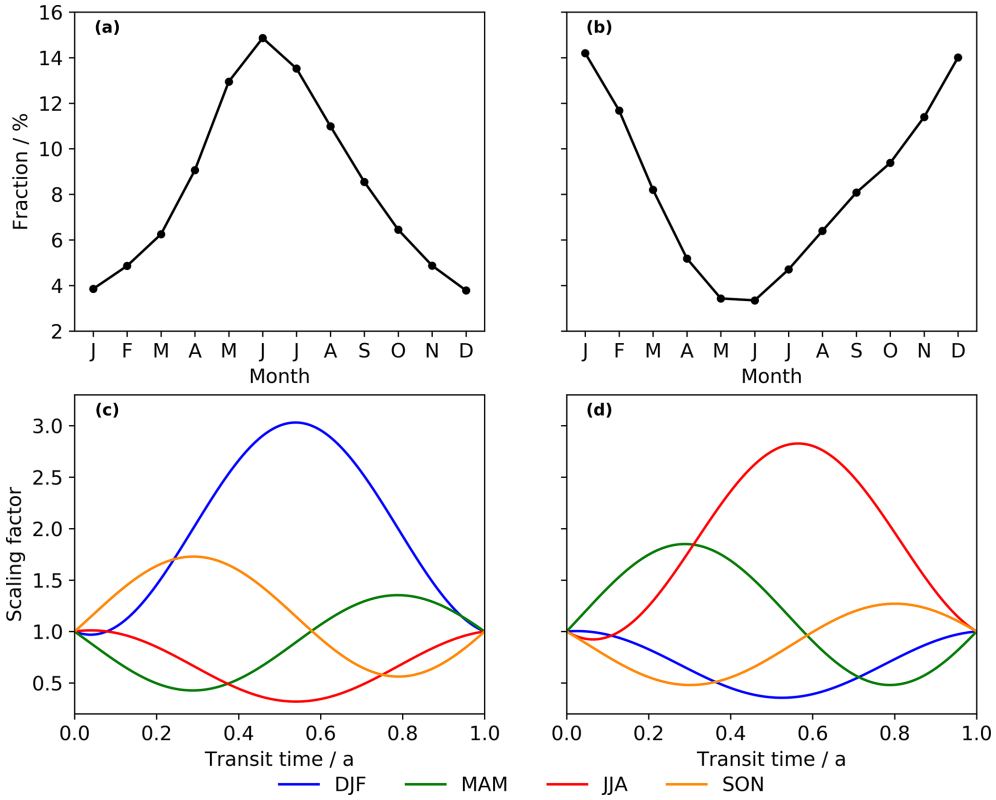

Figure 1. The top row shows the fraction of air masses that enter the stratosphere in each month through the extratropical northern (30–90° N, panel **a**) and southern WMO tropopause (30–90° S, panel **b**) relative to all air masses entering through the defined regions within the CLaMS model simulation (see Sect. 3.1 for details). The fractions are calculated by bin-wise integration and summation of all global stratospheric G_N **(a)** and G_S **(b)**. The bottom row depicts the approximated seasonal scaling factors for inverse age spectra referring to the northern **(c)** and southern **(d)** extratropical tropopause sections. Note that increasing transit time is equivalent to going backward in real time. Month-based abbreviations are used so that identical seasons have inverted colors in both hemispheres. See Sect. 2.2.2 for details on the derivation of the scaling factors. The fractions are normalized to equal 100 % when cumulated in each hemisphere.

higher-order peaks between the CLaMS reference and inverted age spectra as these modes are expected to appear at matching transit times. However, all global CLaMS age spectra are integrated and cumulated so that the resulting seasonality of the fractions is an average measure, and no information about the exact shape is transferred from CLaMS to the inverse method. All inverse age spectra in one specific season are moreover scaled with the same factor globally, which implies that the intrinsic amplitude of the monomodal inverse spectra must be well-retrieved as otherwise the scaling would nevertheless lead to deviating modes. Since the discovered seasonality in entrainment is also in good agreement with the upward ozone flux in the subtropical jet stream region (Yang et al., 2016) and with the seasonality derived from observations in the NH (Bönisch et al., 2009), the derived scaling factors are deemed a robust estimator for the presented extended inverse approach with the specified NH and SH tropopause sections.

2.2.3 Limitations

The extended inverse ansatz keeps the benefit of an inversion with a single parameter, but it also holds some disadvantages that require the use of output from atmospheric transport models. The goal of this study is to reduce the amount of necessary model output as much as possible for the inversion and evaluation of age spectra, but it must be stated clearly that it is not feasible to provide a method based solely on observations. While all $G_i\left(\boldsymbol{x}, t, t'\right)$ can be well-retrieved and evaluated to investigate the BDC without explicit use of the origin fractions $f_i\left(\boldsymbol{x}, t\right)$ from models, they must be known beforehand to calculate the composite age spectrum $G\left(\boldsymbol{x}, t, t'\right)$ as a superposition of all $G_i\left(\boldsymbol{x}, t, t'\right)$. This piece of information must be provided by a model simulation. Also, the choice of a prescribed inverse Gaussian function might not be valid for any point in the stratosphere, particularly for cross-hemispheric PDFs (i.e., $G_{\mathrm{S}}\left(\boldsymbol{x}, t, t'\right)$ in the NH and vice versa). However, it is expected that the fractions of interhemispheric exchange are vanishingly low in the lowermost stratosphere, making those age spectra negligible. For the remaining distributions it is assumed that an inverse Gaussian shape provides a robust approximation of both tropical and extratropical age spectra with a low amount of necessary input data. This seems a valid approach as modeled tropical age spectra (Li et al., 2012; Ploeger and Birner, 2016) exhibit strong similarities with an inverse Gaussian function only with multiple modes. Still, the constrained shape might lead to inaccuracies to an unknown extent.

Above all, the performance of the inverse method depends crucially on the physically precise quantification of the chemical lifetime for each trace gas, since chemistry and transport show a strong interrelationship. Due to this close link, the lifetime is considered to be dependent on transit times along an average Lagrangian pathway through the stratosphere (Schoeberl et al., 2000). Although Hauck et al. (2019) demonstrate that due to the consideration of multiple trace gases in the optimization process a pseudo-random error of up to $\pm 20\,\%$ in the chemical lifetime can be compensated for, the correct determination of the local lifetimes along transit time remains a considerable problem. A probable strategy could be an advancement of the ansatz by Holzer and Waugh (2015) where not only observations of (very) short-lived substances but also a set of long-lived trace gases are involved in a Monte Carlo simulation to derive lifetimes and age spectra in a stepwise fashion. The chemical lifetimes are hereby set to constant values, which describe chemistry effectively (see Sect. 2.2.4). This approach has the advantage that it reduces the influence of model output but relies on the goodness of the observations, especially for long-lived trace gases.

2.2.4 Statistical inversion process

The study of Holzer and Waugh (2015) provides the basis to derive a representative chemical lifetime for each substance from observational data together with statistical techniques. For that purpose, Eq. (12) has to be slightly tweaked. All transit-time-dependent lifetimes are replaced by the concept of effective stratospheric lifetimes $\tau_{i,\mathrm{eff}}(\boldsymbol{x}, t)$. Those quantify chemistry for any given age spectrum along all relevant transport pathways effectively by a single scalar. This leads to

$$\chi\left(\boldsymbol{x}, t\right) = \int_0^\infty \chi_{0,i}\left(t - t'\right) \cdot e^{-\frac{t'}{\tau_{i,\mathrm{eff}}(\boldsymbol{x}, t)}} \cdot G_i\left(\boldsymbol{x}, t, t'\right) \cdot \omega_i\left(t'\right) \cdot n_i\left(\boldsymbol{x}, t\right) \cdot \mathrm{d}t', \tag{14}$$

where $G_i\left(\boldsymbol{x}, t, t'\right)$ is again parameterized by Eq. (3). The effective lifetime for any trace gas can be retrieved numerically based on a prior estimate of the age spectrum $G_i^{\mathrm{prior}}\left(\boldsymbol{x}, t, t'\right)$. If this is derived, a slightly modified version of the K-inversion algorithm will use the prior age spectrum and optimize the effective lifetime for each substance separately using the same numerical methods as above. This is the τ-inversion. The physical difference between Eqs. (12) and (14) lies in the transit time dependence of the mixing ratio. Using effective lifetimes, this gradient is different from the one in the original formulation for a specified age spectrum. However, since the final mixing ratio is identical in both cases, that fact is negligible. In the original form, Holzer and Waugh (2015) apply global tropospheric lifetimes for long-lived substances to gain the prior estimate of the tropospheric age spectrum. In the stratosphere, however, most trace gases undergo considerable chemical loss processes that cannot be estimated well by global lifetimes, which make additional information necessary. Therefore, (very) long-lived trace gases are considered together with short-lived species to constrain the age spectrum. For this study, we select five short-lived brominated trace gases (CH_2Br_2, $CHBr_3$, $CHCl_2Br$, $CHClBr_2$, and CH_2ClBr), five long-lived substances (CF_2Cl_2 (CFC-12), CF_2ClBr (halon 1211), CF_3Br (halon 1301), CH_3Br, and N_2O), and the very long-lived trace gas SF_6, which has been frequently used as a dynamical tracer in the past. All these species were measured during past airborne research campaigns so that a solid data basis can be established.

As stated above, the statistical inversion method requires a prior estimate of an age spectrum to infer the effective chemical lifetime. The outcome of the procedure hinges heavily on this first guess so that we introduce a Monte Carlo cross-validation (MCCV) for all tropopause sections to perturb the dependency and also consider a variety of uncertainties. As a first step, a subset of the trace gases is created, consisting of three selected species of the complete set. The subset is always composed of the dynamical tracer SF_6, one of the five long-lived species, and one of the five short-lived species.

The latter two are pseudo-randomly chosen. With this subset, the first guess of the age spectrum is constructed using the K-inversion on Eq. (14) together with an initial guess for the effective stratospheric lifetimes of the considered species. Other than in Holzer and Waugh (2015), a global lifetime is in general not suitable, as strong local stratospheric loss processes steer the effective lifetimes along all relevant transit times for both long- and short-lived trace gases. This implies that the effective lifetime of a species is generally smaller than its global lifetime. The exception is SF_6, which has its main sink region in the mesosphere at large transit times. For the mainly short transport timescales in the lower stratosphere, the influence of the chemical loss is rather small, yet not negligible. The first-guess effective lifetime of SF_6 is therefore set to be 850 years in accordance with Ray et al. (2017). In the case of the short-lived substances, mixing ratios are most probably steered by local chemical loss processes around the respective entry region. First-guess lifetimes for those species are taken as annual means from Tables 1–4 in Carpenter and Reimann (2014) for the NH and tropical tropopause sections. Long-lived trace gases show the most difficulties when assessing the first guess. On the one hand, global stratospheric lifetimes are likely an overestimation, as they are derived by dividing the global atmospheric burden by the global stratospheric loss rate. Local lifetimes, on the other hand, quantify the strength of localized stratospheric sink processes and thus do not consider that the desired lifetimes must express all relevant chemical depletion effectively for a given age spectrum. Additionally, these lifetimes are in many cases derived from model simulations. This study strives for a reduced model influence, so that the global stratospheric lifetimes from Table 5.6 in SPARC (2013) are turned into lifetimes that consider the stratospheric burden rather than the total atmospheric burden and treat them as first-order approximations of effective loss. The effective lifetime in our formulation is similar to a transit-time-integrated steady state but only considers trace gas burdens and sink processes above the tropopause. Since all mass above the tropopause consists of 10 % of the complete atmospheric mass (Volk et al., 1997), the stratospheric burden of a substance is assumed to contribute only 10 % to its global burden. Dividing burden by loss, this concept translates into lifetimes that are only 10 % of the global stratospheric lifetime. All implemented first-guess lifetimes are shown in Table 2.

These values do not necessarily provide a valid representation so that systematic errors are included in the simulation. The errors were selected pseudo-randomly with uniform distribution for a random number of trace gases in the prior subset. They range from $-50\,\%$ to $+50\,\%$ for the first-guess lifetimes and from $-\sigma$ to $+\sigma$ for $\chi_{0,i}\left(t-t'\right)$ and $\chi\left(\boldsymbol{x},t\right)$. σ denotes the standard deviation of a mixing ratio (see Sect. 3.2 for details). After the prior age spectrum has been determined, it is used to perform the τ-inversion on Eq. (14) during which an effective lifetime is retrieved for every remaining substance that has not been in the prior subset. Again, pseudo-random errors between $-\sigma$ and $+\sigma$ for all $\chi_{0,i}\left(t-t'\right)$ and $\chi\left(\boldsymbol{x},t\right)$ are applied to this set. For solid Monte Carlo statistics, this procedure is repeated 2000 times to cover as many initial subsets as numerically feasible. There is no effective lifetime for SF_6, since this tracer is present in every initial subset. That is done to make full use of SF_6 as a reasonable frame for the age spectrum, which is then convoluted with further trace gas information to get an even more robust and unbiased prior. After completion of the Monte Carlo simulation, the median of the retrieved effective lifetimes is utilized in a final K-inversion for the full trace gas set to determine the desired age spectrum. SF_6 is also not present in this final step to keep its direct influence restricted to the prior. In the rare case that no median effective lifetime can be derived for one of the remaining substances, the species will be omitted during the final K-inversion. To estimate the uncertainty range of the simulation, the lifetime of the 25th and 75th percentiles is taken to derive the upper and lower error margin of all age spectra and related moments.

Table 2. Initial-guess effective lifetimes for all species in this study. The values are annual averages and taken from Ray et al. (2017), SPARC (2013) and Carpenter and Reimann (2014).

	Northern & southern	Tropics
SF_6	850 a	850 a
N_2O	11.6 a	11.6 a
CFC-12	9.6 a	9.6 a
Halon 1211	3.4 a	3.4 a
Halon 1301	7.4 a	7.4 a
CH_3Br	2.6 a	2.6 a
$CHBr_3$	45 d	17 d
CH_2Br_2	451 d	150 d
$CHCl_2Br$	128 d	48 d
$CHClBr_2$	89 d	28 d
CH_2ClBr	529 d	174 d

Although that procedure is numerically expensive and requires multiple simulations for one set of mixing ratios at one location, the outcome of a reduced influence of model output seems promising. This comes at the cost of relatively large uncertainties for the retrieved effective lifetimes and age spectra, which hinge strongly on precise in situ measurements. With the considered errors in the Monte Carlo simulation, it is possible to receive an impression of the influence of these uncertainties on age spectra from observations.

3 Data basis

3.1 CLaMS simulations

Two simulations with the Chemical Lagrangian Model of the Stratosphere (CLaMS) have been performed in a similar

framework as the simulation of Ploeger and Birner (2016). CLaMS uses a Lagrangian perspective to model transport processes and chemistry for trace gases along calculated three-dimensional forward trajectories of single air parcels in combination with a parameterization scheme for small-scale mixing (McKenna, 2002a). That scheme leads to strong mixing in regions where deformations of the background flow are large (Konopka, 2004). CLaMS simulates transport in potential temperature space, where the vertical coordinate is designed as a hybrid between potential temperature in the stratosphere and upper troposphere and an orography-following pressure coordinate in the vicinity of the surface with smooth transition. The vertical speed along this coordinate is steered by the total diabatic heating rates from the reanalysis product that drives the simulation (Pommrich et al., 2014). In this study, CLaMS is driven by meteorological output of the ERA-Interim reanalysis (Dee et al., 2011). The final output of the Lagrangian model is gridded spatially with a resolution of 2° by 2° and 37 vertical potential temperature levels between 280 and 3000 K. Both simulations cover the period from January 1989 to December 2017 as a daily mean. Final model output is evaluated as zonal and seasonal means between December 1999 and November 2009 for the proof of concept.

This setup is suitable for the lower stratosphere, since fast transport processes across the tropopause are well-resolved. Age spectra in the model are derived from completely inert trace gases that are pulsed in certain intervals at the reference surface. Those pulse tracer series are then translated into proper spectra by the method of Ploeger and Birner (2016) for transient simulations. For convenience, these spectra are hereafter named pulse age spectra. In the first simulation (called TpSim), all tracers are initialized at the tropopause in the northern (90 to 30° N), tropical (30° N to 30° S), and southern (30 to 90° S) regions. Although a tropopause based on potential vorticity (PV) is a more suitable choice for dynamical studies, the simulations have been performed using the WMO definition of tropopause. For consistency between model and observations, tropopause hereafter always refers to the WMO definition. The tracer pulses are released as approximate Dirac delta distributions with a mixing ratio of 1 in their respective region and forced to zero when contacting the other two source sections. There are two separated sets of pulses for each source region to get a well-resolved age spectrum. They consist of 24 and 20 tracers, released monthly and semiannually, and cover a period of 2 and 10 years, respectively. If both sets are combined afterwards, the age spectrum will provide a fine monthly resolution up to 2 years and a coarser semiannual resolution for the remaining transit times up to 10 years. After every tracer has been pulsed once, they are reset and re-initialized.

The simulation also features three completely inert trace gases that are constantly released with a mixing ratio of 1 in the three source regions. These tracers provide the origin fractions for the reference surfaces without explicit integration of the age spectra. For the inverse method, 10 trace gases with spatially constant lifetimes ranging from 1 month to 109 months in steps of 12 months are included and released globally at the reference surface. The effective and transit-time-dependent lifetimes are identical for these radioactive tracers. The second simulation is a copy of TpSim, but with all substances being initialized at Earth's surface (called SurfSim) in the three specified regions. All age spectra from pulse tracers are extended to 50 years of transit time using the method described in Ploeger and Birner (2016).

3.2 Observational data

This study uses in situ measurement data obtained during two research campaigns of the High Altitude and Long Range Research Aircraft (HALO; http://www.halo.dlr.de, last access: 16 July 2020). The first campaign, PGS (Oelhaf et al., 2019), took place during December 2015 and March 2016, with the mission base in Kiruna, Sweden. PGS was a combination of the three missions POLSTRACC (Polar Stratosphere in a Changing Climate; https://www.halo.dlr.de/science/missions/polstracc/polstracc.html, last access: 16 July 2020), GW-LCYCLE (Gravity Wave Life Cycle), and SALSA (Seasonality of Air mass transport and origin in the Lowermost Stratosphere). PGS was split into two phases: the first from mid-December 2015 till late January 2016 and the second from late February 2016 till March 2016. The focus of PGS was strongly on the NH upper troposphere and lower stratosphere, as well as the exchange processes around the polar vortex and arctic latitudes. The second campaign, WISE (Wave-driven Isentropic Exchange; http://www.wise2017.de, last access: 16 July 2020), took place between September and October 2017, with the mission base in Shannon, Ireland. The focus of WISE was on isentropic exchange processes between the troposphere and stratosphere around the midlatitude tropopause. The flight tracks for both campaigns are shown in Keber et al. (2020). The campaign data are binned into grids of equivalent latitudes (Allen and Nakamura, 2003) and potential temperature differences to the WMO tropopause, with a bin size of $5° \times 5$ K and treated as phase averages. Bins containing fewer than five data points are omitted. The standard deviation for all mixing ratios is derived during the binning procedure. All halogenated trace gases mentioned in Sect. 2.2.4 were measured by the Gas Chromatograph for Observational Studies using Tracers – Mass Spectrometer (GhOST-MS) operated aboard HALO. GhOST-MS is a dual-channel gas chromatograph coupled with an electron capture detector (ECD) in an isothermal channel and a quadrupole mass spectrometer (MS) in a temperature programmed channel. The setup and relevant precision values are given in Keber et al. (2020). All GhOST-MS data in this study are reported on SIO-05 scales. N_2O was measured during PGS by the TRIHOP instrument (Schiller et al., 2008), an infrared absorption laser spectrometer with three quantum cascade lasers. The setup

for PGS and respective precision values are described in Krause et al. (2018). During WISE, N_2O was measured with the UMAQS instrument (Müller et al., 2015), also an infrared quantum cascade laser spectrometer. The setup for WISE and relevant precisions are given in Kunkel et al. (2019). These N_2O data are reported on the WMO 2006a scale.

An important parameter for the inversion is the entry mixing ratio time series at the specified tropopause sections. We only derive entry mixing ratios for the NH and tropical tropopause, as we show in Sect. 4.1 that the influence of cross-hemispheric transport is negligible. The time series should cover the period from 1960 until November 2017 to retrieve a mathematically precise age spectrum with a range of 50 years of transit time. Unfortunately, there are no consistent measurements available covering the complete period at the surface let alone at the tropopause. That is problematic for the long-lived trace gases in this study (SF_6, N_2O, CFC-12, halon 1211, halon 1301, and CH_3Br), since a strong long-term trend is detected at the surface. To construct a time series for these species, data from the Atmospheric Lifetime Experiment (ALE), the Global Atmospheric Gases Experiment (GAGE), and the Advanced Global Atmospheric Gases Experiment (AGAGE) (Prinn et al., 2018, 2019a) are taken and extended backwards until 1960 with global data from the Representative Concentration Pathways (Meinshausen et al., 2011a) for the two stations Ragged Point in Barbados (RPB – 13° N, 59° W) and Cape Matatula in American Samoa (SMO – 14° S, 171° W). The RCP data are aligned for any substance to suit the general behavior of the corresponding full ALE/GAGE/AGAGE data set but only considered where no measurements are available. All relevant data are reported on SIO-05 scales, except N_2O, which is reported on both SIO-98 (ALE/GAGE) and SIO-16 (AGAGE). Despite the different scale names, N_2O data on SIO-98 and SIO-16 scales are comparable. Both scales are considered to be comparable to WMO 2006A for the purpose of this study (World Meteorological Organization, 2018). Minor temporal gaps are interpolated. It is assumed that the long-lived gases are well-mixed, so that the average of RPB and SMO represents a tropical mixing ratio. As the global tropospheric lifetimes of these trace gases are sufficiently large, except for CH_3Br (1.6 years according to Table 5.6 in SPARC, 2013), the extended ALE/GAGE/AGAGE data are lagged to the tropical tropopause by 2 months ± 0.5 months. The validity of that approach is shown in Andrews et al. (1999) with CO_2 data. In the case of CH_3Br, some chemical loss processes might already occur while propagating towards the tropopause, but since the time lag is still much smaller than the global tropospheric lifetime, the lagged mixing ratio is assumed to be representative.

For the NH tropopause section, the net flux across the section is downward (Olsen et al., 2004), so that tropospheric air mixes with descending stratospheric air, characterized by lower mixing ratios due to the chemical loss regions in the stratosphere. At the extratropical tropopause the mixing ratio should thus be lower than in the tropics. Additionally, the trace gas burden at the extratropical tropopause consists of a mixture of air from the tropics and extratropics, aggravating a straightforward lag approach. The tropical origin fraction from the CLaMS simulation SurfSim provides a suitable tool to characterize the most important surface source section. The annual mean origin fraction indicates that at the NH tropopause section, approximately $88 \pm 4\,\%$ of all air masses originate from the surface in the tropics, with a corresponding mean AoA of 1 year ± 0.25 years. All tropical ALE/GAGE/AGAGE data are lagged by this value to retrieve the mixing ratio time series at the NH extratropical tropopause. Since the main sink of CH_3Br in the troposphere is the temperature-dependent reaction with the hydroxyl radical, chemical loss processes in the cold middle and upper troposphere are again treated as first-order negligible compared to the transport timescale. The standard deviation for these time series is derived from the respective measurement error and the deviation that emerges when the uncertainty of the lag time is implemented, especially relevant for RCP data as these do not provide a measurement error. The short-lived species (CH_2Br_2, $CHBr_3$, $CHCl_2Br$, $CHClBr_2$, and CH_2ClBr) show weak long-term trends at the tropopause. For the tropics, the mixing ratios of the upper TTL in Tables 1–4 of Engel and Rigby (2019) are considered to be the annual mean entry mixing ratio, as the potential temperature range matches the WMO tropopause of ERA-Interim in the specified tropical region. The mixing ratios at the NH tropopause section are taken directly from the PGS and WISE data, which are averaged between 30 and 90° N of equivalent latitude and between the tropopause and 30 K above, as this is specified as a region of strong tropospheric influence (Hoor et al., 2004). The large interval of 30 K has been introduced to incorporate the strong seasonal variability of the WMO tropopause in the NH throughout the year into the mixing ratios and to regard general discrepancies between the dynamical (PV-based) and WMO tropopause. To be consistent, the first 30 K above the tropopause is then omitted in the inversion procedure. The uncertainty values for all short-lived substances at the NH tropopause section are derived as the standard deviation from the average. In the tropics, the standard deviation given by Engel and Rigby (2019) is applied.

4 Results

4.1 Origin fractions for different entry regions

Origin fractions are a valuable tool to quantify the importance of air entrainment through each specified tropopause section and cross-hemispheric transport for air mass composition in the stratosphere. Figure 2 shows global cross sections of all annually and seasonally averaged origin fractions from TpSim as a function of potential temperature and latitude. The model setup is consistent overall, as the frac-

tions at each location sum up to circa 100 % in the stratosphere. On annual average, the general distribution of the origin fractions resembles the pattern of the BDC quite well with strong upwelling in the tropics and a downward motion at NH and SH extratropical latitudes. The sharp borders of all fractions at the tropopause around 30° N and S are caused by the definition of the source regions in the model. It is apparent that the tropical tropopause constitutes the predominant source region for the complete stratosphere above 450 K, with the tropical origin fraction (panel "Annual" in middle row) reaching more than 70 %. Below 450 K, the NH (panel "Annual" in top row) and SH (panel "Annual" in bottom row) tropopause sections gain significant influence in the extratropics, manifesting in a rise of the respective origin fractions when approaching the tropopause. Cross-hemispheric transport is negligible, since the northern fraction in the SH and the southern fraction in the NH are vanishingly low and only reach values up to 10 %. Therefore, the corresponding cross-hemispheric age spectra can be omitted as they contribute only marginally to the composite spectrum. Both the NH and SH origin fractions show a sharp latitudinal gradient directly at the Equator accompanied by a strong increase in the tropical fraction, visible as a beam of deep red shading around the Equator throughout the stratosphere. This might be an effect of the subtropical transport barriers that enclose the tropics, separate them from the extratropics, and inhibit exchange processes (Neu and Plumb, 1999).

All origin fractions undergo a pronounced seasonality (panels DJF to SON in all rows). For the NH fraction (top row), the maximum above the tropopause is visible in SON reaching up to almost 500 K in the tropics with extensive values between 50 % and 75 % in the lower stratosphere up to circa 380 K, while the minimum is found with a 6-month offset in MAM. JJA and DJF show a transition state between the maximum and minimum, which follows the seasonality of the mass fluxes in Sect. 2.2.2. As it takes some time for the air to propagate from the NH tropopause section upward into the stratosphere, the maximum NH origin fraction, i.e., a flushing of the NH with fresh tropospheric air, is modeled with some delay in SON. The same principle applies to the minimum of the NH fraction. Since the maximum downward forcing through the 380 K level is simulated in late January, the NH origin fraction attains its minimum in MAM. The isolated area of enhanced NH fraction at circa 380 K and 30° N in JJA could be related to the Asian summer monsoon, which is known to transport fresh air into the NH (sub)tropical stratosphere (Vogel et al., 2019) and matches well with the findings of Yang et al. (2016). For the SH origin fraction (bottom row), the correlation with the mass flux is not as clear as in the north. Intuitively, maxima and minima should be shifted by 6 months, with maximum SH fraction in MAM and minimum in SON. While the fraction in MAM appears strongest between 30 and ca. 55° S in the lower stratosphere with a pronounced vertical structure and values of 40 % to 75 %, a large area of strongly enhanced SH fraction (up to 75 %) is visible in SON at high latitudes. This is most likely linked to the initialization of the tracers at the WMO tropopause, which is found at high altitudes due to the very low temperatures inside the SH polar vortex. Apart from that, seasonal fluctuations seem weaker in general for the SH fraction. The tropical origin fraction in the lower stratosphere shows the weakest seasonality and spreads deep into the extratropics with values around 70 % to 80 % during minimal phases of the NH and SH fraction (especially MAM and JJA in the north and JJA and SON in the south, which is in accordance with the results of Hegglin and Shepherd, 2007). The maximum of the tropical fraction follows the tropical upward mass flux (Rosenlof, 1995) and shifts from the southern edge of the tropics in JJA to the northern edge in DJF, with the latter showing a slightly broader structure. The presented origin fractions reveal that the assumption of single entry through the TTL appears robust in the tropics and above 450 K globally. Age spectra, however, will lack important features of stratospheric transport in the extratropical lower stratosphere if only the tropical section is considered. To retrieve a precise composite age spectrum in both the model and inverse method, the tropical and the respective extratropical spectrum, north or south, must be determined and superimposed. Since the influence of cross-hemispheric transport is vanishingly low, the related cross-hemispheric age spectra are now omitted to simplify the setup.

4.2 Proof of concept

4.2.1 Age-of-air spectra

Hauck et al. (2019) provide an extensive proof of the inverse concept for the age of air for the tropical tropopause entry, so this study focuses on the NH and SH spectra in the midlatitudes of the respective hemisphere close to the local tropopause. All presented age spectra are normalized to avoid dependency on the CLaMS origin fractions. Figure 3 shows the normalized pulse (solid lines; see Sect. 3.1 for details) and inverse age spectra from the radioactive tracers (dashed lines; see Sect. 2.2.1 and 2.2.2 for details) with reference at the NH tropopause at 56° N and 370 K as annual (black) and seasonal (colored) means. To ease comparison, transit times below 1 month are excluded from all inverse spectra, as this is the minimum resolution the pulse tracer experiment provides. The annual mean inverse spectrum (panel a) matches well with the pulse spectrum and exhibits a very similar shape with one pronounced peak at similar transit times and no further modes. This indicates that the seasonal scaling works properly as it cancels out on annual average. The amplitude of the inverse spectrum is slightly larger than the pulse spectrum, although it appears as if the mode of the pulse spectrum is clipped off by the 1-month resolution, leading to a slightly right-tilted peak. A more frequent pulsing of the tracers could improve the alignment of the inverse method and pulse spectra. For the seasonal spectra (panels b

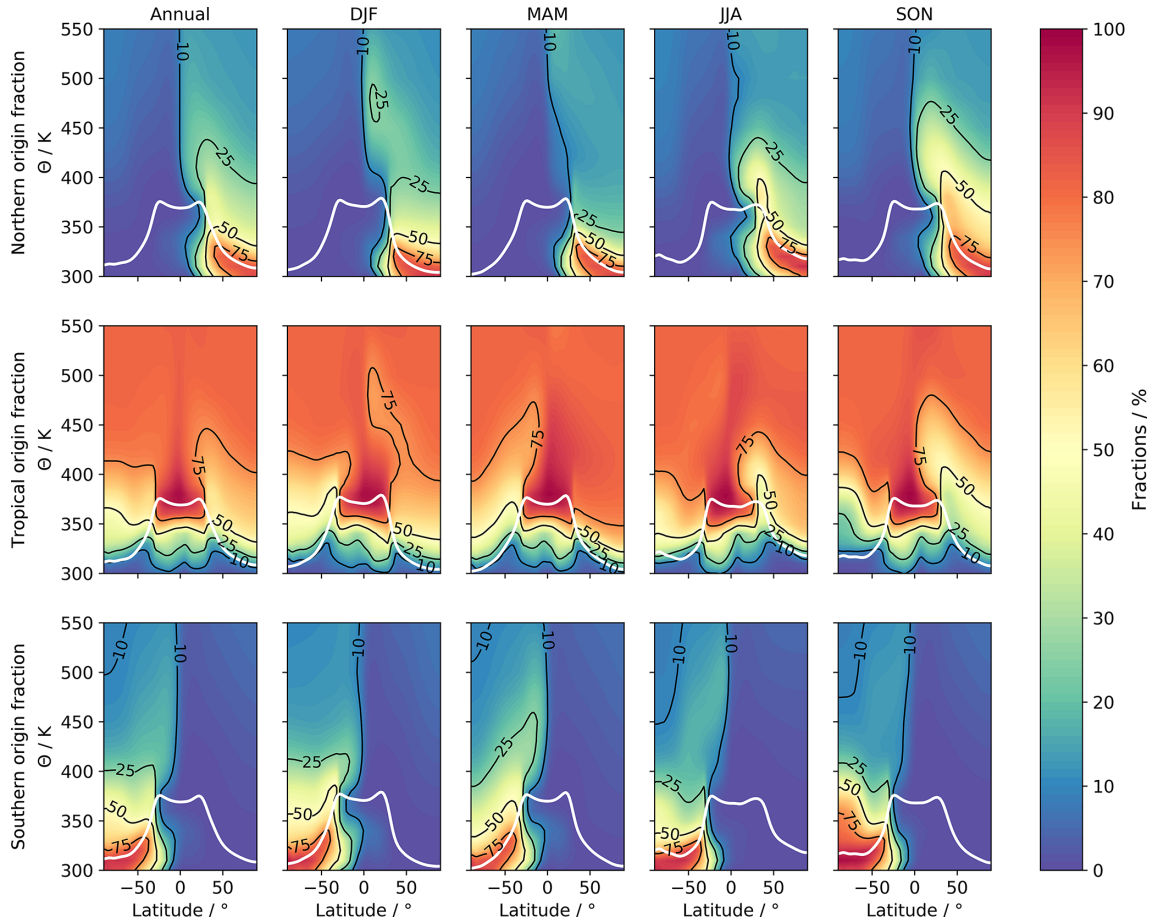

Figure 2. CLaMS origin fractions from TpSim as annual (left column) and seasonal (remaining four columns) mean global cross sections from the northern hemispheric (top row), the tropical (middle row), and the southern hemispheric (bottom row) tropopause source region (for definition see text). The solid white line indicates the WMO tropopause from ERA-Interim output. Negative latitudes always denote the Southern Hemisphere.

to e), the performance of the inverse method and its coupled seasonal scaling factor seems robust. Although the scaling factor is derived from the seasonal cycle in CLaMS and thus is expected to produce matching modes, the amplitude of the monomodal inverse spectra must be well-retrieved as otherwise the scaling would lead to deviating peaks and troughs. The amplitude of the first mode is well-reproduced in DJF and JJA, while MAM and SON are overestimated by approximately 50 %. Just as for the annual mean, the pulse spectra primary peak in MAM, JJA, and SON and in DJF appear to be slightly cutoff by the resolution of the tracer pulsing with a similarly right-tilted shape. Even though the shown NH seasonal inverse spectra are independent of the respective CLaMS origin fraction, they correctly reproduce a maximum of air entrainment in the JJA and SON spectra with almost twice as large maxima (5.18 and 5.77 a^{-1}) as in DJF and MAM (2.17 and 3.05 a^{-1}). This follows the maximum of the NH origin fraction in Fig. 2 (SON) very well and implies that the inverse spectra correctly reproduce the seasonality in cross-tropopause transport in the NH without explicit consideration of the fraction.

Figure 4 correspondingly displays the normalized CLaMS pulse (solid lines) and inverse (dashed lines) age spectra at 56° S and 370 K as annual (black) and seasonal (colored) averages with origin at the SH tropopause. The performance of the annual mean inverse spectrum (panel a) is similar to that of the NH spectrum with slightly better agreement of the main mode amplitude. The timing of the main peak coincides again with the pulse spectra. No further modes are visible in annual mean pulse and inverse spectra, indicating that the SH scaling factor seems to also work as intended on an annual scale. The right-tilted shape of the pulse spectrum peak indicates that some features of transport are clipped off in the spectra due to its transit time resolution. On the seasonal scale (panels b to e), the inverse method reproduces the general shape of the pulse spectra a bit better than in the NH, with well-matching primary modes. Only in SON is the pulse spectra amplitude underestimated by circa 25 %. This might

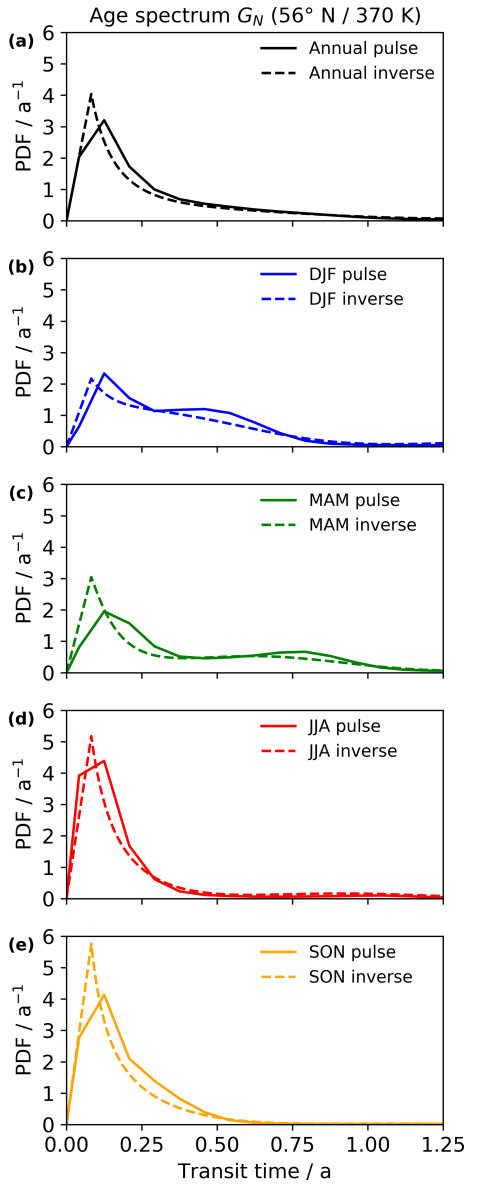

Figure 3. Normalized age spectra with reference at the northern hemispheric tropopause region G_N at 56° N and 370 K as annual **(a)** and seasonal **(b–e)** means. The solid line denotes age spectra from CLaMS pulse tracers, and the dashed line denotes inverse method age spectra.

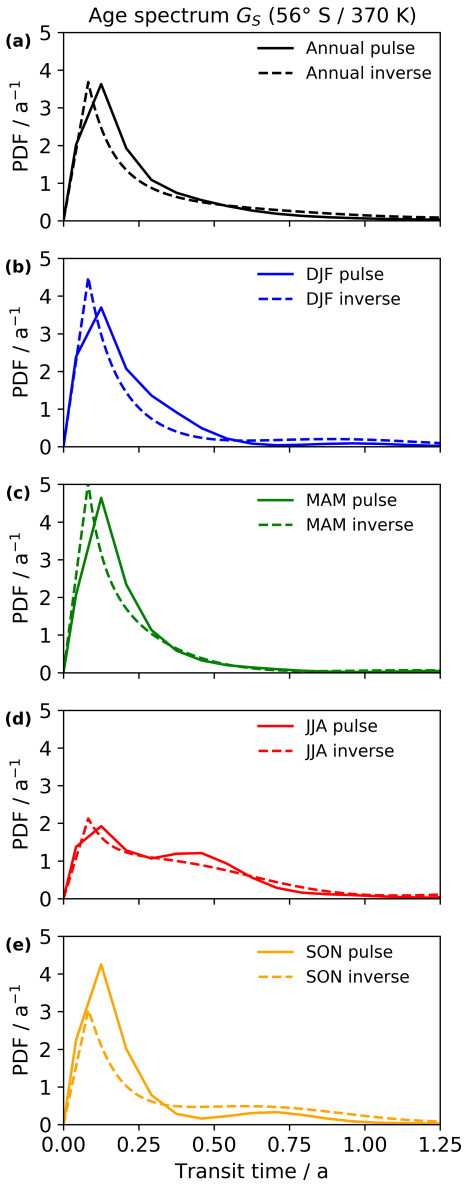

Figure 4. Normalized age spectra with reference at the southern hemispheric tropopause region G_S at 56° S and 370 K as annual **(a)** and seasonal **(b–e)** means. The solid line denotes age spectra from CLaMS pulse tracers, and the dashed line denotes inverse method age spectra.

be related to the WMO tropopause in this region. Consistently, all seasonal pulse spectra suffer from the same cutoff effect at small transit times as the NH spectra. Higher-order maxima and minima of the inverse spectra are in good agreement with the pulse spectra, which is expected as for the NH spectra above. During SH winter (JJA), a similar underestimation of the amplitude is visible as in NH winter (DJF) of Fig. 3. This might be related to the assumed inverse Gaussian shape. In terms of transport seasonality, the inverse age spectra follow the SH origin fraction again quite well without considering them explicitly. The maximum of transport is visible in the DJF and MAM spectra with amplitudes of 4.49 and 5.07 a^{-1}, while JJA and SON constitute phases of weaker transport (2.13 and 3.04 a^{-1}). Compared to the NH, the seasonality is in general not as strong and pronounced, similar to the seasonality of the SH fraction (Fig. 2).

Despite its restriction to an intrinsically inverse Gaussian shape, the extended inverse method with the newly introduced extratropical scaling factors appears to retrieve precise age spectra in the NH and SH midlatitude lower stratosphere

if chemical lifetime and mixing ratios are well-constrained. All derived inverse age spectra then capture important features of transport from the CLaMS model on a seasonal scale without direct influence of the modeled origin fractions.

4.2.2 Mean age of air

For a full global-scale assessment, Fig. 5 shows cross sections of mean age of air derived from the composite pulse (top row) and composite inverse age spectra (bottom row). The first column (annual) shows annual mean absolute values, while the remaining four columns (DJF to SON) depict seasonal percentage differences relative to the respective annual average. Although a tropopause-relative coordinate system is generally preferable for an analysis of mean AoA close to the tropopause to incorporate the variable tropopause height throughout the year, absolute coordinates are chosen for this comparison to ease comparability with Fig. 8 in Hauck et al. (2019). Changes in tropopause height should affect the data in both rows of the figure similarly so that a comparison between CLaMS pulse and inverse mean AoA is not inhibited. A seasonal analysis of the composite spectrum is advantageous to assess the behavior of all three different age spectra – northern, tropical, and southern – simultaneously, but weighted by their geographical importance. Since all origin fractions undergo a distinct seasonality, which is not necessarily identical with the seasonality of the age spectra, the composite spectrum of CLaMS pulse spectra and the inverse method is calculated for this specific comparison only with annual mean origin fractions in Eq. (8) (inserted into Eq. 6). This ensures that the presented seasonal differences are only steered by the inverted age spectra and preserves the weighting of the individual age spectra at the same time. On annual average, good agreement between inverse and pulse mean AoA is detected, where both show very similar spatial structures. The inverse method correctly reproduces the low mean AoA values of the pulse mean AoA in the tropics and the positive gradient towards the poles. Even the area of enhanced mean AoA at high SH latitudes between 400 and 500 K is emulated, although it extends down below 380 K. The inverse mean AoA is generally biased and exhibits larger mean AoA than the pulse spectra. This fact is in accordance with the results of Hauck et al. (2019), who also found an overestimation of mean AoA by the inverse method and link it to the prescribed inverse Gaussian shape of the age spectra. To quantify comparably in this study, the globally averaged bias both above and below a threshold of 1.5 years of mean AoA is retrieved (see Hauck et al., 2019, for details on the threshold). We find that the deviation decreases from +44.3 % below the threshold in Hauck et al. (2019) to only +13.8 % in this study. Above, the bias remains almost steady at +12.4 % compared to +13.3 % before. This improvement demonstrates the benefit of the extended approach, although some improvement might also be attributed to the finer pulse resolution, especially around the tropopause.

Seasonal differences give a similar impression with spatial patterns of inverse mean AoA that match those of the pulse mean AoA in the stratosphere qualitatively well. Only the amplitude of the differences appears enhanced for the inverse method, e.g., the darker shading of red at 50° S and 600 K in SON, but coincides with the detected bias on the annual scale. In the lower stratosphere, all positive and negative fluctuations are correctly retrieved by the inverse method. That is an improvement over Hauck et al. (2019), as they found inverted seasonal structures, i.e., positive seasonal differences in the pulse and negative differences in the inverse mean AoA, in the NH lower stratosphere during MAM and SON. Only in DJF directly above the tropopause in the NH midlatitudes and at the south pole does the sign appear different. That might be an artifact of the close proximity to the tropopause where an inverse Gaussian shape might not resemble the pulse spectrum correctly. Both pulse and inverse mean AoA exhibit a flushing of the subtropical and extratropical lower stratosphere with fresh tropospheric air during summer and fall of the respective hemisphere. That coincides well with the season of maximum amplitude of the NH and SH age spectra in Figs. 3 and 4 and shows their importance for a seasonally precise description of transport in the lower extratropical stratosphere. In the tropics, the maximum of tropospheric air is visible in MAM, but some strong entrainment is already visible around 30° N in DJF and around 30° S in JJA. This follows the seasonality of the tropical origin fraction in the tropics shown in Fig. 2 without explicit inclusion of the seasonal factors in the composite age spectrum.

The results of the idealized proof of concept demonstrate the significantly improved performance of the extended inverse ansatz for age spectra in the lower extratropical stratosphere, which has previously been identified as a critical region for the tropical age spectra by Hauck et al. (2019). The inverse method retrieves the NH and SH age spectra correctly and the newly inferred seasonal cycles impose modes at transit times that correspond to the CLaMS pulse age spectra very well both locally in the NH and SH midlatitudes and on the global scale as a composite with the tropical spectra. In its extended state, the inverse method can probably provide insight into transport mechanisms involving the tropical and extratropical tropopause. However, since this section provided only a highly idealized test scenario, the performance of the method and the statistical retrieval procedure for chemical lifetimes is assessed under more realistic conditions in the next sections.

4.3 Observational data

4.3.1 Mean age of air

The focus of the following sections is on the application of the inverse method to in situ measurements of 11 chemically active trace gases (SF_6, N_2O, CFC-12, halon 1211,

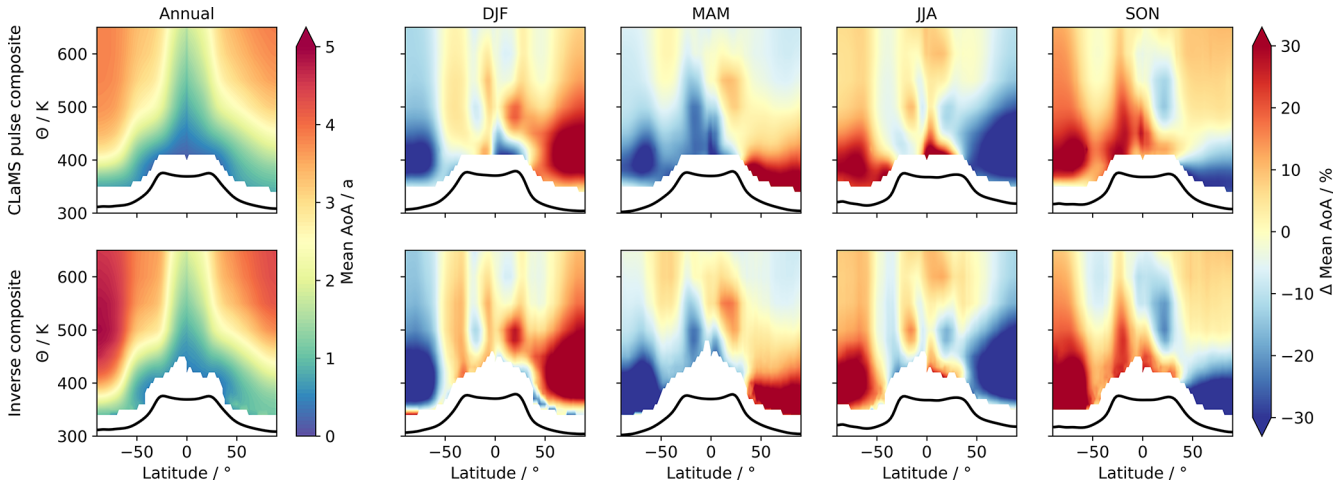

Figure 5. Global cross sections of mean age of air derived from the CLaMS pulse composite age spectra (top row) and from the inverse composite spectra (bottom row). The first column shows absolute values as the annual mean, and the right four columns show seasonal percentage differences relative to the annual mean. In all panels, the black line indicates the tropopause. The composite age spectra are calculated for this specific comparison using only annual mean origin fractions of the CLaMS model to focus explicitly on seasonality in mean AoA. Note that in the bottom row the larger areas of undefined values at the tropical tropopause are caused by the inversion algorithm not finding a valid solution for the transport parameter in that region. The first 30 K above the tropopause is omitted in all panels.

halon 1301, CH_3Br, CH_2Br_2, $CHBr_3$, $CHCl_2Br$, $CHClBr_2$, and CH_2ClBr) taken during the two aircraft campaigns PGS (phase 1 in winter 2015/2016, phase 2 in early spring 2016) and WISE (fall 2017). Results are evaluated under consideration of findings in previous studies. Note that the following sections use solely equivalent latitude as horizontal and potential temperature difference to the local tropopause as the vertical coordinate. All presented age spectra are independent of any modeled origin fractions. Figure 6 depicts cross sections of mean AoA from the normalized inverse age spectra referring to the NH entry (top row) and tropical tropopause entry (middle row) during PGS phase 1 (first column), PGS phase 2 (second column), and WISE (third column). The absolute difference between NH and tropical mean AoA is shown in the bottom row of the figure. The spatial distribution and quantitative range of inverse mean AoA in both rows appear meaningful and coherent in general, showing smaller values towards the tropics and an increase with latitude and altitude. For PGS phase 1 and PGS phase 2, the spatial distribution seems consistent with the data in Fig. 3 of Krause et al. (2018), although their observational-based mean AoA values refer to Earth's surface in the tropics and therefore regard transport across both tropical and NH tropopause regions. The quantitative range of mean AoA in Krause et al. (2018) should be larger than in this study, as tropospheric transport up to the tropopause sections is included in their mean AoA.

Mean AoA referring to the NH tropopause (top row) is found to show the largest values of all data during PGS phase 2 with scattered bins of mean AoA older than 3 years around 90 K and 75° N. While both PGS phase 1 and PGS phase 2 cover a wide latitudinal range from 35 up to 85° N, WISE is strongly confined and centered around 50° N with vertical extent similar to PGS 1. For WISE, mean AoA is slightly smaller than during PGS in the same spatial region. Minimum inverse mean AoA values of all three campaigns are retrieved for PGS phase 1 between 40 and 45° N below 50 K and even below 40 K at circa 70° N with bins of less than 0.1 years. This implies a strong entrainment of fresh tropospheric air into the lowermost stratosphere across the NH tropopause during summer and fall. On the one hand, this manifests in already diminished mean AoA during WISE, i.e., early fall 2017, and, on the other hand, in minimum mean AoA values for PGS phase 1, i.e., winter 2015/2016, where air that entered prior to the campaign already had some time to propagate upward from the tropopause. That seasonality in local entrainment across the tropopause is consistent with the results of the SPURT aircraft campaign in Fig. 6 of Bönisch et al. (2009), showing a maximum of air with tropospheric origin in the lowermost stratosphere in October ($> 80\,\%$) and a minimum in April ($< 20\,\%$) due to strong local quasi-isentropic mixing processes across the subtropical jet stream in summer and fall.

Mean AoA referring to the NH tropopause is generally smaller than the tropical counterpart, with an average difference ranging from -0.3 years for WISE to -0.36 years for PGS phase 2 and -0.46 years for phase 1. The difference is smaller at lower latitudes and increases with latitude and distance from the tropopause (see bottom row). Maximum mean AoA of tropical origin (middle row) is retrieved for PGS phase 2 with values of more than 4 years but with a larger vertical extent down to 55 K at 75° N. Similar to

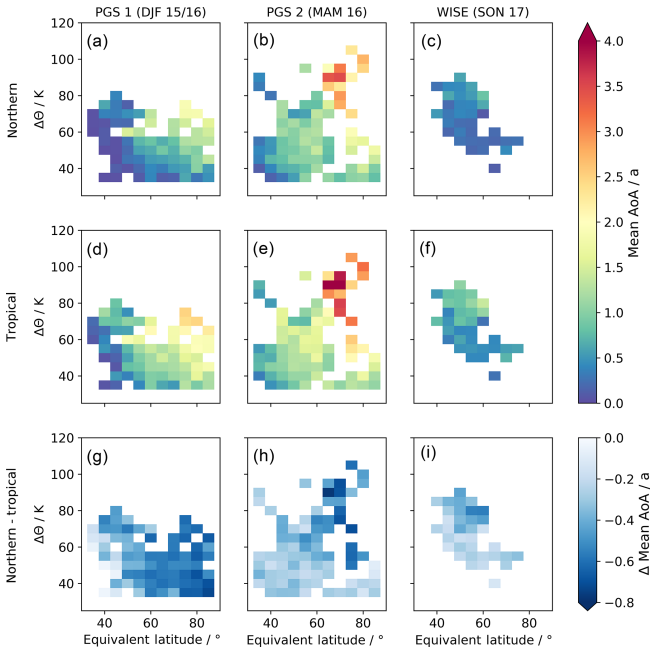

Figure 6. Cross sections of binned mean age of air calculated using the age spectra retrieved with the inverse method in the Monte Carlo simulation (see Sect. 2.2.4). The top row shows mean AoA referring to the northern hemispheric tropopause section, while mean AoA in the middle row refers to the tropical tropopause section. The left column displays data of PGS phase 1, middle column data of PGS phase 2, and right column data of WISE. The bottom row gives the absolute differences between the data in the top and middle rows. The potential temperature difference to the local tropopause $\Delta\Theta$ is used as the vertical coordinate and equivalent latitude as the horizontal coordinate.

above, minimum mean AoA in the midlatitudes between 50 and 70° N is found during WISE, but only slightly smaller than during PGS. The absolute minimum of mean AoA during all campaigns is retrieved again in PGS 1 ($\sim$ 0.1 years at 40° N and 50 K), although the spatial distribution of the minimum is much more confined to low latitudes than for mean AoA with the NH tropopause as reference. The generally lower mean AoA values derived during WISE with origin at the tropical tropopause are expected, as NH winter is characterized as the season where the tropical upward mass flux attains its maximum (Rosenlof, 1995). Therefore, entry of fresh tropospheric air through the tropical tropopause peaks during NH winter and manifests in lower mean AoA with some delay during JJA and SON in the NH extratropical lowermost stratosphere.

Although these findings coincide robustly with results of previous studies, the strong similarity between the spatial distribution of mean AoA with NH and tropical tropopause as reference is quite nonintuitive. Since transport processes to a specified location starting at the NH extratropical tropopause should be different from those beginning at the tropical tropopause, one could expect that mean AoA fields are more individually shaped. To check that this is not caused by the inversion concept in general, the raw model output of CLaMS TpSim (see Sect. 3.1) has been interpolated onto the HALO flight tracks for PGS and WISE. CLaMS pulse mean AoA fields are shown together with the corresponding inverse mean AoA in Figs. S1 and S2 in the Supplement to this study. Results reveal that CLaMS models a similarity between mean AoA with origin at the NH and tropical tropopause analogous to the inverse method based on observational data.

4.3.2 Campaign-averaged age-of-air spectra and mean age of air

Figure 7 presents the campaign-averaged age spectra derived by the inverse method with reference at the NH tropopause (panel a) and tropical tropopause (panel b) for PGS phase 1 (DJF, blue), PGS phase 2 (MAM, green), and WISE (SON, orange). To ensure comparability, the campaign average is constructed by selecting only bins that are present in both PGS phases and WISE. Shaded areas denote the derived uncertainty range from the Monte Carlo simulation (see Sect. 2.2.4 for details). For the inverse spectra with reference at the NH tropopause, the maximum amplitude is detected during WISE (8.81 a^{-1}), followed by PGS phase 1 (4.65 a^{-1}) and PGS phase 2 (1.09 a^{-1}). The transit times at the spectra maxima (i.e, modal age) come out equally for WISE and PGS phase 1, both around 0.5 months. This implies that a flushing event with extratropical tropospheric air due to mixing across the NH tropopause section is retrieved for early fall 2017 prior to WISE and early winter 2015/2016 prior to PGS phase 1. That is corroborated by the inverse spectrum for PGS phase 2, which displays its first mode at a modal age of circa 2 months, equivalent to midwinter 2015/2016. While the age spectrum for WISE rapidly decreases after its primary mode and reaches its first minimum at circa 0.8 years of transit time, the inverse age spectra during PGS phases 1 and 2 exhibit a saddle point up to transit times of 0.5 and 0.75 years, respectively. However, those secondary peaks are parametrized by the seasonal scaling factor and can therefore not be considered as a real signal of transport. Mean AoA values for the spectra in panel (a) of Fig. 7 are shown in panel (a) of Fig. 8 and quantitatively emphasize the seasonality in transport visible on a larger scale in Fig. 6. For WISE, mean AoA is retrieved to be considerably lower (0.25 years) than for PGS phase 1 (0.7 years) and phase 2 (1.10 years), which is in accordance with the seasonality found by Bönisch et al. (2009) for the SPURT campaign.

All primary modes of the age spectra with origin at the tropical tropopause show smaller amplitudes and generally broader peaks compared to the northern counterparts but with an identical order of the campaigns. The maximum is found for WISE (6.04 a^{-1}), followed by PGS phase 1 (2.81 a^{-1}) and PGS phase 2 (1.07 a^{-1}). Modal ages are similar for WISE and PGS phase 1, both with circa 1 month. For PGS

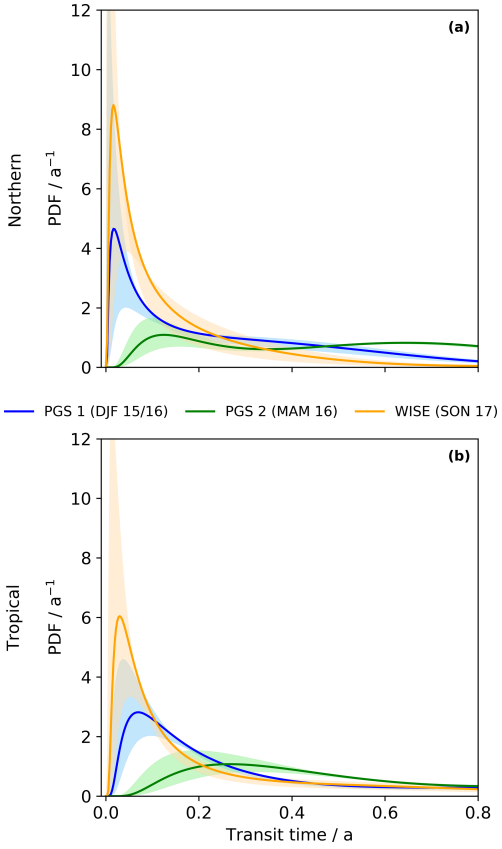

Figure 7. Campaign-averaged age spectra for PGS phase 1 (blue), PGS phase 2 (green), and WISE (orange). Panel **(a)** shows normalized inverse age spectra G_N referring to the northern hemispheric tropopause section, while **(b)** shows normalized inverse age spectra G_T referring to the tropical tropopause section. Colored shadings give the uncertainty range of the spectra derived from the Monte Carlo simulation (see Sect. 2.2.4 for details).

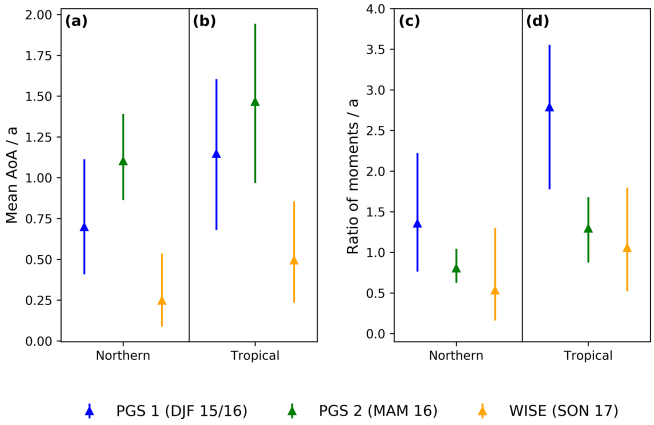

Figure 8. Campaign-averaged mean AoA **(a, b)** and ratio of moments **(c, d)** derived from inverse age spectra for PGS phase 1 (blue), phase 2 (green), and WISE (orange). Data in **(a)** and **(c)** refer to the northern hemispheric tropopause section, while data in **(b)** and **(d)** use the tropical tropopause as reference. Error bars denote the mean uncertainties from the Monte Carlo simulation (see Sect. 2.2.4).

phase 2 an increase is visible, reaching a modal age of 3 months. These age spectra imply that entry of fresh tropospheric air through the tropical tropopause has peaked in early fall 2017 and also early winter 2015/2016 but is less strong than for the NH inverse spectra. This is a rather unexpected feature, since according to the seasonality in the tropical upward mass flux in NH winter, the maximum of the age spectra with reference at the tropical tropopause should be located at transit times that correspond to winter (e.g., 0.75 years for a spectrum in SON). Possible causes might be the shallow branch of the BDC in proximity to the tropopause or the subtropical jet stream drifting around the border of the specified tropical and NH extratropical tropopause section that both could interfere with the seasonality of transport across the tropical tropopause. Corresponding campaign-averaged mean AoA values in panel (b) of Fig. 8 match the general tendency of mean AoA in the bottom row of Fig. 6. The lowest values are retrieved for WISE (0.50 years), while mean AoA of PGS phase 1 and phase 2 shows larger values (1.15 and 1.47 years, respectively). To again check that these features are not caused by the inversion procedure, campaign-averaged pulse age spectra interpolated from CLaMS TpSim are shown together with the retrieved inverse age spectra in Fig. S3. This shows that CLaMS models similar age spectra for PGS and WISE as retrieved by the inverse method without direct influence of model output on the inversion.

4.3.3 Campaign-averaged ratio of moments

Multiple studies in the past focused on the derivation of age-of-air spectra and mean AoA from observations in the lower stratosphere and not only constrain the shape of the age spectrum by the inverse Gaussian function of Eq. (3) but also regard a constant ratio of variance to mean AoA. This quantity is called ratio of moments μ. For instance, Volk et al. (1997) consider a ratio of moments of 1.25 ± 0.5 years between 60° N and 70° S up to 20 km altitude, while Engel et al. (2017) and previous assessments use 0.7 years for the NH midlatitudes up to 30 km. Those values are based on model results by Hall and Plumb (1994) and might be an underestimation, since Hauck et al. (2019) demonstrate in their model simulation that the tail of the spectrum amplifies the ratio of moments considerably. They propose a ratio of moments of 2 years in the midlatitude lower stratosphere on annual average, but they state that a seasonality in μ is present. Recently, the significant influence of the ratio of moments on the derivation of mean AoA from SF_6 measurements is further evaluated by Fritsch et al. (2019).

This study provides a suitable frame to reassess the assumptions for the ratio of moments. Therefore, the campaign-averaged ratios of moments for the inverse age

spectra in Fig. 7 are displayed in Fig. 8c, d. It is evident that the ratio undergoes a seasonality for the inverse spectra referring to the NH tropopause section (panel c), and the maximum and minimum are retrieved as 1.36 years in PGS phase 1 and as 0.53 years during WISE. The seasonality therefore differs slightly from that found for mean AoA. The shown quantitative range of the retrieved ratio of moments matches the applied values of Volk et al. (1997) and Engel et al. (2002) reasonably well, although a solely constant value might not fully capture seasonal variations in the age spectra. In the case of the inverse age spectra with reference to the tropical tropopause (panel d), values for the ratio of moments are found to range from a 1.06-year minimum in WISE up to a 2.79-year maximum in PGS phase 1. The seasonality pattern is again different from the corresponding mean AoA seasonality but similar to the ratio of moments derived from the age spectra with NH tropopause origin. PGS phase 1 for the tropical tropopause age spectra is the only data set where the ratio of moments cannot be found in the range of values used by Volk et al. (1997) and Engel et al. (2002).

In order to constrain matching seasonal age spectra when using the ratio of moments, a value of 0.7 years or 1.25 ± 0.5 years might not be matching universally, since results for PGS and WISE reveal that μ presents a pronounced seasonality. The inverse method could be considered as a promising alternative as the presented results show a robust performance for NH and tropical age spectra and mean AoA on a seasonal and wider geographical scale without prior constraints to the moments of the spectra, especially as the presented results demonstrated the good performance of the method compared to previous studies on transport in the NH lowermost stratosphere. However, the statistical uncertainties remain considerably high. The following section therefore provides a summary of the results as well as a critical discussion of the method's capabilities and its limitations.

5 Summary and discussion

This study presents an extension and application of the inverse method by Hauck et al. (2019) to derive age spectra from trace gas mixing ratios in the lowermost stratosphere by considering entry of tropospheric air across a northern (90–30° N), a tropical (30° N–30° S), and a southern (30–90° S) tropopause section, each with a distinct age spectrum. In the first part of this study, the concept of the extended method is tested in an idealized CLaMS model simulation framework. In the second part, the extended inverse method is applied to observational data of short- and long-lived halogenated trace gases measured in the NH lower stratosphere during the research campaigns PGS and WISE of the HALO research aircraft.

The newly established origin fractions turn out to be a valuable tool to assess and quantify the importance of different regions for cross-tropopause transport on a seasonal scale. Model results indicate solidly that above 450 K the stratosphere is prevalently steered by entrainment across the tropical tropopause throughout the year. Below, transport across the NH and SH tropopause gains influence, but only for the related hemisphere as cross-hemispheric transport processes appear negligible in all seasons in the model. The maximum of entrainment across the NH tropopause section is found in general around JJA and SON. That coincides with the results of Bönisch et al. (2009), who find an enhancement of quasi-isentropic mixing across the weak NH subtropical jet stream during NH summer and fall. The maximum of intrusion in the SH midlatitudes can be detected accordingly with a shift of 6 months and reduced strength compared to the north around DJF and MAM. However, these seasonality patterns are contrary to the findings of multiple studies of seasonality using the hemispherically integrated upward mass fluxes across the tropopause that indicate a maximum in late fall (Olsen et al., 2004; Schoeberl, 2004; Škerlak et al., 2014). Our results might be an indication that the NH and SH origin fractions and age spectra in CLaMS are steered primarily by the intrusion processes across the jet stream around the subtropical border of the defined source regions. It is likely that if the boundary region is confined to higher latitudes, the seasonality of the related quantities will change as well.

The performance of the inverse method in the idealized proof of concept seems consistent, and retrieval of respective age spectra in the NH and SH midlatitudes at 370 K works soundly. On the global scale, the general agreement of inverse and pulse mean AoA proves to be robust, matching both spatially and quantitatively on annual average. The seasonal cycle of mean AoA, especially during MAM and SON in the NH lowermost stratosphere, is now correctly reproduced compared to the seasonality found in Hauck et al. (2019). The improved performance of the inversion indicates the importance of transport across the extratropical tropopause for correctly retrieved seasonal age spectra in the vicinity of the tropopause. Admittedly, some improvements are certainly attributed to the fine transit time resolution (1 month) of the pulse spectra in CLaMS. If the resolution is increased in future simulations, the agreement of spectra and mean AoA will probably further advance as well, due to fully captured first modes in the age spectra. For PGS and WISE data, the inverse method retrieves age spectra and mean AoA with meaningful quantitative range and spatial and seasonal features for both the tropical and NH tropopause regions. Retrieved mean AoA referring to the NH tropopause is lower during WISE than during PGS phase 1 and phase 2. Campaign-averaged inverse age spectra consistently display a strong entrainment of tropospheric air across the NH tropopause section in fall 2017 and with reduced strength in early winter 2015/2016. Mean AoA with origin at the tropical tropopause also shows the lowest values for WISE and again an increase between PGS phase 1 and phase 2. Campaign-averaged inverse spectra indicate a strong

unexpected intrusion across the tropical tropopause prior to WISE and PGS phase 1 that might be related to entrainment around the subtropical jet stream. For a thorough assessment, the ratio of moments is presented for all campaigns as it is an important quantity for the derivation of mean AoA from SF_6 and CO_2 in the past (Volk et al., 1997; Engel et al., 2002). Previous studies assume a constant ratio of moments, usually between 0.7 and 1.75 years, for many spatial regions in the stratosphere. Campaign-averaged results of the inverse spectra in this study indicate that the ratio of moments shows a significant seasonality, which could be incorporated in future studies for a precise mean AoA retrieval when applying the ratio of moments to constrain the age spectrum.

Although the presented results show a robust performance of the inverse method for the application to observational data, where seasonal and structural key features of transport are well-emulated and congruent with findings of earlier studies, there are multiple critical aspects that must be recognized. Although inverted age spectra and related moments retrieved from PGS and WISE data are compared to some findings in previous studies, a thorough comparison is difficult as past studies use different reference surfaces than in this study. As comparable observationally derived mean AoA values and age spectra could become available in the future, a proper comparison with the inverse method is an important task for future studies. Moreover, inverse age spectra are restricted to the seasonal scale, and an extension to finer scales (monthly) might be useful to incorporate rapid transport processes but remains difficult due to increasing variability. As indicated, the overall uncertainty of the inverse spectra and their moments is very large, and multiple factors contribute to that highly uncertain nature. The most critical aspect is the derived effective lifetimes for the species considered in this study. Holzer and Waugh (2015) indicate that their concept is applicable to derive transit time spectra in the troposphere, but errors grow significantly for stratospheric application due to the strong chemical loss process and spatial variability of most of the trace gases. We quantify these uncertainties partly by the Monte Carlo simulation to examine a variety of initial sets of trace gases together with strong statistical errors, but it is not feasible to include all possible states in the inverse method. That implies that the provided error range should be treated as a minimum. Effective lifetimes must be considered to be a highly theoretical concept and cannot be interpreted without their associated age spectrum and mixing ratio of the trace gas. A comparison to known global or local stratospheric lifetimes is not useful since effective lifetimes describe chemistry along a pathway determined by the underlying age spectrum. For completeness, resulting effective lifetimes are shown without further discussion in Fig. S4 for the campaign-averaged inverse age spectra (Sect. 4.3.2). Future studies could reassess our results by using modeled chemical lifetimes that depend explicitly on transit time from a pulsing experiment similar to Plumb et al. (1999), but resulting age spectra will then depend strongly on the chosen model setup.

This study tries to achieve a reduction of model influence by separate consideration of tropical and NH age spectra, although some information from global atmospheric models is inevitably necessary. For a fully retrieved composite age spectrum, the origin fractions must be provided by a model. The entry mixing ratio time series for all long-lived species are primarily constructed from ALE/GAGE/AGAGE measurements and extension back to 1960 using aligned mixing ratios from the RCP data set, which might not certainly constitute a precise description. Also, the time lag from the surface to the tropopause, which is assumed to be constant, might cause inaccuracies, especially in case of the NH tropopause, since the time lag is directly taken from a CLaMS simulation. All these uncertainties are considered within the applied error of entry mixing ratios of the Monte Carlo simulation, but it is not guaranteed that they are captured to their full extent. Improvements in measurement networks and technologies in the future could provide more accurate data for the tropopause sections and lead to improved age spectra. The same applies to the measured mixing ratios during PGS and WISE. These are always processed together with their standard deviation, but variability and data quality in general are crucial factors that influence the inverted age spectra significantly and contribute to the large uncertainty range of the results. Improvements to measurement data in the future, even for single species, could lead to an enhanced performance. Finally, the inverted age spectra must be evaluated carefully if assessing seasonality in transport. Since all higher-order maxima and minima in the inverse age spectra are imposed by a scaling factor that repeats for every year of transit time, possible stronger or weaker phases of real atmospheric transport are not included in the modes. Additionally, the scaling factors are derived from integrated CLaMS output and thus particularly created for the specific tropopause sections in this study. Although the seasonality matches results in previous work quite well and indicates that the subtropical jet stream is likely a dominant source region, it is likely that the retrieved scaling factors must be changed if the boundaries of the sections are shifted. Future studies could reassess these results using model output from other model simulations or differently defined NH and SH tropopause sections. Nevertheless, our results demonstrate that with the improvements to the inverse method in this study, age spectra and mean AoA can be inferred from mixing ratio measurements of atmospheric trace gases and deliver plausible results for seasonal aspects of stratospheric transport in the NH lower stratosphere. Although results must always be seen in the light of their uncertainty range, additional information on top of mean AoA can be retrieved by inclusion of further chemically active trace gas species. This might contribute to a deepened understanding of seasonal variability for future studies.

Data availability. In situ data from HALO are available via the HALO database (http://halo-db.pa.op.dlr.de, German Aerospace Center, 2020). ALE/GAGE/AGAGE and RCP mixing ratio data are available online (http://agage2.eas.gatech.edu/data_archive/, Prinn et al., 2019b and http://www.pik-potsdam.de/~mmalte/rcps/index.htm, Meinshausen et al., 2011b). CLaMS model output can be made accessible on request to the authors.

Supplement. The supplement related to this article is available online at: https://doi.org/10.5194/acp-20-8763-2020-supplement.

Author contributions. MH wrote the manuscript, performed the data processing and evaluation, and prepared the figures for this paper. MH and AE developed the extended principle of the inverse method in close collaboration. FP and MH planned, conducted, and postprocessed the CLaMS simulations. AE, HB, PH, TK, and FP were an active part in the PGS campaign and in the evaluation of data. AE, MH, PH, TK, FP, and TJS were an active part in the WISE campaign and in the evaluation of data. All co-authors contributed to the research in this paper during many discussions.

Competing interests. The authors declare that they have no conflict of interest.

Acknowledgements. This work is funded by the German Research Foundation (DFG) priority program 1294 (HALO) under the project numbers EN367/14-1, HO4225/8-1, and HO4225/7-1. The authors gratefully acknowledge the computing time for the CLaMS simulations granted on the supercomputer JURECA at Jülich Supercomputing Centre (JSC) under the VSR project ID JICG11. The authors greatly acknowledge all people involved with the ALE/GAGE/AGAGE network for their persistent effort in measuring atmospheric gas constituents and for provision of their data, especially people in charge at the ALE/GAGE/AGAGE stations American Samoa (Jens Mühle, Chris Harth, Paul B. Krummel and Ray Wang) and Ragged Point (Simon O'Doherty, Dickon Young, Paul B. Krummel and Ray Wang). AGAGE is supported principally by NASA (USA) grants to MIT and SIO and also by BEIS (UK) and NOAA (USA) grants to Bristol University, CSIRO and BoM (Australia), FOEN grants to Empa (Switzerland), NILU (Norway), SNU (Korea), CMA (China), NIES (Japan), and Urbino University (Italy). Finally, the authors would like to thank all organizers and participants of the PGS and WISE campaign, which provided the frame to retrieve the necessary data for this study.

Financial support. This research has been supported by the Deutsche Forschungsgemeinschaft (grant nos. EN367/14-1, HO4225/8-1, and HO4225/7-1).

This open-access publication was funded by the Goethe University Frankfurt.

Review statement. This paper was edited by Martin Dameris and reviewed by Eric Ray and two anonymous referees.

References

Abalos, M., Legras, B., Ploeger, F., and Randel, W. J.: Evaluating the advective Brewer-Dobson circulation in three reanalyses for the period 1979–2012, J. Geophys. Res., 120, 7534–7554, https://doi.org/10.1002/2015JD023182, 2015.

Allen, D. R. and Nakamura, N.: Tracer Equivalent Latitude: A Diagnostic Tool for Isentropic Transport Studies, J. Atmos. Sci., 60, 287–304, https://doi.org/10.1175/1520-0469(2003)060<0287:TELADT>2.0.CO;2, 2003.

Andrews, A. E., Boering, K. A., Daube, B. C., Wofsy, S. C., Hintsa, E. J., Weinstock, E. M., and Bui, T. P.: Empirical age spectra for the lower tropical stratosphere from in situ observations of CO_2: Implications for stratospheric transport, J. Geophys. Res., 104, 26581–26595, https://doi.org/10.1029/1999JD900150, 1999.

Appenzeller, C., Holton, J. R., and Rosenlof, K. H.: Seasonal variation of mass transport across the tropopause, J. Geophys. Res., 101, 15071–15078, https://doi.org/10.1029/96JD00821, 1996.

Austin, J. and Li, F.: On the relationship between the strength of the Brewer-Dobson circulation and the age of stratospheric air, Geophys. Res. Lett., 33, L17807, https://doi.org/10.1029/2006GL026867, 2006.

Birner, T. and Bönisch, H.: Residual circulation trajectories and transit times into the extratropical lowermost stratosphere, Atmos. Chem. Phys., 11, 817–827, https://doi.org/10.5194/acp-11-817-2011, 2011.

Bönisch, H., Engel, A., Birner, Th., Hoor, P., Tarasick, D. W., and Ray, E. A.: On the structural changes in the Brewer-Dobson circulation after 2000, Atmos. Chem. Phys., 11, 3937–3948, https://doi.org/10.5194/acp-11-3937-2011, 2011.

Bönisch, H., Engel, A., Curtius, J., Birner, Th., and Hoor, P.: Quantifying transport into the lowermost stratosphere using simultaneous in-situ measurements of SF_6 and CO_2, Atmos. Chem. Phys., 9, 5905–5919, https://doi.org/10.5194/acp-9-5905-2009, 2009.

Boothe, A. C. and Homeyer, C. R.: Global large-scale stratosphere–troposphere exchange in modern reanalyses, Atmos. Chem. Phys., 17, 5537–5559, https://doi.org/10.5194/acp-17-5537-2017, 2017.

Butchart, N.: The Brewer-Dobson circulation, Rev. Geophys., 52, 157–184, https://doi.org/10.1002/2013RG000448, 2014.

Carpenter, L. J. and Reimann, S.: Chapter 1: Update on Ozone-Depleting Substances (ODSs) and Other Gases of Interest to the Montreal Protocol, in: Scientific Assessment of Ozone Depletion 2014, Global Ozone Research and Monitoring Project, Global Ozone Research and Monitoring Project – Report No. 55, 55, World Meteorological Organization, Geneva, Switzerland, 21–125, 2014.

Chabrillat, S., Vigouroux, C., Christophe, Y., Engel, A., Errera, Q., Minganti, D., Monge-Sanz, B. M., Segers, A., and Mahieu, E.: Comparison of mean age of air in five reanalyses using the BASCOE transport model, Atmos. Chem. Phys., 18, 14715–14735, https://doi.org/10.5194/acp-18-14715-2018, 2018.

Dee, D. P., Uppala, S. M., Simmons, A. J., Berrisford, P., Poli, P., Kobayashi, S., Andrae, U., Balmaseda, M. A., Balsamo, G., Bauer, P., Bechtold, P., Beljaars, A. C. M., van de Berg, L., Bid-

lot, J., Bormann, N., Delsol, C., Dragani, R., Fuentes, M., Geer, A. J., Haimberger, L., Healy, S. B., Hersbach, H., Hólm, E. V., Isaksen, L., Kållberg, P., Köhler, M., Matricardi, M., McNally, A. P., Monge-Sanz, B. M., Morcrette, J.-J., Park, B.-K., Peubey, C., de Rosnay, P., Tavolato, C., Thépaut, J.-N., and Vitart, F.: The ERA-Interim reanalysis: configuration and performance of the data assimilation system, Q. J. Roy. Meteor. Soc., 137, 553–597, https://doi.org/10.1002/qj.828, 2011.

Diallo, M., Legras, B., and Chédin, A.: Age of stratospheric air in the ERA-Interim, Atmos. Chem. Phys., 12, 12133–12154, https://doi.org/10.5194/acp-12-12133-2012, 2012.

Ehhalt, D. H., Rohrer, F., Blake, D. R., Kinnison, D. E., and Konopka, P.: On the use of nonmethane hydrocarbons for the determination of age spectra in the lower stratosphere, J. Geophys. Res., 112, 26581, https://doi.org/10.1029/2006JD007686, 2007.

Engel, A. and Rigby, M.: chap. 1: Update on Ozone-Depleting Substances (ODSs) and Other Gases of Interest to the Montreal Protocol, in: Scientific Assessment of Ozone Depletion 2018, Global Ozone Research and Monitoring Project, Global Ozone Research and Monitoring Project – Report No. 58, 58, World Meteorological Organization, Geneva, Switzerland, 2019.

Engel, A., Strunk, M., Müller, M., Haase, H.-P., Poss, C., Levin, I., and Schmidt, U.: Temporal development of total chlorine in the high-latitude stratosphere based on reference distributions of mean age derived from CO_2 and SF_6, J. Geophys. Res., 107, 4483, https://doi.org/10.1029/2001JD000584, 2002.

Engel, A., Möbius, T., Bönisch, H., Schmidt, U., Heinz, R., Levin, I., Atlas, E., Aoki, S., Nakazawa, T., Sugawara, S., Moore, F., Hurst, D., Elkins, J., Schauffler, S., Andrews, A., and Boering, K.: Age of stratospheric air unchanged within uncertainties over the past 30 years, Nat. Geosci., 2, 28–31, https://doi.org/10.1038/NGEO388, 2009.

Engel, A., Bönisch, H., Ullrich, M., Sitals, R., Membrive, O., Danis, F., and Crevoisier, C.: Mean age of stratospheric air derived from AirCore observations, Atmos. Chem. Phys., 17, 6825–6838, https://doi.org/10.5194/acp-17-6825-2017, 2017.

Fritsch, F., Garny, H., Engel, A., Bönisch, H., and Eichinger, R.: Sensitivity of Age of Air Trends on the derivation method for non-linear increasing tracers, Atmos. Chem. Phys. Discuss., https://doi.org/10.5194/acp-2019-974, in review, 2019.

Fueglistaler, S., Dessler, A. E., Dunkerton, T. J., Folkins, I., Fu, Q., and Mote, P. W.: Tropical tropopause layer, Rev. Geophys., 47, RG1004, https://doi.org/10.1029/2008RG000267, 2009.

Garcia, R. R. and Randel, W. J.: Acceleration of the Brewer–Dobson Circulation due to Increases in Greenhouse Gases, J. Atmos. Sci., 65, 2731–2739, https://doi.org/10.1175/2008JAS2712.1, 2008.

Garny, H., Birner, T., Bönisch, H., and Bunzel, F.: The effects of mixing on age of air, J. Geophys. Res., 119, 7015–7034, https://doi.org/10.1002/2013JD021417, 2014.

German Aerospace Center (DLR): The High Altitude and LOng Range database (HALO-DB), DLR, available at: http://halo-db.pa.op.dlr.de, last access: 22 July 2020.

Haine, T. W. N., Zhang, H., Waugh, D. W., and Holzer, M.: On transit-time distributions in unsteady circulation models, Ocean Model., 21, 35–45, https://doi.org/10.1016/j.ocemod.2007.11.004, 2008.

Hall, T. M. and Plumb, R. A.: Age as a diagnostic of stratospheric transport, J. Geophys. Res., 99, 1059, https://doi.org/10.1029/93JD03192, 1994.

Hauck, M., Fritsch, F., Garny, H., and Engel, A.: Deriving stratospheric age of air spectra using an idealized set of chemically active trace gases, Atmos. Chem. Phys., 19, 5269–5291, https://doi.org/10.5194/acp-19-5269-2019, 2019.

Haynes, P. H., McIntyre, M. E., Shepherd, T. G., Marks, C. J., and Shine, K. P.: On the "Downward Control" of Extratropical Diabatic Circulations by Eddy-Induced Mean Zonal Forces, J. Atmos. Sci., 48, 651–678, https://doi.org/10.1175/1520-0469(1991)048<0651:OTCOED>2.0.CO;2, 1991.

Hegglin, M. I. and Shepherd, T. G.: O_3-N_2O correlations from the Atmospheric Chemistry Experiment: Revisiting a diagnostic of transport and chemistry in the stratosphere, J. Geophys. Res., 112, D19301, https://doi.org/10.1029/2006JD008281, 2007.

Holton, J. R., Haynes, P. H., McIntyre, M. E., Douglass, A. R., Rood, R. B., and Pfister, L.: Stratosphere-troposphere exchange, Rev. Geophys., 33, RG02097, https://doi.org/10.1029/95RG02097, 1995.

Holzer, M. and Hall, T. M.: Transit-Time and Tracer-Age Distributions in Geophysical Flows, J. Atmos. Sci., 57, 3539–3558, 2000.

Holzer, M. and Primeau, F. W.: Improved constraints on transit time distributions from argon 39: A maximum entropy approach, J. Geophys. Res., 115, C12021, https://doi.org/10.1029/2010JC006410, 2010.

Holzer, M. and Waugh, D. W.: Interhemispheric transit time distributions and path-dependent lifetimes constrained by measurements of SF 6 CFCs, and CFC replacements, Geophys. Res. Lett., 42, 4581–4589, https://doi.org/10.1002/2015GL064172, 2015.

Hoor, P., Gurk, C., Brunner, D., Hegglin, M. I., Wernli, H., and Fischer, H.: Seasonality and extent of extratropical TST derived from in-situ CO measurements during SPURT, Atmos. Chem. Phys., 4, 1427–1442, https://doi.org/10.5194/acp-4-1427-2004, 2004.

Hoor, P., Fischer, H., and Lelieveld, J.: Tropical and extratropical tropospheric air in the lowermost stratosphere over Europe: A CO-based budget, Geophys. Res. Lett., 32, L07802, https://doi.org/10.1029/2004GL022018, 2005.

Keber, T., Bönisch, H., Hartick, C., Hauck, M., Lefrancois, F., Obersteiner, F., Ringsdorf, A., Schohl, N., Schuck, T., Hossaini, R., Graf, P., Jöckel, P., and Engel, A.: Bromine from short-lived source gases in the extratropical northern hemispheric upper troposphere and lower stratosphere (UTLS), Atmos. Chem. Phys., 20, 4105–4132, https://doi.org/10.5194/acp-20-4105-2020, 2020.

Kida, H.: General Circulation of Air Parcels and Transport Characteristics Derived from a Hemispheric GCM, J. Meteorol. Soc. Jpn., 61, 510–523, https://doi.org/10.2151/jmsj1965.61.4_510, 1983.

Konopka, P.: Mixing and ozone loss in the 1999–2000 Arctic vortex: Simulations with the three-dimensional Chemical Lagrangian Model of the Stratosphere (CLaMS), J. Geophys. Res., 109, D02315, https://doi.org/10.1029/2003JD003792, 2004.

Krause, J., Hoor, P., Engel, A., Plöger, F., Grooß, J.-U., Bönisch, H., Keber, T., Sinnhuber, B.-M., Woiwode, W., and Oelhaf, H.: Mixing and ageing in the polar lower stratosphere in winter 2015–2016, Atmos. Chem. Phys., 18, 6057–6073, https://doi.org/10.5194/acp-18-6057-2018, 2018.

Kunkel, D., Hoor, P., Kaluza, T., Ungermann, J., Kluschat, B., Giez, A., Lachnitt, H.-C., Kaufmann, M., and Riese, M.: Evidence

of small-scale quasi-isentropic mixing in ridges of extratropical baroclinic waves, Atmos. Chem. Phys., 19, 12607–12630, https://doi.org/10.5194/acp-19-12607-2019, 2019.

Laube, J. C., Elvidge, E. C. L., Adcock, K. E., Baier, B., Brenninkmeijer, C. A. M., Chen, H., Droste, E. S., Grooß, J.-U., Heikkinen, P., Hind, A. J., Kivi, R., Lojko, A., Montzka, S. A., Oram, D. E., Randall, S., Röckmann, T., Sturges, W. T., Sweeney, C., Thomas, M., Tuffnell, E., and Ploeger, F.: Investigating stratospheric changes between 2009 and 2018 with aircraft, AirCores, and a global model focusing on CFC-11, Atmos. Chem. Phys. Discuss., https://doi.org/10.5194/acp-2020-62, in review, 2020.

Li, F., Austin, J., and Wilson, J.: The Strength of the Brewer–Dobson Circulation in a Changing Climate: Coupled Chemistry–Climate Model Simulations, J. Climate, 21, 40–57, https://doi.org/10.1175/2007JCLI1663.1, 2008.

Li, F., Waugh, D. W., Douglass, A. R., Newman, P. A., Pawson, S., Stolarski, R. S., Strahan, S. E., and Nielsen, J. E.: Seasonal variations of stratospheric age spectra in the Goddard Earth Observing System Chemistry Climate Model (GEOSCCM), J. Geophys. Res., 117, D05134, https://doi.org/10.1029/2011JD016877, 2012.

McKenna, D. S.: A new Chemical Lagrangian Model of the Stratosphere (CLaMS) 1. Formulation of advection and mixing, J. Geophys. Res., 107, 1435, https://doi.org/10.1029/2000JD000114, 2002a.

McKenna, D. S.: A new Chemical Lagrangian Model of the Stratosphere (CLaMS) 2. Formulation of chemistry scheme and initialization, J. Geophys. Res., 107, 4256, https://doi.org/10.1029/2000JD000113, 2002b.

Meinshausen, M., Smith, S. J., Calvin, K., Daniel, J. S., Kainuma, M. L. T., Lamarque, J.-F., Matsumoto, K., Montzka, S. A., Raper, S. C. B., Riahi, K., Thomson, A., Velders, G. J. M., and van Vuuren, D. P. P.: The RCP greenhouse gas concentrations and their extensions from 1765 to 2300, Climatic Change, 109, 213–241, https://doi.org/10.1007/s10584-011-0156-z, 2011a.

Meinshausen, M., S. J. Smith, K. V. Calvin, J. S. Daniel, M. L. T. Kainuma, J.-F. Lamarque, K. Matsumoto, S. A. Montzka, S. C. B. Raper, K. Riahi, A. M. Thomson; G. J. M. Velders and D. van Vuuren: The Representative Concentration Pathways (RCP) Greenhouse Gas Data, Potsdam Institute for Climate Impact Research (PIK), available at: http://www.pik-potsdam.de/~mmalte/rcps/index.htm (last access: 22 July 2020), 2011b.

Morley, S. K., Brito, T. V., and Welling, D. T.: Measures of Model Performance Based On the Log Accuracy Ratio, Space Weather, 16, 69–88, https://doi.org/10.1002/2017SW001669, 2018.

Müller, S., Hoor, P., Berkes, F., Bozem, H., Klingebiel, M., Reutter, P., Smit, H. G. J., Wendisch, M., Spichtinger, P., and Borrmann, S.: In situ detection of stratosphere-troposphere exchange of cirrus particles in the midlatitudes, Geophys. Res. Lett., 42, 949–955, https://doi.org/10.1002/2014GL062556, 2015.

Neu, J. L. and Plumb, R. A.: Age of air in a "leaky pipe" model of stratospheric transport, J. Geophys. Res., 104, 19243–19255, https://doi.org/10.1029/1999JD900251, 1999.

Oberländer-Hayn, S., Meul, S., Langematz, U., Abalichin, J., and Haenel, F.: A chemistry-climate model study of past changes in the Brewer-Dobson circulation, J. Geophys. Res., 120, 6742–6757, https://doi.org/10.1002/2014JD022843, 2015.

Oberländer-Hayn, S., Gerber, E. P., Abalichin, J., Akiyoshi, H., Kerschbaumer, A., Kubin, A., Kunze, M., Langematz, U., Meul, S., Michou, M., Morgenstern, O., and Oman, L. D.: Is the Brewer-Dobson circulation increasing or moving upward?, Geophys. Res. Lett., 43, 1772–1779, https://doi.org/10.1002/2015GL067545, 2016.

Oelhaf, H., Sinnhuber, B.-M., Woiwode, W., Bönisch, H., Bozem, H., Engel, A., Fix, A., Friedl-Vallon, F., Grooß, J.-U., Hoor, P., Johansson, S., Jurkat-Witschas, T., Kaufmann, S., Krämer, M., Krause, J., Kretschmer, E., Lörks, D., Marsing, A., Orphal, J., Pfeilsticker, K., Pitts, M., Poole, L., Preusse, P., Rapp, M., Riese, M., Rolf, C., Ungermann, J., Voigt, C., Volk, C. M., Wirth, M., Zahn, A., and Ziereis, H.: POLSTRACC: Airborne Experiment for Studying the Polar Stratosphere in a Changing Climate with the High Altitude and Long Range Research Aircraft (HALO), B. Am. Meteorol. Soc., 100, 2634–2664, https://doi.org/10.1175/BAMS-D-18-0181.1, 2019.

Olsen, M. A., Schoeberl, M. R., and Douglass, A. R.: Stratosphere-troposphere exchange of mass and ozone, J. Geophys. Res., 109, 15071, https://doi.org/10.1029/2004JD005186, 2004.

Ploeger, F. and Birner, T.: Seasonal and inter-annual variability of lower stratospheric age of air spectra, Atmos. Chem. Phys., 16, 10195–10213, https://doi.org/10.5194/acp-16-10195-2016, 2016.

Ploeger, F., Legras, B., Charlesworth, E., Yan, X., Diallo, M., Konopka, P., Birner, T., Tao, M., Engel, A., and Riese, M.: How robust are stratospheric age of air trends from different reanalyses?, Atmos. Chem. Phys., 19, 6085–6105, https://doi.org/10.5194/acp-19-6085-2019, 2019.

Plumb, I. C., Vohralik, P. F., and Ryan, K. R.: Normalization of correlations for atmospheric species with chemical loss, J. Geophys. Res., 104, 11723–11732, https://doi.org/10.1029/1999JD900014, 1999.

Plumb, R. A.: Stratospheric Transport, J. Meteorol. Soc. Jpn., 80, 793–809, https://doi.org/10.2151/jmsj.80.793, 2002.

Podglajen, A. and Ploeger, F.: Retrieving the age of air spectrum from tracers: principle and method, Atmos. Chem. Phys., 19, 1767–1783, https://doi.org/10.5194/acp-19-1767-2019, 2019.

Pommrich, R., Müller, R., Grooß, J.-U., Konopka, P., Ploeger, F., Vogel, B., Tao, M., Hoppe, C. M., Günther, G., Spelten, N., Hoffmann, L., Pumphrey, H.-C., Viciani, S., D'Amato, F., Volk, C. M., Hoor, P., Schlager, H., and Riese, M.: Tropical troposphere to stratosphere transport of carbon monoxide and long-lived trace species in the Chemical Lagrangian Model of the Stratosphere (CLaMS), Geosci. Model Dev., 7, 2895–2916, https://doi.org/10.5194/gmd-7-2895-2014, 2014.

Prinn, R. G., Weiss, R. F., Arduini, J., Arnold, T., DeWitt, H. L., Fraser, P. J., Ganesan, A. L., Gasore, J., Harth, C. M., Hermansen, O., Kim, J., Krummel, P. B., Li, S., Loh, Z. M., Lunder, C. R., Maione, M., Manning, A. J., Miller, B. R., Mitrevski, B., Mühle, J., O'Doherty, S., Park, S., Reimann, S., Rigby, M., Saito, T., Salameh, P. K., Schmidt, R., Simmonds, P. G., Steele, L. P., Vollmer, M. K., Wang, R. H., Yao, B., Yokouchi, Y., Young, D., and Zhou, L.: History of chemically and radiatively important atmospheric gases from the Advanced Global Atmospheric Gases Experiment (AGAGE), Earth Syst. Sci. Data, 10, 985–1018, https://doi.org/10.5194/essd-10-985-2018, 2018.

Prinn, R. G., Weiss, R. F., Arduini, J., Arnold, T., Fraser, P. J., Ganesan, A. L., Gasore, J., Harth, C. M., Hermansen, O., Kim, J., Krummel, P. B., Li, S., Loh, Z. M., Lunder, C. R., Maione, M., Manning, A. J., Miller, B. R., Mitrevski,

B., Mühle, J., O'Doherty, S., Park, S., Reimann, S., Rigby, M., Salameh, P. K., Schmidt, R., Simmonds, P. G., Steele, L. P., Vollmer, M. K., Wang, R. H., and Young, D.: The ALE/GAGE/AGAGE Network (DB1001), OSTI.GOV, United States, https://doi.org/10.3334/CDIAC/ATG.DB1001, 2019a.

Prinn, R. G., Weiss, R. F., Arduini, J., Arnold, T., Fraser, P. J., Ganesan, A. L., Gasore, J., Harth, C. M., Hermansen, O., Kim, J., Krummel, P. B., Li, S., Loh, Z. M., Lunder, C. R., Maione, M., Manning, A. J., Miller, B. R., Mitrevski, B., Mühle, J., O'Doherty, S., Park, S., Reimann, S., Rigby, M., Salameh, P. K., Schmidt, R., Simmonds, P. G., Steele, L. P., Vollmer, M. K., Wang, R. H., and Young, D.: The ALE/GAGE/AGAGE Data Base, AGAGE, available at: http://agage2.eas.gatech.edu/data_archive/ (last access: 22 July 2020), 2019b.

Ray, E. A., Moore, F. L., Rosenlof, K. H., Davis, S. M., Sweeney, C., Tans, P., Wang, T., Elkins, J. W., Bönisch, H., Engel, A., Sugawara, S., Nakazawa, T., and Aoki, S.: Improving stratospheric transport trend analysis based on SF_6 and CO_2 measurements, J. Geophys. Res., 119, 14110–14128, https://doi.org/10.1002/2014JD021802, 2014.

Ray, E. A., Moore, F. L., Elkins, J. W., Rosenlof, K. H., Laube, J. C., Röckmann, T., Marsh, D. R., and Andrews, A. E.: Quantification of the SF_6 lifetime based on mesospheric loss measured in the stratospheric polar vortex, J. Geophys. Res., 122, 4626–4638, https://doi.org/10.1002/2016JD026198, 2017.

Reithmeier, C., Sausen, R., and Grewe, V.: Investigating lower stratospheric model transport: Lagrangian calculations of mean age and age spectra in the GCM ECHAM4, Clim. Dynam., 30, 225–238, https://doi.org/10.1007/s00382-007-0294-1, 2008.

Rosenlof, K. H.: Seasonal cycle of the residual mean meridional circulation in the stratosphere, J. Geophys. Res., 100, 5173, https://doi.org/10.1029/94JD03122, 1995.

Rosenlof, K. H. and Holton, J. R.: Estimates of the stratospheric residual circulation using the downward control principle, J. Geophys. Res., 98, 10465, https://doi.org/10.1029/93JD00392, 1993.

Schiller, C. L., Bozem, H., Gurk, C., Parchatka, U., Königstedt, R., Harris, G. W., Lelieveld, J., and Fischer, H.: Applications of quantum cascade lasers for sensitive trace gas measurements of CO, CH_4, N_2O and HCHO, Appl. Phys. B, 92, 419–430, https://doi.org/10.1007/s00340-008-3125-0, 2008.

Schoeberl, M. R., Sparling, L. C., Jackman, C. H., and Fleming, E. L.: A Lagrangian view of stratospheric trace gas distributions, J. Geophys. Res., 105, 1537–1552, https://doi.org/10.1029/1999JD900787, 2000.

Schoeberl, M. R.: Extratropical stratosphere-troposphere mass exchange, J. Geophys. Res., 109, D13303, https://doi.org/10.1029/2004JD004525, 2004.

Schoeberl, M. R., Douglass, A. R., Polansky, B., Boone, C., Walker, K. A., and Bernath, P.: Estimation of stratospheric age spectrum from chemical tracers, J. Geophys. Res., 110, 32295, https://doi.org/10.1029/2005JD006125, 2005.

Shepherd, T. G.: Transport in the Middle Atmosphere, J. Meteorol. Soc. J., 85, 165–191, https://doi.org/10.2151/jmsj.85B.165, 2007.

Shepherd, T. G. and McLandress, C.: A Robust Mechanism for Strengthening of the Brewer–Dobson Circulation in Response to Climate Change: Critical-Layer Control of Subtropical Wave Breaking, J. Atmos. Sci., 68, 784–797, https://doi.org/10.1175/2010JAS3608.1, 2011.

Škerlak, B., Sprenger, M., and Wernli, H.: A global climatology of stratosphere–troposphere exchange using the ERA-Interim data set from 1979 to 2011, Atmos. Chem. Phys., 14, 913–937, https://doi.org/10.5194/acp-14-913-2014, 2014.

Solomon, S., Rosenlof, K. H., Portmann, R. W., Daniel, J. S., Davis, S. M., Sanford, T. J., and Plattner, G.-K.: Contributions of stratospheric water vapor to decadal changes in the rate of global warming, Science, 327, 1219–1223, https://doi.org/10.1126/science.1182488, 2010.

SPARC: SPARC Report on the Lifetimes of Stratospheric Ozone-Depleting Substances, Their Replacements, and Related Species, edited by: Ko, M. K. W., Newman, P. A., Reimann, S., and Strahan, S. E., SPARC Report No. 6, WCRP-15/2013, available at: https://www.sparc-climate.org/publications/sparc-reports/sparc-report-no-6/ (last access: 16 July 2020), 2013

Stiller, G. P., Fierli, F., Ploeger, F., Cagnazzo, C., Funke, B., Haenel, F. J., Reddmann, T., Riese, M., and von Clarmann, T.: Shift of subtropical transport barriers explains observed hemispheric asymmetry of decadal trends of age of air, Atmos. Chem. Phys., 17, 11177–11192, https://doi.org/10.5194/acp-17-11177-2017, 2017.

Vogel, B., Müller, R., Günther, G., Spang, R., Hanumanthu, S., Li, D., Riese, M., and Stiller, G. P.: Lagrangian simulations of the transport of young air masses to the top of the Asian monsoon anticyclone and into the tropical pipe, Atmos. Chem. Phys., 19, 6007–6034, https://doi.org/10.5194/acp-19-6007-2019, 2019.

Volk, C. M., Elkins, J. W., Fahey, D. W., Dutton, G. S., Gilligan, J. M., Loewenstein, M., Podolske, J. R., Chan, K. R., and Gunson, M. R.: Evaluation of source gas lifetimes from stratospheric observations, J. Geophys. Res., 102, 25543–25564, https://doi.org/10.1029/97JD02215, 1997.

Waugh, D. and Hall, T. M.: Age of stratospheric air: Theory, observations, and models, Rev. Geophys., 40, 4483, https://doi.org/10.1029/2000RG000101, 2002.

World Meteorological Organization: WMO WDCGG Data Summary: World Data Centre For Greenhouse Gases No. 42 – Global Atmospheric Watch Data, Volume IV – Greenhouse Gases and Other Atmospheric Gases, Japan Meteorological Agency, Japan, 2018.

Yang, H., Chen, G., Tang, Q., and Hess, P.: Quantifying isentropic stratosphere-troposphere exchange of ozone, J. Geophys. Res., 121, 3372–3387, https://doi.org/10.1002/2015JD024180, 2016.

Paper III: Bromine from short–lived source gases in the extratropical northern hemispheric upper troposphere and lower stratosphere (UTLS)

Published as:

Keber, T., Bönisch, H., Hartick, C., Hauck, M., Lefrancois, F., Obersteiner, F., Ringsdorf, A., Schohl, N., Schuck, T., Hossaini, R., Graf, P., Jöckel, P., and Engel, A.: *Bromine from short–lived source gases in the extratropical northern hemispheric upper troposphere and lower stratosphere (UTLS)*, Atmospheric Chemistry and Physics, 20, 4105-4132, DOI: https://doi.org/10.5194/acp-20-4105-2020, 2020

Author Contributions:

The manuscript was mainly written by Andreas Engel and Timo Keber.

Timo Keber, Andreas Engel, Harald Bönisch and Florian Obersteiner took leading roles in the development process of the GhOST instrument, as well as in the operation during the research campaigns and evaluation and interpretation of gained data.

Marius Hauck was strongly involved in the operation of the GhOST instrument during WISE, provided code and help for the evaluation and interpretation of gained data, together with Fides Lefrancois and Tanja Schuck.

Marius Hauck provided code and help for the postprocessing and interpretation of the model data in the study.

All co-authors proofread the original and revised manuscripts and contributed to the review process.

Nils Schohl, Carl Hartick and Akima Ringsdorf participated in the evaluation and interpretation of modeled and observational data.

Ryan Hossaini, Phoebe Graf and Patrick Jöckel conducted the model simulations and provided the resulting data as well as help for the postprocessing and interpretation.

All co-authors contributed to the preparation of the paper in many useful discussions.

Frankfurt am Main

_____

Marius Hauck

Atmos. Chem. Phys., 20, 4105–4132, 2020
https://doi.org/10.5194/acp-20-4105-2020

Atmospheric Chemistry and Physics
Open Access
EGU

Bromine from short-lived source gases in the extratropical northern hemispheric upper troposphere and lower stratosphere (UTLS)

Timo Keber[1], Harald Bönisch[1,a], Carl Hartick[1,b], Marius Hauck[1], Fides Lefrancois[1], Florian Obersteiner[1,a], Akima Ringsdorf[1,c], Nils Schohl[1], Tanja Schuck[1], Ryan Hossaini[2], Phoebe Graf[3], Patrick Jöckel[3], and Andreas Engel[1]

[1]Institute for Atmospheric and Environmental Sciences, University of Frankfurt, Altenhöferallee 1, 60438 Frankfurt, Germany
[2]Lancaster Environment Centre, Lancaster University, Lancaster, LA1 4YQ, UK
[3]Institut für Physik der Atmosphäre, Deutsches Zentrum für Luft- und Raumfahrt (DLR), Oberpfaffenhofen, Germany
[a]now at: Karlsruhe Institute of Technology, Institute of Meteorology and Climate Research, Hermann-von-Helmholtz-Platz 1, 76344 Eggenstein-Leopoldshafen, Germany
[b]now at: Research Centre Jülich, Institute for Agrosphere (IBG-3), Wilhelm-Johnen-Straße, 52428 Jülich, Germany
[c]now at: Atmospheric Chemistry Division, Max Planck Institute for Chemistry, Hahn-Meitner-Weg 1, 55128 Mainz, Germany

Correspondence: Timo Keber (keber@iau.uni-frankfurt.de) and Andreas Engel (an.engel@iau.uni-frankfurt.de)

Received: 4 September 2019 – Discussion started: 27 September 2019
Revised: 17 February 2020 – Accepted: 19 February 2020 – Published: 6 April 2020

Abstract. We present novel measurements of five short-lived brominated source gases (CH_2Br_2, $CHBr_3$, CH_2ClBr, $CHCl_2Br$ and $CHClBr_2$). These rather short-lived gases are an important source of bromine to the stratosphere, where they can lead to depletion of ozone. The measurements have been obtained using an in situ gas chromatography and mass spectrometry (GC–MS) system on board the High Altitude and Long Range Research Aircraft (HALO). The instrument is extremely sensitive due to the use of chemical ionization, allowing detection limits in the lower parts per quadrillion (ppq, 10^{-15}) range. Data from three campaigns using HALO are presented, where the upper troposphere and lower stratosphere (UTLS) of the northern hemispheric mid-to-high latitudes were sampled during winter and during late summer to early fall. We show that an observed decrease with altitude in the stratosphere is consistent with the relative lifetimes of the different compounds. Distributions of the five source gases and total organic bromine just below the tropopause show an increase in mixing ratio with latitude, in particular during polar winter. This increase in mixing ratio is explained by increasing lifetimes at higher latitudes during winter. As the mixing ratios at the extratropical tropopause are generally higher than those derived for the tropical tropopause, extratropical troposphere-to-stratosphere transport will result in elevated levels of organic bromine in comparison to air transported over the tropical tropopause. The observations are compared to model estimates using different emission scenarios. A scenario with emissions mainly confined to low latitudes cannot reproduce the observed latitudinal distributions and will tend to overestimate organic bromine input through the tropical tropopause from CH_2Br_2 and $CHBr_3$. Consequently, the scenario also overestimates the amount of brominated organic gases in the stratosphere. The two scenarios with the highest overall emissions of CH_2Br_2 tend to overestimate mixing ratios at the tropical tropopause, but they are in much better agreement with extratropical tropopause mixing ratios. This shows that not only total emissions but also latitudinal distributions in the emissions are of importance. While an increase in tropopause mixing ratios with latitude is reproduced with all emission scenarios during winter, the simulated extratropical tropopause mixing ratios are on average lower than the observations during late summer to fall. We show that a good knowledge of the latitudinal distribution of tropopause mixing ratios and of the fractional contributions of tropical and extratropical air is needed to derive stratospheric inorganic bromine in the lowermost strato-

sphere from observations. In a sensitivity study we find maximum differences of a factor 2 in inorganic bromine in the lowermost stratosphere from source gas injection derived from observations and model outputs. The discrepancies depend on the emission scenarios and the assumed contributions from different source regions. Using better emission scenarios and reasonable assumptions on fractional contribution from the different source regions, the differences in inorganic bromine from source gas injection between model and observations is usually on the order of 1 ppt or less. We conclude that a good representation of the contributions of different source regions is required in models for a robust assessment of the role of short-lived halogen source gases on ozone depletion in the UTLS.

1 Introduction

Following the detection of the ozone hole during springtime over Antarctica (Farman et al., 1985) and the attribution of the decline in both polar and global ozone to the emissions of anthropogenic halogenated compounds (see Molina and Rowland, 1974; Solomon, 1999; Engel and Rigby, 2018), production and use of long-lived halogenated species, in particular chlorofluorocarbons (CFCs), have been regulated by the Montreal Protocol (WMO, 2018). This has led to decreasing levels of chlorine in the atmosphere (Engel and Rigby, 2018), despite recent concerns over ongoing emissions of CFC-11, which have been attributed to unreported and thus illegal production (Montzka et al., 2018; Engel and Rigby, 2018; Rigby et al., 2019). Bromine reaching the stratosphere has been identified as an even stronger catalyst for the depletion of stratospheric ozone than chlorine (Wofsy et al., 1975; Sinnhuber et al., 2009). Its relative efficiency on a per molecule basis is currently estimated to be 60–65 times larger than that of chlorine (see discussion in Daniel and Velders, 2006). Long-lived bromine gases include CH_3Br with partly natural and partly anthropogenic sources and halons, which are of purely anthropogenic origin. Next to long-lived gases, some chlorine and bromine from so-called "very-short-lived substances" (VSLS), i.e. substances with atmospheric lifetimes less than 6 months, can reach the stratosphere. It has been estimated that, for the year 2016, about 25 % of the bromine entering the stratosphere is from VSLS (Engel and Rigby, 2018). Due to the decline in chlorine and bromine from long-lived species, the relative contribution of short-lived species to stratospheric halogen loading is expected to increase, which is also driven by increasing anthropogenic emissions of some short-lived chlorinated halocarbons (Hossaini et al., 2017, 2019; Oram et al., 2017; Leedham Elvidge et al., 2015; Engel and Rigby, 2018).

A number of factors control the abundance of ozone at mid latitudes, including influences from dynamics, chemical destruction, aerosol loading and the solar cycle (e.g. Feng et al., 2007; Harris et al., 2008; Dhomse et al., 2015). In the lowermost stratosphere, the breakdown of VSLS provides a significant bromine source in a region where (a) ozone loss cycles involving bromine chemistry are known to be important (e.g. Salawitch et al., 2005) and (b), on a per molecule basis, ozone perturbations have a relatively large radiative effect (Hossaini et al., 2015). At present, VSLS are estimated to supply a total of ~ 5 (3–7) ppt (parts per trillion, 10^{-12}) Br to the stratosphere, with source gas injection estimated to provide 2.2 (0.8–4.2) ppt Br and product gas injection 2.7 (1.7–4.2) ppt Br (Engel and Rigby, 2018). Attribution of lower stratospheric ozone trends is complex and trends in this region are highly uncertain (Steinbrecht et al., 2017; Ball et al., 2018; Chipperfield et al., 2018). It has been suggested that continuing negative ozone trends observed in the lower stratosphere (defined as about 13 to 24 km in the mid latitudes) may partly be related to increasing anthropogenic and natural VSLS (Ball et al., 2018). While Chipperfield et al. (2018) suggested that the main driver for variability and trends in lower stratospheric ozone is dynamics rather than chemistry, the bromine budget of the upper troposphere and lower stratosphere (UTLS) needs to be well understood.

In the past, the main focus of upper tropospheric bromine studies for VSLS has been on the tropics, as this is the main entry region for air masses to reach above 380 K potential temperatures (see discussion in Engel and Rigby, 2018) and thus for the main part of the stratosphere. However, as many authors have shown, the lowermost stratosphere, i.e. the part of the stratosphere situated below 380 K but above the extratropical stratosphere, is influenced by transport from the tropics and from the extratropics (e.g. Holton et al., 1995; Gettelman et al., 2011; Fischer et al., 2000; Hoor et al., 2005). Some authors have quantified the fraction of air in the lowermost stratosphere, which did not pass the tropical tropopause, from tracer measurements (Hoor et al., 2005; Bönisch et al., 2009; Ray et al., 1999; Werner et al., 2010) and others have used trajectory analyses to study mass fluxes and stratosphere–troposphere exchange (e.g. Stohl et al., 2003; Wernli and Bourqui, 2002; Škerlak et al., 2014; Appenzeller et al., 1996). Based on tracer measurements of mainly CO, Hoor et al. (2005) estimated that the fraction of air with extratropical origin in the mid-latitude lowermost stratosphere of the Northern Hemisphere ranged between about 35 % during winter and spring to about 55 % during summer and fall. Using a different approach based on CO_2 and SF_6 observations, Bönisch et al. (2009) found a similar seasonality but higher extratropical fractions, which were consistently higher than 70 % during summer and fall and above 90 % in the entire lowermost stratosphere during October. Similarly, Bönisch et al. (2009) also derived much lower fractions of air with recent extratropical origin during winter and spring, which were sometimes as low as 20 % during April. It has also been argued that the relative role of different source regions for the UTLS could alter with a changing circulation (Boothe and Homeyer, 2017).

Both extratropical and tropical source regions are important for the lowermost stratosphere. A recent compilation of entry mixing ratios of brominated VSLS to the stratosphere (Engel and Rigby, 2018) has focused on mixing ratios representative of the tropical tropopause. Two pathways for input of halogens from short-lived gases are discussed. Halogen atoms can be transported to the stratosphere in the form of the organic source gas (source gas injection (SGI)) or in the inorganic form as photochemical breakdown products of source gases (product gas injection (PGI)). Halogens from product gases are readily available for catalytic ozone depletion reactions. Source gases have to undergo a photochemical transformation into inorganic bromine, which can then interact with ozone. Due to the short lifetimes of VSLS, this release is expected to occur in the lowest part of the stratosphere. Therefore, brominated VSLS are particularly effective with respect to ozone chemistry in the lower and lowermost stratosphere, below about 20 km, with the associated ozone decreases exerting a significant radiative effect (Hossaini et al., 2015). It has been shown that observed and modelled ozone show a better agreement if bromine from short-lived species is included in models (Sinnhuber and Meul, 2015; Fernandez et al., 2017; Oman et al., 2016). In particular for the Antarctic ozone hole, an enhancement in size by 40 % and an enhancement in mass deficit by 75 % was simulated due to VSLS (Fernandez et al., 2017) in comparison with a model run without VSLS. A delay in polar ozone recovery by about a decade has also been reported due to the inclusion of brominated VSLS (Oman et al., 2016). In order to have solid projections on the effect of VSLS on ozone and climate, a good knowledge of their atmospheric distribution is thus needed for models.

Observations indicate that the main source of brominated VSLS is from oceans and in particular from coastal regions. Four global emission scenarios of short-lived brominated gases have been proposed (Warwick et al., 2006; Ordóñez et al., 2012; Ziska et al., 2013; Liang et al., 2010), with variations in VSLS source strengths of more than a factor of 2 between them (Engel and Rigby, 2018). In the past, these scenarios have been compared to each other and to observations; large differences have been identified in modelled tropospheric mixing ratios of $CHBr_3$ and CH_2Br_2, along with estimates of stratospheric bromine input (Hossaini et al., 2013, 2016; Sinnhuber and Meul, 2015). Hossaini et al. (2013) concluded that the lowest suggested emissions of $CHBr_3$ (Ziska et al., 2013) and the lowest suggested emissions of CH_2Br_2 (Liang et al., 2014) yielded the overall best agreement in the tropics and thus the most realistic input of stratospheric bromine from VSLS. They also concluded that "Averaged globally, the best agreement between modelled $CHBr_3$ and CH_2Br_2 with long-term surface observations made by NOAA/ESRL is obtained using the top-down emissions proposed by Liang et al. (2010)". It has also been proposed that VSLS emissions may have increased by 6 %–8 % between 1979 and 2013 (Ziska et al., 2017), although no observational evidence for this has been found (Engel and Rigby, 2018). A further future increase has been suggested (Ziska et al., 2017; Falk et al., 2017), although this projection is very uncertain and the processes associated with the oceanic production of brominated VSLS are still poorly understood. It has also been proposed that certain source regions could be more effective with respect to transport to the stratosphere, in particular the Indian Ocean, the Maritime Continent and the tropical western Pacific (Liang et al., 2014; Fernandez et al., 2014; Tegtmeier et al., 2012). The Asian monsoon has also been named as a possible pathway for transport of bromine from VSLS to the stratosphere (Liang et al., 2014; Fiehn et al., 2017; Hossaini et al., 2016).

While most investigations of natural VSLS focused on tropical injection of bromine to the stratosphere, this study focuses on the extratropical bromine VSLS budget. In order to investigate the regional variability of bromine input into the lowermost stratosphere, we have performed a range of airborne measurement campaigns using an in situ gas chromatograph (GC) coupled to a mass spectrometer (MS) on board the High Altitude and Long Range Research Aircraft (HALO). The differences in stratospheric inorganic bromine from observations and from models are discussed. In Sect. 2 we give a brief introduction to the instrument, the available observations and the models used for this study. Typical distributions of brominated VSLS derived from these observations are then presented in Sect. 3 and compared to model output from two different atmospheric models run with the different emission scenarios mentioned above in Sect. 4. Finally, in Sect. 5 the implications of the observations for inorganic bromine in the stratosphere are discussed.

2 Observations and models

2.1 Instrumentation and observations

The data presented here have been measured with the in situ Gas chromatograph for Observational Studies using Tracers – Mass Spectrometer (GhOST-MS) deployed on board HALO. GhOST-MS is a two-channel GC instrument. An electron capture detector (ECD) is used in an isothermal channel in a similar set-up as used during the SPURT campaign (Bönisch et al., 2009, 2008; Engel et al., 2006) to measure SF_6 and CFC-12 with a time resolution of 1 min. The second channel is temperature programmed and uses a cryogenic pre-concentration system (Obersteiner et al., 2016; Sala et al., 2014) and a mass spectrometer (MS) for detection. It is similar to the set-up described by Sala et al. (2014) and measures halocarbons in the chemical ionization mode (e.g. Worton et al., 2008) with a time resolution of 4 min. As explained in Sala et al. (2014), CH_2BrCl_2 and CH_2Br_2 are not separated chromatographically during normal measurements with GhOST-MS, as this would require too much time. Instead, a correlation between the two species from either in-

dependent measurements or measurements of the two species from dedicated flights are used. Such dedicated flights have been performed during the WISE and PGS campaigns (defined below). The procedure of how $CHBrCl_2$ and CH_2Br_2 are derived from the single chromatographic peak with this additional information is explained in Sala et al. (2014). While CH_4 has been used as chemical ionization gas for the TACTS campaign (defined below) and for the tropical measurements discussed in Sala et al. (2014), a change in chemical ionization gas was necessary for later measurements due to safety reasons. During the PGS campaign pure Argon was used, which resulted in very good sensitivities but also an interference with water vapour. In order to avoid this interference for the mid-latitude (more humid) measurements during WISE, a mixture of Argon and methane (non-burnable, below 5 % methane) was used as ionization gas. These (and some other) changes resulted in different performances of the instrument during different campaigns. Typical performance details of the instrument are given for the WISE and PGS campaigns in Table 1 for the brominated hydrocarbons.

The instrument is tested for non-linearities, memory and blank signals, which are corrected where necessary (see the description in Sala, 2014, and Sala et al., 2014, for details). Table 1 also includes typical local lifetimes of the different VSLS species and the global lifetimes of the long-lived species. The instrument was deployed during several campaigns of the German research aircraft HALO, providing observations in the UTLS over a wide range of latitudes and different seasons mainly in the Northern Hemisphere. Some observations from the Southern Hemisphere are also available, but, due to their sparsity, they will not be part of this work.

GhOST-MS measurements from three HALO missions will be presented and discussed here. The first atmospheric science mission of HALO was TACTS (Transport and Composition in the Upper Troposphere/Lowermost Stratosphere), conducted between August and September 2012, with a focus on the Atlantic sector of the mid latitudes of the Northern Hemisphere. The second campaign was PGS, a mission consisting of three sub-missions: POLSTRACC (Polar Stratosphere in a Changing Climate), GW-LCYCLE (Investigation of the Life cycle of gravity waves) and SALSA (Seasonality of Air mass transport and origin in the Lowermost Stratosphere). PGS took place mainly in the Arctic between December 2015 and March 2016. Finally, the GhOST-MS was deployed during the WISE (Wave-driven ISentropic Exchange) mission between September and October 2017. The dates of the missions and some parameters on the available observations are summarized in Table 2, and the flight tracks are shown in Figs. 1 and 2. As the WISE and TACTS campaigns covered a similar time of the year and latitude range, the data from the two campaigns have been combined into a single dataset, which we will refer to as "WISE_TACTS". Vertical profiles of the two major bromine VSLS, CH_2Br_2 and $CHBr_3$, for the TACTS and WISE campaigns are shown separately in Fig. S1 in the Supplement. For this combined dataset, some observations from the TACTS campaign have been omitted, where some extremely high values of VSLS (up to a factor of 10 above typical tropospheric mixing ratios) were observed in the UTLS, which are suspected of being contaminated. The source of the contamination is, however, unknown. Figure 3 shows an example time series of halon 1301 (CF_3Br), CH_2Br_2 and $CHBr_3$, ozone and mean age of air calculated from the SF_6 measurements obtained during a typical flight in the Arctic in January 2016. It is clearly visible that the halocarbons are correlated amongst each other, whereas they are anticorrelated with ozone and mean age. It is further evident from Fig. 3 that the shortest-lived halocarbon measured by GhOST-MS, i.e. $CHBr_3$, decreases much faster with increasing ozone than the longer-lived CH_2Br_2 or the long- lived source gas halon 1301. Note that the local lifetimes of the halocarbons may differ significantly from their typical mid-latitude lifetimes shown in Table 1. Lifetimes generally increase with (a) decreasing temperature for species with a sink through the reaction with the OH radical and (b) with decreasing solar irradiation for species with direct photolytic sink. Therefore, in particular during winter, lifetimes are estimated to increase considerably with increasing latitude due to the decreased solar illumination and low temperatures.

2.2 Models and meteorological data

Data from two different models were used in this study: ESCiMo (Earth System Chemistry Integrated Modelling) data from the EMAC (ECHAM/MESSy Atmospheric Chemistry) chemistry climate model (CCM) and the TOMCAT (Toulouse Off-line Model of Chemistry And Transport) chemistry transport model (CTM).

For EMAC data, we used results from the simulations in the so-called specified dynamics (SD) mode, for which the model was nudged (by Newtonian relaxation) towards ERA-Interim meteorological reanalysis data from the European Centre for Medium-Range Weather Forecasts (ECMWF; Dee et al., 2011). T42 spectral model resolution was used, corresponding to a quadratic Gaussian grid of approximately 2.8° by 2.8° horizontal resolution, and the vertical resolution comprised 90 hybrid sigma-pressure levels up to 0.01 hPa. The model output has been subsequently interpolated to pressure levels between 1000 and 0.01 hPa. The emissions of VSLS were taken from the emission scenario 5 in Warwick et al. (2006). The EMAC SD simulations with 90 vertical levels, as described in detail by Jöckel et al. (2016), were integrated with an internal model time step length of 12 min, and the data have been output every 10 h from which the monthly averages on pressure levels have been derived. The SC1SD-base-01 simulation, which has been used here, has been branched off from RC1SD-base-10 (see Jöckel et al., 2016) at 1 January 2000 using the RCP8.5 emissions and greenhouse gas scenario.

Table 1. Brominated species measured with Gas chromatograph for Observational Studies using Tracers – Mass Spectrometer (GhOST-MS) during three High Altitude and Long Range Research Aircraft campaigns, described in Table 2. Tropospheric mole fractions (parts per trillion, ppt; 10^{-12}) of the halons are taken from Table 1-1 in Engel and Rigby (2018) and from Table 1-7 for the bromocarbons (marine boundary layer value mixing ratios). Lifetimes of bromocarbons are local lifetimes for upper tropospheric conditions (10 km altitude, 25–60° N) from Table 1-5 in Carpenter and Reimann (2014) and global/stratospheric lifetimes are from Table A-1 in WMO 2018 (Burkholder, 2018). Local lifetimes are given in days (d), while global and stratospheric lifetimes are given in years (yr). Reproducibilities and detection limits of GhOST have been determined during the WISE and the PGS campaigns. For the TACTS campaign instrument, performance was similar to that reported in Sala et al. (2014).

Name	Formula	Troposph.	GhOST-MS characteristics				Typical lifetime			
			Reprod.		Decetion limit		Fall	Winter	Global	Strat.
			PGS	WISE	PGS	WISE				
		(ppt)	(%)	(%)	(ppq)	(ppq)	(d)	(d)	(yr)	(yr)
Halon 1301	CF_3Br	3.36	0.4	1	7	50	n/a	n/a	72	73.5
Halon 1211	$CBrClF_2$	3.59	0.2	0.5	2	6	n/a	n/a	16	41
Halon 1202	CBr_2F_2	0.014	2.8	7.6	1	6	n/a	n/a	2.5	36
Halon 2402	$CBrF_2CBrF_2$	0.41	0.6	1.5	2	7	n/a	n/a	28	41
Dibromomethane	CH_2Br_2	0.9	0.2	0.7	3	11	405	890	n/a	n/a
Tribromomethane	$CHBr_3$	1.2	0.6	2.2	9	85	44	88	n/a	n/a
Bromochloromethane	CH_2BrCl	0.1	2.3	9.2	20	130	470	1050	n/a	n/a
Dichlorobromomethane	$CHBrCl_2$	0.3	0.8	3.4	3	2	124	250	n/a	n/a
Dibromochloromethane	$CHBr_2Cl$	0.3	0.7	2.2	4	2	85	182	n/a	n/a

n/a: not applicable.

Table 2. Brief description of measurement campaigns with the High Altitude and Long Range Research Aircraft (HALO) used for this study.

Name	Time period	Campaign base	Brief description
TACTS: Transport and Composition in the Upper Troposphere/Lowermost Stratosphere	late August 2012–September 2012	Oberpfaffenhofen, Germany, and Sal, Cabo Verde	Covers changes in UTLS chemical composition during the transition from summer to fall
WISE: Wave-driven ISentropic Exchange	September–October 2017	Shannon, Ireland	Study on troposphere–stratosphere exchange in mid latitudes
PGS, POLSTRACC, GW-LCYCLE, SALSA*	December 2015–March 2016	Kiruna, Sweden	Study the polar UTLS during winter, including the effect of chemical ozone depletion.

* PGS is a synthesis of three measurement campaigns: POLSTRACC (The Polar Stratosphere in a Changing Climate), GW-LCYCLE (Investigation of the Life cycle of gravity waves) and SALSA (Seasonality of Air mass transport and origin in the Lowermost Stratosphere).

The TOMCAT model (Chipperfield, 2006; Monks et al., 2017) is driven by analysed wind and temperature fields taken 6-hourly from the ECMWF ERA-Interim product. Here, the model was run with T42 horizontal resolution (2.8° by 2.8°) and with 60 vertical levels, extending from the surface to ~ 60 km. The internal model time step was 30 min, and tracers were output as monthly means. This configuration of the model has been used in a number of VSLS-related studies and is described by Hossaini et al. (2019). In this study, three different VSLS emission scenarios are used with TOMCAT (Liang et al., 2010; Ordóñez et al., 2012; Ziska et al., 2013). In the case of the Liang et al. (2010) scenario, their scenario A has been used. Chemical breakdown by reaction with OH and photolysis in the model for all VSLS ($CHBr_3$, CH_2Br_2, CH_2BrCl, $CHBr_2Cl$ and $CHBrCl_2$) are calculated using the relevant kinetic data from Burkholder et al. (2015).

Local tropopause information for the flights with HALO have been derived from ERA-Interim data. The climatological tropopause has been calculated based on potential vorticity (PV) according to the method described in Škerlak et al. (2015) and Sprenger et al. (2017) based on the ERA-Interim reanalysis. As the PV tropopause is not physically meaningful in the tropics, the level with a potential temperature of 380 K has been adapted for the tropopause where the 2 PVU (potential vorticity unit) level is located above the 380 K level.

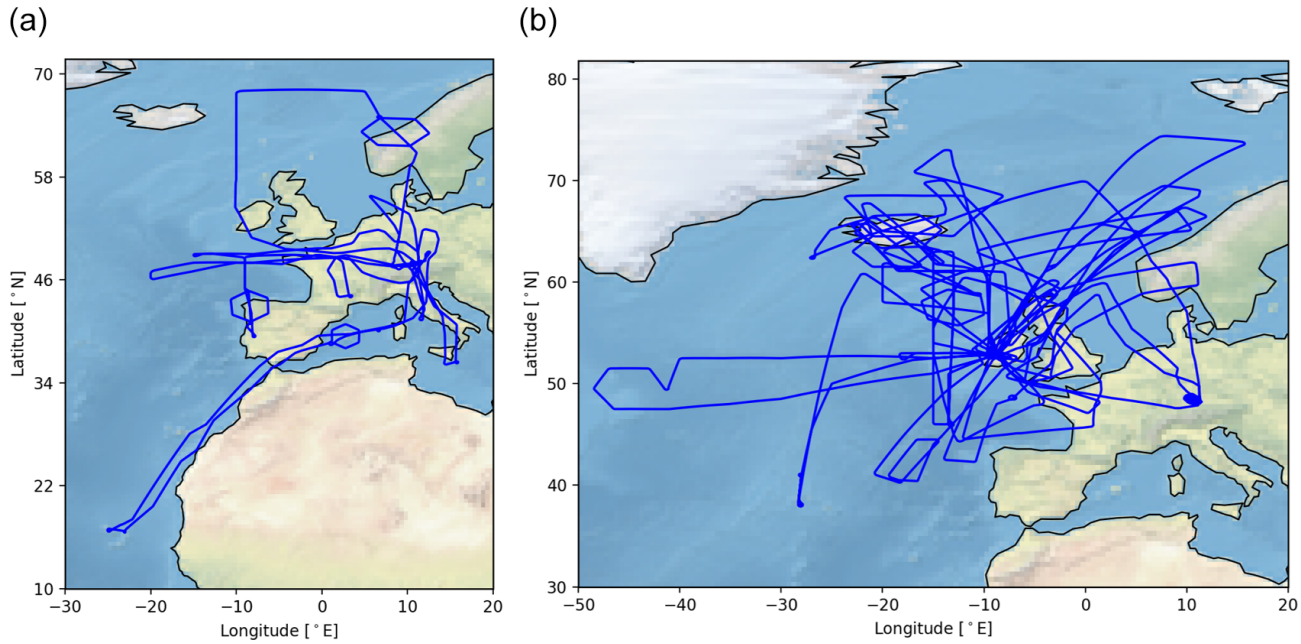

Figure 1. Flight tracks of HALO during the **(a)** TACTS campaign (late August and September 2012) and **(b)** WISE campaign (September–October 2017). The basis of the TACTS campaign was mainly Oberpfaffenhofen (near Munich in Germany), while the basis of the WISE campaign was Shannon (Ireland).

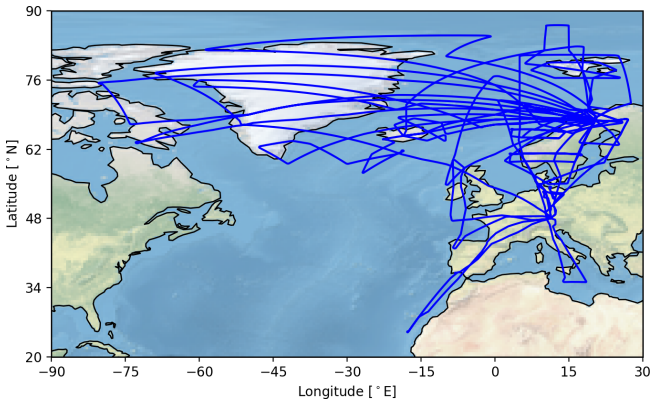

Figure 2. Flight tracks of HALO during the PGS campaign (December 2015 to April 2016). The basis of the campaign was mainly Kiruna in northern Sweden.

3 Observed distribution and atmospheric gradients of different brominated VSLS

Spatial distributions are shown in tropopause-relative coordinates and as functions of equivalent latitude. As equivalent latitude is mainly a useful horizontal coordinate for the stratosphere, we chose to use standard latitude for all measurements below the tropopause and equivalent latitude for all measurements above the tropopause. We refer to this coordinate as equivalent latitude*. As the observations typically cover a range of latitudes, vertical profiles are shown for 20° bins. In the vertical direction, three different coordinates are used in this paper. These are potential temperature θ, potential temperature above the local tropopause $\Delta\theta$ and finally a coordinate we refer to as θ^*, which is calculated by adding the potential temperature of the mean tropopause to $\Delta\theta$. We used the dynamical tropopause, defined by a potential vorticity of 2 PVU or by a potential temperature of 380 K in the tropics (see Sect. 2), as a reference surface.

3.1 Mean vertical profiles

All measurements from the individual campaigns have been binned into 10 K potential temperature bins between −40 and 100 K of $\Delta\theta$. For potential temperature binning, the 10 K bins have been chosen ranging from 40 K below the mean tropopause to 100 K above the mean tropopause. In this way, the centres of the $\Delta\theta$ and θ bins are the same relative to the mean tropopause observed during the measurements. The results are presented for the two main VSLS bromine source gases CH_2Br_2 and $CHBr_3$, averaged over equivalent latitude* of 40–60° N in Fig. 4 for PGS (northern hemispheric winter) and the WISE_TACTS combined dataset (late summer to fall, Northern Hemisphere). Results for the minor VSLS and total organic bromine are shown in Figs. S2 and S3. Only bins which contain at least five data points have been included in the analysis. The results are also summarized in Tables 3 and 4 for the same latitude intervals for all species and for total organic bromine derived from the five brominated VSLS. The tropopause mole fractions shown in Ta-

bles 3 and 4 have been derived as the average of all values in that latitude interval and within 10 K below the tropopause. The potential temperature of the average tropopause has been used for θ averaging, while the potential temperature difference to the local tropopause has been used as reference when averaging in $\Delta\theta$ coordinates. Due to this different sampling, a higher range in $\Delta\theta$ is achieved than in θ, as the actual tropopause altitude varies. We have checked the validity of using means to represent the data, by comparing means and medians. Differences were always below 5 % of the mean tropopause mixing ratios. We have thus chosen to use means throughout this paper. The uncertainties given in all figures are 1σ standard deviations of these means, both for the vertical and horizontal error bars. In the WISE_TACTS dataset, total organic bromine at the dynamical tropopause between 40 and 60° N was 4.05 and 3.5 ppt, using $\Delta\theta$ and θ as vertical coordinates, respectively. Higher mixing ratios of total organic bromine were found during the winter campaign PGS, when average tropopause mixing ratios were 5.2 and 4.9 ppt both using $\Delta\theta$ and θ as vertical coordinates. These mixing ratios are considerably higher than the tropical tropopause values of organic bromine derived in the vicinity of the tropical tropopause (Engel and Rigby, 2018) as will be discussed in detail below. When using the WMO definition of the tropopause, the total organic bromine at mid latitudes was lower by up to 0.5 ppt than using the PV tropopause, reflecting the fact that the WMO tropopause is usually slightly higher than the dynamical tropopause using the 2 PVU definition (e.g. Gettelman et al., 2011).

$CHBr_3$ showed the largest vertical gradients of all species discussed here, followed by $CHBr_2Cl$. This is well in line with their atmospheric lifetimes (see Table 1), which will generally decrease with an increase in bromine atoms in the molecule and is shortest for $CHBr_3$, followed by $CHBr_2Cl$. The relationship between lifetime and vertical gradient is less clear for the longer-lived species, where vertical profiles are expected to be more influenced by transport. In particular, the vertical gradient of $CHBrCl_2$ is closer to the vertical gradient of CH_2Br_2 than to that of $CHBr_2Cl$, although the lifetime should be closer to $CHBr_2Cl$. This could be related to the way that $CHBrCl_2$ is derived, as it is not chromatographically separated from CH2Br2 (see Sect. 2.1 and Sala et al., 2014). The strongest vertical gradients with respect to both θ and $\Delta\theta$ were observed during the winter campaign PGS, with the exception of $CHBr_3$, which was nearly completely depleted for all campaigns at 40 K above the tropopause and thus shows very similar averaged gradients over this potential temperature region. When evaluated only for the first 20 K above the tropopause, the gradient of $CHBr_3$ was also much larger during PGS then during WISE and TACTS. The short lifetime and strong vertical gradient of $CHBr_3$ is also reflected in the largest relative variability (see Tables 3 and 4).

We further determined the variability of the different species in 10 K intervals of θ and $\Delta\theta$. For all campaigns, the variability averaged over the four lowest stratospheric bins when using $\Delta\theta$ was always lower than in the four lowest bins above the climatological tropopause using θ as a coordinate (see Tables 3 and 4). This shows that using the tropopause-centred coordinate system $\Delta\theta$ reduces the variability in the stratosphere, and it is therefore the best suited coordinate system to derive typical distributions. In the troposphere, the variability is larger when using $\Delta\theta$ coordinates than for θ, indicating that the variability in the free troposphere is not influenced by the potential temperature of the tropopause. The observed variabilities were found to be very similar for the WMO and PV tropopause definitions (not shown). As the dynamical PV tropopause is generally expected to be better suited for tracer studies, we decided to reference all data to the dynamical tropopause.

3.2 Latitude–altitude cross sections

We slightly diverge from the coordinate system used to present zonal mean latitude–altitude distributions used in previous work (e.g. Bönisch et al., 2011; Engel et al., 2006), where equivalent latitude and potential temperature were used as horizontal and vertical coordinates. We use equivalent latitude* as a horizontal coordinate, i.e. latitude for all tropospheric observations and equivalent latitude for observations at or above the tropopause. As a vertical coordinate we have chosen to use a modified potential temperature coordinate θ^* (see explanation above, Sect. 3). In this way, all measurements are presented relative to a climatological tropopause, which has been derived from ERA-Interim reanalysis as zonal mean for the latitude of interest and the specific months of the campaign (see Sect. 2 for campaign details). This is expected to reduce variability by applying the information from $\Delta\theta$, yet the absolute vertical information is also maintained. In order to ensure that this tropopause value is representative also of the period of our observations, we compare the potential temperature of the campaign-based tropopause with the climatological tropopause. The campaign-based tropopause has been calculated by averaging the tropopause at all locations for which observations are available during the campaign. For the latitude band between 40 and 60° N, the climatological PV tropopause for the TACTS_WISE time period was derived to be at 329 K, in excellent agreement with the campaign-based tropopause, which was also at 329 K. For the PGS campaign, both the climatological tropopause and the campaign-based tropopause were found to be at 312 K. In contrast to the campaign-based tropopause, the climatological tropopause is also available for latitude bands and longitudes not covered by our observations and will be more representative of typical conditions during the respective season and latitude.

Figure 5 shows the distributions of the two main VSLS bromine source gases, CH_2Br_2 and $CHBr_3$, in the coordinate system discussed above for the two campaign seasons (PGS: winter; WISE_TACTS: late summer to early fall). The

Table 3. Averaged mole fractions (parts per trillion, ppt; 10^{-12}) and vertical gradients of brominated very-short-lived substances from the combined WISE and TACTS dataset, representative of 40–60° N during late summer to early fall (data from late August to October). Data have been averaged using potential temperature, θ, and potential temperature difference to the tropopause, $\Delta\theta$, as vertical profile coordinates. Tropopause (TP) mixing ratios are from the 10 K bin below the dynamical tropopause (see text for details). The 10 K bin standard deviations in the table represent the variability averaged over the four lowest stratospheric bins. The average potential temperature of the tropopause during the WISE and TACTS campaigns has been calculated from the European Centre for Medium-Range Weather Forecasts data at the locations of our measurements.

WISE and TACTS	θ				$\Delta\theta$			
	Mole fraction (ppt)		Gradient	10 K bin σ (TP − TP + 40 K)	Mole fraction (ppt)		Gradient	10 K bin σ (TP − TP + 40 K)
	TP	TP + (30–40 K)	(% K^{-1})	(ppt)	TP	TP + (30–40 K)	(% K^{-1})	(ppt)
CH_2Br_2	0.79 ± 0.07	0.67 ± 0.15	0.39	0.12	0.83 ± 0.08	0.59 ± 0.09	0.74	0.09
$CHBr_3$	0.45 ± 0.18	0.26 ± 0.28	1.08	0.20	0.56 ± 0.26	0.11 ± 0.05	1.99	0.11
CH_2BrCl	0.18 ± 0.1	0.17 ± 0.08	0.08	0.1	0.23 ± 0.11	0.15 ± 0.07	0.8	0.1
$CHBrCl_2$	0.16 ± 0.03	0.13 ± 0.03	0.48	0.03	0.16 ± 0.02	0.12 ± 0.02	0.73	0.02
$CHBr_2Cl$	0.12 ± 0.03	0.09 ± 0.04	0.74	0.04	0.13 ± 0.03	0.06 ± 0.02	1.28	0.03
Total Br	3.52 ± 0.73	2.48 ± 1.18	0.73	0.83	3.99 ± 1.15	1.89 ± 0.42	1.31	0.50

Table 4. Averaged mole fractions and vertical gradients of brominated VSLS during the PGS campaign. Data have been averaged using potential temperature, θ, and potential temperature difference to the tropopause, $\Delta\theta$, as vertical profile coordinates. Tropopause (TP) mixing ratios are from the 10 K bin below the dynamical tropopause (see text for details). The 10 K bin standard deviations in the table represent the variability averaged over the four lowest stratospheric bins. The average potential temperature of the tropopause during the PGS campaign has been calculated from ECMWF data at the locations of our measurements.

PGS	θ				$\Delta\theta$			
	Mole fraction (ppt)		Gradient	10 K bin σ	Mole fraction (ppt)		Gradient	10 K bin σ
	TP	TP + (30–40 K)	(% K^{-1})	(ppt)	TP	TP + 40 K	(% K^{-1})	(ppt)
CH_2Br_2	1.08 ± 0.08	0.50 ± 0.09	1.34	0.18	1.09 ± 0.13	0.53 ± 0.09	1.28	0.11
$CHBr_3$	0.66 ± 0.12	0.07 ± 0.04	2.22	0.26	0.75 ± 0.3	0.07 ± 0.03	2.26	0.13
CH_2BrCl	0.25 ± 0.03	0.13 ± 0.02	1.16	0.05	0.26 ± 0.05	0.14 ± 0.02	1.14	0.03
$CHBrCl_2$	0.20 ± 0.01	0.09 ± 0.02	1.35	0.03	0.20 ± 0.02	0.10 ± 0.02	1.29	0.02
$CHBr_2Cl$	0.16 ± 0.02	0.04 ± 0.01	1.89	0.04	0.16 ± 0.04	0.04 ± 0.01	1.86	0.03
Total Br	4.91 ± 0.54	1.53 ± 0.34	1.72	1.28	5.20 ± 1.25	1.60 ± 0.33	1.73	0.70

data have been binned in 5° latitude and 5 K intervals of the modified potential temperature coordinate θ^*. As expected, the distributions closely follow the tropopause (indicated by the dashed line), with mixing ratios decreasing with distance to the tropopause and also with increasing equivalent latitude. The distributions observed during the WISE and the TACTS campaigns show rather high levels of CH_2Br_2 in the lower stratosphere, with a depletion of only about 35 % at 40–50 K above the tropopause. This is consistent with the rather long lifetime of CH_2Br_2 in the cold upper troposphere and lower stratosphere (Hossaini et al., 2010). The shorter-lived $CHBr_3$ is depleted by about 85 % already at 20–30 K above the tropopause during the winter campaign PGS. In the case of the winter campaign PGS, mixing ratios close to zero at the highest flight altitudes are also observed for the longer-lived CH_2Br_2, indicating that in the most stratospheric air masses observed during PGS nearly all bromine from VSLS has been converted to inorganic bromine. This stratospheric character is in agreement with the observation of air masses with very high mean age of air derived from SF_6 observations of GhOST-MS (see Fig. 3), reaching up to 5 years for the oldest air (not shown). This is air which has descended inside the polar vortex and has not been in contact with tropospheric sources for a long time, allowing even the longer-lived CH_2Br_2 to be nearly completely depleted.

3.3 Upper tropospheric latitudinal gradients

If air is transported into the lowermost stratosphere via exchange with the extratropical upper troposphere, the levels of organic bromine compounds are likely to be different than for air being transported into the stratosphere via the tropical tropopause. In order to investigate the variability and the gradient in the upper tropospheric input region, we binned our data according to latitude and to potential tem-

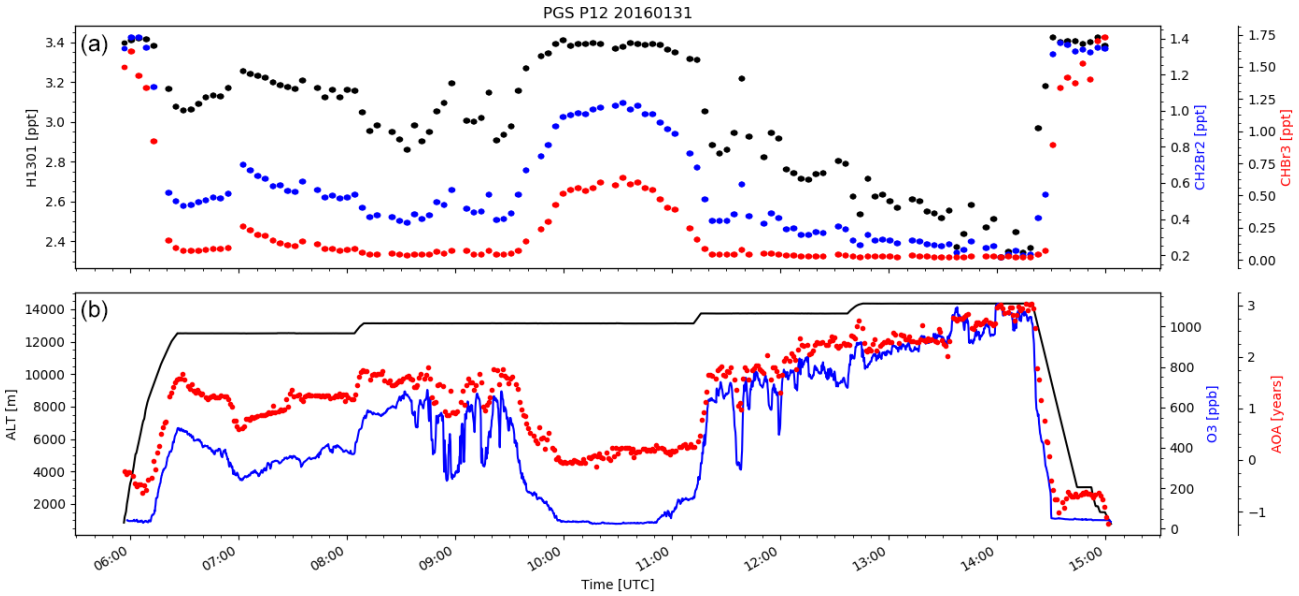

Figure 3. Example of data gathered during a single flight of HALO during the PGS campaign. The flight PGS 12 started on 31 January 2016 from Kiruna in northern Sweden. Panel **(a)** shows measurements of the long-lived brominated source gas halon 1301 (CF_3Br) and the short-lived source gases CH_2Br_2 and $CHBr_3$, all measured with the GhOST-MS. Panel **(b)** shows flight altitude, ozone (parts per billion, ppb; 10^{-9}; measured by the FAIRO instrument; Zahn et al., 2012) and mean age of air derived from SF_6 measurements from the ECD channel of the GhOST-MS (1 min time resolution; see Bönisch et al., 2009, for a description of the measurement technique). An air mass with low ozone and also low mean age of air was observed during the middle of the flight between about 10:00 and 11:00 UTC. High mixing ratios of all three source gases are found in this region, as well as during take-off and landing of the aircraft. $CHBr_3$ mixing ratios are close to detection limit when flying in aged stratospheric air masses, indicating a complete conversion of the bromine to its inorganic form.

perature difference to the tropopause. All data in a range of 10 K below the local dynamical tropopause have been averaged to characterize the upper tropospheric input region. For these upper tropospheric data, standard latitude has been chosen and not equivalent latitude as for the stratospheric data. The latitudinal gradients are shown in Fig. 6 for CH_2Br_2, $CHBr_3$ and total organic bromine derived from the sum of all VSLS (including the mixed bromochlorocarbons CH_2BrCl, $CHBrCl_2$ and $CHBr_2Cl$), each weighted by the number of bromine atoms. For the tropical tropopause, input mixing ratios from different measurement campaigns have recently been reviewed by Engel and Rigby (2018). They found that total organic bromine from these five compounds averaged between 375 and 385 K; i.e. around the tropical tropopause it was 2.2 (0.8–4.2) ppt and in the upper tropical tropopause layer (TTL) (365–375 K potential temperature) it was around 2.8 (1.2–4.6) ppt. These upper TTL mixing ratios have also been included as reference in Fig. 6 (see also Table 5). The average mixing ratios derived here for the 10 K interval below the extratropical tropopause are larger. For data in the late summer to early fall from TACTS and WISE (Table 3), they increase from 2.6 ppt around 30° N (20–40° N equivalent latitude*) to 3.8 ppt around 50° N (40–60° N equivalent latitude*), while no further increase is found for higher latitudes with a total organic bromine mixing ratio of 3.4 ppt. For the winter measurements during PGS (Table 4), a clear increase with latitude is observed from 3.3 ppt around 30° N (20–40° N equivalent latitude*) via 3.8 ppt around 50° N (40–60° N equivalent latitude*) to 5.5 ppt in the high latitudes (60–80° N equivalent latitude*). There is considerable variability in these values derived in the upper troposphere, due to the short lifetime of these compounds and the high variability in emissions depending on the source region. Nevertheless, there is a clear tendency for an increase in tropopause mixing ratios with latitude, particularly during northern hemispheric winter. This is most probably related to the increase in lifetime with latitude, as especially during the wintertime PGS campaign the photolytical breakdown in higher latitudes is slower than in lower latitudes. Additional effects due to the sources and their latitudinal, seasonal and regional variability cannot be excluded. However, we note that emissions are most likely to be largest during summer, as shown in Hossaini et al. (2013), which would not explain the large mixing ratios of brominated VSLS in the upper troposphere in high latitudes during winter.

4 Comparison with model-derived distributions

As bromocarbons are an important source of stratospheric bromine, it is worthwhile to investigate if current models can reproduce the observed distributions shown in Sect. 3. This is a prerequisite to realistically simulate the input of bromine

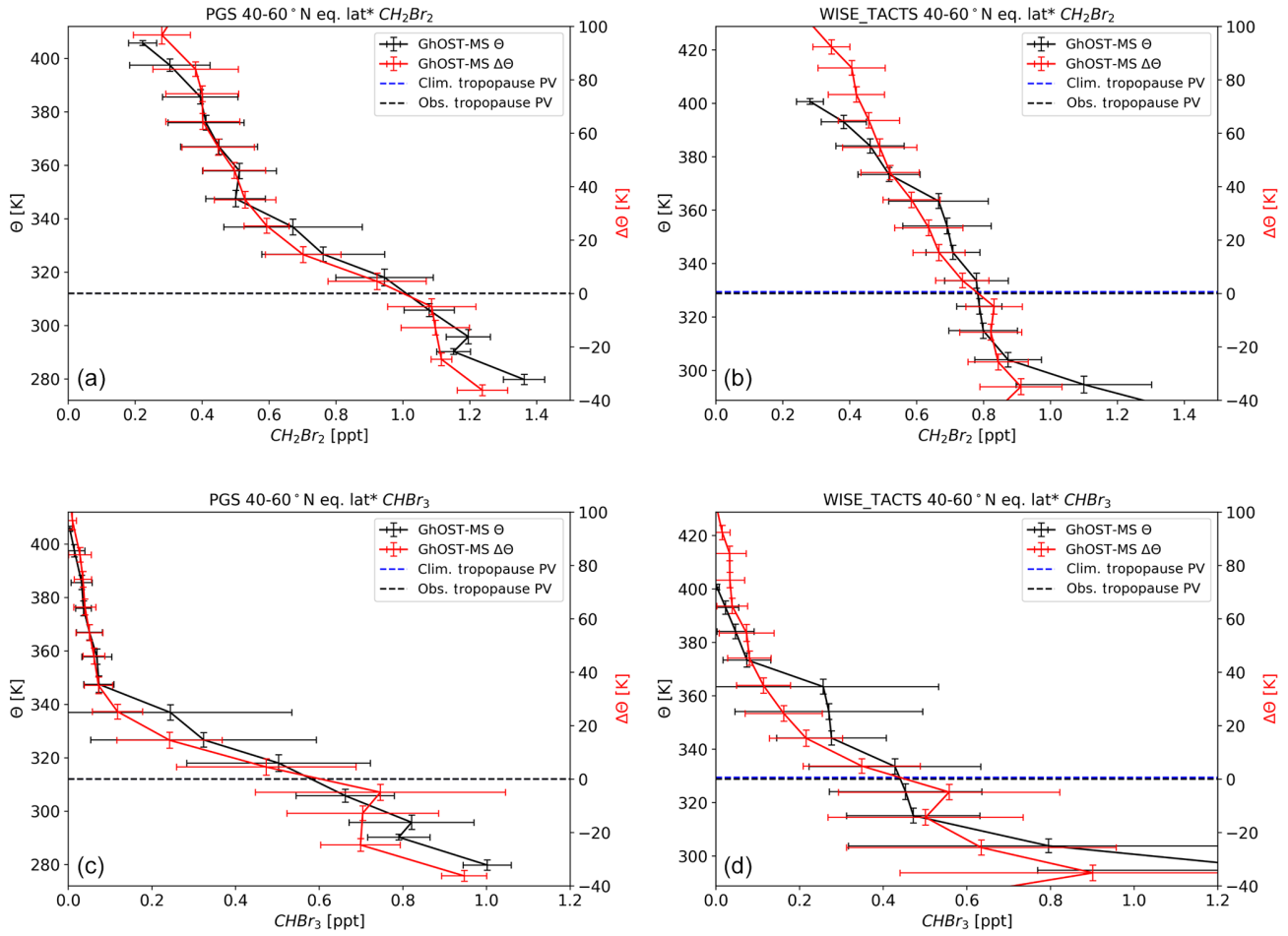

Figure 4. Vertical profiles of CH_2Br_2 **(a, b)** and $CHBr_3$ **(c, d)** averaged over 40–60° of equivalent latitude* and all flights during the PGS campaign (**a, c**, late December 2015 to March 2016) and from the merged dataset from the TACTS and WISE campaigns (**b, d**, representative of late summer to fall). The data are displayed as a function of potential temperature and potential temperature above the tropopause. The dashed blue line shows the zonal mean dynamical tropopause derived from ERA-Interim during September and October of the respective years in the Northern Hemisphere between 40 and 60° latitude, while the dashed black line is the average dynamical tropopause derived for the times and locations of our observations. Both vertical and horizontal error bars denote 1σ variability.

Table 5. Mixing ratios of organic VSLS bromine in air at the tropical, and respectively extratropical (40–60° N), tropopause ($Br_{org}^{ex\text{-}trop}$ and Br_{org}^{trop}) used in the calculation of inorganic bromine (Br_y) for the observation (OBS), and respectively the models, using the emission scenarios of Liang et al. (2010), Ordóñez et al. (2012), Ziska et al. (2013) and Warwick et al. (2006). For the Warwick et al. (2006) scenario, the data have been derived from the EMAC model, while for the other scenarios the TOMCAT model has been used. For the tropics, annual average for the years 2012 to 2016 have been calculated between 10° N and 10° S in a potential temperature range from 365 to 375 K. The tropical mixing ratios for the observations are from the observations compiled in the 2018 WMO report (Engel and Rigby, 2018) in the tropics between 365 and 375 K potential temperature. All data presented are shown in parts per trillion.

	Tropics			Extratropics WISE and TATS			Extratropics PGS		
	CH_2Br_2	$CHBr_3$	TOT	CH_2Br_2	$CHBr_3$	TOT	CH_2Br_2	$CHBr_3$	TOT
OBS	0.73	0.28	2.80	0.83	0.56	3.99	1.09	0.75	5.20
LIANG	0.82	0.26	3.06	0.70	0.32	2.84	0.99	1.00	5.73
ORDONEZ	0.91	0.28	3.30	0.79	0.44	3.27	1.10	1.21	6.58
ZISKA	1.13	0.10	3.18	0.87	0.18	2.77	1.13	0.69	5.10
WARWICK	1.28	0.84	5.48	0.83	0.37	3.07	1.16	0.62	4.59

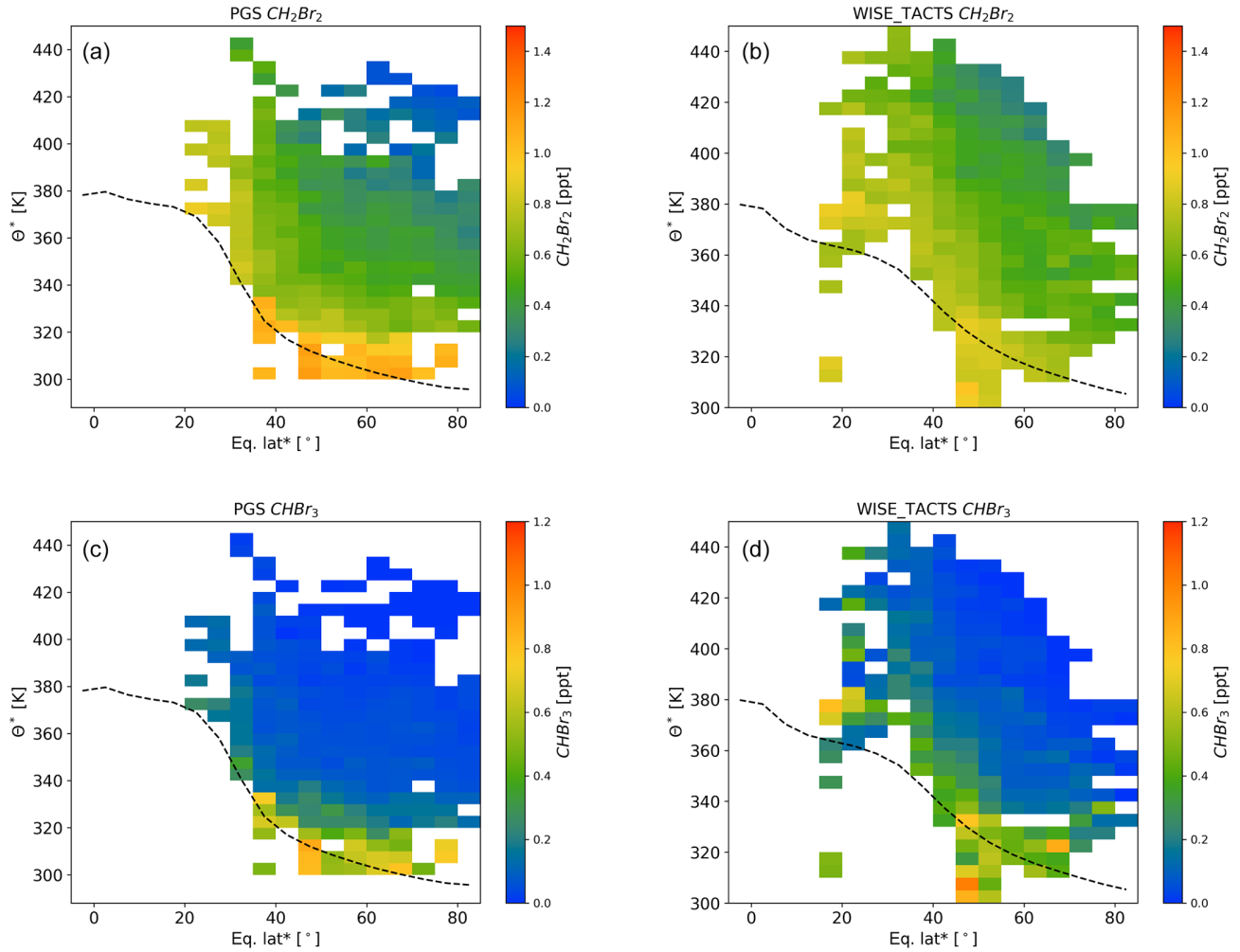

Figure 5. Altitude–latitude cross sections of CH_2Br_2 **(a, b)** and $CHBr_3$ **(c, d)** compiled from all flights during the PGS campaign from late December 2015 to March 2016 **(a, c)** and the TACTS WISE campaigns representative of conditions in late summer to early fall **(b, d)**. The data are displayed as a function of θ^* (see description in Sect. 2) and equivalent latitude*. The dynamical tropopause (dashed line) has been derived from the ERA-Interim reanalysis, providing a climatological mean zonal mean value of the tropopause.

from VSLS source gases to the stratosphere and also the further chemical breakdown and the transport processes related to the propagation of these gases in the stratosphere. As explained in Sect. 2, we used two different models with different emission scenarios for the brominated very-short-lived source gases. The ESCiMo simulation results from the chemistry climate model EMAC (Jöckel et al., 2016) are based on the emission scenario by Warwick et al. (2006), while the TOMCAT model (Hossaini et al., 2013) was run with three different emission scenarios (Ordóñez et al., 2012; Ziska et al., 2013; Liang et al., 2010). Both models have been used in the past to investigate the effect of brominated VSLS on the stratosphere (e.g. Sinnhuber and Meul, 2015; Hossaini et al., 2012, 2015; Wales et al., 2018; Graf, 2017). For the EMAC model, we have chosen to use results from a so-called "specified dynamics" simulation, which has been extended from the ESCiMo simulations to cover our campaign time period (see Sect. 2). The model data have been extracted for the time period and latitude ranges of the observations and have been zonally averaged. Here we compare vertical profiles, latitude–altitude cross sections and latitudinal gradients between our observations and the model results in a similar way as the observations have been presented in Sect. 3. We also compare results for total organic bromine. Only the scenarios of Warwick et al. (2006) and Ordóñez et al. (2012) contain emissions of the mixed bromochlorocarbons CH_2BrCl, $CHBrCl_2$ and $CHBr_2Cl$. For the calculation of total VSLS organic bromine, based on the emission scenarios by Liang et al. (2010) and Ziska et al. (2013), we have adopted the results from the TOMCAT model using the emissions by Ordóñez et al. (2012). The contribution from these mixed bromochlorocarbons to total VSLS organic bromine is typically on the order of 20 %, while about 80 % of total VSLS organic bromine in the upper troposphere and lower stratosphere is due to

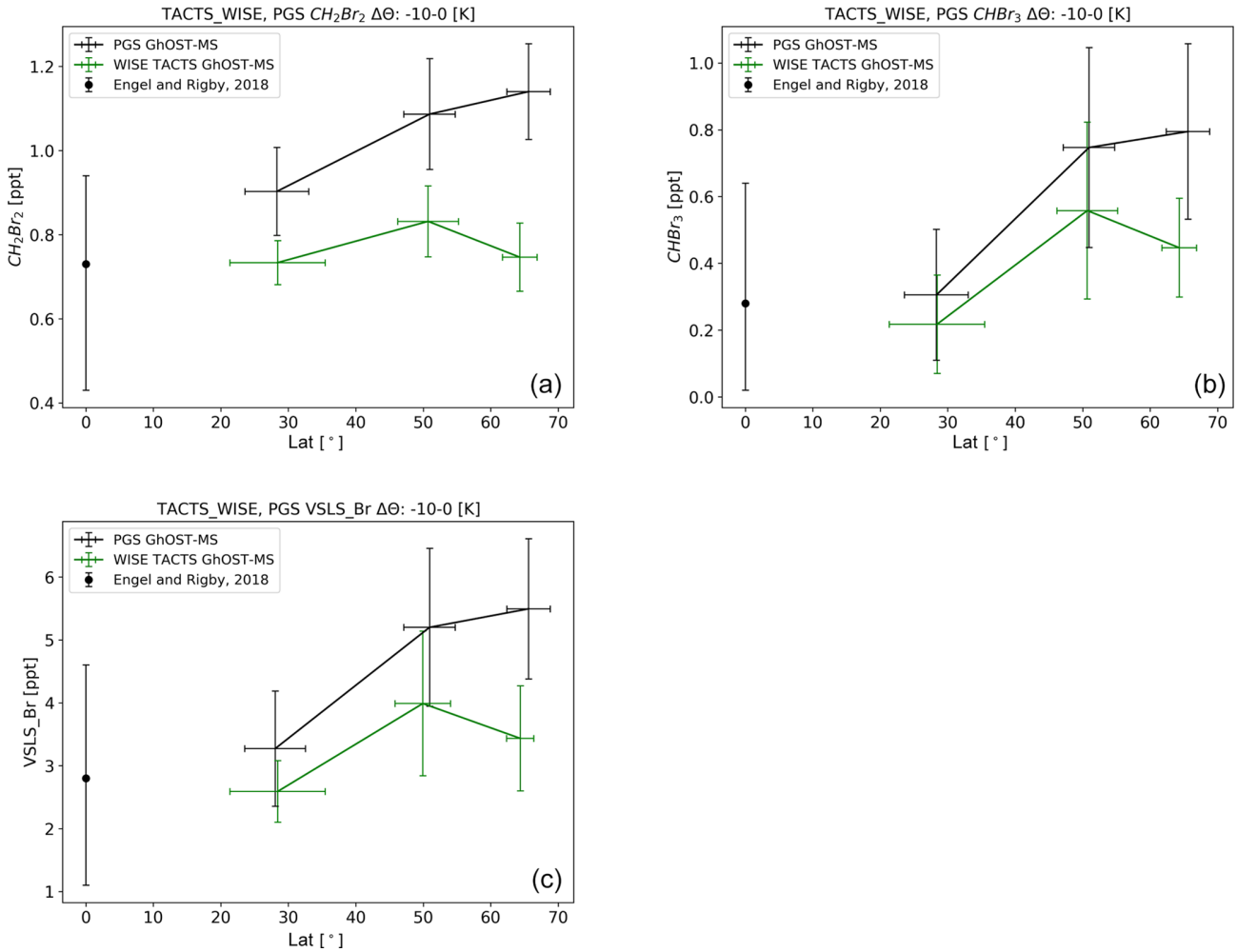

Figure 6. Latitudinal cross section of CH_2Br_2 **(a)**, $CHBr_3$ **(b)** and total organic VSLS bromine **(c)** for all three campaigns, binned by latitude and averaged within 10 K below the local dynamical tropopause. Also included are the reference mixing ratios for the tropical tropopause (Engel and Rigby, 2018).

CH_2Br_2 and $CHBr_3$. This relative contribution of 20 % from minor VSLS is found in our observations (Tables 3 and 4) as well as in the values compiled in Engel and Rigby (2018) (see Table 5), and it is slightly larger than that derived, for example, in Fernandez et al. (2014).

4.1 Mean vertical profiles

Observed vertical profiles are available up to the maximum flight altitude of HALO, which is about 15 km, corresponding to about 400 K in potential temperature. Due to the variability of the tropopause potential temperature, this translates into a maximum of about 100 K for $\Delta\theta$. The emphasis of this section is on the mid latitudes of the Northern Hemisphere, i.e. between 40 and 60° equivalent latitude*. All comparisons are shown as a function of $\Delta\theta$. As no direct tropopause information was available for the TOMCAT output, we have chosen to derive $\Delta\theta$ for this comparison from the difference between model potential temperature and the potential temperature of the climatological zonal mean tropopause, which has been derived as explained in Sect. 2. As we are comparing our observations to the models in tropopause relative coordinates, we have also compared this climatological tropopause with the tropopause derived from the EMAC model results for the time of our campaigns. The potential temperature of the EMAC tropopause and the climatological tropopause differed by less than 3 K for all campaigns at mid latitudes.

Figure 7 presents the model–measurement comparisons for the two main VSLS bromine source gases for the winter PGS campaign and for the combined dataset from WISE and TACTS. A similar figure for the minor VSLS is shown in the Supplement (Fig. S4). Overall the Liang et al. (2010) and the Ordoñez et al. (2012) emission scenarios give the best agreement with our observations of CH_2Br_2. The averaged deviation is 0.1 ppt or less, averaged over all campaigns and all stratospheric measurements in the 40–60° N equivalent lati-

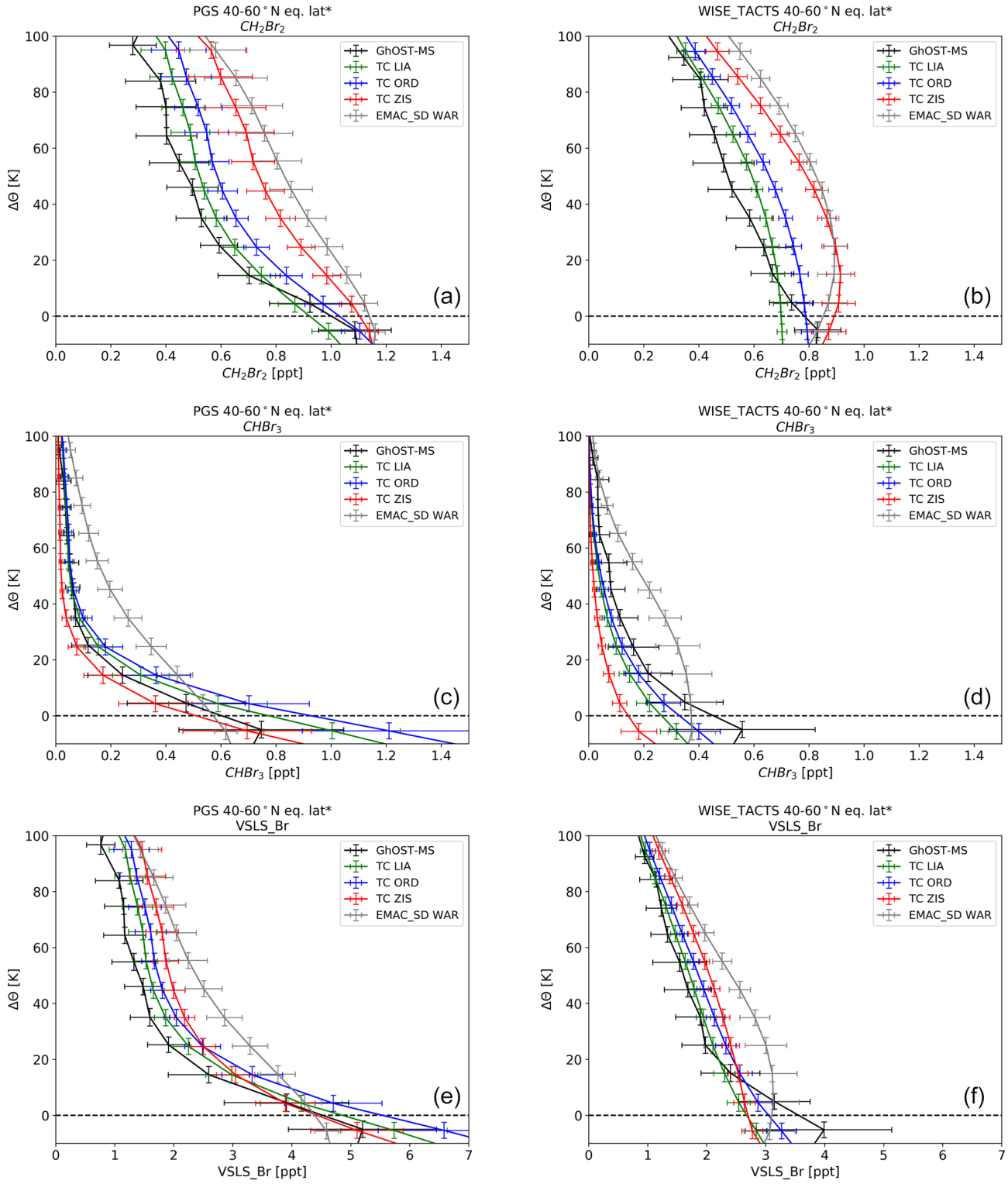

Figure 7. Vertical profiles of CH_2Br_2 **(a, b)**, $CHBr_3$ **(c, d)** and total organic VSLS bromine **(e, f)** averaged over 40–60° of equivalent latitude* and all flights during the PGS campaign from late December 2015 to March 2016 (left-hand side) and from the combined WISE_TACTS dataset, representative of conditions in late summer to fall. Also shown are model results from the TOMCAT and EMAC model using different emission scenarios (see text for details). The data are displayed as a function of potential temperature above the dynamical tropopause. In the case when no model information on the tropopause altitude was available (TOMCAT), climatological tropopause values have been used (see text for details).

tude band, corresponding to a mean absolute percentage difference (MAPD) on the order of 10 %–25 %. Using the Ziska et al. (2013) emissions, CH_2Br_2 is overestimated in the mid-latitude lowest stratosphere during both campaigns by about 0.2 ppt, corresponding to about 40 %–60 % overestimation. The overestimation is even larger with 0.25–0.3 ppt (50 %–70 %) when using the Warwick et al. (2006) emissions in the EMAC model. As $CHBr_3$ is nearly completely depleted in the upper part of the profiles, differences will become negligible there. Therefore, we only compared mixing ratios in the lowest 50 K potential temperature above the tropopause. In this region, the best agreement is again found with the Liang et al. (2010) and Ordoñez et al. (2012) emission scenarios, with mean differences always below 0.1 ppt, corresponding to a MAPD of about 20 %–30 %. Using the Ziska et al. (2013) emission scenario, we find an underestimation on the order of 0.05–0.1 ppt (40 %–70 %), while $CHBr_3$ is overestimated by about 0.15 ppt (120 %–180 %) in the EMAC model based on the Warwick et al. (2006) emission scenario.

Using the Ziska et al. (2013) emission scenario, the overestimation of CH_2Br_2 and the underestimation of $CHBr_3$ tend to cancel out. When adding the contribution from minor VSLS based on the scenario by Ordóñez et al. (2012), this results in a reasonable agreement in total VSLS organic bromine. The EMAC model with the Warwick et al. (2006) emissions substantially overestimates both CH_2Br_2 and $CHBr_3$ in the lowermost stratosphere of the mid latitudes. The vertical profiles of CH_2Br_2 and $CHBr_3$ from the EMAC model with the Warwick et al. (2006) emission scenario is therefore completely different from the observations, showing a maximum around the tropopause or even above.

We additionally compare model data from EMAC simulations using all four emission scenarios (Graf, 2017) in order to investigate if the large deviation of the Warwick et al. (2006) emission scenario is due to the EMAC model or due to the specific emission scenario. These simulations are only available for the time period up to 2011. This comparison for the January–March period (representative for the PGS campaign) is shown in Fig. 8 for CH_2Br_2 and $CHBr_3$. Figure 8 looks qualitatively very similar to the comparisons in Fig. 7; i.e. both CH_2Br_2 and $CHBr_3$ using the Warwick et al. (2006) emission scenario show highest mixing ratios in the lower stratosphere, and $CHBr_3$ shows the least pronounced vertical gradients. Also, the pattern for the Ziska et al. (2013) emission scenario is the same, with the second highest CH_2Br_2 values and lowest $CHBr_3$ values. Differences between the different models are certainly a factor in the explanation of model–observation differences. However, it is clear that the pattern when comparing all scenarios in the EMAC model is similar to that described above and that differences in the emission scenarios are the main driver of model–observation differences.

4.2 Latitude–altitude cross sections

As has been shown in the comparison of the vertical profiles, differences between model results and observations are found, especially in the case of the Ziska et al. (2013) emissions in the TOMCAT model and in the case of the Warwick et al. (2006) emissions in the EMAC model for the northern hemispheric mid latitudes (40–60° N). To visualize these differences, we present latitude–altitude cross sections of the model datasets and the differences to our observations in Figs. 9–12. While we use equivalent latitude* as the latitudinal coordinate for the observations and θ^* as vertical coordinate, the zonal mean data are displayed as a function of latitude and potential temperature, θ, for the model results. The comparison is shown here for the winter dataset from PGS, for which the observational set covers a wide range of latitudes and also reaches very low tracer mole fractions. The comparison for the campaign in late summer to fall (TACTS and WISE) gives a rather similar picture (not shown). The overall best agreement in the vertical profiles has been found for the TOMCAT model using the emission scenarios by Liang et al. (2010) and Ordóñez et al. (2012). The latitude–altitude cross section for these two datasets is shown in Figs. 9 and 10. Using these two emission scenarios, the TOMCAT model tends to overestimate high-latitude tropospheric mole fractions of $CHBr_3$ during this winter campaign. However, the stratospheric distribution is rather well reproduced with absolute deviations to the model mostly being below 0.1 ppt. In the case of CH_2Br_2, overall stratospheric mole fractions are slightly larger in the model results compared to the observations. The deviations between the TOMCAT model using the Ziska et al. (2010) emissions and the EMAC model using the Warwick et al. (2006) emissions are substantially larger. These are shown in Figs. 11 and 12 again for the PGS campaign. As noted above, the TOMCAT model with the Ziska et al. (2013) emissions overestimates stratospheric CH_2Br_2, while stratospheric $CHBr_3$ is reasonably well captured. The largest discrepancies between model and observations are observed in the case of the EMAC model with the Warwick et al. (2006) emissions. In this case, both CH_2Br_2 and $CHBr_3$ are overestimated in the lower stratosphere.

In the case of $CHBr_3$, the two emission scenarios which have a more even distribution of emissions with latitude, i.e. the emission scenarios by Liang et al. (2010) and Ordoñez et al. (2012), show the best agreement with the observations. The emission scenario by Warwick et al. (2006) yields much higher mole fractions in the tropics and has the poorest agreement with measurement data. The emission scenario by Ziska et al. (2013) yields overall much lower $CHBr_3$ in large parts of the atmosphere and seems to be the only set-up in which mid-latitude tropopause mixing ratios of $CHBr_3$ are underestimated in comparison to our observations. For CH_2Br_2, again the Ordoñez et al. (2012) and Liang et al. (2010) emission scenarios in the TOMCAT model show

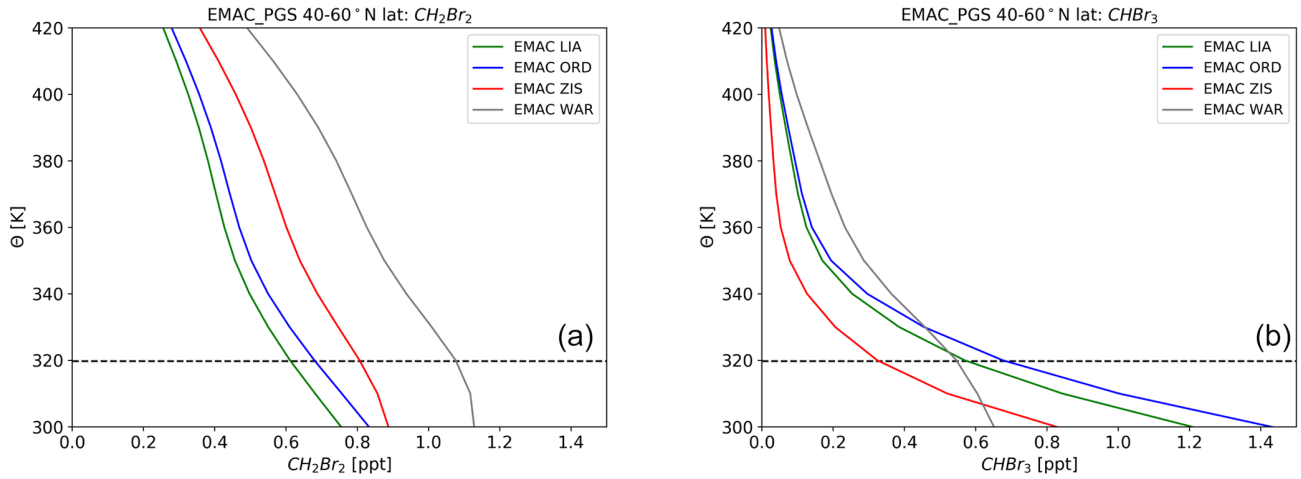

Figure 8. Vertical profiles of CH_2Br_2 **(a)** and $CHBr_3$ **(b)** averaged over 40–60° latitude from four model simulations with the EMAC model using the emission scenarios by Liang et al. (2010), Warwick et al. (2006), Ordóñez et al. (2012) and Ziska et al. (2013). The data have been averaged for the period from January to March, i.e. representative of the time period covered by the PGS campaign. The dashed line represents the model tropopause. Model results are nudged simulations of EMAC but do not cover the time period of our observations.

rather similar distributions and rather good agreement with our observations. In the case of the TOMCAT model with the Ziska emissions, very high mole fractions of CH_2Br_2 are simulated throughout the tropics. Our low-latitude observations from HALO during late summer and fall (WISE and TACTS) and the values compiled in the WMO 2018 report for the tropics (Engel and Rigby, 2018) are lower by about 0.3–0.5 ppt than the mixing ratios of CH_2Br_2 in the tropics using the Warwick et al. (2006) and Ziska et al. (2013) emissions. The latitudinal distribution in the upper troposphere in models and observations is therefore investigated in more detail in the next section.

4.3 Upper tropospheric latitudinal gradients

Knowledge of the input of organic bromine into the stratosphere is crucial in understanding the stratospheric bromine budget and, therefore, also in determining the amount of inorganic bromine available for catalytic reactions involved in ozone depletion. For air masses in the stratosphere above about 400 K, it is generally assumed that the input is nearly exclusively through the tropical tropopause. For the lowermost stratosphere, however, input via the extratropical tropopause is also expected to play an important role (e.g. Holton et al., 1995; Gettelman et al., 2011). In order to investigate if the models are able to represent the latitudinal gradient in upper tropospheric mole fractions, we compare the observed extratropical mole fractions of the brominated VSLS in the upper troposphere (Sect. 3.3) and compiled tropical observations (Engel and Rigby, 2018) with those determined from the different model set-ups. For this purpose, the model data have been averaged in an interval of 10 K below the climatological (TOMCAT), or respectively modelled (EMAC), tropopause. The results are shown for the two main bromine VSLS, CH_2Br_2 and $CHBr_3$, as well as for total VSLS organic bromine in Fig. 13 and Table 5 for the two campaign periods in comparison to observations. Note that for the scenarios by Liang et al. (2010) and Ziska et al. (2013), no estimates of emissions for the mixed bromochlorocarbons are available; instead, we have used the model results based on the Ordóñez et al. (2012) emissions for the calculation of total VSLS organic bromine.

During the two campaigns in late summer to fall (TACTS and WISE), all model set-ups show a decrease of CH_2Br_2 mixing ratios with latitude. Although, the latitudinal gradients are much steeper when the scenarios by Warwick et al. (2006) and Ziska et al. (2013) are used, which is due to overestimated mixing ratios at low latitudes. This is in good agreement with findings by Hossaini et al. (2013), who showed that TOMCAT using the Warwick et al. (2006) emission scenario overestimated HIAPER[1] Pole-to-Pole Observations (HIPPO) in northern hemispheric mid latitudes. An increase in observed mixing ratios with latitude was found, especially during the winter PGS campaign, which is presumably related to the increase in atmospheric lifetime of compounds in the cold and dark high-latitude tropopause region during winter. This feature is qualitatively reproduced by the TOMCAT simulations with Liang et al. (2010) and Ordóñez et al. (2012) scenario, but not for the Ziska et al. (2013) and Warwick et al. (2006) scenario-based results, which show a moderate decrease and no latitudinal gradient. This feature is consistent with emissions in these two scenarios being more strongly biased towards the tropics.

For $CHBr_3$, the observations show an increase with latitude, especially during the PGS campaign. The data in late

[1] high-performance instrumented airborne platform for environmental research

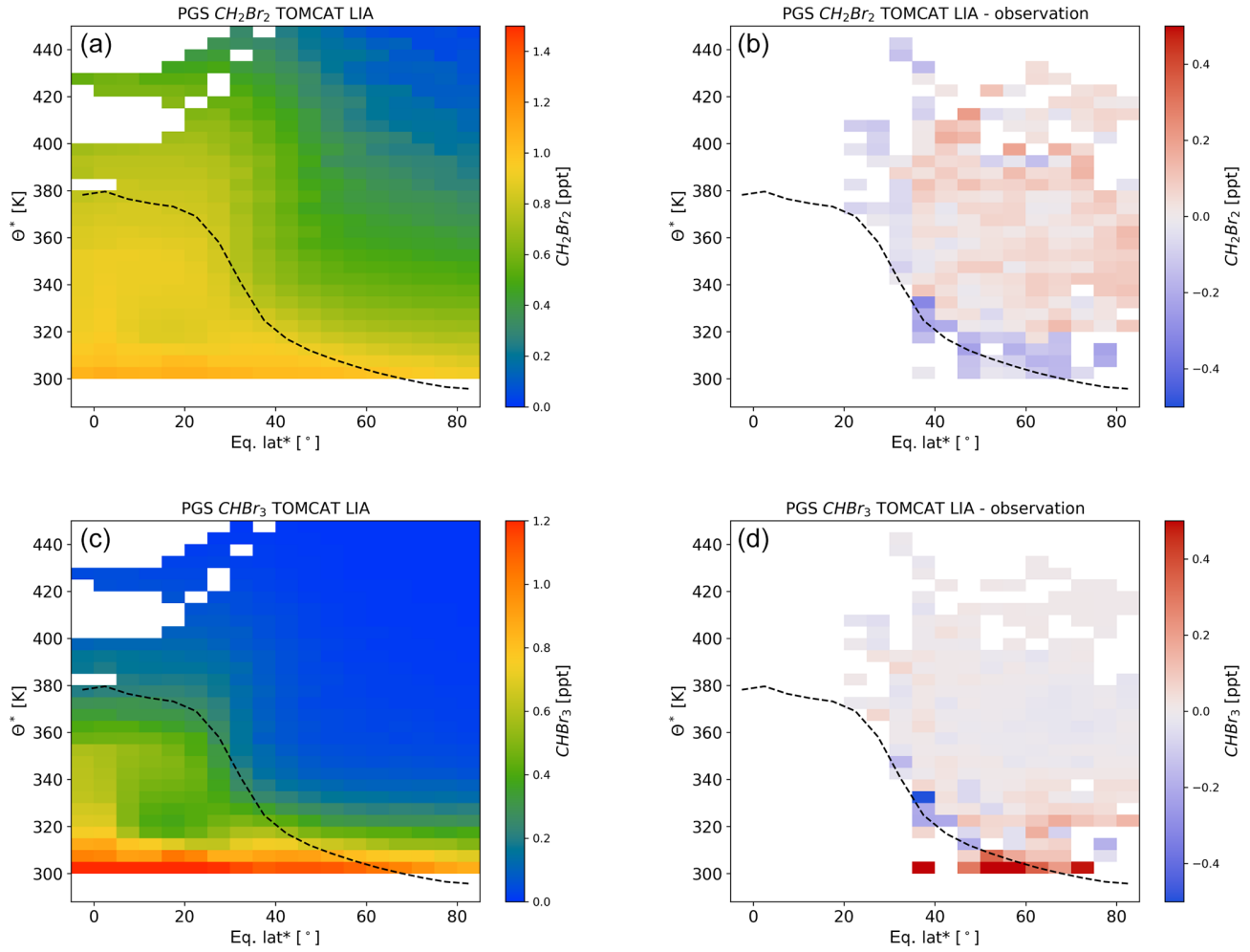

Figure 9. Latitude–altitude cross section of CH_2Br_2 **(a, b)** and $CHBr_3$ **(c, d)** for the TOMCAT model using the Liang et al. (2010) emission scenario **(a, c)** and differences to the observations **(b, d)** for all flights during the PGS campaign from late December 2015 to March 2016. The data are binned using equivalent latitude* and θ^* as coordinates (see text for details). Also shown in the climatological mean tropopause (see text for details; dashed line). Boxes in which, due to the vertical resolution of the model, no values are available are left blank.

summer to fall from TACTS and WISE show a less clear picture, with an increase between the subtropics and mid latitudes but a decrease towards high latitudes. This general tendency during the wintertime is reproduced by the TOMCAT model using all emission scenarios. Nonetheless, the gradient in the EMAC model results with the Warwick et al. (2006) emissions is reversed, which is mainly caused by the larger tropical mixing ratios and also evident from the latitude–altitude cross sections shown before. We also note that the subtropical mixing ratios based on the Ziska et al. (2013) emissions are lower than the observations.

The results for total organic bromine, including the three mixed bromochlorocarbons, can be mainly understood as a combination of the behaviour of CH_2Br_2 and $CHBr_3$. In the case of the TOMCAT model with Ziska et al. (2013) emissions, a certain compensation is observed; i.e. total organic bromine is better reproduced than each compound by itself. This is due to an overestimation of CH_2Br_2, especially at low latitudes, and an underestimation of $CHBr_3$. Total organic bromine from VSLS in the EMAC model using the Warwick et al. (2006) emissions is very different from the observations. It shows nearly constant mixing ratios with latitude during northern hemispheric winter (PGS) and a strong decrease during the period from late summer to fall of the TACTS and WISE campaigns. Most importantly, the overall levels, especially in the low latitudes, are much higher than our observations and also much higher than the tropical observations compiled in the WMO report (Engel and Rigby, 2018). We also note that poleward of 40° N and below 320 K (see Figs. 9 and 10) there is a small negative model bias for CH_2Br_2 at the extratropical tropopause when using the scenarios by Liang et al. (2010) and Ordóñez et al. (2012). At the same time the model simulations using these two scenarios yield a substantial positive bias for $CHBr_3$ in the same

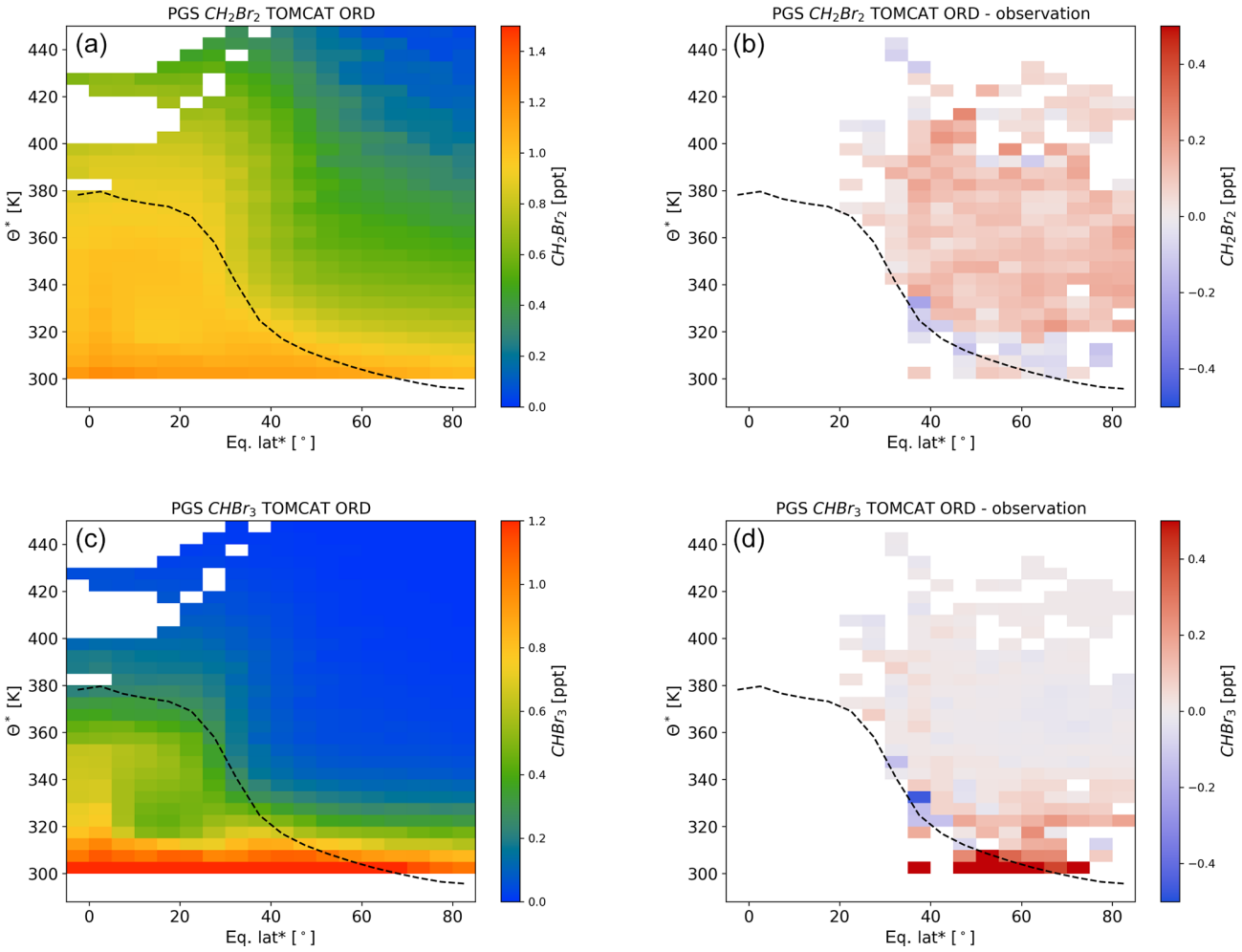

Figure 10. As Fig. 9 but using the Ordóñez et al. (2012) emission scenario.

region. This will result in a misrepresentation of the input of brominated VSLS source gases to the lowermost stratosphere via the different pathways.

5 Implications for stratospheric inorganic bromine

As shown in the previous section, discrepancies exist between the various combinations of models and emission scenarios with respect to our observations, both around the tropopause and in the lower stratosphere. In this section, we will discuss the possible implications for inorganic bromine in the lower and lowermost stratosphere. Inorganic bromine is of key importance, as this is the form of bromine which can influence ozone through, for example, catalytic ozone depletion cycles. Note that this discussion only focuses on the input of bromine in the form of organic source gases (so-called source gas injection, SGI; see Engel and Rigby, 2018) from VSLS. The inorganic bromine from SGI can be derived as the difference between the organic bromine in the source region (tropopause) and the organic bromine still observed or modelled at a certain stratospheric location. The input of bromine into the stratosphere in the inorganic form (product gas injection) is expected to add more bromine in addition to the SGI discussed here. However, PGI cannot be investigated with the source gas measurements used in this study. Here, we focus on assessing what the different mixing ratios of bromine source gases at the tropical and extratropical tropopause in both observations and in model results imply for the total (organic and inorganic) bromine and inorganic bromine content of the lower and lowermost stratosphere.

We have shown in Sects. 3 and 4 that the organic bromine around the tropopause shows significant variability and also latitudinal gradients. In addition, large differences between the different model set-ups and observations are found. As mentioned in the introduction, the air in the extratropical lower and lowermost stratosphere is influenced by transport through the tropical and extratropical tropopause. As both regions show different levels or organic bromine source gases, the relative contribution of these source regions needs to be known to derive total bromine which entered the stratosphere

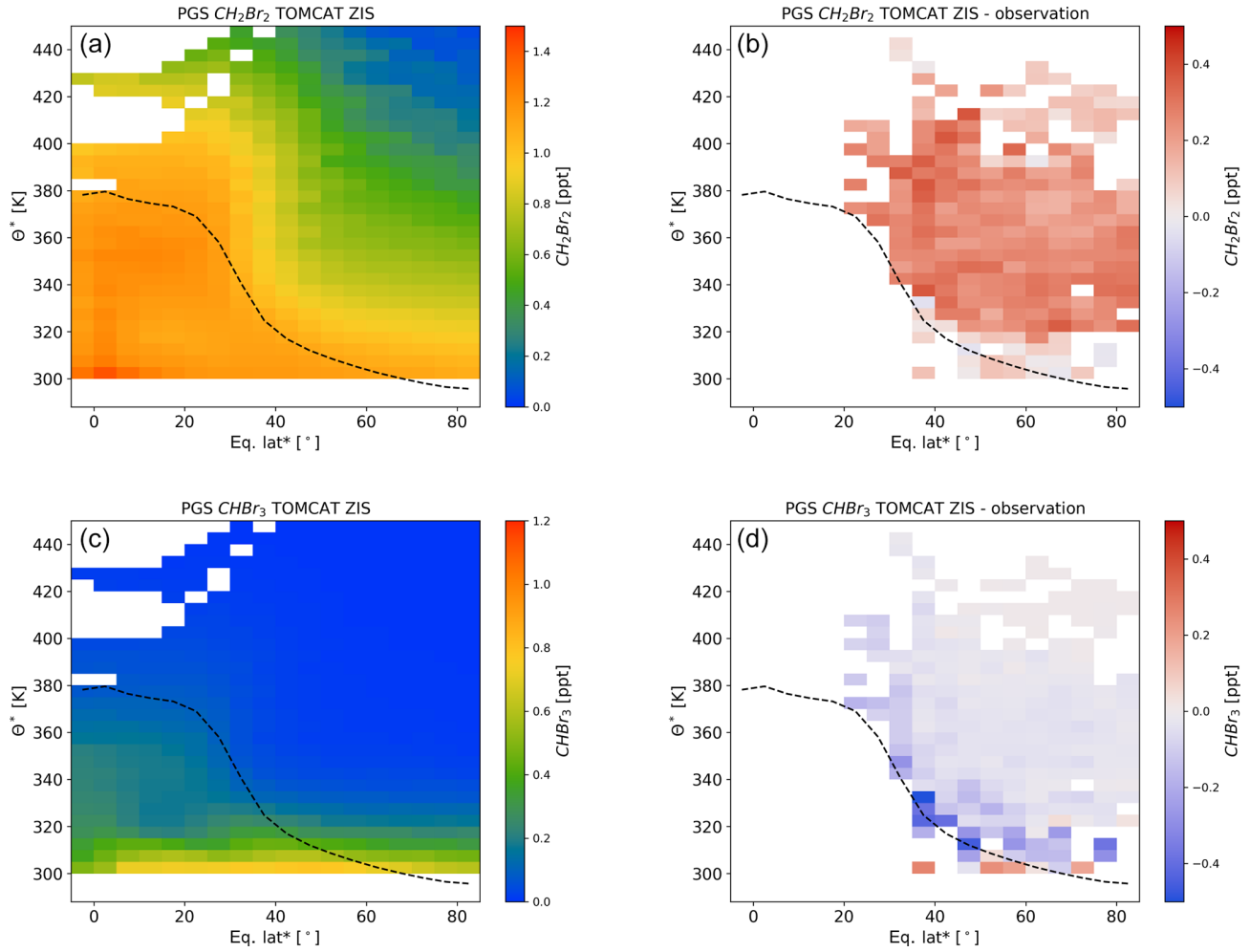

Figure 11. As Figs. 9 and 10 but using the Ziska et al. (2013) emission scenario.

and thus also inorganic bromine from SGI. Several authors have attempted to quantify the relative fractions of air masses from the different source regions based on tracer measurements (e.g. Hoor et al., 2005; Bönisch et al., 2009; Ray et al., 1999; Werner et al., 2010). No studies on mass fractions are available for the campaigns discussed here, so we will rely on previous studies for these fractions as discussed in the introduction to estimate the fractions of tropical and extratropical air in the lowermost stratosphere. The differences in Br_y discussed here should thus be taken as a sensitivity study, and the values derived below can only be considered to be estimates showing how much the inorganic bromine may differ between different model set-ups and observations. In general, air masses close to the extratropical tropopause will be mainly of extratropical origin, while air masses near 400 K will almost be entirely of tropical origin. As a simplified approach, we have therefore chosen to assume that at the extratropical tropopause ($\Delta\theta = 0$), the extratropical fraction is 100 % and that this fraction decreases linearly to 0 % at 100 K above the tropopause. The organic bromine species transported into the stratosphere are chemically or photochemically depleted, and the bromine is transferred to the inorganic form. The total (organic and inorganic) bromine content from VSLS SGI in an air parcel in the lowermost stratosphere at $\Delta\theta$ above the tropopause, $\mathrm{Br}_{\mathrm{tot}}(\Delta\theta)$, is thus the sum of organic, $\mathrm{Br}_{\mathrm{org}}(\Delta\theta)$, and inorganic, $\mathrm{Br}_{\mathrm{inorg}}(\Delta\theta)$, bromine. Inorganic bromine is usually referred to as Br_y.

$$\mathrm{Br}_{\mathrm{tot}}(\Delta\theta) = \mathrm{Br}_y(\Delta\theta) + \mathrm{Br}_{\mathrm{org}}(\Delta\theta) \tag{1}$$

The total bromine can also be described by summing up the organic bromine transported to the stratosphere via input through the tropical and extratropical tropopause.

$$\begin{aligned}\mathrm{Br}_{\mathrm{tot}}(\Delta\theta) = {} & f^{\text{ex-trop}}(\Delta\theta) \cdot \mathrm{Br}_{\mathrm{org}}^{\text{ex-trop}}(\Delta\theta = 0) \\ & + f^{\mathrm{trop}}(\Delta\theta) \cdot \mathrm{Br}_{\mathrm{org}}^{\mathrm{trop}}(\Delta\theta = 0),\end{aligned} \tag{2}$$

where $f^{\text{ex-trop}}$ and f^{trop} are the fractions of air of extratropical and of tropical origin, respectively, and $\mathrm{Br}_{\mathrm{org}}^{\text{ex-trop}}(\Delta\theta = 0)$ and $\mathrm{Br}_{\mathrm{org}}^{\mathrm{trop}}(\Delta\theta = 0)$ are the total organic VSLS bromine

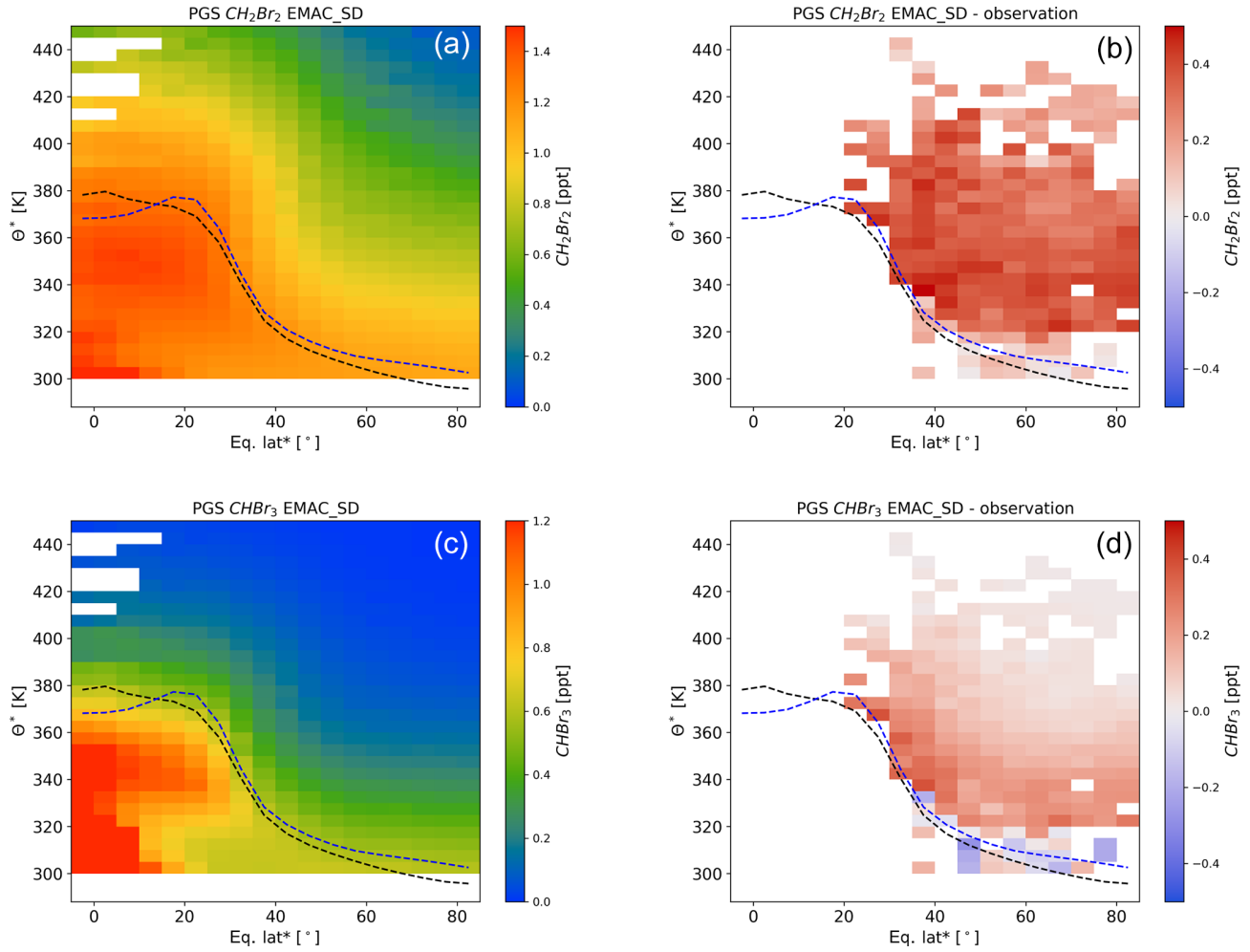

Figure 12. As Figs. 9–11 but for the EMAC model using the Warwick et al. (2006) emission scenario.

contents in air at the extratropical (40–60° N) and tropical tropopause, respectively, i.e. at $\Delta\theta = 0$. For observations only, the extratropical $\mathrm{Br}_{\mathrm{org}}^{\text{ex-trop}}(\Delta\theta = 0)$ is available from our HALO campaigns. $\mathrm{Br}_{\mathrm{org}}^{\text{trop}}(\Delta\theta = 0)$ for the observations is therefore taken from observations at the tropical tropopause compiled in the 2018 WMO ozone assessment (Engel and Rigby, 2018). For the different model set-ups, $\mathrm{Br}_{\mathrm{org}}^{\text{ex-trop}}(\Delta\theta = 0)$ and $\mathrm{Br}_{\mathrm{org}}^{\text{trop}}(\Delta\theta = 0)$ are derived from the global model fields. For the tropical input mixing ratios, the model output has been averaged between 10° S and 10° N in a potential temperature range from 365 to 375 K in a similar way as used for the observations (Engel and Rigby, 2018). Extratropical mixing ratios have been derived by averaging the model results, and respective observations, in a range of 10 K below the tropopause. In order to be consistent between models and observations, extratropical reference mixing ratios are derived for the time of the campaign, while the tropical tropopause mixing ratios are taken as seasonal mean.

Due to mass conservation, the sum of $f^{\text{ex-trop}}$ and f^{trop} must be unity, so we can rewrite Eq. (2) to yield

$$\mathrm{Br}_{\mathrm{tot}}(\Delta\theta) = f^{\text{ex-trop}}(\Delta\theta) \cdot \mathrm{Br}_{\mathrm{org}}^{\text{ex-trop}}(\Delta\theta = 0) + \left(1 - f^{\text{ex-trop}}(\Delta\theta)\right) \cdot \mathrm{Br}_{\mathrm{org}}^{\text{trop}}(\Delta\theta = 0)\,. \quad (3)$$

If we assume that $f^{\text{ex-trop}}$ increases linearly from 0 at $\Delta\theta = 0$ K to 1 at $\Delta\theta = 100$ K, the total bromine from VSLS SGI can be derived and the inorganic bromine, $\mathrm{Br}_y(\Delta\theta)$, is then calculated by combining Eqs. (1) and (3):

$$\mathrm{Br}_y(\Delta\theta) = \left(f^{\text{ex-trop}}(\Delta\theta) \cdot \mathrm{Br}_{\mathrm{org}}^{\text{ex-trop}}(\Delta\theta = 0) + \left(1 - f^{\text{ex-trop}}(\Delta\theta)\right) \cdot \mathrm{Br}_{\mathrm{org}}^{\text{trop}}(\Delta\theta = 0)\right) - \mathrm{Br}_{\mathrm{org}}(\Delta\theta)\,, \quad (4)$$

where $\mathrm{Br}_{\mathrm{org}}(\Delta\theta)$ is the organic bromine measured, and respectively simulated, at $\Delta\theta$ above the tropopause.

Figure 14 compares the vertical profiles of total and inorganic bromine derived in this way from the observa-

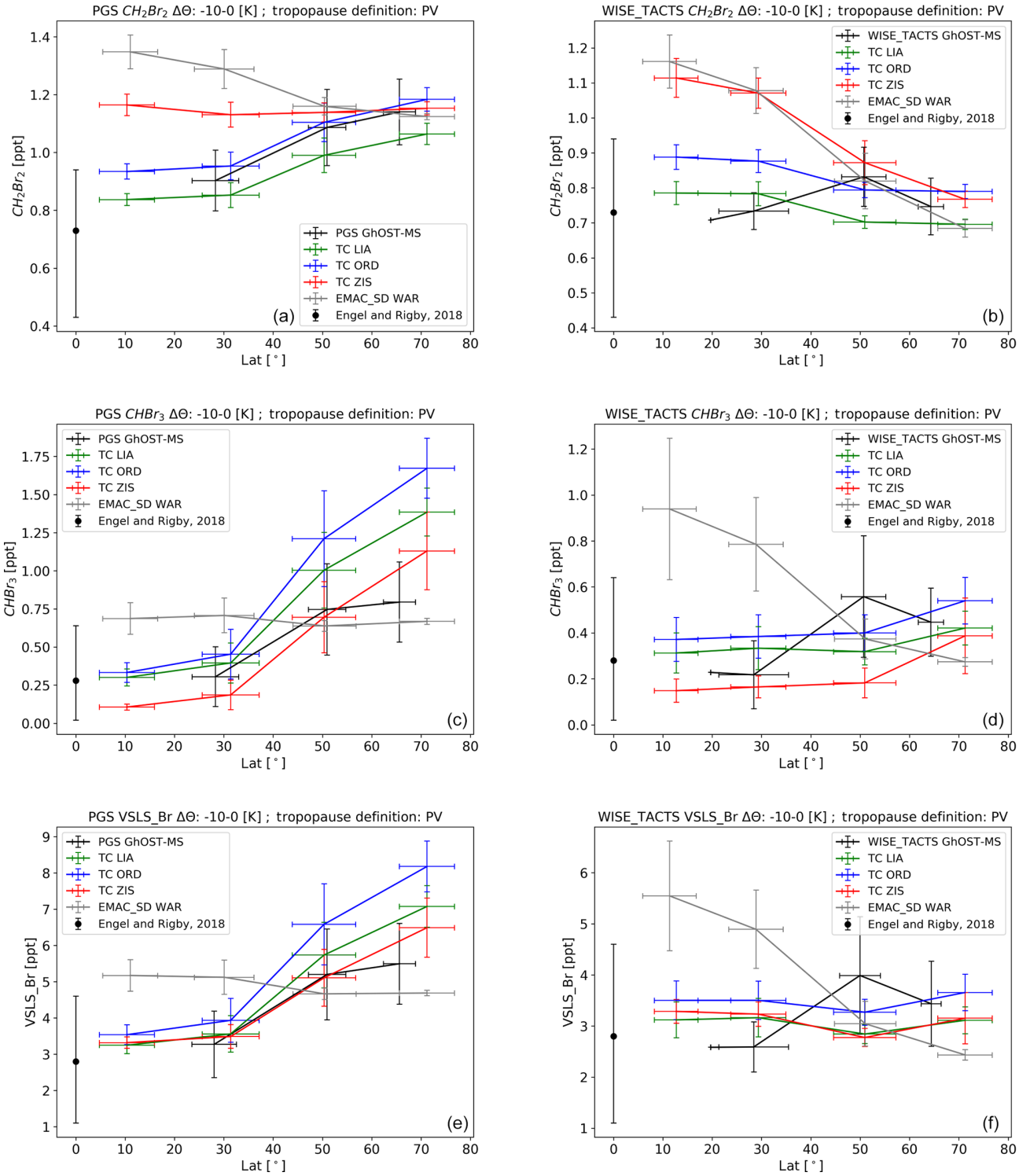

Figure 13. Latitude cross section of tropopause representative mixing ratios of CH_2Br_2 **(a, b)** $CHBr_3$ **(c, d)** and total organic VSLS bromine **(a, b)** for all the measurements from the PGS campaign **(a, c, e)** and WISE_TACTS dataset **(b, d, f)** from observations in comparison to all model emissions scenario combinations. Data are binned by latitude and averaged over 10 K below the tropopause. Due to the different sampling of the observations and the models, the centres of the different latitude bins are not the same for observations and models.

tions and the different model set-ups for the PGS campaign and the combined WISE_TACTS dataset. The values of $Br_{org}^{ex\text{-}trop}(\Delta\theta = 0)$ and $Br_{org}^{trop}(\Delta\theta = 0)$ used for the models, and respectively the observations, are shown in Table 5.

Due to the nature of the set-up for the calculation of the SGI contribution to Br_y described above, both model- and observation-derived Br_y is close to zero at the extratropical tropopause. The assumed fractional contribution of tropical air increases with altitude, and thus the amount of organic bromine assumed at the tropical tropopause becomes more important in the calculation of total bromine and thus also in Br_y. Overall, all model set-ups capture Br_y from CH_2Br_2 rather well. For all campaigns, the Br_y estimate from the observations is smaller than the model calculations above about 60 K above the tropopause and larger below this level. Under the given assumptions about fractional input, the larger Br_y values derived in the model calculations above 60 K are caused by the higher total bromine values from CH_2Br_2, which are caused by the higher CH_2Br_2 levels at the tropical tropopause in comparison to the observations. For the campaigns in late summer to early fall, this difference is largest for the TOMCAT model with the Ziska et al. (2013) emissions and the EMAC model with the Warwick et al. (2006) emissions, consistent with these two model set-ups having the largest CH_2Br_2 mixing ratios at the tropical tropopause (1.13 and 1.28 ppt; see Table 5). Under the given assumptions about fractional input, the discrepancy in the lower part is more due to higher simulated CH_2Br_2 in the lowermost stratosphere than found in the observations. Using the emission scenarios by Liang et al. (2010) and Ordóñez et al. (2012), the differences are usually below 0.3 ppt of Br_y, corresponding to a MAPD of less than 40 %.

Much larger variations are found in the amount of Br_y derived from $CHBr_3$. As can be seen from Fig. 7, the remaining organic bromine in the form of $CHBr_3$ is very small for all three set-ups using the TOMCAT model and the observations already at about 30 to 40 K above the tropopause. The Br_y from $CHBr_3$ (solid lines in Fig. 14) is thus close to the total bromine in the form of $CHBr_3$ (dotted lines in Fig. 14). In contrast, EMAC results using the Warwick et al. (2006) emissions still show substantial amounts of $CHBr_3$ in the organic form even at 50 K above the tropopause and above. For the EMAC set-up, the Br_y derived from $CHBr_3$ is thus influenced by both the assumed input and the remaining organic $CHBr_3$ in the stratosphere. However, the tropical input of $CHBr_3$ in the EMAC model using the Warwick et al. (2006) emissions is very large (0.84 ppt, corresponding to about 2.5 ppt of bromine). Therefore, despite the fact that EMAC still shows substantial remaining $CHBr_3$ rather deep into the lowermost stratosphere, this model set-up overestimates the amount of Br_y due to $CHBr_3$ in comparison to the observations. We find differences of about 1.5 ppt of Br_y at about 100 K above the tropopause, which is about a factor of 3 higher than the mixing ratio derived from the observations. The amount of Br_y from $CHBr_3$ in the different emission scenarios used in TOMCAT is mainly determined by the amount of $CHBr_3$ reaching the stratosphere, and especially for regions with $\Delta\theta$ above 50 K by the tropical input. As the TOMCAT model with the Ziska et al. (2013) emissions underestimates these tropical tropopause mixing ratios, it shows Br_y amounts that are too small from $CHBr_3$ throughout the stratosphere. In contrast, the tropical tropopause mixing ratio of $CHBr_3$ from the Ordóñez et al. (2012) and Liang et al. (2010) scenarios are in better agreement with the observations presented here, and thus Br_y estimates at 100 K above the tropopause are in good agreement with the observation-based estimates.

The total Br_y from VSLS SGI can be understood mainly as an addition of the contributions of CH_2Br_2 and $CHBr_3$, as these are responsible for about 80 % of total VSLS organic bromine. As the differences are largest for $CHBr_3$, this dominates the differences in total Br_y from VSLS SGI. Interestingly, while the Ziska et al. (2013) emissions in TOMCAT showed some significant differences, in particular for $CHBr_3$ at the tropopause, the differences in total Br_y are not as large. The underestimation of Br_y from $CHBr_3$ is partly compensated by an overestimation of Br_y from CH_2Br_2. The EMAC model with the Warwick et al. (2006) emissions overestimates Br_y from both CH_2Br_2 and $CHBr_3$, so that in total a difference in Br_y of more than 2 ppt is derived, corresponding to an overestimation by a factor of more than 2 with respect to observation-derived values. This difference is expected to have a significant effect on ozone chemistry in the lower stratosphere.

The Br_y mixing ratios derived in the approach described above depend on the assumed input mixing ratios but also on the assumed fractional contribution of air from the tropics and the extratropics. In order to test the sensitivity of the results on the assumed fractions, we have varied the fractional input. Figure 15 shows the Br_y, derived from CH_2Br_2 and $CHBr_3$ for the PGS campaign at 40 K above the tropopause, as a function of the assumed fractional contribution from the extratropical source region ($f^{ex\text{-}trop}$); the tropical fraction f^{trop} is then always $(1 - f^{ex\text{-}trop})$. A similar figure (Fig. S5) is shown for the WISE_TACTS dataset in the Supplement. While the differences are not very large for CH_2Br_2, which shows a much less pronounced latitudinal gradient, differences for $CHBr_3$ can be very large. This is particularly true for the EMAC model with the Warwick et al. (2006) scenario, where the dependency of Br_y on the fractional input behaves in an opposite way to the $CHBr_3$ observations and the other model-emission scenario combinations. This shows that for the calculation of Br_y in the lowermost stratosphere from observations, it is necessary to have a good knowledge of the relative contributions and that for models it is necessary to have a realistic representation not only of chemistry but also of transport in the lowermost stratosphere.

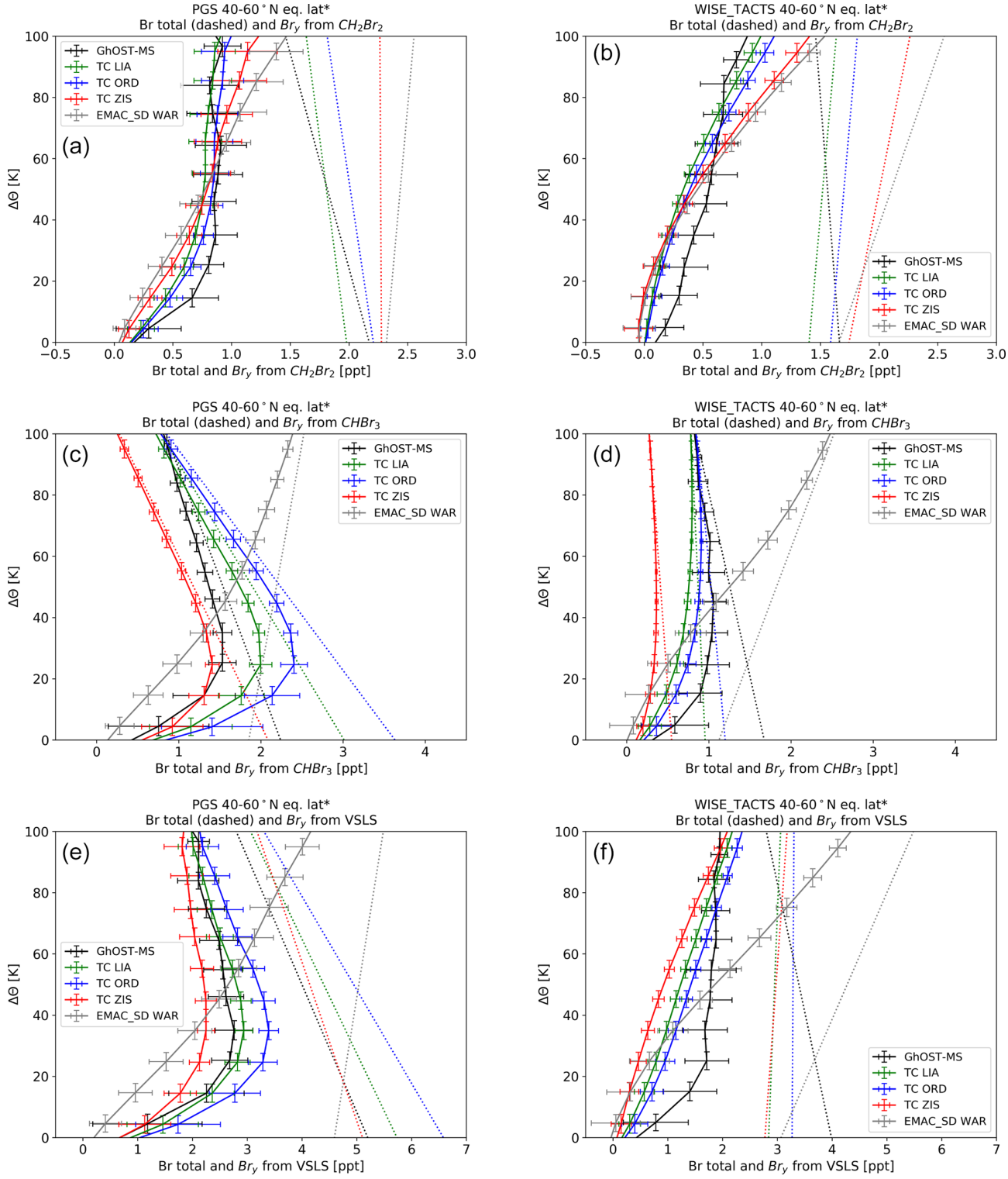

Figure 14. Vertical profiles of Br_y (solid lines) and total bromine (dotted lines) from CH_2Br_2, $CHBr_3$ and total organic VSLS bromine averaged over 40–60° of equivalent latitude* for the winter PGS campaign (**a, c, e**, late December 2015 to March 2016) and the period form late summer to early fall (**b, d, f**, WISE and TACTS campaigns) in comparison to model results from the TOMCAT and the EMAC model using different emission scenarios (see text for details on calculation of Br_y). Total bromine is calculated from data at the tropical and extratropical tropopause and using assumptions about fractional input from these two source regions (see text for details). The data are displayed as a function of potential temperature above the tropopause. In the case when no model information on the tropopause altitude was available (TOMCAT), climatological tropopause values have been used (see text for details).

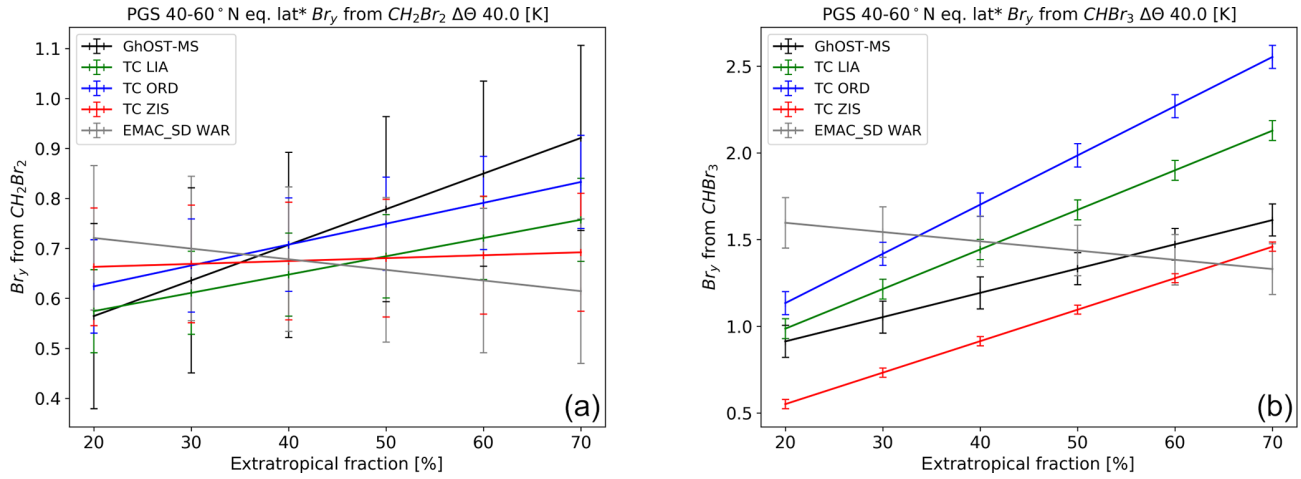

Figure 15. Sensitivity of Br_y from CH_2Br_2 and $CHBr_3$ at $\Delta\theta = 40$ K as a function of the fraction of extratropical air for the PGS campaign from January to April 2016 for observations in comparison to the different model calculations.

6 Summary and outlook

We present a large dataset of around 4000 in situ measurements of five brominated VSLS with the GhOST-MS instrument in the UTLS region using HALO. We used data from the three HALO missions: TACTS, WISE and PGS. Data are presented in tropopause-relative coordinates, i.e. the difference in potential temperature relative to the dynamical tropopause, defined by the value of 2 PVU. Stratospheric data are sorted by equivalent latitude, while we used normal latitude for tropospheric data. We find systematic variabilities with latitude, altitude and season. The shortest-lived VSLS mixing ratios decrease fastest with altitude. During polar winter, vertical gradients are larger than during late summer to early fall, which is in line with the well-known diabatic descent of stratospheric air during polar winter. An important aspect of the observed distributions is that $CHBr_3$ mixing ratios at the extratropical tropopause are systematically higher than those at the tropical tropopause. A similar feature is found for CH_2Br_2, although the latitudinal gradient is less pronounced than in the case of $CHBr_3$. The increase of VSLS mole fractions is especially clear during northern hemispheric winter, when lifetimes become very long at high latitudes.

We further compared the observed distributions with a range of modelled distributions from TOMCAT and EMAC, run with different global emission scenarios. The features of the observed distribution are partly reproduced by the model calculations, with large differences caused by the different emissions. Overall, for CH_2Br_2, we find much better agreement between observations and model output for simulations using the emission scenarios by Liang et al. (2010) and Ordóñez et al. (2012), which have lower overall emissions than the scenarios by Ziska et al. (2013) and Warwick et al. (2006). This is in agreement with a recently proposed revision of the best estimate of global CH_2Br_2 emissions towards the lower edge of previous estimates (Engel and Rigby, 2018) . In the case of $CHBr_3$, the use of the emission scenario by Ziska et al. (2013), which has the lowest global emissions, results in mixing ratios that are too low at the tropical tropopause and also at the extratropical tropopause. The use of the emission scenario by Warwick et al. (2006) results in strongly elevated mixing ratios of $CHBr_3$ at the tropical tropopause and a reversed latitudinal gradient at the tropopause in comparison to the observations. These findings are in good agreement with previous comparisons of the different emission scenarios (Hossaini et al., 2013, 2016) for CH_2Br_2. For $CHBr_3$, Hossaini et al. (2016) found that the lower emissions in the Ziska et al. (2013) scenario generally gave best agreement with ground-based observations in the tropics. However, the tropopause mixing ratios derived with this scenario are too low, both in the tropics and in the extratropics. In a recent paper, Fiehn et al. (2018) discussed that a modified version of the Ziska et al. (2013) scenario, with seasonally varying emissions, yielded significantly higher tropopause values. The Ordóñez et al. (2012) scenario, which has higher emissions than the Ziska et al. (2013) scenario, yielded mixing ratios of $CHBr_3$ that are too high during the winter period. It is clear that no scenario is able to capture tropical and extratropical values from our observations. However, it is clear from the comparison with the scenario by Warwick et al. (2006), which restricts emissions to latitudes below 50°, that the sources of these short-lived brominated compounds are not only in the tropics, because significant emissions must also occur at higher latitudes. This is consistent with comparison of tropospheric data (see Fig. 6 in Hossaini et al., 2013). For improved emission scenarios, more emphasis on the seasonality of the sources might also lead to an improvement.

Air in the lowermost stratosphere is composed of air masses originating from both the tropical and the extratropical upper troposphere. The latitudinal gradient of VSLS will therefore impact the amount of bromine transported into the stratosphere and thus also the amount of reactive, inorganic bromine (Br_y) in the lowermost stratosphere able to contribute to catalytic ozone depletion. The bromine budget in the lower stratosphere will depend on the relative fraction of air from the tropical and extratropical tropopause. The relative contribution of extratropical air decreases with latitude and reaches zero at about 400 K potential temperature. Using simplified assumptions about the fractional distributions, we derive substantial differences in stratospheric Br_y, depending on the emission scenario. These can be as high as 2 ppt, corresponding to a difference of a factor of 2 relative to observation-derived values, when using the scenario by Warwick et al. (2006). Typical differences in Br_y when using the other scenarios are on the order of 1 ppt. This is expected to have an impact on modelled ozone depletion in the lower stratosphere. For example, it has been shown that inclusion of about 5 ppt of Br_y from VSLS leads to an expansion of the ozone hole area of $\sim 5 \times 10^6$ km^2 and an increase in maximum Antarctic ozone hole depletion by up to 14 % (Fernandez et al., 2017). The impact of bromine on ozone is most pronounced in the lowest part of the stratosphere (Hossaini et al., 2015). Further, as the efficiency of bromine to destroy ozone depends on the amount of available chlorine, it is also likely that modelled temporal trends of ozone will be influenced, even if there are no long-term changes in VSLS bromine. If relative contributions of the different pathways (tropical vs. extratropical air) change, e.g. due to changes in stratospheric circulation, this could further influence ozone due to the different amounts of bromine in these air masses. As shown in our sensitivity study (Sect. 5), the assumptions on the relative contribution of the different source regions has a substantial impact especially on the Br_y produced from $CHBr_3$ in the lowermost stratosphere.

While the dataset presented here provides a much better picture of the distribution of brominated VSLS in the UTLS region than previously available, there are still considerable gaps in our knowledge of the distribution of these species. Only data in late summer to fall and winter have been presented here for the Northern Hemisphere. Spring and early summer are less well covered, as is the Southern Hemisphere. Southern hemispheric distributions are expected to differ from northern hemispheric distributions, as the main sources of many brominated VSLS are believed to be from coastal ocean regions. Due to the different distribution of oceans, land and coastal areas between the hemispheres, it is not possible to extrapolate northern hemispheric observations to the Southern Hemisphere. Further, while no signs of increasing emissions of natural brominated VSLS have been observed so far, such an increase is possible in a changing climate and needs to be monitored.

Data availability. The observational data are available via the HALO Database (halo-db.pa.op.dlr.de/). The data of the ESCiMo simulations using the EMAC model will be made available in the Climate and Environmental Retrieval and Archive (CERA) database at the German Climate Computing Centre (DKRZ; https://cera-www.dkrz.de, Jöckel et al., 2016); the simulations results of Graf (2017) are available upon request. TOMCAT model data will be uploaded to the Lancaster University data repository upon article acceptance. Access to data may be dependent on the signature of a data protocol.

Supplement. The supplement related to this article is available online at: https://doi.org/10.5194/acp-20-4105-2020-supplement.

Author contributions. TK, FO, HB and AE were involved in developing the GhOST instrument and operating it in the field during the missions, data evaluation and interpretation. FL, MH and TS were also involved in the operation, evaluation and interpretation. NS, AR and CH were involved in the evaluation and interpretation. RH, PG and PJ have provided model data and also participated in the discussion of the data and the comparisons. AE and TK have mainly written the article. All co-authors were involved in the discussion and iterations of the article.

Competing interests. The authors declare that they have no conflict of interest.

Acknowledgements. The work carried out at the University Frankfurt has been funded through several projects by the German Science Foundation (DFG) for the development and operation of GHOST-MS and for the measurement campaigns (EN367/5, EN367/8, EN367/11, EN367/13 and EN367/14). Andreas Engel would like to thank CSIRO in Aspendale, Australia, for a Frohlich Fellowship, during which parts of this analysis was performed. Many thanks also to Kieran Stanley for proof reading and improving the article. We would further like to thank the DLR staff, including pilots and ground staff, for the operation of HALO and the support during the campaigns. The good collaboration with the other groups involved in the HALO campaigns is also acknowledged. We would like to thank Andreas Zahn from KIT Karlsruhe for provision of the ozone data in Fig. 3. We further thank Jens-Uwe Grooß from Forschungszentrum Jülich for the calculation of the tropopause and equivalent latitude for the HALO campaigns and Michael Sprenger from ETH Zürich for the provision of the climatological dynamical tropopause from ERA-Interim data. Ryan Hossaini is supported by a NERC Independent Research Fellowship (NE/N014375/1). The EMAC simulations have been performed at the German Climate Computing Centre (DKRZ) through support from the Bundesministerium für Bildung und Forschung (BMBF). DKRZ and its scientific steering committee are gratefully acknowledged for providing the high-performance computing and data archiving resources for this consortial project (ESCiMo: Earth System Chemistry integrated Modelling).

Financial support. This research has been supported by the Deutsche Forschungsgemeinschaft (DFG) (grant nos. EN367/5, EN367/8, EN367/11, EN367/13 and EN367/14).

Review statement. This paper was edited by Farahnaz Khosrawi and reviewed by Rafael Pedro Fernandez, Stefanie Falk, and one anonymous referee.

References

Appenzeller, C., Holton, J. R., and Rosenlof, K. H.: Seasonal variation of mass transport across the tropopause, J. Geophys. Res.-Atmos., 101, 15071–15078, 1996.

Ball, W. T., Alsing, J., Mortlock, D. J., Staehelin, J., Haigh, J. D., Peter, T., Tummon, F., Stübi, R., Stenke, A., Anderson, J., Bourassa, A., Davis, S. M., Degenstein, D., Frith, S., Froidevaux, L., Roth, C., Sofieva, V., Wang, R., Wild, J., Yu, P., Ziemke, J. R., and Rozanov, E. V.: Evidence for a continuous decline in lower stratospheric ozone offsetting ozone layer recovery, Atmos. Chem. Phys., 18, 1379–1394, https://doi.org/10.5194/acp-18-1379-2018, 2018.

Bönisch, H., Hoor, P., Gurk, C., Feng, W., Chipperfield, M., Engel, A., and Bregman, B.: Model evaluation of CO_2 and SF6 in the extratropical UT/LS region, J. Geophys. Res.-Atmos., 113, D06101, https://doi.org/10.1029/2007jd008829, 2008.

Bönisch, H., Engel, A., Curtius, J., Birner, Th., and Hoor, P.: Quantifying transport into the lowermost stratosphere using simultaneous in-situ measurements of SF_6 and CO_2, Atmos. Chem. Phys., 9, 5905–5919, https://doi.org/10.5194/acp-9-5905-2009, 2009.

Bönisch, H., Engel, A., Birner, T., Hoor, P., Tarasick, D. W., and Ray, E. A.: On the structural changes in the Brewer-Dobson circulation after 2000, Atmos. Chem. Phys., 11, 3937–3948, https://doi.org/10.5194/acp-11-3937-2011, 2011.

Boothe, A. C. and Homeyer, C. R.: Global large-scale stratosphere–troposphere exchange in modern reanalyses, Atmos. Chem. Phys., 17, 5537–5559, https://doi.org/10.5194/acp-17-5537-2017, 2017.

Burkholder, J. B.: (Lead Author) Hodnebrog, Ø., and Orkin, V. L.: Summary of Abundances, Lifetimes, Ozone Depletion Potentials (ODPs), Radiative Efficiencies (REs), Global Warming Potentials (GWPs), and Global Temperature change Potentials (GTPs) Appendix 1 to Scientific Assessment of Ozone Depletion: 2018, Global Ozone Research and Monitoring Project-Report No. 58, World Meteorological Organization, Geneva, Switzerland, 2018.

Burkholder, J. B., Sander, S. P., Abbatt, J., Barker, J. R., Huie, R. E., Kolb, C. E., Kurylo, M. J., Orkin, V. L., Wilmouth, D. M., and Wine, P. H. C. K. A. P. D. F. U. I. A. S.: Chemical kinetics and photochemical data for use in atmospheric studies, Evaluation number 18, JPL Publication 15-10, Jet Propulsion Laboratory, 2015.

Carpenter, L. J., Reimann, S., Burkholder, J. B., Clerbaux, C., Hall, B. D., Hossaini, R., Laube, J. C., and Yvon-Lewis, S. A.: Ozone-Depleting Substances (ODSs) and Other Gases of Interest to the Montreal Protocol, Chapter 1 in *Scientific Assessment of Ozone Depletion: 2014*, Global Ozone Research and Monitoring Project – Report No. 55, World Meteorological Organization, Geneva, Switzerland, 2014.

Chipperfield, M. P.: New version of the TOMCAT/SLIMCAT off-line chemical transport model: Intercomparison of stratospheric tracer experiments, Q. J. Roy. Meteor. Soc., 132, 1179–1203, https://doi.org/10.1256/qj.05.51, 2006.

Chipperfield, M. P., Dhomse, S., Hossaini, R., Feng, W., Santee, M. L., Weber, M., Burrows, J. P., Wild, J. D., Loyola, D., and Coldewey-Egbers, M.: On the Cause of Recent Variations in Lower Stratospheric Ozone, Geophys. Res. Lett., 45, 5718–5726, https://doi.org/10.1029/2018GL078071, 2018.

Daniel, J. S., and Velders, G. J. M., Douglass, A. R., Forster, P. M. D., Hauglustaine, D. A., Isaksen, I. S. A., Kuijpers, L. J. M., Mc-Culloch, A., and Wallington, T.: JHalocarbon scenarios, ozonedepletion potentials, and global warming potentials, chap. 8, in: World Meteorological Organization: Scientific assessment ofozone depletion: 2006, Global Ozone Research and MonitoringProject – Report No. 50, Geneva, 2006.

Dee, D. P., Uppala, S. M., Simmons, A. J., Berrisford, P., Poli, P., Kobayashi, S., Andrae, U., Balmaseda, M. A., Balsamo, G., Bauer, P., Bechtold, P., Beljaars, A. C. M., van de Berg, L., Bidlot, J., Bormann, N., Delsol, C., Dragani, R., Fuentes, M., Geer, A. J., Haimberger, L., Healy, S. B., Hersbach, H., Hólm, E. V., Isaksen, L., Kållberg, P., Köhler, M., Matricardi, M., McNally, A. P., Monge-Sanz, B. M., Morcrette, J.-J., Park, B.-K., Peubey, C., de Rosnay, P., Tavolato, C., Thépaut, J.-N., and Vitart, F.: The ERA-Interim reanalysis: configuration and performance of the data assimilation system, Q. J. Roy. Meteor. Soc., 137, 553–597, https://doi.org/10.1002/qj.828, 2011.

Dhomse, S. S., Chipperfield, M. P., Feng, W., Hossaini, R., Mann, G. W., and Santee, M. L.: Revisiting the hemispheric asymmetry in midlatitude ozone changes following the Mount Pinatubo eruption: A 3-D model study, Geophys. Res. Lett., 42, 3038–3047, https://doi.org/10.1002/2015gl063052, 2015.

Engel, A. and Rigby, M., Burkholder, J. B., Fernandez, R. P., Froidevaux, L., Hall, B. D., Hossaini, R., Saito, T., Vollmer, M. K., and Yao, B.: Update on Ozone-Depleting Substances (ODS) and Other Gases of Interest to the Montreal Protocol, chap. 1, in: Scientific Assessment of Ozone Depletion: 2018, Global Ozone Research and Monitoring Project-Report No. 58, World Meteorological Organization, Geneva, Switzerland, 2018.

Engel, A., Bönisch, H., Brunner, D., Fischer, H., Franke, H., Günther, G., Gurk, C., Hegglin, M., Hoor, P., Königstedt, R., Krebsbach, M., Maser, R., Parchatka, U., Peter, T., Schell, D., Schiller, C., Schmidt, U., Spelten, N., Szabo, T., Weers, U., Wernli, H., Wetter, T., and Wirth, V.: Highly resolved observations of trace gases in the lowermost stratosphere and upper troposphere from the Spurt project: an overview, Atmos. Chem. Phys., 6, 283–301, https://doi.org/10.5194/acp-6-283-2006, 2006.

Falk, S., Sinnhuber, B. M., Krysztofiak, G., Jöckel, P., Graf, P., and Lennartz, S. T.: Brominated VSLS and their influence on ozone under a changing climate, Atmos. Chem. Phys., 17, 11313–11329, https://doi.org/10.5194/acp-17-11313-2017, 2017.

Farman, J. C., Gardiner, B. G., and Shanklin, J. D.: Large Losses of Total Ozone in Antarctica Reveal Seasonal Clox/Nox Interaction, Nature, 315, 207–210, https://doi.org/10.1038/315207a0, 1985.

Feng, W., Chipperfield, M. P., Dorf, M., Pfeilsticker, K., and Ricaud, P.: Mid-latitude ozone changes: studies with a 3-D CTM forced by ERA-40 analyses, Atmos. Chem. Phys., 7, 2357–2369, https://doi.org/10.5194/acp-7-2357-2007, 2007.

Fernandez, R. P., Salawitch, R. J., Kinnison, D. E., Lamarque, J. F., and Saiz-Lopez, A.: Bromine partitioning in the tropical tropopause layer: implications for stratospheric injection, Atmos. Chem. Phys., 14, 13391–13410, https://doi.org/10.5194/acp-14-13391-2014, 2014.

Fernandez, R. P., Kinnison, D. E., Lamarque, J.-F., Tilmes, S., and Saiz-Lopez, A.: Impact of biogenic very short-lived bromine on the Antarctic ozone hole during the 21st century, Atmos. Chem. Phys., 17, 1673–1688, https://doi.org/10.5194/acp-17-1673-2017, 2017.

Fiehn, A., Quack, B., Hepach, H., Fuhlbrügge, S., Tegtmeier, S., Toohey, M., Atlas, E., and Krüger, K.: Delivery of halogenated very short-lived substances from the west Indian Ocean to the stratosphere during the Asian summer monsoon, Atmos. Chem. Phys., 17, 6723–6741, https://doi.org/10.5194/acp-17-6723-2017, 2017.

Fiehn, A., Quack, B., Stemmler, I., Ziska, F., and Krüger, K.: Importance of seasonally resolved oceanic emissions for bromoform delivery from the tropical Indian Ocean and west Pacific to the stratosphere, Atmos. Chem. Phys., 18, 11973–11990, https://doi.org/10.5194/acp-18-11973-2018, 2018.

Fischer, H., Wienhold, F. G., Hoor, P., Bujok, O., Schiller, C., Siegmund, P., Ambaum, M., Scheeren, H. A., and Lelieveld, J.: Tracer correlations in the northern high latitude lowermost stratosphere: Influence of cross-tropopause mass exchange, Geophys. Res. Lett., 27, 97–100, 2000.

Gettelman, A., Hoor, P., Pan, L. L., Randel, W. J., Hegglin, M. I., and Birner, T.: The extratropical upper troposphere and lower stratosphere, Rev. Geophys., 49, RG3003, https://doi.org/10.1029/2011rg000355, 2011.

Graf, P.: The impact of very short-lived substances on the stratospheric chemistry and interactions with the climate, Ph.D. thesis, Ludwig-Maximilians-Universität München, 123 pp., http://nbn-resolving.de/urn:nbn:de:bvb:19-207510 (last access: 30 March 2020), 2017.

Harris, N. R. P., Kyrö, E., Staehelin, J., Brunner, D., Andersen, S. B., Godin-Beekmann, S., Dhomse, S., Hadjinicolaou, P., Hansen, G., Isaksen, I., Jrrar, A., Karpetchko, A., Kivi, R., Knudsen, B., Krizan, P., Lastovicka, J., Maeder, J., Orsolini, Y., Pyle, J. A., Rex, M., Vanicek, K., Weber, M., Wohltmann, I., Zanis, P., and Zerefos, C.: Ozone trends at northern mid- and high latitudes – a European perspective, Ann. Geophys., 26, 1207–1220, https://doi.org/10.5194/angeo-26-1207-2008, 2008.

Holton, J. R., Haynes, P. H., Mcintyre, M. E., Douglass, A. R., Rood, R. B., and Pfister, L.: Stratosphere-Troposphere Exchange, Rev. Geophys., 33, 403–439, 1995.

Hoor, P., Fischer, H., and Lelieveld, J.: Tropical and extratropical tropospheric air in the lowermost stratosphere over Europe: A CO-based budget, Geophys. Res. Lett., 32, L07802, https://doi.org/10.1029/2004gl022018, 2005.

Hossaini, R., Chipperfield, M. P., Monge-Sanz, B. M., Richards, N. A. D., Atlas, E., and Blake, D. R.: Bromoform and dibromomethane in the tropics: a 3-D model study of chemistry and transport, Atmos. Chem. Phys., 10, 719–735, https://doi.org/10.5194/acp-10-719-2010, 2010.

Hossaini, R., Chipperfield, M. P., Feng, W., Breider, T. J., Atlas, E., Montzka, S. A., Miller, B. R., Moore, F., and Elkins, J.: The contribution of natural and anthropogenic very short-lived species to stratospheric bromine, Atmos. Chem. Phys., 12, 371–380, https://doi.org/10.5194/acp-12-371-2012, 2012.

Hossaini, R., Mantle, H., Chipperfield, M. P., Montzka, S. A., Hamer, P., Ziska, F., Quack, B., Krüger, K., Tegtmeier, S., Atlas, E., Sala, S., Engel, A., Bönisch, H., Keber, T., Oram, D., Mills, G., Ordóñez, C., Saiz-Lopez, A., Warwick, N., Liang, Q., Feng, W., Moore, F., Miller, B. R., Marécal, V., Richards, N. A. D., Dorf, M., and Pfeilsticker, K.: Evaluating global emission inventories of biogenic bromocarbons, Atmos. Chem. Phys., 13, 11819–11838, https://doi.org/10.5194/acp-13-11819-2013, 2013.

Hossaini, R., Chipperfield, M. P., Montzka, S. A., Rap, A., Dhomse, S., and Feng, W.: Efficiency of short-lived halogens at influencing climate through depletion of stratospheric ozone, Nat. Geosci., 8, 186–190, https://doi.org/10.1038/ngeo2363, 2015.

Hossaini, R., Patra, P. K., Leeson, A. A., Krysztofiak, G., Abraham, N. L., Andrews, S. J., Archibald, A. T., Aschmann, J., Atlas, E. L., Belikov, D. A., Bönisch, H., Carpenter, L. J., Dhomse, S., Dorf, M., Engel, A., Feng, W., Fuhlbruegge, S., Griffiths, P. T., Harris, N. R. P., Hommel, R., Keber, T., Krueger, K., Lennartz, S. T., Maksyutov, S., Mantle, H., Mills, G. P., Miller, B., Montzka, S. A., Moore, F., Navarro, M. A., Oram, D. E., Pfeilsticker, K., Pyle, J. A., Quack, B., Robinson, A. D., Saikawa, E., Saiz-Lopez, A., Sala, S., Sinnhuber, B.-M., Taguchi, S., Tegtmeier, S., Lidster, R. T., Wilson, C., and Ziska, F.: A multi-model intercomparison of halogenated very short-lived substances (TransCom-VSLS): linking oceanic emissions and tropospheric transport for a reconciled estimate of the stratospheric source gas injection of bromine, Atmos. Chem. Phys., 16, 9163–9187, https://doi.org/10.5194/acp-16-9163-2016, 2016.

Hossaini, R., Chipperfield, M. P., Montzka, S. A., Leeson, A. A., Dhomse, S. S., and Pyle, J. A.: The increasing threat to stratospheric ozone from dichloromethane, Nat. Commun., 8, 15962, https://doi.org/10.1038/ncomms15962, 2017.

Hossaini, R., Atlas, E., Dhomse, S. S., Chipperfield, M. P., Bernath, P. F., Fernando, A. M., Mühle, J., Leeson, A. A., Montzka, S. A., Feng, W., Harrison, J. J., Krummel, P., Vollmer, M. K., Reimann, S., O'Doherty, S., Young, D., Maione, M., Arduini, J., and Lunder, C. R.: Recent Trends in Stratospheric Chlorine From Very Short-Lived Substances, J. Geophys. Res.-Atmos., 124, 2318–2335, https://doi.org/10.1029/2018jd029400, 2019.

Jöckel, P., Tost, H., Pozzer, A., Kunze, M., Kirner, O., Brenninkmeijer, C. A. M., Brinkop, S., Cai, D. S., Dyroff, C., Eckstein, J., Frank, F., Garny, H., Gottschaldt, K. D., Graf, P., Grewe, V., Kerkweg, A., Kern, B., Matthes, S., Mertens, M., Meul, S., Neumaier, M., Nützel, M., Oberländer-Hayn, S., Ruhnke, R., Runde, T., Sander, R., Scharffe, D., and Zahn, A.: Earth System Chemistry integrated Modelling (ESCiMo) with the Modular Earth Submodel System (MESSy) version 2.51, Geosci. Model Dev., 9, 1153–1200, https://doi.org/10.5194/gmd-9-1153-2016, 2016.

Leedham Elvidge, E. C., Oram, D. E., Laube, J. C., Baker, A. K., Montzka, S. A., Humphrey, S., O'Sullivan, D. A., and Brenninkmeijer, C. A. M.: Increasing concentrations of dichloromethane, CH_2Cl_2, inferred from CARIBIC air samples collected 1998–2012, Atmos. Chem. Phys., 15, 1939–1958, https://doi.org/10.5194/acp-15-1939-2015, 2015.

Liang, Q., Stolarski, R. S., Kawa, S. R., Nielsen, J. E., Douglass, A. R., Rodriguez, J. M., Blake, D. R., Atlas, E. L., and Ott, L. E.: Finding the missing stratospheric Bry: a global modeling study

of $CHBr_3$ and CH_2Br_2, Atmos. Chem. Phys., 10, 2269–2286, https://doi.org/10.5194/acp-10-2269-2010, 2010.

Liang, Q., Atlas, E., Blake, D., Dorf, M., Pfeilsticker, K., and Schauffler, S.: Convective transport of very short lived bromocarbons to the stratosphere, Atmos. Chem. Phys., 14, 5781–5792, https://doi.org/10.5194/acp-14-5781-2014, 2014.

Molina, M. J. and Rowland, F. S.: Stratospheric Sink for Chlorofluoromethanes – Chlorine Atomic-Catalysed Destruction of Ozone, Nature, 249, 810–812, https://doi.org/10.1038/249810a0, 1974.

Monks, S. A., Arnold, S. R., Hollaway, M. J., Pope, R. J., Wilson, C., Feng, W., Emmerson, K. M., Kerridge, B. J., Latter, B. L., Miles, G. M., Siddans, R., and Chipperfield, M. P.: The TOMCAT global chemical transport model v1.6: description of chemical mechanism and model evaluation, Geosci. Model Dev., 10, 3025–3057, https://doi.org/10.5194/gmd-10-3025-2017, 2017.

Montzka, S. A., Dutton, G. S., Yu, P., Ray, E., Portmann, R. W., Daniel, J. S., Kuijpers, L., Hall, B. D., Mondeel, D., Siso, C., Nance, J. D., Rigby, M., Manning, A. J., Hu, L., Moore, F., Miller, B. R., and Elkins, J. W.: An unexpected and persistent increase in global emissions of ozone-depleting CFC-11, Nature, 557, 413–417, https://doi.org/10.1038/s41586-018-0106-2, 2018.

Obersteiner, F., Bönisch, H., Keber, T., O'Doherty, S., and Engel, A.: A versatile, refrigerant- and cryogen-free cryofocusing–thermodesorption unit for preconcentration of traces gases in air, Atmos. Meas. Tech., 9, 5265–5279, https://doi.org/10.5194/amt-9-5265-2016, 2016.

Oman, L. D., Douglass, A. R., Salawitch, R. J., Canty, T. P., Ziemke, J. R., and Manyin, M.: The effect of representing bromine from VSLS on the simulation and evolution of Antarctic ozone, Geophys. Res. Lett., 43, 9869–9876, https://doi.org/10.1002/2016gl070471, 2016.

Oram, D. E., Ashfold, M. J., Laube, J. C., Gooch, L. J., Humphrey, S., Sturges, W. T., Leedham-Elvidge, E., Forster, G. L., Harris, N. R. P., Mead, M. I., Samah, A. A., Phang, S. M., Ou-Yang, C. F., Lin, N. H., Wang, J. L., Baker, A. K., Brenninkmeijer, C. A. M., and Sherry, D.: A growing threat to the ozone layer from short-lived anthropogenic chlorocarbons, Atmos. Chem. Phys., 17, 11929–11941, https://doi.org/10.5194/acp-17-11929-2017, 2017.

Ordóñez, C., Lamarque, J. F., Tilmes, S., Kinnison, D. E., Atlas, E. L., Blake, D. R., Santos, G. S., Brasseur, G., and Saiz-Lopez, A.: Bromine and iodine chemistry in a global chemistry-climate model: description and evaluation of very short-lived oceanic sources, Atmos. Chem. Phys., 12, 1423–1447, https://doi.org/10.5194/acp-12-1423-2012, 2012.

Ray, E. A., Moore, F. L., Elkins, J. W., Dutton, G. S., Fahey, D. W., Vomel, H., Oltmans, S. J., and Rosenlof, K. H.: Transport into the Northern Hemisphere lowermost stratosphere revealed by in situ tracer measurements, J. Geophys. Res.-Atmos., 104, 26565–26580, https://doi.org/10.1029/1999jd900323, 1999.

Rigby, M., Park, S., Saito, T., Western, L. M., Redington, A. L., Fang, X., Henne, S., Manning, A. J., Prinn, R. G., Dutton, G. S., Fraser, P. J., Ganesan, A. L., Hall, B. D., Harth, C. M., Kim, J., Kim, K. R., Krummel, P. B., Lee, T., Li, S., Liang, Q., Lunt, M. F., Montzka, S. A., Mühle, J., O'Doherty, S., Park, M. K., Reimann, S., Salameh, P. K., Simmonds, P., Tunnicliffe, R. L., Weiss, R. F., Yokouchi, Y., and Young, D.: Increase in CFC-11 emissions from eastern China based on atmospheric observations, Nature, 569, 546–550, https://doi.org/10.1038/s41586-019-1193-4, 2019.

Sala, S.: Entwicklung und Einsatz eines flugzeuggetragenen GC/MS – Systems zum Nachweis halogenierter Kohlenwasserstoffe in der Atmosphäre, PhD Thesis, Goethe University Frankfurt, Frankfurt, Germany, 206 pp., 2014.

Sala, S., Bönisch, H., Keber, T., Oram, D. E., Mills, G., and Engel, A.: Deriving an atmospheric budget of total organic bromine using airborne in situ measurements from the western Pacific area during SHIVA, Atmos. Chem. Phys., 14, 6903–6923, https://doi.org/10.5194/acp-14-6903-2014, 2014.

Salawitch, R. J., Weisenstein, D. K., Kovalenko, L. J., Sioris, C. E., Wennberg, P. O., Chance, K., Ko, M. K. W., and McLinden, C. A.: Sensitivity of ozone to bromine in the lower stratosphere, Geophys. Res. Lett., 32, L05811, https://doi.org/10.1029/2004gl021504, 2005.

Sinnhuber, B.-M. and Meul, S.: Simulating the impact of emissions of brominated very short lived substances on past stratospheric ozone trends, Geophys. Res. Lett., 42, 2449–2456, https://doi.org/10.1002/2014GL062975, 2015.

Sinnhuber, B.-M., Sheode, N., Sinnhuber, M., Chipperfield, M. P., and Feng, W.: The contribution of anthropogenic bromine emissions to past stratospheric ozone trends: a modelling study, Atmos. Chem. Phys., 9, 2863–2871, https://doi.org/10.5194/acp-9-2863-2009, 2009.

Škerlak, B., Sprenger, M., and Wernli, H.: A global climatology of stratosphere–troposphere exchange using the ERA-Interim data set from 1979 to 2011, Atmos. Chem. Phys., 14, 913–937, https://doi.org/10.5194/acp-14-913-2014, 2014.

Škerlak, B., Sprenger, M., Pfahl, S., Tyrlis, E., and Wernli, H.: Tropopause folds in ERA-Interim: Global climatology and relation to extreme weather events, J. Geophys. Res.-Atmos., 120, 4860–4877, https://doi.org/10.1002/2014jd022787, 2015.

Solomon, S.: Stratospheric ozone depletion: A review of concepts and history, Rev. Geophys., 37, 275–316, 1999.

Sprenger, M., Fragkoulidis, G., Binder, H., Croci-Maspoli, M., Graf, P., Grams, C. M., Knippertz, P., Madonna, E., Schemm, S., Škerlak, B., and Wernli, H.: Global Climatologies of Eulerian and Lagrangian Flow Features based on ERA-Interim, B. Am. Meteorol. Soc., 98, 1739–1748, https://doi.org/10.1175/bams-d-15-00299.1, 2017.

Steinbrecht, W., Froidevaux, L., Fuller, R., Wang, R., Anderson, J., Roth, C., Bourassa, A., Degenstein, D., Damadeo, R., Zawodny, J., Frith, S., McPeters, R., Bhartia, P., Wild, J., Long, C., Davis, S., Rosenlof, K., Sofieva, V., Walker, K., Rahpoe, N., Rozanov, A., Weber, M., Laeng, A., von Clarmann, T., Stiller, G., Kramarova, N., Godin-Beekmann, S., Leblanc, T., Querel, R., Swart, D., Boyd, I., Hocke, K., Kämpfer, N., Maillard Barras, E., Moreira, L., Nedoluha, G., Vigouroux, C., Blumenstock, T., Schneider, M., García, O., Jones, N., Mahieu, E., Smale, D., Kotkamp, M., Robinson, J., Petropavlovskikh, I., Harris, N., Hassler, B., Hubert, D., and Tummon, F.: An update on ozone profile trends for the period 2000 to 2016, Atmos. Chem. Phys., 17, 10675–10690, https://doi.org/10.5194/acp-17-10675-2017, 2017.

Stohl, A., Bonasoni, P., Cristofanelli, P., Collins, W., Feichter, J., Frank, A., Forster, C., Gerasopoulos, E., Gäggeler, H., James, P., Kentarchos, T., Kromp-Kolb, H., Krüger, B., Land, C., Meloen, J., Papayannis, A., Priller, A., Seibert, P., Sprenger, M., Roelofs, G. J., Scheel, H. E., Schnabel, C., Siegmund, P., Tobler, L.,

Trickl, T., Wernli, H., Wirth, V., Zanis, P., and Zerefos, C.: Stratosphere-troposphere exchange: A review, and what we have learned from STACCATO, J. Geophys. Res.-Atmos., 108, 8516, https://doi.org/10.1029/2002jd002490, 2003.

Tegtmeier, S., Krüger, K., Quack, B., Atlas, E. L., Pisso, I., Stohl, A., and Yang, X.: Emission and transport of bromocarbons: from the West Pacific ocean into the stratosphere, Atmos. Chem. Phys., 12, 10633–10648, https://doi.org/10.5194/acp-12-10633-2012, 2012.

Wales, P. A., Salawitch, R. J., Nicely, J. M., Anderson, D. C., Canty, T. P., Baidar, S., Dix, B., Koenig, T. K., Volkamer, R., Chen, D., Huey, L. G., Tanner, D. J., Cuevas, C. A., Fernandez, R. P., Kinnison, D. E., Lamarque, J.-F., Saiz-Lopez, A., Atlas, E. L., Hall, S. R., Navarro, M. A., Pan, L. L., Schauffler, S. M., Stell, M., Tilmes, S., Ullmann, K., Weinheimer, A. J., Akiyoshi, H., Chipperfield, M. P., Deushi, M., Dhomse, S. S., Feng, W., Graf, P., Hossaini, R., Jöckel, P., Mancini, E., Michou, M., Morgenstern, O., Oman, L. D., Pitari, G., Plummer, D. A., Revell, L. E., Rozanov, E., Saint-Martin, D., Schofield, R., Stenke, A., Stone, K. A., Visioni, D., Yamashita, Y., and Zeng, G.: Stratospheric Injection of Brominated Very Short-Lived Substances: Aircraft Observations in the Western Pacific and Representation in Global Models, J. Geophys. Res.-Atmos., 123, 5690–5719, https://doi.org/10.1029/2017JD027978, 2018.

Warwick, N. J., Pyle, J. A., Carver, G. D., Yang, X., Savage, N. H., O'Connor, F. M., and Cox, R. A.: Global modeling of biogenic bromocarbons, J. Geophys. Res.-Atmos., 111, D24305, https://doi.org/10.1029/2006jd007264, 2006.

Werner, A., Volk, C. M., Ivanova, E. V., Wetter, T., Schiller, C., Schlager, H., and Konopka, P.: Quantifying transport into the Arctic lowermost stratosphere, Atmos. Chem. Phys., 10, 11623–11639, https://doi.org/10.5194/acp-10-11623-2010, 2010.

Wernli, H. and Bourqui, M.: A Lagrangian "1-year climatology" of (deep) cross-tropopause exchange in the extratropical Northern Hemisphere, J. Geophys. Res.-Atmos., 107, 4021, https://doi.org/10.1029/2001jd000812, 2002.

WMO: (World Meteorological Organization), Scientific Assessment of Ozone Depletion: 2018, Global Ozone Research and Monitoring Project-Report No. 58, World Meteorological Organization, Geneva, Switzerland, 2018.

Wofsy, S. C., McElroy, M. B., and Yung, Y. L.: The chemistry of atmospheric bromine, Geophys. Res. Lett., 2, 215–218, https://doi.org/10.1029/GL002i006p00215, 1975.

Worton, D. R., Mills, G. P., Oram, D. E., and Sturges, W. T.: Gas chromatography negative ion chemical ionization mass spectrometry: Application to the detection of alkyl nitrates and halocarbons in the atmosphere, J. Chromatogr. A, 1201, 112–119, https://doi.org/10.1016/j.chroma.2008.06.019, 2008.

Zahn, A., Weppner, J., Widmann, H., Schlote-Holubek, K., Burger, B., Kühner, T., and Franke, H.: A fast and precise chemiluminescence ozone detector for eddy flux and airborne application, Atmos. Meas. Tech., 5, 363–375, https://doi.org/10.5194/amt-5-363-2012, 2012.

Ziska, F., Quack, B., Abrahamsson, K., Archer, S. D., Atlas, E., Bell, T., Butler, J. H., Carpenter, L. J., Jones, C. E., Harris, N. R. P., Hepach, H., Heumann, K. G., Hughes, C., Kuss, J., Krueger, K., Liss, P., Moore, R. M., Orlikowska, A., Raimund, S., Reeves, C. E., Reifenhaeuser, W., Robinson, A. D., Schall, C., Tanhua, T., Tegtmeier, S., Turner, S., Wang, L., Wallace, D., Williams, J., Yamamoto, H., Yvon-Lewis, S., and Yokouchi, Y.: Global sea-to-air flux climatology for bromoform, dibromomethane and methyl iodide, Atmos. Chem. Phys., 13, 8915–8934, https://doi.org/10.5194/acp-13-8915-2013, 2013.

Ziska, F., Quack, B., Tegtmeier, S., Stemmler, I., and Krüger, K.: Future emissions of marine halogenated very-short lived substances under climate change, J. Atmos. Chem., 74, 245–260, https://doi.org/10.1007/s10874-016-9355-3, 2017.